Geodätisch-geophysikalische Arbeiten in der Schweiz

(Fortsetzung der Publikationsreihe
«Astronomisch-geodätische Arbeiten in der Schweiz»)

herausgegeben von der

Schweizerischen Geodätischen Kommission
(Organ der Schweizerischen Akademie der Naturwissenschaften)

Neunundvierzigster Band
Volume 49

OPTICAL ASTROMETRY OF FAST MOVING OBJECTS USING CCD DETECTORS

Thomas Schildknecht

1994

Geodätisch-geophysikalische Arbeiten in der Schweiz

(Fortsetzung der Publikationsreihe
«Astronomisch-geodätische Arbeiten in der Schweiz»)

herausgegeben von der

Schweizerischen Geodätischen Kommission
(Organ der Schweizerischen Akademie der Naturwissenschaften)

Neunundvierzigster Band
Volume 49

OPTICAL ASTROMETRY OF FAST MOVING OBJECTS USING CCD DETECTORS

Thomas Schildknecht

1994

Adresse der Schweizerischen Geodätischen Kommission:

Institut für Geodäsie und Photogrammetrie
Eidg. Technische Hochschule Zürich
ETH-Hönggerberg
CH-8093 Zürich
Switzerland

Redaktion des 49. Bandes:
Dr. Th. Schildknecht
Dr. B. Bürki

Druck: OWADRUCK, CH - 3173 Oberwangen

VORWORT

Astrometrie, nach Prof. Jean Kovalevsky die Vermessung der Position der Gestirne einschliesslich ihrer Ausdehnung und Form, hat sich in den letzten 30 Jahren grundlegend gewandelt. In der optischen Himmelsbeobachtung wurde die Photographie abgelöst durch die CCD-Technik (Charge Coupled Devices). Zudem wurde die optische Astrometrie konkurrenziert von der Radiointerferometrie, welche heute einen Quasar-Katalog unerhörter Präzision anbietet.

In der Satellitengeodäsie wurde die Ära der optischen Beobachtung Mitte der 70-er Jahre abrupt durch das Zeitalter der Laser-Distanzmessung zu geodätischen Satelliten und das der Dopplermessung von Signalen aktiver Satelliten abgelöst. Bedauerlich ist, dass mit diesem Umbruch die Verankerung der Satellitengeodäsie in das Referenzsystem der Fixsterne verloren ging. Das Bezugssystem wird heute durch die Bewegungsgleichungen der Himmelsmechanik und durch die Radioastronomie nur indirekt in die Satellitengeodäsie eingebracht.

Die Realisierung des optischen Referenzsystems ist ein zentrales Motiv für die vorliegende Arbeit von Herrn Thomas Schildknecht: Das optische Referenzsystems der Fixsterne kann nämlich mit dem der Quasare mittelbar via optische und lasertelemetrische resp. Doppler- Beobachtungen zu künstlichen Erdsatelliten verknüpft werden. Das Prinzip ist einfach: durch optische Beobachtungen wird die Bahn der Satelliten im optischen Referenzsystem, durch die anderen Beobachtungen im quasarfesten System bestimmt.

Ein Vergleich der beiden Bahnen liefert -zum betreffenden Zeitpunkt- Elemente der Transformation zwischen beiden Systemen. Es war schon vor Inangriffnahme dieser Arbeit -der Inauguraldissertation von Herrn Schildknecht an der phil.-nat. Fakultät der Universität Bern- klar, dass diese die höchste Genauigkeit verlangende Aufgabe mit dem zur Verfügung stehenden Teleskop und den heutigen Sternkatalogen noch nicht in Angriff genommen werden konnte. Erst mit dem neuen Zimmerwalder 1m-Teleskop und dem HIPPARCOS Sternkatalog wird sich Herr Schildknecht mit seiner Gruppe mit dieser Problematik befassen können.

Die nötigen Voraussetzungen wurden indessen mit der vorliegenden Arbeit geschaffen: Herr Schildknecht hat die Beobachtungsmethodik von Grund auf neu erarbeitet. Die sehr kurzen Expositionen (Sekundenbruchteile und nicht zehn oder mehr Minuten wie in der photographischen Astrometrie oder bei den CCD Anwendungen in der Astrophysik), das sehr kleine nutzbare Gesichtsfeld (wenige Bogenminuten anstelle von fünf oder mehr Grad) sowie die sehr schnelle Bewegung der Messobjekte verlangen nach neuen und originellen Ansätzen für die mathematische Beschreibung der Abbildung des Himmels auf den CCD-Array. Dies gilt auch für die Erfassung kurzperiodischer Refraktionsanomalien.

Dass sich schon mit den bescheidenen, Herrn Schildknecht während der Arbeit zur Verfügung stehenden Hilfsmitteln durchaus interessante Resultate erzielen lassen, entnimmt man Kapitel 6. Die Vermessung geostationärer Satelliten unterstreicht auch eindrücklich die Bedeutung der neuen Technik für die Praxis: Viele Objekte dieser Art können nur mit optischen Hilfsmitteln mit der für eine genaue Bahnbestimmung und Positionierung notwendigen Genauigkeit erfasst werden.

Die vorliegende Abhandlung von Herrn Thomas Schildknecht darf als wichtiger Meilenstein für den Wiedereinstieg in die optische Astrometrie mit neuesten Methoden angesehen werden. Mit dem ab 1996 zur Verfügung stehenden neuen Teleskop der schweizerischen astronomisch-geodätischen Fundamentalstation Zimmerwald werden sich auch anspruchsvollste Projekte der optischen Fundamentalastronomie angehen lassen. Die Schweizerische Geodätische Kommission (SGK) dankt daher Herrn Dr. Th. Schildknecht für seinen zukunftsweisenden Beitrag.

Die Schweizerische Akademie der Naturwissenschaften (SANW) hat die Druckkosten dieses Bandes übenommen, wofür die SGK ihren Dank ausspricht.

Prof. Dr. G. Beutler
Direktor des Astronomischen Instituts der Universität Bern

Direktor F. Jeanrichard
Bundesamt für Landestopographie
Vizepräsident der SGK

Prof. Dr. H.-G. Kahle
ETH-Zürich
Präsident der SGK

PREFACE

L'astrométrie, qui selon la définition du professeur Jean Kovalevsky est la détermination de la position, de la dimension et de la forme des astres, a subi une transformation radicale durant les trente dernières années. La technique CCD (Charge coupled devices) a remplacé la photographie dans le domaine de l'observation du ciel et l'astronomie optique a été concurrencée par la radiointerférométrie qui permet aujourd'hui d'établir un catalogue des quasars d'une précision inouïe.

Dans le domaine de la géodésie par satellites, les observations optiques et les mesures DOPPLER ont été remplacées brusquement au milieu des années septante par des mesures de distances au LASER vers des satellites géodésiques. Il est regrettable que, par ce changement, la relation entre la géodésie par satellites et le système de référence formé par les étoiles fixes ait disparu. Le système de référence ne peut être réintroduit actuellement dans la géodésie par satellites qu'indirectement par les équations de mouvements de la mécanique céleste et par la radio-astronomie.

Le thème central du travail de Thomas Schildknecht est la réalisation d'un système optique de référence: le système de référence des étoiles fixes peut être relié à celui des quasars directement par des observations optiques et télémétriques avec LASER ou encore à l'aide d'observations DOPPLER sur satellites artificiels. Le principe est simple: l'orbite des satellites est déterminée dans le premier système de référence au moyen d'observations optiques et dans le système des quasars au moyen des autres observations.

La comparaison des orbites dans les deux systèmes permet, pour un moment donné, de calculer les éléments de la transformation entre les deux systèmes. Mais déjà avant de commencer ce travail - qui forme la thèse de M. Schildknecht présentée à la faculté des sciences naturelles de l'Université de Berne-, il est apparu que la précision exigée ne serait pas atteinte avec le téléscope et le catalogue d'étoiles actuels. Ce n'est qu'avec le nouveau téléscope à la focale d'un mètre et le catalogue d'étoiles HIPPARCOS que M. Schildknecht et son groupe pourront s'attaquer à ce problème.

Mais en attendant, le présent travail contribue à créer les conditions nécessaires à la poursuite des investigations: M. Schildknecht a réexaminé complètement la méthode d'observation. Les temps d'exposition très courts (des fractions de seconde et non plus dix minutes ou plus dans le cas d'astrométrie photographique ou d'application des techniques CCD en astrophysique), le champ visuel utilisable très restreint (quelques minutes d'arc au lieu de cinq degrés ou plus), ainsi que le mouvement très rapide des objets observés exigent des idées nouvelles et originales pour la description mathématique de la représentation du ciel sur des arrays CCD. Ceci vaut également pour la détection d'anomalies à courtes périodes de la réfraction.

Le chapitre 6 montre que M. Schildknecht a déjà atteint des résultats intéressants malgré les moyens modestes à disposition actuellement. La détermination de la position de satellites géostationaires souligne également de façon impressionnante l'importance de la nouvelle technique pour la pratique: de nombreux objets de ce genre ne peuvent être détectés qu'avec des moyens optiques qui seuls permettent d'obtenir une détermination d'orbite et un positionnement d'une précision suffisante.

Le présent ouvrage de M. Schildknecht représente une étappe importante pour la réhabilitation de l'astrométrie optique au moyen de méthodes les plus modernes. Le nouveau téléscope de la station fondamentale astro-géodésique de Zimmerwald, qui sera à disposition dès 1996, permettra de mettre en oeuvre des projets importants en astronomie optique fondamentale. La Commission géodésique suisse remercie sincèrement M. Thomas Schildknecht de sa précieuse contribution au développement futur de l'astronomie.

La Commission géodésique suisse exprime sa gratitude à l'Académie suisse des sciences naturelles (ASSN) pour la prise en charge des frais d'impression de ce volume.

Prof. Dr. G. Beutler
Directeur de l' Institut d'astronomie
de l' Université de Berne

F. Jeanrichard, Directeur
de l' Office fédéral de topographie
Vice-président de la CGS

Prof. Dr. H.-G. Kahle
ETH Zurich
Président de la CGS

PREFACE

Astrometry, according to Prof. Jean Kovalewsky the science of measuring position, velocity and shape of objects in the sky, underwent a profound change over the last 30 years. In the optical domain the photoghraphic plate was replaced by the CCD array (Charce Coupled Devices). In addition, radiointerferometry became a powerful competitor in astrometry: today a quasar catalogue of an unprecedented inner consistency and accuracy is available.

In satellite geodesy the optical era came to an abrupt end with the development of laser telemetry and with the use of the Doppler measurements of active satellites. Unfortunately satellite geodesy lost its direct observational relation to the celestial reference frame through this revolution. Today the reference frame is defined by radioastronomy and it enters only through the equations of motion into satellite geodesy.

The realization of a celestial reference frame was a central motivation for Thomas Schildknecht's PhD thesis: The optical reference frame, materialized by the stars, may be related to the quasar system using optical and laser (or Doppler) observations to artificial earth satellites. The principle is simple: the orbit of a satellite is established in the reference frame of the fixed stars through astrometrical observations, through laser and/or Doppler measurements in the quasar-fixed system.

A comparison of the two orbits gives us -as a function of time- the elements of the transformation between the two systems. It was clear at the outset that this task, asking for highest observational accuracy, could not be dealt with using the equipment and the star catalogues available to Thomas Schildknecht for his thesis. The situation will become more favourable in the near future when the new 1m astrometry telescope in Zimmerwald and the HIPPARCOS star catalogue will become available.

However, in this PhD thesis the tools for future more ambitious projects were prepared: the peculiarities of earth-bound CCD astrometry, namely short exposure times, a small field of view, and short period refraction anomalies, led to a completely new observational concept. In particular, the mapping of the sky to the CCD array had to be carefully analyzed before an operational concept could be developed.

Although the instruments available to Thomas Schildknecht were rather modest, the results are interesting and encouraging (see chapter 6). The results achieved with geostationary satellites underline the impact of the CCD technology for applied problems of orbital mechanics: many objects in the geostationary belt may only be observed with CCD detectors with an accuracy sufficient for precise orbit determination and (active) positioning.

This volume may be considered as a milestone for the comeback of optical astrometry in fundamental astronomy. With the new telescope, to become operational at the Swiss fundamental station Zimmerwald in 1996, it will be possible to contribute to the most demanding projects in optical astrometry of the future.

The Swiss Geodetic Commission (SGC) wishes to thank Dr. Thomas Schildknecht for his valuable contribution. The SGC gratefully acknowledges that the printing costs of this volume were covered by the Swiss Academy of Sciences (SANW).

Prof. Dr. G. Beutler
Director of the Astronomical Institute, University of Berne

Director F. Jeanrichard
Federal Office of Topography
Vice president SGC

Prof. Dr. H.-G. Kahle
ETH Zurich
President SGC

Contents

List of Tables

List of Figures

Chapter 1

Introduction

This work has to be seen in the context of a development which was essentially triggered by an idea of Bauersima (1984) to use optical observations of artificial satellites in order to establish a link between different celestial reference frames. This project, called the "Coupled Quasar, Satellite, and Star Positioning (CQSSP)", proposes a new technique in an effort to tie the conventional inertial coordinate reference frames defined by the very long baseline (radio) interferometry (VLBI) positions of selected extragalactic radio sources, primarily quasars, to the reference frames established by optical observations of stars. All classical techniques proposed in recent years use a direct approach in the sense that certain objects are observed with both, the VLBI as well as optical techniques. This may be done by either observing the optical positions of radio emitting extragalactic objects or the positions of the radio centers of radio stars.

The principal difficulties in these approaches stem from several facts. The first is that there are relatively few compact extragalactic radio emitting objects which are strong enough to be accurately positioned by VLBI observations and are sufficiently bright in the visible part of the electromagnetic spectrum to provide good optical images. The second is that most stars emit only a small fraction of energy in the radio region of the spectrum. The third is that one must assume that the radio and the optical photocenters of the objects are coincident. The small number of suitable objects (a few tens up to one hundred) thus leads to large angular distances between these optically faint objects and the reference stars defining the optical frame. Consequently these distances have to be bridged using relative astrometric observations of many intermediate stars (absolute astrometric methods are ruled out due to the faintness of the objects). This method is, however, severely hampered by the propagating errors of the optical refraction.

The CQSSP proposes an alternative technique, namely the use of artificial satellites as transfer objects: Because the orbits of certain artificial satellites are known in an earth fixed reference frame with an accuracy of a few decimeters

and because the transfer between the terrestrial and the celestial reference frame may be established using the VLBI based set of earth orientation parameters we may express the topocentric directions of these objects in the VLBI extragalactic reference frame to within a few milliarcseconds. The link between the radio and the optical reference frame may now be established through optical astrometric (more precisely astrographic) observations of these satellites relative to known reference stars. We may use geodynamics satellites like Lageos I and Lageos II which are very accurately tracked by satellite laser ranging (SLR) or the system of the (currently) 26 Global Positioning System (GPS) satellites as transfer objects. The orbits of the latter satellites are determined by radio-interferometric techniques and precise ephemerides made available through the International GPS Service for Geodynamics (IGS) (Beutler et al. 1994). By selecting close encounters between the transfer objects and the reference stars the critical influence of differential refraction may be reduced to a negligible amount. Furthermore the effects of atmospheric turbulence (short periodic refraction anomalies) are highly correlated for angular distances smaller than one arcminute and thus their impact on the observed differential positions of the two objects is reduced significantly. In addition the CQSSP allows selection of a homogeneously distributed set of reference stars and the problem of the coincidence of the optical and radio photocenters of the extragalactic radio sources is avoided.

First optical test observations with the 0.6 m Cassegrain telescope in Zimmerwald were performed in 1985. The detector consisted of a first generation photoelectric image intensifier (of the so-called proximity focus type) installed in front of photographic film. Although the intensifier showed a remarkable gain of about 10^4, the system had severe deficiencies. The output of the light intensifier (a phosphor screen) was coupled to the photographic film by means of a fiber optic bundle. The efficiency of this coupling tended to be smaller than 0.1. Furthermore the passage through the fiber optics transforms the image in a very complex way which rules out these devices for precise astrometry (the individual fibers in the bundle are not perfectly parallel to each other, the transmission is not homogeneous, etc.). In addition the exposure epochs were defined by a mechanical shutter allowing only insufficient temporal accuracy of a few milliseconds (see also section 4.2). Also due to the mechanical transportation of the film and the manual positioning of the telescope, fast series of exposures during close encounters were virtually impossible.

After these first experiences a new observation technique, a CCD camera system mounted on the 0.5 m SLR Telescope in Zimmerwald, was installed in 1990. Although this telescope has a smaller aperture and an inferior optical quality than the 0.6 m Cassegrain its computer controlled mount capable of high tracking rates (up to several degrees per second) was the main reason to use the SLR telescope for our first CCD tests. A big effort was the development of the data acquisition and processing software. The big angular velocities of the objects with respect

to the reference stars or with respect to an earth fixed direction complicates the observations considerably compared to classical astrography: Predictions for the satellite orbits of interest are required to provide tracking data for the telescope but also for the selection of the reference stars (with close encounters). The series of observations during the encounters have to be accurately timed, the epochs of the exposure should be registered with an accuracy better than 1 ms with respect to UTC. Special techniques for the determination of the mapping function between the sky and the CCD are necessary due to the lack of an ensemble of reference stars on each individual exposure (caused by the small field of view), etc.

The CQSSP project is extremely ambitious in terms of the necessary accuracy as well as in terms of the amount of individual optical observations. It was thus obvious that the development of an appropriate observing technique would be a long-term project and that even the feasibility tests would take a considerable time span. The scope of the new observing technique was subsequently broadened considerably. At present the project includes astrometric observation of fast moving objects (predominantly satellites) for a wide variety of applications with a broad spectrum of accuracy demands. It turned out that astrometric observations of moving objects are in many cases of interest even if only a moderate accuracy of 0.″5 to 1″ can be provided. Let us give the following list:

- Study of the long-term evolution of the orbits of uncontrolled (dead) geostationary satellites (and apogee boost motors). The scientific goal of these investigations is e.g. the detection of time variations of those low degree/order terms of the geopotential which are resonant with the orbits of geosynchronous satellites. Data is contributed (in a lose collaboration) to the international COGEOS project (International Campaign for Optical Observations of Geosynchronous Satellites; for a description of the project see Nobili (1987); for astrometric results see section 6.2). The goal can be achieved through astrometric observations with an accuracy of only 1″ to 2″!

- Determination of earth rotation parameters by combining optical direction observations of artificial satellites with precise range (or range rate) measurements. The latter may either be laser ranging or interferometric range difference data as for the GPS. This application is in fact identical with one part of the CQSSP namely the "Coupled Satellite, and Star Positioning" (CSSP). The idea is strikingly simple. The orbits of geodetic laser satellites or of the system of GPS satellites are very accurately determined (on the 0.1 m or few milliarcsecond level) in an earth fixed reference frame. By observing the orientation of the orbital planes of these satellites with respect to reference stars an independent method to determine the earth rotation parameters in the fundamental stellar reference frame (e.g. the FK5 frame)

is provided. Two aspects have to be emphasized in this context: a) Modern satellite geodetic techniques based on range and range rate measurements have no access to the inertial frame i.e. they need the direction information to be provided by an independent technique. Today only the VLBI technique is providing inertial directions with a comparable accuracy. b) It is not necessary for the optical technique to provide milliarcsecond accuracy at the single observation level. Many observations may be combined to estimate a few parameters only. We recommend conducting a detailed feasibility study for this combination of techniques in the near future.

- Orbit improvement using optical direction observations in support of scientific space missions. Geostationary satellites are in most cases controlled from a single ground station. Consequently the orbits determined from the range measurements of this station have a moderate accuracy of 1 to 5 km. The requirements of some scientific missions like e.g. the Hipparcos space astrometry project (see section 6.2.3) are more stringent.

- Co-location of geostationary satellites. In order to allow the co-location of several satellites in the same 0.1° slot, optimized station keeping strategies and a precise knowledge of the actual positions of the objects are indispensable.

With the introduction of a digital image acquisition system and the increasing amount of observation data it was necessary to automate the data processing to the fullest extent possible. A crucial part of the data reduction is the automatic recognition of the moving objects as well as of the reference star(s). The experience gained in this field allowed expansion of the area of application of the technique to search and survey tasks. In the context of an ESA study we are currently developing algorithms for the detection and recognition of space debris in the geostationary ring and in geostationary transfer orbits (Schildknecht et al. 1994).

In the following chapters the observation technique is discussed in detail. Results will be presented in Chapter 6 but we will not focus on an individual application. Special attention is paid to all kinds of error sources. Unfortunately a comparison of the technique and the results with the contributions from other research workers in the field is almost impossible due to the following reasons: a) Optical astrometric observations of artificial satellites were abandoned by the astronomers in the late 60s. b) essential progress in the field (including the application of modern sensors) was achieved exclusively in the context of military surveillance projects. There is little or no information available from such projects. For a very comprehensive review of modern optical astrometric techniques for the observation of "static" objects we mention the review paper by Monet (1988).

An overview over the relevant characteristics of moving objects for optical observations is given in Chapter 2. In particular the impact on the selection of the optical sensor will be discussed.

Chapter 3 is devoted to the observation technique. In a first part the general concepts are introduced and the main aspects of the classical astrographic reduction technique are reviewed. Atmospheric refraction and turbulence and their significance for optical observations are discussed in a second part. Finally the chapter concludes with an overall error budget listing statistical errors and possible biases for different sources.

Technical aspects like object recognition and centroiding or the shuttering and epoch registration technique are covered in Chapter 4.

A description of the current experimental setup is given in Chapter 5. In particular the CCD camera system and the Zimmerwald 0.5 m SLR telescope are discussed. In addition the specifications of the planned 1 m combined SLR and astrometry telescope will be presented. A first design study has been completed and the detailed design phase has been initiated. Installation of this instrument is planned for mid 1995. A brief overview over the software system (including real time components), the hardware platforms, and the data links may also be found in this chapter.

Real observations are analyzed in Chapter 6. In a first part different types of calibration observations are discussed. Then, a selection of observations of objects near the geostationary ring and in geostationary transfer orbits for a variety of applications are presented. Finally some photometric results from observations of GPS satellites are included.

Chapter 2

Fast Moving Objects — Characteristics and Impacts on the Selection of the Sensor

The expression "fast moving object" may generate a variety of associations. Even in astronomy there is an extreme bandwidth for the terms "fast moving" and "object". It is therefore necessary to define these terms precisely.

In the field of "astrometry " or "astronomy of positions", a movement (velocity) always means a relative angular displacement measured in arcseconds per second or radians per second. As "fast" we understand every observed object with a topocentric angular velocity essentially exceeding a few arcseconds per second (it may also be the velocity with respect to reference objects (e.g. catalogue stars)). In our case an "object" can be every optically visible source as long as it is observed as a point source.

2.1 Order of magnitudes, implications on the observing technique

From the observational point of view, the two most important characteristics of moving objects are the object's *apparent magnitude* and *angular velocity* relative to reference stars. Values for typical representative satellites in four different orbit categories are listed in Table 2.1. The categories were selected according to the orbital altitude and thus to the relative angular velocity.

The table includes values for the 0.5 m SLR telescope at the Zimmerwald observatory (which is by far not optimized for this task) and for the planned 1 m combined Zimmerwald Laser Ranging and Astrometric Telescope (ZIMLAT)

which should be operational in late 1995. We currently use a 512 x 512 pixel CCD camera (see section 5.1.2) in the $f/2$ prime focus of the SLR telescope which results in a pixel size of 4".1 and a field of view diameter of about 35'. The pixel size of the $f/4$ focus of the ZIMLAT telescope will be about 1" and the maximum field of view diameter (given by the telescope design) about 50'. For further details concerning the telescopes and the CCD camera see Chapter 5.

Fast moving objects observational characteristics					
		ECS4[1]	GPS	LAGEOS	ERS1
Altitude	[km]	36 000	20 000	6000	750
Size	[m x m]	2x14	3x5	0.6x0.6	3x12
Max. Motion	[arcs s^{-1}]	15	30	240	2000
Magnitude	[m_v]	11	8 – 14	14	< 6
Pixel Crossing Time	[ms]				
SLR		273	138	17	2
ZIMLAT		66	33	4	0.5
FOV Crossing Time	[s]				
SLR		140	70	9	1
ZIMLAT		200	100	13	1.5
Illuminance	[ph s^{-1}]				
SLR		70 800	> 4470	4470	$> 7 \cdot 10^6$
ZIMLAT		346 000	$> 21\,800$	21 800	$> 3 \cdot 10^7$

[1]Satellites:

ECS4	European Communication Satellite
GPS	Global Positioning System (Navstar) Satellite
LAGEOS	Laser Geodynamics Satellite
ERS1	European Remote Sensing Satellite

Table 2.1: Observational characteristics of fast moving objects. Values for the SLR telescope are based on an aperture of 0.52 m, 4".1 pixel size and a combined atmosphere and telescope transmittance of 0.45. The corresponding values for the ZIMLAT instrument are 1.0 m, 1" and 0.55 respectively. For the computation of the illuminance a solar spectral distribution of the source radiation and the spectral sensitivity function of the PM512 CCD (see Figure 2.2) were used.

Approximate mean values for the angular velocities may be derived from simple geometrical considerations assuming circular orbits with a given height and

considering all ranges of inclination. In the case of geostationary satellites their velocity in a topocentric frame is zero. Consequently it is constant if measured with respect to the stars (about 15 $arcs\,s^{-1}$, depending on the observers geographic coordinates).

Visual magnitudes on the other hand are more difficult to estimate. In principle any magnitude/velocity combination may occur. For a given distance (orbit height) the observed topocentric magnitude depends on the characteristics of the object's surface (geometric albedo, scattering function, etc.), the illuminating source (spectral distribution), the illumination angle, and on the intervening atmosphere. For the values listed in Table 2.1 we assumed sun illuminated spherical Lambertian scatterers with a bond albedo of 0.3 and reasonable values for the remaining parameters.

In order to answer the central question of signal strength seen by the detector we have to specify the telescope characteristics and the tracking scheme. For the following considerations let us assume a 1 m telescope with a 1" detector pixel size. By "pixel" we do not necessarily mean a picture element of a two-dimensional array, but we just denote in general the smallest spatial element which can be resolved simultaneously by the detector. So we leave the question of the detector type (integrating array or photon counter) open for the discussion in section 2.2. We could in principle either track the moving object or the reference stars or we may even use a general tracking velocity (which also might include the case of a fixed telescope). The selection of the tracking scheme must be guided by the goal of achieving the best possible position measurements. There will be a tradeoff between the best signal to noise ratio (S/N) for the faint objects which calls for tracking them as long as possible, and the capabilities to model the telescope movement (see section 3.1.2). For the remainder of this section we are interested in the relative angular speed of the object images with respect to the detector and we assume the telescope to be fixed (drive off).

For an object in a 500 km orbit we have an angular velocity $\nu = 2900''s^{-1}$ and the object will spend only 350 μs within one pixel. Even geostationary satellites stay just 66 ms within one pixel. For the remainder of the exposure time the pixel will accumulate noise from both the sky background and the detector itself. In other words, the integration time should not be much longer than the pixel crossing time which for integrating detectors in most practical cases is synonymous with "as short as possible". On the other hand many sensors (apart from the photon counting devices) are limited to the very short integration ranges. Astronomical CCD cameras, for example, use mechanical shutters in front of the detector. They allow, at best, a minimum integration time of 10 ms (depending on the shutter aperture). An additional characteristic of CCD cameras is their low readout rate (e.g. 5 s to read out a 512 x 512 pixel frame) leading to long "dead times" (5 s vs. 10 ms).

High angular velocities do not only ask for short but also for well defined exposure intervals. If we aim at position accuracies of about 0.1 pixel which is a reasonable value as will be shown in section 4.1.3, we need the observation epochs to be defined with an accuracy of 35 μs for a 500 km orbit! This has two consequences: a) the need for a station clock synchronized to UTC with the required accuracy, b) the shuttering process must be controllable (calibratable) with the same accuracy. The latter requirement poses no problems when using photon counting systems, but can definitely not be achieved by mechanical means in the case of integrating detectors.

2.2 Selecting the optical sensor

The considerations of the previous section show that the light detector or optical sensor is one of the crucial components of the instrumentation of the experiment. It was obvious that photographic material would not be the best choice. Apart from that the proper choice among the electro-optical devices available is not trivial at all. A set of system specifications is indispensable. The first subsection is therefore devoted to a brief review of the system requirements. In a next step we shall discuss the fundamental properties of the detection processes. The necessary quantities and some basic equations are derived in this second subsection. An overview of the most important detectors, their operation principles, characteristics, and limitations is given in the third subsection. We conclude this section with a critical discussion and a comparison of the two principal techniques "photon counting" versus "integration".

2.2.1 Brief discussion of detection system requirements

The faintness and high angular velocities of the objects of interest lead to the following stringent requirements for the detector and the entire system:

- *High quantum efficiency of the detector* as well as *small system and detector readout noise.* Both are necessary because of the small photon flux from the sources but, and this is more important, also due to the very limited integration times. The latter are limited by the movement of the source with respect to the detector (pointing direction of the telescope).

- *High temporal resolution.* Temporal resolution in the sub-millisecond range is a "must" to achieve astrometric positions of fast moving objects with accuracies below 1″.

- *High geometric stability of the detector.* This is a primary requirement for astrographic applications not allowing a calibration of the geometry of the detector for every single exposure (see also section 3.2.1). In classical astrography transformation parameters for every photographic plate have to be determined using reference stars in the field of view. An alternative approach for the calibration of the geometry, based on the geometric stability of the detector, is a key feature of our observing technique.

- *High repetition rate.* This may often also be described as "short readout time". The dead time between exposures reduces the total amount of information which can be acquired during a given time interval. When working with very fast moving objects the integration times are strongly limited (a few milliseconds) and hence the information in a single exposure (number

of photons) is modest. We may cure this by increasing the number of exposures. However, if the total observation time interval is small (as in the case when the object passes a reference star) the total information will be proportional to the exposure to dead time ratio. This requirement is rather unusual for detectors in astronomy. In most astronomical applications readout dead times may be neglected, because they are small compared to the integration times (in the range of minutes to hours).

- *High linearity.* A good linear response of the detector to the incident light improves (and simplifies) the centroiding process. Every centroiding algorithm explicitly or implicitly assumes a certain shape of the resultant image of a point source. This so-called *point spread function* (PSF) is usually independent of the detected intensities or, in other words, perfect linearity of the detector is assumed. If the latter premise does not hold the detector response must be calibrated and this additional dependency has to be incorporated into the centroiding algorithm. In general there is a strong correlation between the centroiding process and the estimation of photometric parameters (where detector linearity is an important issue) (see Verdun (1993)).

- *High dynamical range.* The ability to record sources with a broad intensity range simultaneously has several distinct advantages. Bright objects do not saturate the sensor as quickly as in photographic observations. This characteristic is particularly important given the fact that the catalogue stars may be several orders of magnitude brighter than the objects of interest.

2.2.2 Detection limits

Incoherent detection

At optical wavelengths up to several hundred microns, photons have enough energy to be detected coherently. This is done by exploring the particle nature of the radiation mainly using the photoelectric effect in which single photons excite electrons. This method allows detection either of individual photons or integration of the incident photons on the detector and recording of the cumulative effect. The first technique is used in the class of the so-called "photon counting detectors" where the photomultiplier is the classical representative. These devices are mostly single channeled. The output signal is a voltage or charge proportional to the number of incident photons and their gain is sufficient to detect single photons. Detectors using the second technique form the class of integrating detectors. Usually multi channeled they are mainly used to record images at the focus of a telescope. The classical photographic materials and charge coupled devices (CCD) are the most widely used devices of this class. Their internal gain as

well as the readout rate are insufficient for single photon event detection. After the exposure the accumulated, photon generated, charge is either transformed into a permanent record e.g. a developed photographic grain or may be sensed as a voltage after an electronic readout process.

Photon statistics

At optical wavelengths the radiation from a steady source can be described as a continuous flux of photons with some random variations. The variations may be described by a Poisson distribution. If $p(n,t)$ is the probability that n photons cross a given area during the time interval t we have

$$p(n,t) = \frac{(\dot{s}t)^n}{n!} e^{-\dot{s}t}, \tag{2.1}$$

where $\dot{s}$ is the average flux from the source crossing a given area. The distribution has two important properties: a) the standard deviation σ of the mean flux $\dot{s}$ simply is $\sigma = \sqrt{\dot{s}}$, this is the so-called photon noise or "shot noise", and b) for large $\dot{s}t$ the distribution may be approximated by a normal or Gaussian distribution.

This noise is of great importance because it will be dominant in most of our applications. More generally modern optical detectors are almost always shot noise limited when operated at short exposure times.

It is important to emphasize that the shot noise is proportional to the square root of the number of photons and *not* to the energy. When discussing detector performance it is therefore useful to express any spectral energy distribution of a source in terms of photon flux. The relation between photon flux $\dot{s}$ and energy flux F depends on frequency where $\dot{s}(\nu) = F(\nu)/h\nu$ or, expressed with the wavelength as argument $\dot{s}(\lambda) = \lambda F(\lambda)/hc$.

Signal and noise components

The ability to detect an astronomical source is limited by the signal from the source, the efficiency (aperture, transmission and optical quality) of the telescope and detector system, and of the sum of the noise stemming from many different sources. The signal at the output of the detection system is a superposition of

1. the flux from the source of interest,
2. the sky and atmospheric background, and
3. signals produced inside the detector.

As examples of signals produced inside the detector we mention the so-called dark current of optoelectronic devices (this is actually a current from thermally exited electrons and therefore proportional to the integration time). Multichanneled devices may also contain defective zones like "dead" and "hot" pixels or, in the case of photographic material, any kind of defect in the emulsion. These "internal" sources are either well known and can thus be calibrated and eliminated during the data reduction process or they are spurious in the sense that they are unique for each exposure (e.g. emulsion defects).

The noise which compromises every observation may be separated into the following components:

1. Shot noise associated with the source but also with all background signal components. This noise is proportional to the square root of the number of detected photons and hence to the square root of the integration time (see equation 2.1).

2. Noise from atmospheric seeing and scintillation effects. The characteristics of these components are complex and vary significantly with time.

3. Noise associated with the dark current generated inside the detector. Dark current has the same characteristics as any photon flux and the noise thus is described by a Poisson distribution.

4. Noise added during the detector readout and signal amplification process. Although not stemming from charge inside the detector this noise is preferably expressed in terms of the equivalent number of (photo-)electrons in order to make it comparable with the other noise components. Readout noise is constant and adds up once per exposure and image pixel.

5. Digitization noise due to the conversion of the analogue signal into discrete (digital) units. The origin of this noise resides in rounding effects which take place when electrons (or more precisely the amplified signal from the electrons) are converted into smaller digital units (often called analogue to digital conversion units or ADU). The rounding errors are equally distributed and depend on the overall system gain. Digitization noise is in most cases negligible compared to other noise constituents provided that the system gain is sufficiently high (a few electrons per ADU).

6. Processing noise accumulated during the image processing steps. Digital manipulations of the images like addition or subtraction of frames always increase the noise. In particular, all calibration steps have to be taken into account in the overall noise budget. A second kind of processing noise stems from rounding effects. They are encountered in cases where integer operations are preferred due to data storage (memory) or speed optimization.

Often additional (unwanted) signal components are denoted as noise although they are in many cases not strictly noise in the sense that they can be described by a stochastic model. As an example, we mention the so-called "pattern noise" which is actually a fixed pattern generated by dark current or due to an inhomogeneous sensitivity in a multichannel detector and thus has a signal as well as a noise part (it may be regarded as noise with respect to its position relative to an arbitrary object position).

There are also cases where the characteristics of the noise are unknown or very hard to model. Unstable interference patterns from the electronics, spurious signals, etc. pertain to this category.

For the following discussions it is necessary to define a few general terms more precisely:

Sky background The unavoidable dominant background components are summarized in this term. The contributions to the sky brightness may be divided into: atmospheric airglow, scattered natural and artificial light, zodiacal light, emissions from unresolved stars and from diffuse galactic and extragalactic sources. A typical night sky brightness at a good astronomical site is in the order of 22 $m_v\,arcs^{-2}$ in the visual and increases by about 0.5 $m_v\,arcs^{-2}$ in the near infrared part of the spectrum. This quantity may, however, vary significantly for different sites and from night to night given the strong dependence on atmospheric conditions and on artificial light pollution. The mean measured sky brightness at Zimmerwald is e.g. about 19 $m_v\,arcs^{-2}$ in the visible. An important property from the observational point of view is the fact that the sky brightness is actually a surface brightness which allows the "dilution" of this background by increasing the telescope's focal length or, in other words, the magnification. This aspect will be considered in the discussion of the optimum image scale.

Dark current By using the term "dark current" for the detector generated background signal we restrict the discussion to optoelectric devices (the counterpart for photographic material would be the so-called "fog"). Fortunately for most detectors this effect may be reduced significantly by cooling. Depending on the actual detector a great part of the dark current is produced thermally e.g. through electron-hole pairs in silicon diodes or thermally exited electrons in the photocathode or dynodes of a photomultiplier. A great benefit from cooling the detector (thermoelectrically or with liquid nitrogen) may result due to the almost exponential dependence of the processes on temperature.

Signal to noise ratio The term "signal" has to be understood in the narrow sense as the signal of the source of interest whereas "noise" means the overall

noise including the noise from the object of interest. For a detailed discussion, derivation of equations for static and moving point sources as well as for quantitative results for the SLR and ZIMLAT telescopes see Appendix A.

2.2.3 Detectors

We restrict this overview on detectors to a small selection of promising devices for our application. In particular we will discuss only electro-optical position sensitive (either multi- or single-channeled) sensors. The primary decision has to be made between integrating and photon counting systems. The CCD is the only integrating device in our comparison because there is no doubt concerning the superiority of CCD's in this class of sensors unless a very large focal plane area has to be covered (wide field applications), where we still have to use photographic material. The larger part of this section is devoted to the CCD simply because it will finally be the selected device for our application. When cross-checking the detector characteristics with the specifications listed in section 2.2.1 we should keep in mind the general goal of our investigation: the precise position determination of fast moving objects. It is therefore primarily the geometric stability which has to guide us. This criterion also determined the particular selection of photon counting devices.

Charge Coupled Devices (CCD)

These solid state detectors make use of the photoelectric effect in silicon. The detectors consist essentially of an array of MOS (metal oxide switch) capacitors which are biased in order to generate potential wells. The photo-generated electrons are then collected and stored in these wells. After the exposure the charge packets which have accumulated in each sensing element (called "pixel") are transferred along the columns of the CCD detector (called "parallel registers") towards the top row (also called "serial register") (see Figure 2.1). The serial register is then shifted, pixel by pixel, towards the output node where the charge packets are amplified (on the chip). After having read all pixels from the serial register the next row can be transferred and the process repeats until the entire array has been read out. The charge transfer itself is performed by appropriately changing the potentials at the gate electrodes (there may be a set of 3 to 4 electrodes per row) in such a way that the potential well is moving along the columns from pixel to pixel. The individual columns are perfectly isolated from each other (burried channels) and thus there is no charge transfer possible along the rows.

There are several types of CCD detectors used in astronomical applications. They differ in architecture (the configuration of the electrodes; there may e.g. be

two regions which can be controlled independently), in size, in number of sensing elements, and in thickness. In *front side illuminated* or thick devices the photons have to pass through the (more or less transparent) electrodes first before reaching the silicon. *Backside illuminated* devices are thinned to about 10 μm allowing the photons to reach the silicon directly. The advantage of the latter (also more expensive!) design is an improved overall quantum efficiency and a significant improvement of the blue sensitivity (the spectral response function of uncoated thick devices has a sharp cutoff at about 450 nm!). The thin foil like sensitive area of backside illuminated devices makes them unsuitable for astrometric purposes due to a possible bending of the detector under the influence of gravity or thermal stress.

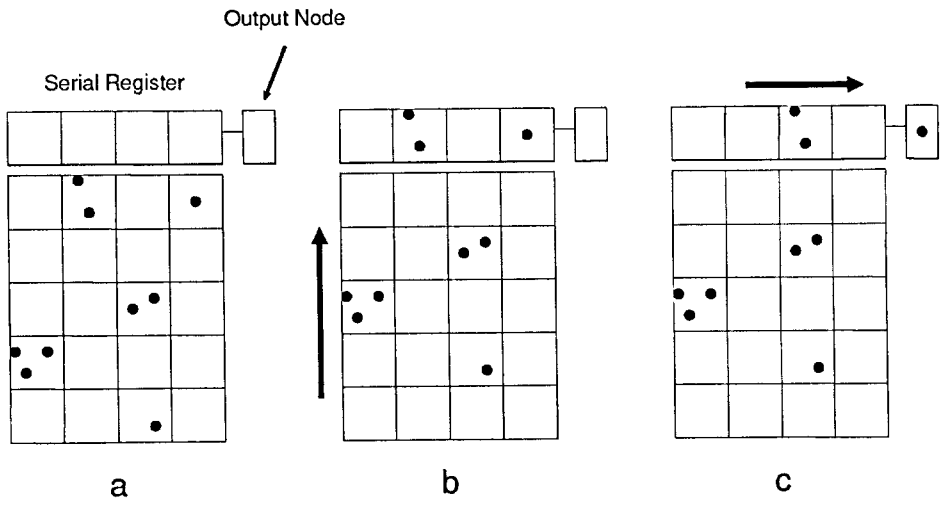

Figure 2.1: CCD readout scheme. (a): During the exposure charge is accumulated in the individual pixels. Before starting the readout process the serial register is cleared (by reading it several times). (b): All rows are shifted in parallel and the top row shifted into the serial register. (c): The serial register is shifted pixel by pixel towards the output node where the charge packets are amplified (on the chip). After all pixels have been read out from the serial register (and the register possibly cleared from residual charge) the next row can be transferred (and the process repeats until the entire array has been read).

In the following paragraphs we will briefly summarize the main characteristics of scientific grade astronomical CCD detectors (there is a wide range of literature for more detailed discussions).

Dimensions (spatial resolution) The majority of current CCDs used in astronomy have pixel sizes of about 15 to 20 μm. Smaller pixels tend to have a reduced quantum efficiency due to the relative increase of the insensitive intra-pixel and electrode covered areas. Arrays of 1000 x 1000 pixels are standard (area about 4 cm^2) whereas 2000 x 2000 pixel chips with areas of about 8 to 25 cm^2 are available but still expensive (35 to 50 ksFr, factor 2 if back side illuminated). If we define the spatial resolution as the dimension of the sensing elements with respect to the total detector size we end up with linear resolutions of 1/500 to 1/2000. (The resolution in lines per mm (in the order of 50 to 100) is of minor interest because the magnification of the optical system may always be adapted to the detector.)

Quantum efficiency The peak quantum efficiency of CCDs varies from about 0.5 for thick to 0.8 for thin specially treated backside illuminated devices. Figure 2.2 shows the spectral sensitivity of our current front side illuminated Photometrics PM512 CCD.

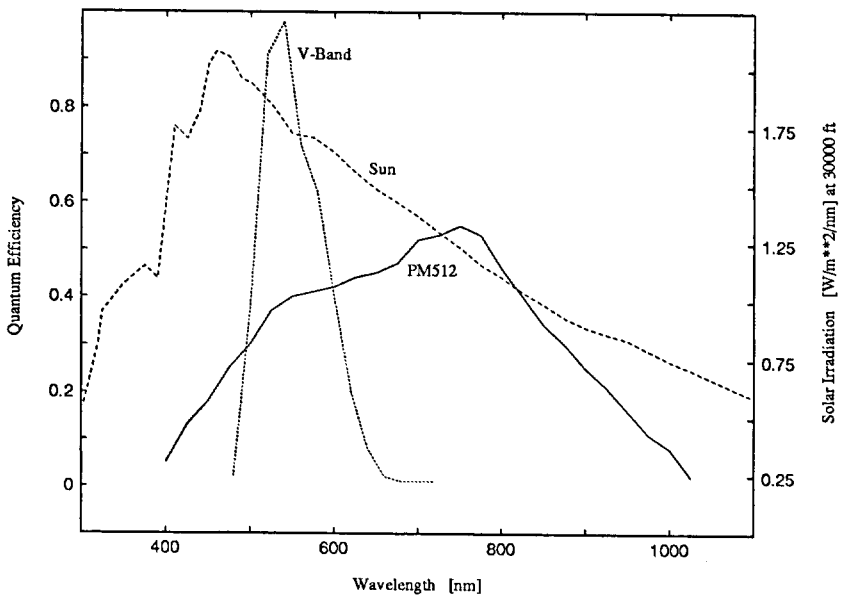

Figure 2.2: Spectral sensitivity curve for the Photometrics PM512 CCD (solid line). For comparison the spectral characteristics of the V-band (UBV photometry, dotted line) as well as the spectral energy distribution for the sun (dashed line) are shown. (The peak of the V-band curve was normalized to 1.)

Dark current and readout noise If appropriately cooled the dark current rates are completely negligible (0.2 $e^-s^{-1}pixel^{-1}$ for -45° C to 0.0002 $e^-s^{-1}pixel^{-1}$ for -120° C; depending on the actual operation mode these numbers may be up to a factor of 10 higher). The so-called readout noise, however, which is the noise added to every individual pixel during the readout process is typically in the order of 5 e^- $pixel^{-1}$ and thus the dominating noise component when observing very faint sources.

Repetition rate (dead time) and temporal resolution Due to the slow readout rates (typically 50 kHz) needed to maintain a good charge transfer efficiency and an acceptable readout noise the repetition rate is in the order of one (full) frame every few seconds. The dead time is thus essentially given by the readout time (e.g. about 5 s for a 512 x 512 pixel full frame). If only a limited fraction of the frame is of interest the use of the so-called "subframe technique" (see section 3.1.3) may reduce the dead time significantly.

Geometric stability The geometric stability of solid state devices is intrinsically very good. Apart from the homogeneous thermal expansion there are no other distortion effects to be expected.

Photometric linearity The individual pixels show a high linearity in the response to incident light. Deviations over the whole dynamical range do not exceed a few percent. Pixel to pixel sensitivity variations (in the order of 5%) may be calibrated using so-called "flat fields" (see section 4.1.1).

Dynamical range At the lower end, the sensor is limited by the readout noise whereas the upper limit is given by the saturation level. The amount of charge which can be stored by a single pixel (without overflowing into adjacent pixels), the so-called "full well capacity", ranges from 100 to 700 ke^- depending on the CCD type and the operation mode. Consequently the dynamic range lies between $2 \cdot 10^4$ and $1 \cdot 10^5$.

Imaging photon counters

There is a multitude of different position sensitive photon counting detector systems used in astronomy. A common feature of all these devices is an intensifier stage where single photons are amplified by a factor of 10^4 to 10^5. The position sensitivity may be achieved by different techniques. One method is to use a grid like device (e.g. a Ronchi ruling) in front of a position insensitive light intensifier

like a photomultiplier or an image dissector tube. The latter consists of a photomultiplier combined with a special first acceleration stage which allows selection (electronically) of electrons from a small area of the cathode (which makes the device in fact position sensitive). A second approach uses imaging light intensifiers (electromagnetically or proximity focussed) in front of TV tubes (e.g. vidicons) or solid state detectors like CCDs. We now briefly list the characteristics of these detectors using the same keywords as for the CCDs. (We do not include "exotic" i.e. very expensive or not commercially available devices like the MAMA (Morgan and Timothy 1988).)

Spatial resolution For systems using TV tubes the resolution is in the order of 1/400. It is difficult to come up with a specific number if the position sensor is a CCD because the resolution will be limited by the particular image intensifier used. In the case of Ronchi rulings there seems to be virtually no limit in the length of the ruling and hence in the resolution (the ruling of the MAP (Gatewood 1987) has a length of 12 in. and the lines and spaces between them are 200 μm wide).

Quantum efficiency The peak quantum efficiency of commonly used semitransparent photocathode materials ranges in the visible light from 0.1 to 0.15 (e.g. S20 material). "Semitransparent" means that the photons enter the cathode from one side and the electrons emerge from the other side. In contrary to the CCD devices there is a steep descent of the sensitivity for most materials for wavelengths longer than about 550 nm whereas the cutoff at the blue end may well be below 300 nm (the peak sensitivity lying at about 400 to 450 nm). In addition there are materials with an excellent efficiency in the UV region. The fact that any pulse discriminator system looses a certain fraction of the incident pulses further reduces the efficiency (not the quantum but the detective efficiency). The detectors are therefore less sensitive in the visible by a factor of 4 to 6 compared to CCDs.

Dark current and readout noise As the gain of photon counting detectors lies between 10^4 and 10^6 the signal amplitude of each photon event exceeds the level of almost all noise sources. The readout noise S_r in equation (A.6) can therefore be neglected for these devices. On the other hand dark current rates, although they may be significantly reduced by cooling the detectors, are on the order of 5 $e^- s^{-1}$ or more.

Repetition rate (dead time) and temporal resolution All photon counting systems have some intrinsic dead (or recovery) time given by the finite length

of the photo-generated pulses. For photomultipliers this dead time is on the order of 10 ns. As a result the actual number of detected photons is reduced by the degree of overlapping of dead times. The effect is also called "pile-up error". Position sensitive photon counters, however, have a much lower temporal resolution because they are all multiplexing their individual channels (in fact a CCD detector also may be regarded as a multiplexed device). Current readout rates are on the order of 1 kHz.

Geometric stability The geometric stability of all systems using an image intensifier device is very critical. These devices are extremely sensitive to power voltage variations and, what is even more important, to all kinds of environmental variations (e.g. electromagnetic fields). The stability of Ronchi rulings on the other hand is excellent.

Photometric linearity If the measurements are reduced correctly e.g. corrected for pile up errors, discriminator losses etc. the photometric linearity of most photon counters is excellent (deviations from linearity $\leq 0.1\%$)!

Dynamical range Due to the maximum readout rate of about 1 kHz the dynamical range is limited to 10^3 at maximum (at a 1 kHz photoelectron rate the system is completely saturated).

2.2.4 Photon counting versus integration

When cross-checking the list of the previous subsections we identify two characteristics where the photon counting imagers are better than the CCD systems:

(a) The virtually nonexistent readout noise and

(b) the higher temporal resolution.

It is not clear whether photon counting systems using Ronchi rulings have some advantages in defining the geometry when compared to solid state arrays like CCDs (see also the discussion of supercalibration of CCDs in section 3.2.2).

If we compare the systems for regimes where the sky (and/or the object) noise is dominating the readout noise (see equation (A.14) and (A.16)) the important advantage of the solid state detectors is the higher quantum efficiency and the larger dynamic range. We may fully explore the advantages of the photon counters only if the observations are readout noise dominated i.e. if the exposure time is very short or a narrow filter passband is used.

Let us illustrate these facts with an example for the ZIMLAT telescope assuming typical atmospheric conditions at Zimmerwald. Assuming a CCD readout noise of 5 e^- and a sky background of 19 $m_v\,pixel^{-1}arcs^{-2}$ resulting in a flux of about 250 photons $pixel^{-1}s^{-1}$ (for the PM512 CCD without any filter) we are almost always sky background dominated except for integration times shorter than 20 ms or passbands smaller than about 20 nm! In addition a photon counter with a maximum rate of about 1000 e^- will be saturated very quickly e.g. in about 0.25 s for $m = 4$, $\dot{S}_o$=16 m_v and $q = 0.15$ (where m is the number of sensing elements over which the source is detected, $\dot{S}_o$ is the signal from the source, and q the quantum efficiency of the detector)!

Figure 2.3 shows the limiting magnitude as a function of integration time for different S/N for a photon counting system (dashed lines) and for a CCD (solid lines). The photon counting system saturates for $m_v < 16$ (1 kHz; dotted part of the lines). The computation is based on the ZIMLAT specifications, the PM512 CCD (no filter!), and a sky background of 19 $m_v\,pixel^{-1}arcs^{-2}$. The curves for both systems are parallel for exposure times > 1 s i.e. in the background dominated region (the offset is due to the difference in the quantum efficiency). The steeper slopes at short integrations times are indicating the object dominated regime. The difference in steepness between the CCD and the photon counter is due to the finite readout noise (constant with time!) of the CCD. From Figure 2.3 we conclude (again) that photon counting systems have some advantages for very low S/N and for integration times below 0.1 s only.

All the above considerations together with the fact that the only suitable imaging photon counters for high precision astrometry are sophisticated prototypes of the Ronchi ruling type, clearly favor the CCD detectors for our applications.

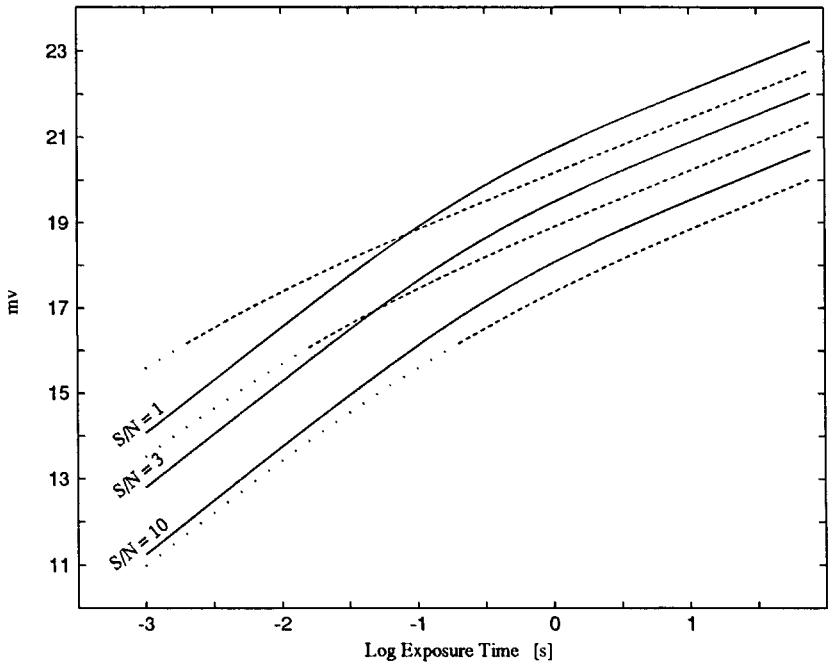

Figure 2.3: Limiting magnitude as a function of integration time for different S/N for a photon counting system (dashed lines) and a CCD (solid lines). The dotted part of the lines are within the region where the photon counting system is saturated (1 kHz).

Chapter 3

Observation Techniques

3.1 Observation scenarios

The nature of the objects to be observed, the characteristics of the detector, and the scientific objective results in rather unusual observation scenarios. Let us compile the main characteristics:

- CCD detectors have a very limited number of sensing elements. Taking into account the optimum scale introduced in section 4.1.3 we end up with a *small field of view.* As an example we may take our 512 x 512 pixel CCD and an optimum image scale of 1" per pixel which results in a field of view of 8′ x 8′. Although CCDs with up to 2000 x 2000 pixels are available and even mosaics of CCD arrays could be constructed the actual constraints are given by the readout rates of these devices. The small 512 x 512 CCD needs at least about 5 s to read out a full frame, where the delay is proportional to the number of pixels! This implies the readout time for a 2000 x 2000 pixel array would be about $16 \cdot 5$ s $= 80$ s! The rapid movement of the objects of interest, on the other hand, may restrict the integration times to a fraction of a second (see discussion below) which in combination with the readout delays (dead time!) would result in unacceptable duty cycles. There is, however, a technical solution to reduce the readout times to a certain extent, namely by reading out only subframes (see section 4.2).

- When observing fast moving objects with a fixed (non tracking) telescope pixel crossing times ranging from a few tenths of a second to a few milliseconds have to be expected. They are given by the angular velocity of the object and the image scale of about 1" per pixel. The optimum integration time will be of the same order of magnitude (or at maximum a factor of 10 longer) as the pixel crossing times mentioned. If we want to maximize

the information during one field of view crossing of the object (lasting a few seconds only!) we need a series of short exposures with minimum dead times in between. What about tracking the objects? Tracking strategies are dictated by S/N considerations (see subsection 3.1.2); they do *not* considerably improve the situation concerning the short exposure times (the relative velocity between the objects and the reference stars remains the same!).

- The final objective, the determination of positions, imposes additional restrictions. If we observe close encounters between the moving object and the reference stars (or more general the reference objects) we can drastically reduce the impact of the refraction, the most pertinent enemy of classical astrometry. We are able to fully explore this advantage due to the fact that we can choose the best suited reference stars along the object's trajectory. As opposed to the situation in classical astrography there will be generally only one reference object in the field of view at a time. Therefore we will have to develop a new approach for the determination of the geometry (see section 3.2).

3.1.1 Expected number of close encounters

The number of close encounters between a moving object and a reference star depends on:

- the spatial density of the star catalogue.
- the observable pass length or the angular velocity of the moving object, depending on the quantity of interest either the number of encounters per pass or per time interval. Observational limitations like maximum zenith distance may further restrict the pass length.
- the accepted range of brightness (minimum and maximum magnitude) of the catalogue stars.
- the maximum value for the minimum angular distance between the object and the reference stars.

Although the real spatial density of catalogue stars varies significantly with the actual location on the sky we assume a homogeneous spatial distribution of the stars to simplify the following estimations.
Given

$N_{1,2}$ the total number of stars within the magnitude interval (m_1, m_2) in the star catalogue considered;

$\bar{N}_{1,2}$ the mean number of stars per steradian within the magnitude interval (m_1, m_2) in the catalogue considered;

l the moving object's pass length in radians;

v the angular velocity in arcseconds per second of the moving object;

d the requested maximum value for the closest approach distance between object and reference star in arcseconds.

The mean number $n_{1,2}$ of stars per pass with $m_1 < m < m_2$ can be expressed as

$$n_{1,2} = \frac{2dl\bar{N}_{1,2}}{206265} \tag{3.1}$$

and the mean number of stars encountered per second is

$$\nu_{1,2} = \frac{2dv\bar{N}_{1,2}}{206265}. \tag{3.2}$$

Star densities for different catalogues are given in Table 3.1. As an example we

m_1 m_2	**PPM** preliminary		**HIPPARCOS** INCA	
[mag]	$N_{1,2}$	$\bar{N}_{1,2}$ [deg^{-2}]	$N_{1,2}$	$\bar{N}_{1,2}$ [deg^{-2}]
– 6	1320	$3 \cdot 10^{-2}$	4200	.12
6 – 7	7059	.17	8510	.21
7 – 8	21214	.51	22250	.54
8 – 9	77491	1.9	41100	1.0
9 – 10	132400	3.2	28410	.69
10 – 11	64740	1.6	9330	.23
11 – 12	20727	.50	2930	$7 \cdot 10^{-2}$
12 – 13	1387	$3 \cdot 10^{-2}$	650	$2 \cdot 10^{-2}$
13 – 14	20	$5 \cdot 10^{-4}$	–	–
14 –	–	–	–	–

Table 3.1: Star densities for different catalogues. The total number of stars per magnitude interval ($N_{1,2}$) and the number of stars per square degree ($\bar{N}_{1,2}$) are given for the PPM and the HIPPARCOS INCA catalogue. The PPM data are extracted from the digital version of the preliminary catalogue as distributed by the Astronomisches Rechen-Institut Heidelberg (Röser and Bastian 1991). Values for the HIPPARCOS INCA catalogue are based on Turon et al. (1992).

calculate the expected number of encounters for two different types of objects and

m_1 m_2 [mag]	**PPM** preliminary		**HIPPARCOS** INCA	
	$n_{1,2}$	$\nu_{1,2}$ [h^{-1}]	$n_{1,2}$	$\nu_{1,2}$ [h^{-1}]
– 6	.45	$8 \cdot 10^{-2}$	1.5	.26
6 – 7	2.6	.43	3.1	.52
7 – 8	7.7	1.3	8.1	1.4
8 – 9	29.	4.8	15.	2.5
9 – 10	48.	8.0	11.	1.8
10 – 11	24.	4.0	3.4	.57
11 – 12	7.5	1.3	1.1	.18
12 – 13	.45	$8 \cdot 10^{-2}$	.24	$4 \cdot 10^{-2}$
13 – 14	$7 \cdot 10^{-3}$	$1 \cdot 10^{-3}$	–	–
14 –	–	–	–	–

Table 3.2: Expected number of encounters for a geostationary satellite. The expected number of encounters within $\pm 5'$ are given. Numbers per pass are in column $n_{1,2}$ (pass length is 90° corresponding to a 6 hour interval) and numbers per hour in column $\nu_{1,2}$. The values are based on the catalogue data given in Table 3.1.

m_1 m_2 [mag]	**PPM** preliminary		**HIPPARCOS** INCA	
	$n_{1,2}$	$\nu_{1,2}$ [min^{-1}]	$n_{1,2}$	$\nu_{1,2}$ [min^{-1}]
– 6	.64	.11	2.0	.35
6 – 7	3.4	.59	4.1	.71
7 – 8	10.	1.7	10.8	1.9
8 – 9	38.	6.6	20.	3.4
9 – 10	62.	11.	14.	2.5
10 – 11	32.	5.5	4.5	.78
11 – 12	10.	1.7	1.4	.50
12 – 13	.64	.11	.32	$5 \cdot 10^{-2}$
13 – 14	$1 \cdot 10^{-2}$	$1 \cdot 10^{-3}$	–	–
14 –	–	–	–	–

Table 3.3: Expected number of encounters for a low earth orbiting satellite at 750 km altitude. The expected number of encounters within $\pm 5'$ are given. Numbers per pass are in column $n_{1,2}$ (topocentric pass length is 120° corresponding to about 5 minutes) and numbers per minute in column $\nu_{1,2}$. The values are based on the catalogue data given in Table 3.1.

a number of star catalogues. Table 3.2 lists values for a geostationary satellite with $v = 15$ arcs sec^{-1} and $l = \pi/2$ (corresponding to a 6 hour observation interval or about one night). A low orbiting satellite at 750 km altitude with a mean velocity $v = 1200mbox\ arcs\,sec^{-1}$ and a pass length of $l = \pi/3$ (corresponding to about 6 minutes) was used as an example to produce Table 3.3. In both cases the maximum value d for the closest approach distance between object and reference star was set to 5′.

Thanks to the big number of reference stars available we may optimize the selection of close encounters to meet the objectives of the particular experiment (e.g. by optimizing the spatial homogeneity of the selected reference stars).

3.1.2 Tracking strategies and optimum integration times

The first steps of the reduction process, after having exposed the frame, consist of (a) recognizing the object and the star(s) and (b) determining their positions with respect to the coordinate system defined by the detector (i.e. the grid of pixels). The actual object recognition and centroiding algorithms will not be discussed in this section (see section 4.1.3) but we have to consider a few general aspects:

- In order to be recognized as a part of an object, each individual object pixel must exceed a value of the order of 1 to 4 in S/N depending strongly on the actual algorithm used.
- The accuracy of the determined positions improves with the S/N of the objects.
- The modeling of the images of the moving sources (moving with respect to the telescope's looking direction) is a critical issue. We emphasize that not only do we have to find the best centroid e.g. of a trailed image but also we should be able to interpret the determined position. In particular we have to specify the observation epoch. This is not a trivial task especially in view of tracking errors and seeing effects!

By tracking the moving objects we obviously improve the S/N of an individual object pixel for a given integration time. The object stays for a longer time and, in the case of "perfect tracking", during the entire exposure time on the same pixels. The S/N gain of the individual pixels is either proportional to the ratio of the integration to pixel crossing time or to the square root of this ratio depending on the detector noise (see equations (A.13),..., (A.15)). There is not only an enhancement of the S/N of single pixels but also of the entire object. Because the object is spread out over a smaller area, fewer pixels are contributing to the readout and background noise. This fact can be seen in equation (A.6) where

tracking just reduces the number of object pixels m. Perfect tracking of the object, however, harms the reference stars (their images will be trailed). The relative velocity of the objects with respect to the reference stars can not be reduced by the observation process. Optimum tracking should therefore aim at comparable image quality (with respect to the centroiding) of the object and the reference star. One possibility consists of adjusting the tracking velocity and direction in such a way that the resulting S/N per pixel is equal for both sources:

If $\boldsymbol{v}_1$ and $\boldsymbol{v}_2$ are the angular topocentric velocities of the object and the reference star respectively the optimum topocentric tracking velocity is

$$\boldsymbol{v}_{track} = \frac{\boldsymbol{v}_2 + \boldsymbol{v}_1 \frac{s_2}{s_1}}{1 + \frac{s_2}{s_1}}, \tag{3.3}$$

where s_1, s_2, are the signals from the two sources. If the apparent brightness is expressed in stellar magnitudes m_1, m_2, we get

$$\boldsymbol{v}_{track} = \frac{\boldsymbol{v}_2 + \boldsymbol{v}_1 10^{-0.4(m_2 - m_1)}}{1 + 10^{-0.4(m_2 - m_1)}}. \tag{3.4}$$

Tracking is always mandatory if, due to the object's faintness and/or high velocity the S/N of the individual object pixels fail to reach the detection threshold.

Optimum integration time calls for a tradeoff between maximum S/N (which in turn calls for a long integration time of the non-moving (tracked) source) and the ability to model the moving object's image. For a "static" object it is obvious that the best S/N is achieved through integrating the object as long as possible. Every readout process would compromise the observation by adding noise and preventing the detector from accumulating information during the so-called dead time. On the other hand, the situation is quite different if the source is moving across the pixels during the exposure. The number of pixels within the image is growing with time. After each pixel crossing time new pixels (which already filled with background noise) are added to the object's image and the same number of pixels (which accumulate noise only from then onwards) are left behind. Therefore the overall S/N soon reaches a maximum after a few pixel crossing times (at least if the signal to background ratio is small). A detailed discussion of the S/N for moving objects (including examples for the SLR and the ZIMLAT telescopes) may be found in Appendix A.

In order to model the object images correctly we have additional reasons to limit the trail length of a moving object and hence the exposure time:

- Tracking is never perfect: Although a wrong tracking velocity is not catastrophic, it tends to elongate the images somewhat but leaves them homogeneous. Any acceleration on the other hand will compromise the centroiding.

The error of an unknown acceleration is, of course, increasing with exposure time (the actual dependency being defined by the particular centroiding algorithm used).

- Temporal changes of the atmospheric refraction (even if common for all objects in the field of view) have the same effect as tracking errors. Again, only the non-linear terms are critical.

- Distortions and aberrations (e.g. coma) in the field may be calibrated for point sources (even taking into account a possible dependency on the object's brightness). Intrinsically very elongated images (due to the movement of the source) may be difficult or impossible to model in the centroiding process.

The first two items need additional comments. In both cases the effects are common to all objects in the field. Both effects are also present in classical astrography but the influence on the results is much less pronounced due to the fact that all stellar images have the same shape and thus the centroiding process reacts in the same way for all stars (depending on the centroiding algorithm there may, however, also exist a more or less distinct magnitude dependency). To a certain extent the much longer integration times randomize the tracking and (common) refraction errors somewhat. Let us summarize the discussion in this section by the following:

Conclusions

Tracking Whether or not tracking is feasible at all depends entirely on the mechanical performance of the telescope and its mount.

- Tracking is possible if the thereby imposed maximum integration interval (given by the tracking errors) is longer than a few pixel crossing times of the moving object (without tracking).

- Optimum tracking as described above should be applied.

Integration time A frame should be exposed until one of the following conditions is met:

- A few pixel crossing times of the fainter source have elapsed.

- The S/N per pixel of the fainter source's image reaches the same value as for the brighter source image (when optimum tracking is used this condition is met right from the beginning and is thus not applicable).

- The maximum integration time due to tracking errors is reached.
- One of the images reaches maximum length due to field distortions.
- One of the sources saturates the detector.

These conditions imply that the object characteristics (like angular velocity and brightness) are known beforehand. If this is not the case a few test exposures must be performed to define the optimum observation parameters.

3.1.3 Observations during single close encounters

As stated above we perform astrometric observations during close encounters between the moving object (program object) and a reference object (star). From the observational point of view a close encounter is defined by the time interval during which the angular distance between the object and the reference star is smaller than the diameter of the field of view of the detector. The aim is, of course, to extract the maximum amount of information about the relative positions of the two objects during this time interval. Given the limitations imposed on the integration times the solution is to expose a series of frames. Figure 3.1 illustrates the situation. A series of 9 frames, each exposed for 0.5 s, were superposed to produce this image. The telescope was tracking the geostationary satellite (drive off) and consequently the reference star passed the satellite from east to west (left to right).

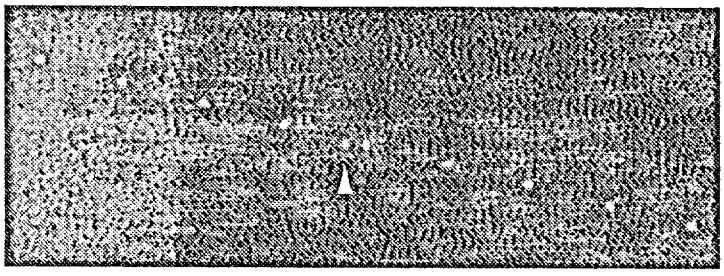

Figure 3.1: Close encounter of the geostationary weather satellite METEOSAT 5 (arrow) and the reference star P512487. The frames were integrated for 0.5 s and spaced by 8 s. The field of view is approximately 16′ x 6′.

In order to get a quantitative impression we want to calculate the number of frames per encounter and the duty cycle.
Let

t_p the pixel crossing time of the moving object;

t_f the frame crossing time of the moving object;

t_e the exposure time;

t_r the readout time including all other relevant dead times.

The number of frames per encounter n_f is thus

$$n_f = \frac{t_f}{t_e + t_r} \tag{3.5}$$

and the duty cycle dc is simply

$$dc = \frac{t_e}{t_r}. \tag{3.6}$$

Values for a set of different objects are listed in Table 3.4. The relevant object characteristics may be found in Table 2.1. The exposure times t_e were set to 5 times the pixel crossing times t_p and the readout time is 5.6 s (corresponding to a full 512 x 512 frame). Calculations for the S/N are based on the parameters of the 0.5 m SLR telescope and the PM512 CCD (see Chapter 5).

	Close encounters			
	ECS	GPS	LAGEOS	ERS1
t_e [msec]	1365	690	85	10
n_f	20	11	1	1
duty cycle	0.20	0.11	0.015	0.0018
S/N per frame	550	20	6	260
S/N total	2500	65	6	260

Table 3.4: Observational characteristics of close encounters. Exposure time t_e, number of frames per encounter n_f, duty cycle (ratio of exposure to readout time) and S/N are given for four different satellites. The corresponding object characteristics are given in Table 2.1. All calculations were made for the Zimmerwald 0.5 m laser ranging telescope and a 512 x 512 pixel CCD with 5.6 s full frame readout time.

The poor duty cycles are caused by long dead times between subsequent exposures. The long readout (dead) time is given by the fact that we read all pixels of the CCD with the highest possible quality although we are only interested in two small regions containing the object and the reference star. CCDs fortunately allow the read out of only portions of a frame, called *subframes*, and skipping of

the content of the remaining pixels at high speed. Let us describe the procedure in more detail using Figure 2.1 as illustration.

We recapitulate the general readout process for a CCD:

1. All rows are parallel shifted towards the serial register by one row, the top row is thereby transferred into the serial register.
2. The content of the serial register is shifted by one pixel towards the output amplifier.
3. The charge at the output node is amplified and digitized in the analog to digital converter (ADC).
4. Step 2 and 3 are again executed until the serial register is empty.
5. Steps 1 to 4 are repeatedly executed until the charge of all pixels is read out.

The difference when reading subframes is that we gain the digitization time (step 3) for the pixels to be skipped. In addition the serial register readout (step 2) can be skipped for all rows not containing any pixels of interest. We still have to transfer all rows but the gain in speed is significant because the total digitization time dominates the total parallel or serial transfer times. The readout time for a subframe may thus be expressed (somewhat simplified) as:

$$t_r = n_p t_{cp} + n_{rsf} n_s t_{cs} + n_{sf} t_{adc}, \tag{3.7}$$

where

n_p, n_s are the parallel and serial dimensions of the CCD respectively;

t_{cp}, t_{cs} are the parallel and the serial transfer times;

t_{adc} is the digitization time;

n_{sf} is the number of pixels in the subframe;

n_{rsf} is the number of rows in the subframe.

Taking into account the elongation of the images (we assume $t_e = 5t_p$), a minimum area for the background determination as well as the uncertainty in the a priori positions of the objects, we may end up with two minimum subframes of 30 x 30 pixels to be read out. Together with the actual parameters of a 512 x 512 CCD we get:

$$t_r = 0.39 \text{ s} \quad \text{instead of} \quad 5.49 \text{ s} \quad \text{for the full frame.} \tag{3.8}$$

The CCD parameters used in (3.8) were:

n_p = 512

n_s = 512

t_{cp} = 390 μs

t_{cs} = 5.2 μs

t_{adc} = 15 μs (moderate camera gain)

n_{sf} = 1800

n_{rsf} = 60 .

The digitization time t_{adc} strongly depends on the effective camera gain (electrons per ADU). The above value corresponds to a gain of 20 e^- per ADU. For a camera gain of 9 e^- per ADU resulting in a digitization time of 31 μs improvement would be even more striking, namely 0.42 s for the subframes instead of 9.69 s for the full frame!

In Table 3.5 the same quantities as in Table 3.4 are listed but for the described subframe technique (t_r = 0.39 s). Figure 3.2 shows the superposition of ten (subframe-) observations of a close encounter between the two geostationary satellites TDF1, TDF2 and a reference star (P509480). We should emphasize,

	Close encounters subframe technique			
	ECS	GPS	LAGEOS	ERS1
t_e [msec]	1365	690	85	10
n_f	79	64	35	2
duty cycle	0.77	0.64	0.18	0.025
S/N per frame	550	20	6	260
S/N total	4900	160	35	370

Table 3.5: Observational characteristics of close encounters when using the subframe readout technique. The impact of the reduced readout time on the number of frames per encounter n_f, the duty cycle and the S/N is obvious (compare with Table 3.4). The values were calculated on the basis of a 512 x 512 pixel CCD and two independent 30 x 30 pixel subframes and a corresponding readout time of 0.39 s. Object and instrument characteristics are the same as in Table 3.4.

however, that this technique is only efficient if the a priori coordinates (with respect to the CCD!) are known with sufficient accuracy. Otherwise the subframes have to be large or the objects may be missed. This not only requires precise

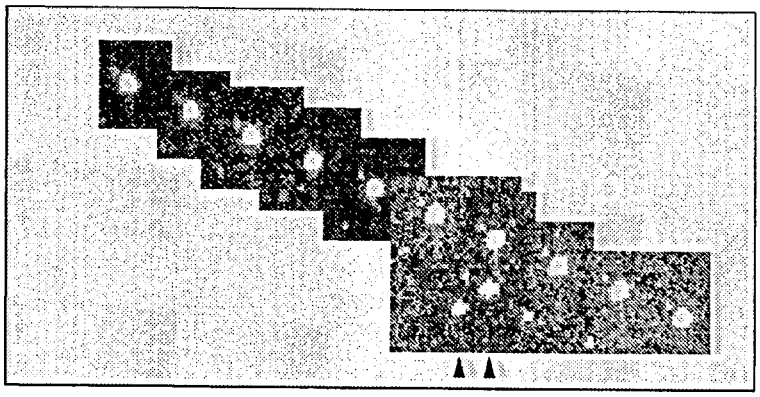

Figure 3.2: Observations of a close encounter using the subframe technique. The series of ten frames were superposed to produce this image. As the telescope was not tracking (drive off), the two geostationary satellites TDF1 and TDF2 (at 19° west) (arrows) remain fixed while the reference star (P509480) is moving across the field (from left to right). The spacing between the exposures was 5 s and the total time span of the encounter about 1 minute. Each individual frame was exposed for 1 s. The image covers 15′ in the east-west direction. Zenith is up.

ephemerides for the moving objects, but a good and well calibrated mount model for the telescope is a requirement as well. If the a priori data are insufficient the objects must first be acquired with a full frame or with larger subframes. By means of real time object recognition and digital filtering the prediction of the object's position on the CCD may successively be improved and the extension of the subframes reduced. One should, on the other hand, be aware of the sophisticated real time software and the large processing power needed to accomplish this task!

3.2 Determination of the mapping geometry

After having discussed the observational techniques in the restricted sense the next step in a classical treatment of the topic would be the description of the "measurement" process. The latter task consists of measuring the positions of the object images on the detector in a coordinate system defined either by the construction of the measuring machine or by the detector itself. In the case of photography, the major tool for astrography in the past 150 years, the plates are measured with a more or less automated machine. Modern systems measure the photographic density with photoelectric devices, the scan position is recorded with optical encoders or even with laser interferometers. When using electronic

detectors, on the other hand, we are in the fortunate position that the image sensor and the measuring machine are identical. The reference frame of a multichannel sensor like a CCD is realized by the grid of its pixels. We may divide the evaluation of the object positions within this coordinate system into several steps:

1. Scanning the exposure (photographic plate) for intensities (photographic densities). The result is an array of relative intensities and of associated coordinates. For electronic devices this step is obviously already performed through the readout process.

2. Object recognition and, if possible, identification.

3. Centroiding of the images of the reference stars and program objects. There is a variety of difficulties encountered during this process. Many are associated with the particular detector or measuring machine. We therefore discuss this topic for our actual application in section 4.1.3.

The remaining part of this section is devoted to the determination of the positions in a celestial reference frame. Only relative positions may be determined because it is necessary to assume a set of a priori known positions of stars (or of other reference objects like artificial satellites!) whose images are among those recorded on the exposures. In a first subsection we introduce the concept of the so-called *standard coordinates* in the tangent plane and the traditional method of (photographic) plate reduction. We will analyze the effect of different error sources (stemming from the instrument and from insufficient projection models) as well as the influence of aberration and refraction. A discussion of more general reduction approaches will provide the link with the next subsection where we will develop the methods for the case of moving objects. The small field of view, the motion of the objects, and the series of observations mean that in most cases only one reference object is recorded on the individual frames; these circumstances force us to abandon the classical method. In particular we will not be able to define instrumental constants (plate constants) from each exposure (plate) but we have to combine the information from several program frames as well as from dedicated calibration observations.

3.2.1 Classical astrometry in the tangent plane

Although the subject is treated in several astronomical textbooks we will outline the basic principles of the classical method of plate reduction as a basis for the discussion of our actual technique to determine the geometry (be presented in the next subsection). For a detailed derivation of the particular formulas we refer to the literature: A comprehensive general introduction is given in Eichhorn

(1974), detailed derivations of the fundamental equations in terms of spherical coordinates may be found in Green (1985) and a more general treatment in vectorial notation in Murray (1983); for generalized adjustment techniques we also refer to Googe et al. (1970).

Let us assume that for each object, so-called plate coordinates or measured coordinates x, y were determined in a rectangular or an other well defined reference frame. For each exposure (we will use this expression instead of "plate") a set of relationships

$$\begin{aligned} f(x_i, y_i; a_{i1}, \cdots, a_{in}; \alpha_i, \delta_i; c_1, \cdots, c_m) &= 0 \\ g(x_i, y_i; a_{i1}, \cdots, a_{in}; \alpha_i, \delta_i; c_1, \cdots, c_m) &= 0 \end{aligned} \tag{3.9}$$

exists between the measured coordinates x_i, y_i of the i-th object image and its celestial coordinates α_i, δ_i. The parameters a_{ik} are related to the object and characterize properties like magnitude, color index, or angular velocity whereas the c_k do not depend on the object but on the particular exposure or the instrument in general (the traditional plate constants would be parameters of the latter type). Generally some of the parameters c_k vary from exposure to exposure, others vary but are in part constrained and some are constant for all exposures.

The evaluation of relative (or astrographic) positions is now done in the following way: the coordinates α_i, δ_i of a subset of the observed objects (reference stars or reference objects) have to be assumed as known a priori and must be taken from a star catalogue or from an ephemeris in the case where a moving object's positions (e.g. an artificial satellite) are used as reference. These celestial coordinates together with the measured coordinates x_i, y_i of all reference and "unknown" objects (program objects) are introduced in the equations (3.9) which thereby become equations of condition for the unknown parameters c_k and the celestial coordinates α_i, δ_i of the unknown objects. The resulting set of condition equations is then solved in a least squares adjustment. In a correct approach not only the x_i, y_i but also the α_i, δ_i of the reference objects must be introduced as observations. From the technical point of view this means that we have to solve also for the positions of the reference objects and must introduce additional equations of condition incorporating the a priori information as properly weighted pseudo-observations. In the same way any a priori information of the c_k might be introduced as pseudo-observations. The object dependent parameters are usually assumed to be known although e.g. the color index may in principle be estimated from observations of the same object at different zenith distances (i.e. at different hour angles) due to the effect of differential color refraction (see also section 3.4.5).

In all astrographic applications a gnomonic (or central) projection is assumed as the basic model ("zero order approximation") for the relations (3.9) provided

the focal surface of the telescope is essentially an Euclidean plane. Significantly different optical systems like e.g. Schmidt telescopes ask for a different projection but the greater part of the following concepts and analyses will nevertheless remain valid after appropriate corrections. The geometry of the gnomonic projection is illustrated in Figure 3.3.

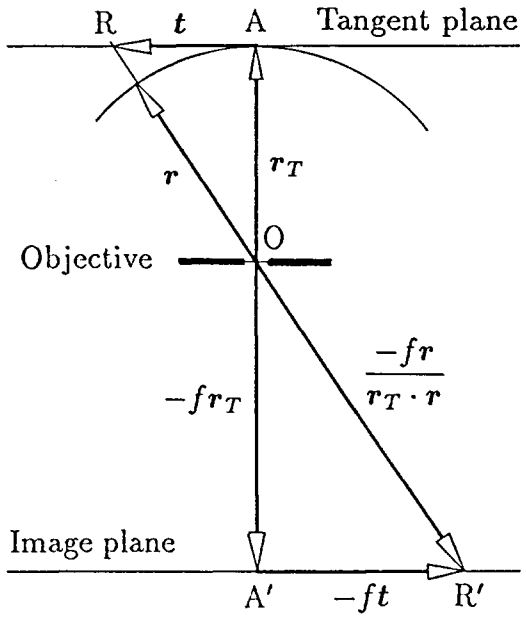

Figure 3.3: Geometry of gnomonic projection.

We thereby imply that the optical system behaves like a pin-hole camera. O is the center of a unit sphere and the unit vector $\boldsymbol{r}_T$ is the direction perpendicular to the image plane. The latter defines the tangent plane to the celestial sphere at the point A. The image of A is A′ (the principal image point). The vector $\boldsymbol{r}$ denotes a general apparent direction and R is the corresponding point in the tangent plane. The tangential coordinates $\boldsymbol{t}$ of $\boldsymbol{r}$ relative to $\boldsymbol{r}_T$ may be written as

$$\boldsymbol{t} = \frac{\boldsymbol{r}}{\boldsymbol{r}_T \cdot \boldsymbol{r}} - \boldsymbol{r}_T. \tag{3.10}$$

If $\boldsymbol{u}$, $\boldsymbol{v}$, $\boldsymbol{w}$ are mutually orthogonal unit vectors with $\boldsymbol{u}$, $\boldsymbol{v}$ lying in the tangent plane we may express the components u, v, w of $\boldsymbol{t}$ in the coordinate system defined by the unit vectors $[\boldsymbol{u}, \boldsymbol{v}, \boldsymbol{w}]$

$$u = \boldsymbol{u} \cdot \boldsymbol{t} = \frac{\boldsymbol{u} \cdot \boldsymbol{r}}{\boldsymbol{r}_T \cdot \boldsymbol{r}}, \qquad v = \boldsymbol{v} \cdot \boldsymbol{t} = \frac{\boldsymbol{v} \cdot \boldsymbol{r}}{\boldsymbol{r}_T \cdot \boldsymbol{r}}, \qquad w = 0. \tag{3.11}$$

It is easily seen that the corresponding image vector between A′ and R′ is equal to $-f\boldsymbol{t}$ where $f \equiv \overline{\mathrm{OA}'}$ is the effective focal length. We may therefore

derive the coordinates of any point R′ with respect to the system $[\boldsymbol{u}, \boldsymbol{v}, \boldsymbol{w}]$ by scaling the corresponding coordinates measured in the image plane $[\boldsymbol{u}', \boldsymbol{v}', \boldsymbol{w}']$ with $-f$.

If we let lie the vectors $\boldsymbol{u}$ and $\boldsymbol{v}$ in the equatorial and the declination plane and orient them in the directions of increasing right ascension and declination respectively then the coordinates u, v of $\boldsymbol{r}$ are called the *"standard (or normal) coordinates"* ξ, η:

$$\xi = \frac{\boldsymbol{u} \cdot \boldsymbol{r}}{\boldsymbol{r}_T \cdot \boldsymbol{r}}, \qquad \eta = \frac{\boldsymbol{v} \cdot \boldsymbol{r}}{\boldsymbol{r}_T \cdot \boldsymbol{r}}, \tag{3.12}$$

$$\boldsymbol{t} = \begin{pmatrix} \xi \\ \eta \\ 0 \end{pmatrix}.$$

Defining the unit vectors $\boldsymbol{r}$ and $\boldsymbol{r}_T$ by their rectangular equatorial coordinates

$$\boldsymbol{r} = \begin{pmatrix} \cos\delta & \cos\alpha \\ \cos\delta & \sin\alpha \\ \sin\delta & \end{pmatrix}, \qquad \boldsymbol{r}_T = \begin{pmatrix} \cos\delta_T & \cos\alpha_T \\ \cos\delta_T & \sin\alpha_T \\ \sin\delta_T & \end{pmatrix} \tag{3.13}$$

we may compute the standard coordinates of $\boldsymbol{r}$ (with respect to the tangent point direction $\boldsymbol{r}_T$) as

$$\begin{pmatrix} \xi \\ \eta \\ 0 \end{pmatrix} = \mathbf{R}_3(\frac{\pi}{2})\mathbf{R}_2(\frac{\pi}{2} - \delta_T)\mathbf{R}_3(\alpha_T)(\frac{\boldsymbol{r}}{\boldsymbol{r}_T \cdot \boldsymbol{r}} - \boldsymbol{r}_T), \tag{3.14}$$

where $\mathbf{R}_i(\varphi)$ is a 3 x 3 matrix characterizing a positive (with respect to the equatorial system) rotation around the angle φ about the axis i. Equation (3.14) may be written explicitly in spherical coordinates as

$$\begin{aligned} \xi &= \frac{\cos\delta \sin(\alpha - \alpha_T)}{\sin\delta_T \sin\delta + \cos\delta_T \cos\delta \cos(\alpha - \alpha_T)} \\ \eta &= \frac{\cos\delta_T \sin\delta - \sin\delta_T \cos\delta \cos(\alpha - \alpha_T)}{\sin\delta_T \sin\delta + \cos\delta_T \cos\delta \cos(\alpha - \alpha_T)}. \end{aligned} \tag{3.15}$$

The inverse transformation may, of course, be performed using the appropriate rotation matrices:

$$\frac{\boldsymbol{r}}{\boldsymbol{r}_T \cdot \boldsymbol{r}} = \mathbf{R}_3(-\alpha_T)\mathbf{R}_2(\delta_T - \frac{\pi}{2})\mathbf{R}_3(-\frac{\pi}{2}) \begin{pmatrix} \xi \\ \eta \\ 0 \end{pmatrix} + \boldsymbol{r}_T \tag{3.16}$$

and explicitly:

$$\begin{aligned} \tan(\alpha - \alpha_T) &= \frac{\xi}{\cos\delta_T - \eta \sin\delta_T} \\ \tan\delta &= \frac{\sin\delta_T + \eta\cos\delta_T}{\cos\delta_T - \eta\sin\delta_T}\cos(\alpha - \alpha_T). \end{aligned} \tag{3.17}$$

Let us now focus on relations (3.9). The basic problem consists of the establishment of a transformation between the measured coordinates x, y and their standard coordinates ξ, η in the tangent plane. When considering the measurement process we can identify a number of instrumental effects (we do not consider errors from the centroiding process but merely properties of the measurement coordinate system):

- Decentering of origin
  There will always be an offset between the origin of the measurement coordinate system and the actual (or adopted) principal image point.
- Orientation of the axes
  The direction of the coordinate axes will deviate from the directions of the corresponding standard coordinate system. Also, we may not assume that the measurement axes are strictly orthogonal.
- Coordinate scales
  The coordinate scales may in general be non-linear (mechanical devices and optical encoders suffer e.g. from periodic errors). These imperfections may often be calibrated independently (assuming stability in time). Linear scale variations, however, (which are most likely different for both axes) have to be considered as unknown.

Each of the above effects may be separated into an a priori known and a residual unknown component. Let X, Y be the raw measured coordinates and Θ_x, Θ_y the angles between the X, Y axes and the corresponding standard coordinate directions $\boldsymbol{u}$, $\boldsymbol{v}$. If we furthermore define f_x, f_y as the focal length expressed in units of X, Y the general linear transformation reads as

$$\begin{aligned} \xi &= a_1 + f_x^{-1}(X\cos\Theta_x - Y\sin\Theta_y) \\ \eta &= b_1 + f_y^{-1}(X\sin\Theta_x + Y\cos\Theta_y), \end{aligned} \tag{3.18}$$

where a_1, b_1 are the offsets of the coordinate system origin (see (a) above). Expressing the measured coordinates in units of the approximate focal length f_0, $x = f_0^{-1}X$, $y = f_0^{-1}Y$ equation (3.18) may be written in the form

$$\begin{aligned} \xi - x &= a_1 + a_2 x + a_3 y \\ \eta - y &= b_1 + b_2 x + b_3 y, \end{aligned} \tag{3.19}$$

where

$$\begin{aligned} a_2 &= f_0 f_x^{-1} \cos\Theta_x - 1 \\ a_3 &= -f_0 f_x^{-1} \sin\Theta_y \\ b_2 &= f_0 f_y^{-1} \sin\Theta_x \\ b_3 &= f_0 f_y^{-1} \cos\Theta_y - 1. \end{aligned} \tag{3.20}$$

Assuming that the X, Y axes are approximately parallel to $\boldsymbol{u}$, $\boldsymbol{v}$ directions (known gross missalignments and offsets are corrected beforehand) and that f_0 is a good estimate of the true focal length the so-called plate constants a_i, b_i will be small values. The plate constants are now determined in an adjustment process by minimizing the quantity $\sum[(\xi - x)^2 + (\eta - y)^2]$.

Different kinds of errors may compromise the outlined ideal reduction procedure and force us to add quadratic and higher order terms in equation (3.19):

(a) The adopted principal image point may not coincide with the true principal image point A′.

(b) There may be deviations from the model of gnomonic projection e.g. due to distortions from imperfections in the optical system.

(c) The computed coordinates differ from the true standard coordinates, e.g. if refraction or aberration were neglected.

(d) The model for the measurement process is insufficient, e.g. if the non-linear terms were not calibrated correctly.

Let us analyze some of these errors in the following paragraphs.

Centering error

When starting the reduction the location of the principal image point A′ (i.e. a_1, b_1 in the equation (3.19)) is not known. The latter must be inferred from a coarse measurement of a few reference stars on the exposure or from the pointing direction of the telescope. Because the direction $\boldsymbol{r}_T$ corresponding to the principal image point A′ is used in the calculation of the standard coordinates it can only

be derived iteratively. In order to asses the influence of an error in the a priori position of the tangent point A we must differentiate equations (3.10) with respect to $\boldsymbol{r}_T$. Expressed in spherical coordinates this yields

$$\begin{aligned} d\xi &= -\cos(\delta_T)d\alpha_T + \sin(\delta_T)d\alpha_T\eta - [\cos(\delta_T)d\alpha_T\xi + d\delta_T\eta]\xi \\ d\eta &= -d\delta_T - \sin(\delta_T)d\alpha_T\xi - [\cos(\delta_T)d\alpha_T\xi + d\delta_T\eta]\eta. \end{aligned} \tag{3.21}$$

The above expressions may be written in the form:

$$\begin{aligned} d\xi &= -p_1 + p_3\eta - (p_1\xi + p_2\eta)\xi \\ d\eta &= -p_2 - p_3\xi - (p_1\xi + p_2\eta)\eta, \end{aligned} \tag{3.22}$$

where p_1, p_2 are the standard coordinates of the true tangent point A with respect to the adopted one. The term p_3 represents a small rotation of the coordinate system in the tangent plane and the quadratic terms (in standard coordinates) are called "tilt terms". To correct the principal image point A we must express (3.22) in terms of measured coordinates x, y. Because the plate constants a_1, a_3, b_1, b_3 in equation (3.20) and the p_i in equation (3.22) are small we may simply substitute $\xi = x + a_1$, $\eta = y + b_1$ in equation (3.22). This yields actually the partial derivatives to be used in the adjustment for the estimation of the coordinates of the principal image point on the sensor. Figure 3.4 illustrates the effect of the tilt terms for a centering error of $d\alpha_T/\cos(\delta_T) = 1'$, $d\delta_T = 1'$ in a 1° x 1° field. The maximum value of the tilt terms is given by $|\boldsymbol{t}||d\boldsymbol{r}_T|$ where $|\boldsymbol{t}| = \sqrt{\xi^2 + \eta^2}$ and $|d\boldsymbol{r}_T| = \sqrt{d\alpha_T^2 cos^2\delta_T + d\delta_T^2}$. Table 3.6 gives the values for various $|\boldsymbol{t}|$ in degrees and $|d\boldsymbol{r}_T|$ in minutes.

Plate tilt

If the plane of the sensor is tilted with respect to the adopted tangential plane this is actually identical with a decentring of the same amount. Suppose we define the tangent point A by the direction of the optical axis (this being defined by the inner and outher principal points of the centered optical system of the telescope). In this case the optical axis will in general not be perpendicular to the plane of the sensor. We then say that the sensor plane is tilted with respect to optical axis. This may be adequate if the optical system produces additional deviations from the gnomonic projection model like radial distortions which are preferably referred to the intersection point of the optical axis with the focal plane. The model of the projection has to be adapted accordingly. This means that quadratic tilt terms of the same form as found in (3.22) have to be introduced in (3.19):

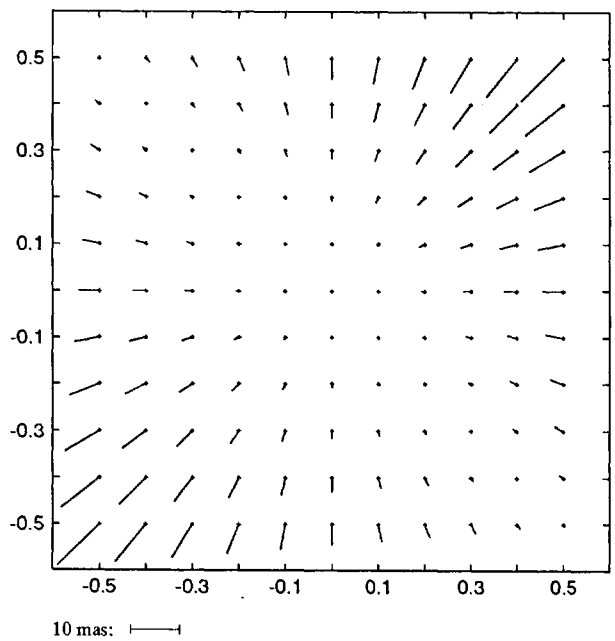

Figure 3.4: Quadratic terms, or "tilt terms", of deformation due to a centering error. The figure represents a 1° x 1° field, right ascension is on the abscissa and declination on the ordinate (west on the right and north on top). Tick mark labels are in units of 0.1°Decentering is assumed to be 1′ in both directions i.e. towards the top right corner ($d\alpha_t/\cos(\delta_T) = -1'$, $d\delta_T = 1'$). The effect is identical for a tilt of the detector plane (with respect to the tangent plane) of 1.4 (around an axis lying in the tangent plane in the top left to bottom right diagonal direction).

$\|t\|$ [deg]	Centering error – quadratic terms in mas									
	dr_T [arcmin]									
	1	2	3	4	5	6	7	8	9	10
.1	0	0	1	1	1	1	1	1	2	2
.2	1	1	2	3	4	4	5	6	7	7
.3	2	3	5	7	8	10	12	13	15	16
.4	3	6	9	12	15	18	20	23	26	29
.5	5	9	14	18	23	27	32	37	41	46
.6	7	13	20	26	33	39	46	53	59	66
.7	9	18	27	36	45	54	63	72	81	90
.8	12	23	35	47	58	70	82	94	105	117
.9	15	30	44	59	74	89	104	118	133	148
1.0	18	37	55	73	91	110	128	146	164	183

Table 3.6: Quadratic terms of the deformation due to a centering error. Values in milliarcseconds are given for various distances $|t|$ from the projection center and various centering errors dr_T. This deformation is equal to the effect produced by a tilt of the projection plane with respect to the tangent direction of the same amount. The terms are therefore also called "tilt terms".

$$\begin{aligned} d\xi_T &= -(p_1\xi + p_2\eta)\xi \\ d\eta_T &= -(p_1\xi + p_2\eta)\eta. \end{aligned} \tag{3.23}$$

We should finally point out again that tilt terms can only be separated from a centering error if the optical axis is defined independently e.g. through optical (radial) distortions referring to it. (These distortions must be a) significant and b) appropriately modeled, i.e. the corresponding terms must be added to (3.22)).

Aberration and refraction

The standard coordinates must be computed from refracted topocentric apparent positions. This means that corrections for precession, nutation, annual and diurnal aberration, and refraction have to be applied to the mean positions of the catalogue stars. With the aid of computers and appropriate software this is simple today. In the classical approach these corrections were neglected and the standard coordinates computed directly from mean positions. This "dramatically" simplified the calculations and in addition also yielded the positions of the unknown objects in the mean system of the catalogue used for the reference

stars (supposed that the quadratic terms in aberration and refraction can be neglected). Obviously no orthogonal transformation (precession and nutation) will affect the validity of equation (3.19). Furthermore all constant and linear terms of refraction and aberration are absorbed by the plate constants a_i, b_i. In order to assess the order of magnitude for these effects we use approximation formulas for the annual aberration and the refraction. The aberration may be expressed as an effect which alters the angle Θ between the apex of the earth's motion $\boldsymbol{r}_0$ and a general direction $\boldsymbol{r}$ in the sense that $d\Theta = k \sin\Theta$ or $d\boldsymbol{r} = k\boldsymbol{r} \times (\boldsymbol{r} \times \boldsymbol{r}_0)$ where k is essentially the aberration constant. The following equations are rigorous to the second order in ξ and η

$$\begin{aligned} d\xi &= -k(\boldsymbol{u} \cdot \boldsymbol{r}_0) + k(\boldsymbol{r}_T \cdot \boldsymbol{r}_0)\xi - \frac{k}{2}(\boldsymbol{u} \cdot \boldsymbol{r}_0)(\xi^2 + \eta^2) \\ d\eta &= -k(\boldsymbol{v} \cdot \boldsymbol{r}_0) + k(\boldsymbol{r}_T \cdot \boldsymbol{r}_0)\eta - \frac{k}{2}(\boldsymbol{v} \cdot \boldsymbol{r}_0)(\xi^2 + \eta^2). \end{aligned} \tag{3.24}$$

The relations (3.24) are of the form

$$\begin{aligned} d\xi &= c_1 + c_2\xi + \frac{c_1}{2}(\xi^2 + \eta^2) \\ d\eta &= c_3 + c_2\xi + \frac{c_3}{2}(\xi^2 + \eta^2). \end{aligned} \tag{3.25}$$

The parameters c_1, c_3 being the actual displacement components of $\boldsymbol{r}_T$ due to aberration are expressed as

$$\begin{aligned} c_1 &= \frac{1}{c}(\dot{Y}\cos\alpha_T - \dot{X}\sin\alpha_T) \\ c_3 &= \frac{1}{c}(\dot{Z}\cos\delta_T - \dot{X}\sin\delta_T\cos\alpha_T - \dot{Y}\sin\delta_T\sin\alpha_T). \end{aligned} \tag{3.26}$$

This is the classical first order approximation formula for the annual aberration where $\dot{X}$, $\dot{Y}$, $\dot{Z}$ are the components of the earth's barycentric velocity vector and c is the speed of light.

Noting that k is of the order of 20″ the first order terms (in ξ and η) may change the plate scale at maximum by about 10^{-4}. The change in scale is the same in both directions $\boldsymbol{u}$ and $\boldsymbol{v}$. The second order terms give rise to an error of 0.″003 for $|\boldsymbol{t}| = 1°$ and up to 0.″075 for $|\boldsymbol{t}| = 5°$ in each coordinate (ξ, η). It may thus be ignored in most cases except in cases where a) a large field of view is used and b) ultimate accuracy is required. Figure 3.5 shows the displacement in a 1° x 1° field due to the second order terms if the apex is at 90° distance in direction of the upper right hand corner of the field (at 90° the effect reaches

maximum due to $(\boldsymbol{u} \cdot \boldsymbol{r}_0)^2 + (\boldsymbol{v} \cdot \boldsymbol{r}_0)^2 = 1$).

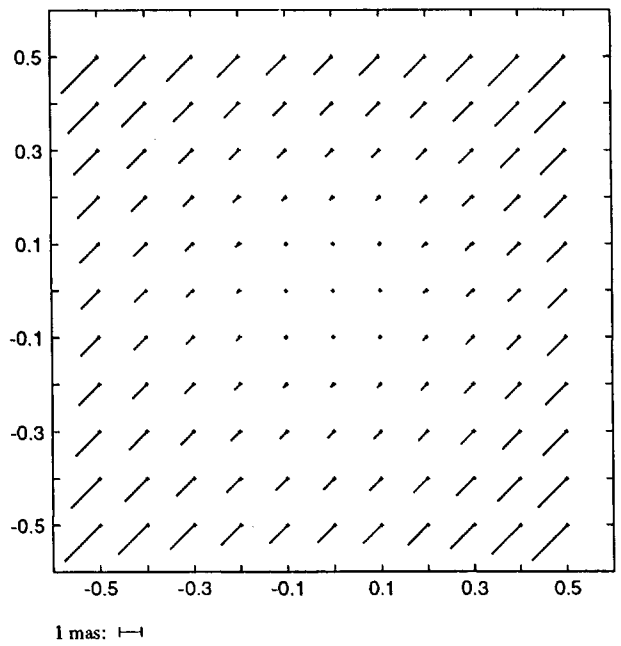

Figure 3.5: Quadratic terms due to aberration. The figure represents a 1° x 1° field. The tick marks units are in degrees. The apex is at 90° distance in direction of the upper right corner of the field.

The simplest model of atmospheric refraction (defined as the difference $d\Theta = \zeta - \Theta_0$ of the true and the apparent zenith distances ζ and Θ_0) can be written as $d\Theta = k \tan \Theta_0$ or $d\boldsymbol{r} = -(k/\cos)\Theta_0\, \boldsymbol{r} \times (\boldsymbol{r} \times \boldsymbol{r}_0)$ where Θ is the angle between the zenith direction $\boldsymbol{r}_0$ and the apparent direction $\boldsymbol{r}$ of the celestial object. The constant k is of the order of 60″ and depends slightly on the atmospheric conditions. For practical reasons we give the formulas in the form of polynomials of the second order in the standard coordinates ξ, η:

$$\begin{aligned} d\xi &= -k[\xi_0 - (1+\xi_0^2)\xi - \xi_0\eta_0\eta \\ &\quad + \xi_0(2+\xi_0^2)\xi^2 + \eta_0(1+2\xi_0^2)\xi\eta + \xi_0(1+\eta_0^2)\eta^2] \\ d\eta &= -k[\eta_0 - \xi_0\eta_0\xi - (1+\eta_0^2)\eta \\ &\quad + \eta_0(1+\xi_0^2)\xi^2 + \xi_0(1+2\eta_0^2)\xi\eta + \eta_0(2+\eta_0^2)\eta^2], \end{aligned} \tag{3.27}$$

where ξ_0, η_0 are the formal standard coordinates of the zenith:

$$\xi_0 = \frac{\boldsymbol{u} \cdot \boldsymbol{r}_0}{\boldsymbol{r}_T \cdot \boldsymbol{r}_0}, \qquad \eta_0 = \frac{\boldsymbol{v} \cdot \boldsymbol{r}_0}{\boldsymbol{r}_T \cdot \boldsymbol{r}_0}. \tag{3.28}$$

In terms of spherical coordinates we have:

$$\begin{aligned} \xi_0 &= \frac{\cos\Phi \sin H}{\sin\delta_T \sin\Phi + \cos\delta_T \cos\Phi \cos H} \\ \eta_0 &= \frac{\cos\delta_T \sin\Phi - \sin\delta_T \cos\Phi \cos H}{\sin\delta_T \sin\Phi + \cos\delta_T \cos\Phi \cos H}, \end{aligned} \tag{3.29}$$

where Φ is the astronomical latitude of the observer's location and H is the hour angle of the tangent point. The first order terms in ξ and η represent a scaling factor of the order of $k(1 + \xi_0^2)$. The maximum value of the scaling factor is given by $k(1 + |\boldsymbol{t}_0|^2)$ and of the second order term by $k(2|\boldsymbol{t}_0| + |\boldsymbol{t}_0|^3)$ where $\boldsymbol{t}_0 = (\xi_0, \eta_0)$. Maximum values for the scale change for various zenith distances z are given in Table 3.7. Table 3.8 lists the maximum values of the quadratic term for various distances $|\boldsymbol{t}|$ from the tangent point and different zenith angles z_T. We again illustrate the effects of the linear and quadratic terms in Figure 3.6 and 3.7 respectively.

	Refraction – linear terms							
	z_T [deg]							
	10	20	30	40	50	60	70	80
scale change $\cdot 10^4$	3.0	3.3	3.9	5.0	7.0	12	25	96
error [mas/deg]	1080	1186	1396	1785	2535	4189	8952	34729

Table 3.7: Scale changes due to refraction for various zenith distances z_T are given in the first row. The second row indicates the induced maximum position error in milliarcseconds at 1 degree distance from the projection center. (Scale factor := 1+ scale change).

The formulas (3.27) may be transformed from (ξ, η) to (x, y). The resulting corrections dx, dy will then also be polynomials in x, y. These corrections may be precomputed and applied to the measured coordinates x, y to let the latter appear as if mean instead of observed positions had been recorded by the sensor.

These considerations are, of course, only valid if k is constant over the entire field and for all objects. The first condition is certainly true for zenith distances not too large but k may vary for objects with different intrinsic colors! We may deal with this so-called "color refraction" in three different ways:

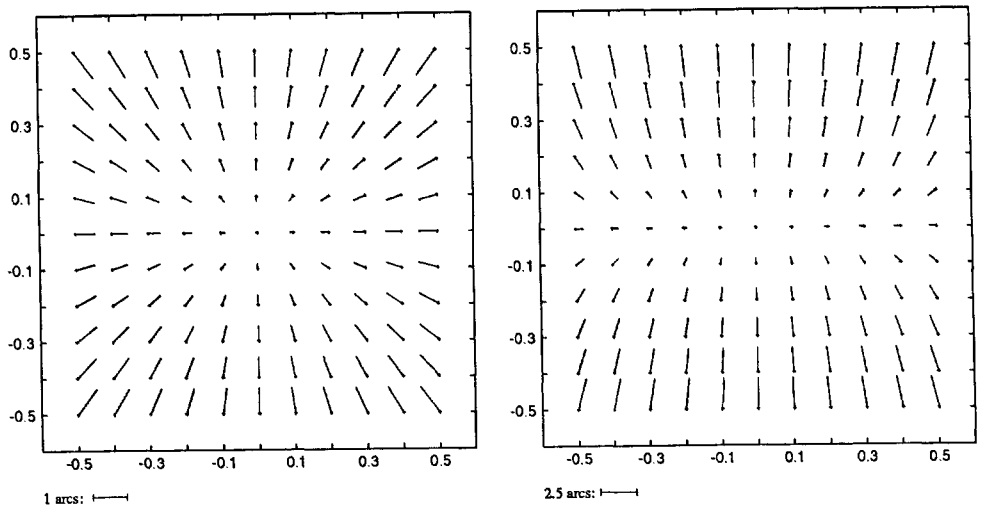

(a) $z_T = 30°$ (b) $z_T = 60°$

Figure 3.6: Linear terms of the deformation due to refraction. The figure represents two 1° x 1° fields (same orientation and scaling as in Figure 3.4). The center of the field (a) is at 30° zenith distance and at 60° for (b), zenith always in direction of north (i.e. the fields are in the meridian).

$\|\boldsymbol{t}\|$ [deg]	Refraction – quadratic terms in mas							
	z_T [deg]							
	10	20	30	40	50	60	70	80
.1	0	0	0	1	1	2	5	36
.2	0	1	1	2	4	8	21	146
.3	1	2	3	5	9	17	48	328
.4	2	3	6	9	15	30	85	583
.5	2	5	9	14	24	47	132	911
.6	4	8	13	20	35	68	191	1312
.7	5	10	17	28	47	93	260	1786
.8	6	13	23	36	62	122	339	2333
.9	8	17	28	46	78	154	429	2952
1.0	10	21	35	57	96	190	530	3645

Table 3.8: Quadratic terms of the deformation due to refraction. Values in milliarcseconds are given for various distances $|\boldsymbol{t}|$ from the projection center and zenith distances z_T. ($|\boldsymbol{t}|$ is defined in the sense $|\boldsymbol{t}| = z - z_T$.)

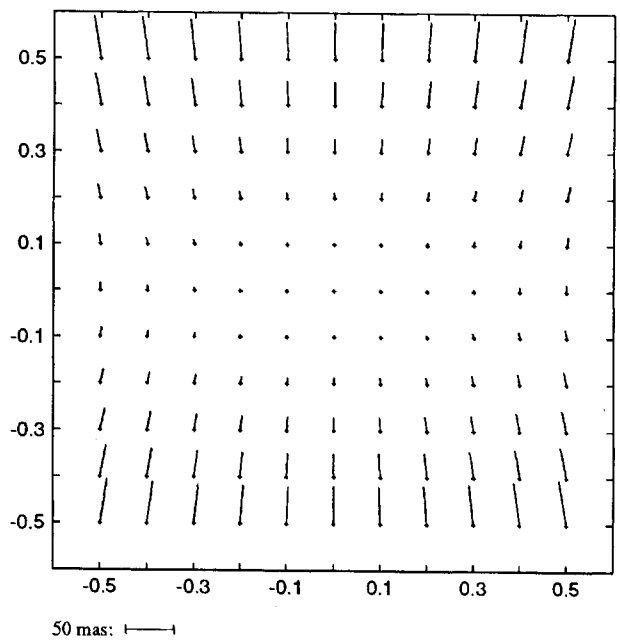

Figure 3.7: Quadratic terms due to refraction. The figure represents a 1° x 1° field (same orientation and scaling as in Figure 3.4). The field is in the meridian at $z_T = 60°$.

(a) The colors of the objects are known from an independent source and hence the correct (color dependent) refraction constant k may be computed and applied.

(b) Appropriate parameters have to be introduced and estimated using observations of the same objects at various zenith distances (for details see section 3.4.5)).

(c) The observations may be performed in a narrow passband ($\ll$ 100nm). This, however, reduces the overall efficiency of the detector system considerably (by a factor of 5 or more!).

Errors due to imperfections in the optical system

There is a wide variety of possible deviations from the gnomonic projection model due to imperfections in the optical system. Quadratic and higher order terms would have to be added to the right hand side of relation (3.19). They can either be modeled empirically or by analyzing the functional form of the deviations. Furthermore, coma and chromatic aberrations may give rise to magnitude and color dependent effects.

3.2.2 Astrographic reduction model for moving objects

The most important difference between the classical technique and the new approach for the moving objects resides in the fact that the classical plate constants are determined individually for each plate by means of an ensemble of reference stars whereas the observation technique for moving objects as described in section 3.1.3 generally results in frames with one reference star only. It is therefore not possible to determine all "plate" constants for each single frame. There is even not enough information to assess these constants from a series of observations of the object of interest passing the same reference star (series of frames during single close encounter). These circumstances force us (at least for some of the model parameters) to combine observations from several close encounters and probably also from dedicated calibration sessions. This, however, is allowed only if we may assume that:

1. all plate constants which cannot be determined from a single frame (the majority) are either stable over a certain time interval (this time interval should be long enough to allow for the necessary "calibration" observations) or can be accurately modeled (e.g. as functions of the telescope position, the derotator position angle or the time). All parameters (or "secondary constants") of these model functions have to be determined together with the "primary plate constants".

2. unmodeled components of differential refraction are constant over the same time interval (differential effects of refraction anomalies).

These requirements can be met only under the condition that all known effects are correctly modeled, i.e. no ("known") contributions of the refraction or aberration should be absorbed into the plate constants a_i and b_i. The final goal is to relate the plate constants to (hopefully stable) characteristics and to the actual state of the instrument only, i.e. to the position of the instrument, to characteristics of the optics, the sensor and to their mutual location and orientation. This requires in particular that

1. the standard coordinates must be computed from refracted (possibly color dependent) topocentric apparent positions,

2. the principal image point and/or the plate tilt are determined iteratively by introducing the appropriate quadratic terms into the model. (The plate tilt can only be separated from the location of the principal image point if radial distortions from the optics are significant and simultaneously modeled.)

Relationship between celestial and plate coordinates for an alt-azimuth mounted telescope

If the telescope mount is of the alt-azimuth type as it is the case for the Zimmerwald SLR instrument (and also for the planned ZIMLAT) the orientation of the detector coordinate system is approximately constant with respect to this altitude-azimuth system (and not with respect to the equatorial system as assumed for the classical standard coordinate concept, see (3.12)). It is therefore convenient to introduce a new intermediate coordinate system and to use "modified standard coordinates" where the axes of the system are oriented along the axes of the local topocentric horizon system. Using the same notation as in section 3.2.1 and defining $\boldsymbol{u}$ to be oriented in opposite direction of increasing azimuth and $\boldsymbol{v}$ in direction of the zenith (increasing altitude) these "modified standard coordinates" can be derived from the classical ones by applying an additional rotation $\mathbf{R}_3(s)$ around the third axis or explicitly (see also equation (3.14))

$$\begin{pmatrix} \xi \\ \eta \\ 0 \end{pmatrix} = \mathbf{R}_3(s)\mathbf{R}_3(\frac{\pi}{2})\mathbf{R}_2(\frac{\pi}{2} - \delta_T)\mathbf{R}_3(\alpha_T)(\frac{\boldsymbol{r}}{\boldsymbol{r}_T \cdot \boldsymbol{r}} - \boldsymbol{r}_T), \tag{3.30}$$

where s is the angle between the direction to the zenith and the direction to the celestial pole (the so-called parallactic angle). This angle is given by

$$\begin{aligned} \cos s \sin z_T &= \sin\varphi \cos\delta_T - \cos\varphi \sin\delta_T \cos H_T \\ \sin s \sin z_T &= \cos\varphi \sin H_T \\ \tan s &= \frac{\cos\varphi \sin H_T}{\sin\varphi \cos\delta_T - \cos\varphi \sin\delta_T \cos H_T}, \end{aligned} \tag{3.31}$$

where H_T and δ_T are the hour angle and the declination of the tangent point respectively, and φ, λ the station coordinates, astronomical latitude and longitude referred to the celestial ephemeris pole. The latter are thus correctly given by

$$\begin{pmatrix} \cos\varphi \cos\lambda \\ \cos\varphi \sin\lambda \\ \sin\varphi \end{pmatrix} = \mathbf{R}_1(y_p)\mathbf{R}_2(x_p)\boldsymbol{x}, \tag{3.32}$$

where $\boldsymbol{x}$ are the astronomical coordinates of the observer in the International Terrestrial Reference Frame (ITRF) and x_p, y_p the corresponding pole coordinates. The hour angle H is expressed by

$$H = \Theta_0 + \lambda - \alpha_T + Eq, \tag{3.33}$$

where Θ_0 is the Greenwich mean sidereal time and Eq the equation of equinoxes. The right ascension of the tangent point (α_T) should be a true apparent refracted position.

There is an other particular feature of the SLR telescope to be considered in the general reduction model, namely the presence of a rotating table adapter between the focal plane and the detector. This adapter is never rotated between individual frames of a single close encounter. It is used to intentionally orient the CCD for special experiments, e.g. for "time delayed integration" (or "drift scan") exposures, or in certain calibration procedures where we try to separate effects produced by the optical system and the detector.

Let us define (see Figure 3.8)

(a) an orthogonal coordinate system $[u_T, v_T, w_T]$ where w_T is parallel to the optical axis of the telescope, u_T, v_T lie in the focal plane and the origin is located at the intersection of the optical axis with the focal plane; u_T, v_T should be oriented approximately parallel to and fixed with respect to u, v;

(b) an orthogonal coordinate system $[u_R, v_R, w_R]$ where w_R is parallel to the rotation axis of the rotating table, the origin is at the intersection of the focal plane with the rotation axis; u_R, v_R are fixed with respect to the CCD detector;

(c) a coordinate system $[u_D, v_D, w_D]$ with u_D, v_D in the CCD detector plane oriented parallel to the pixel rows and columns. The origin may be arbitrarily fixed e.g. at a CCD corner but we assume that the nodal line of the $[u_R, v_R]$ plane with respect to the $[u_D, v_D]$ plane contains the origin of the $[u_R, v_R, w_R]$ system. The latter may be achieved by shifting the CCD along the optical axis (i.e. focussing); this system is not necessarily orthogonal i.e. the scales in the directions u_D, v_D may be different.

We may in addition assume that the inclinations (a) between the focal and the rotation plane and (b) between the rotation plane and the CCD detector plane are small. As we also assume the $[u_R, v_R, w_R]$ system to be fixed with respect to the $[u_D, v_D, w_D]$ system we define the $[u_R, v_R]$ plane to be approximately aligned with $[u_D, v_D]$ (small rotations only). The CCD detector is fixed inside the camera and the camera is fixed on the rotating table (as long as the camera is not removed from the telescope).

Let r, r', r'', r''' represent the direction to a general point in the sky expressed in the $[u, v, w]$, $[u_T, v_T, w_T]$, $[u_R, v_R, w_R]$ and $[u_D, v_D, w_D]$ system respectively. In an attempt to separate the effects in a very general way we express the transformations between the systems as follows (see also Figure 3.8):

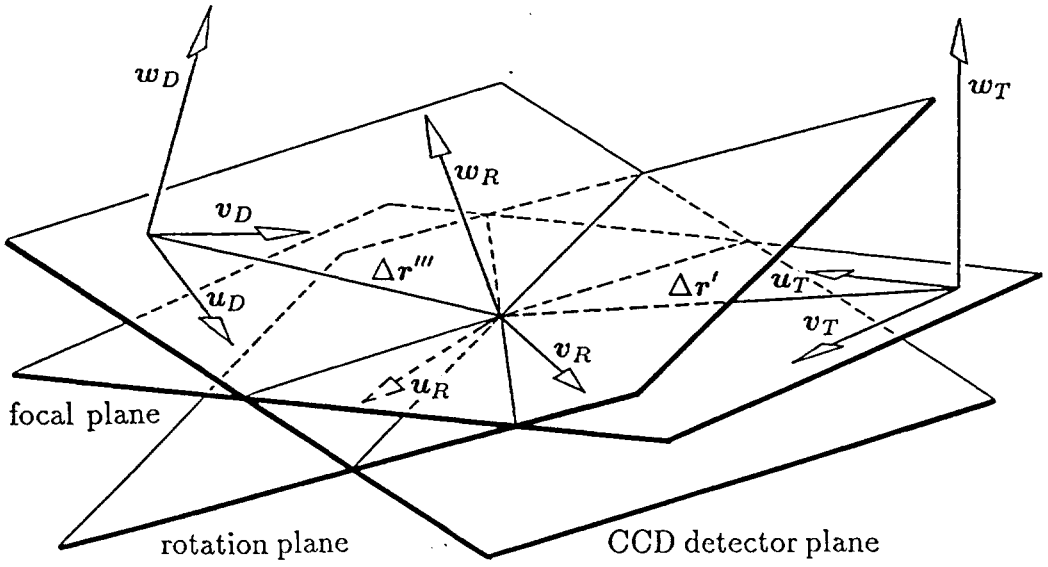

Figure 3.8: CCD detector, rotation and focal plane

$$\begin{aligned} \boldsymbol{r} &= \mathbf{R}_3(\varepsilon_3 + \varepsilon_m)\mathbf{O}_2\boldsymbol{r}' \\ \boldsymbol{r}' &= -\Delta\boldsymbol{r}' + \mathbf{T}_2\mathbf{R}_3(\varepsilon_2 + \omega)\boldsymbol{r}'' \\ \boldsymbol{r}'' &= \mathbf{R}_3(\varepsilon_1)\mathbf{T}_1\mathbf{O}_1(\boldsymbol{r}''' - \Delta\boldsymbol{r}'''), \end{aligned} \tag{3.34}$$

where

$\mathbf{R}_i(\varphi)$	is a 3 x 3 matrix characterizing a rotation around the angle φ about the axis i;
ε_i	are (unknown) infinitesimal angles; $i = 1, 2, 3$
ω	is a known angle ω;
ε_m	is an infinitesimal (known) angle given by the mount model;
$\mathbf{O}_2$	denotes the general (infinitesimal) transformation describing the deviation from the gnomonic projection model (deformations due to imperfect optics);
$\mathbf{O}_1$	denotes an infinitesimal transformation expressing the non-orthogonality of the detector coordinate system (given by the pixel matrix);
$\mathbf{T}_i$	are transformations resulting from the tilt of the different $[\boldsymbol{u}\ldots, \boldsymbol{v}\ldots]$ planes with respect to each other;

$\Delta r'$ are the coordinates of the origin of the $[u_R, v_R, w_R]$ system with respect to the $[u_T, v_T, w_T]$ system;

$\Delta r'''$ are the coordinates of the origin of the $[u_R, v_R, w_R]$ system with respect to the $[u_D, v_D, w_D]$ system.

In order to determine the parameters of the relationship between r''' and r'' observations at different angles ω have to be performed. On the other hand the movement of the camera around the w_R axis is not repeatable with sufficient accuracy (no ball bearings or similar construction). The geometry is therefore calibrated for fixed ω only (the camera orientation is changed for special purposes only, e.g. "drift scan" observations). We nevertheless introduced this intermediate $[u_R, v_R, w_R]$ system because on the new ZIMLAT telescope the camera will be located in a high precision de-rotator device and hence the calibration of the transformation between the detector and the rotator coordinate system will probably be possible. For the sake of the following discussion we simplify the relationship between the standard coordinates and the detector coordinates by omitting the rotator device (see Figure 3.9):

$$\begin{aligned} r &= \mathbf{R}_3(\varepsilon_3 + \varepsilon_m)\mathbf{O}_2 r' \\ r' &= \mathbf{R}_3(\omega)\mathbf{T}\mathbf{O}_1(r''' - \Delta r'''). \end{aligned} \tag{3.35}$$

The translation $\Delta r'''$ may be arbitrarily chosen (e.g. the center of the CCD ex-

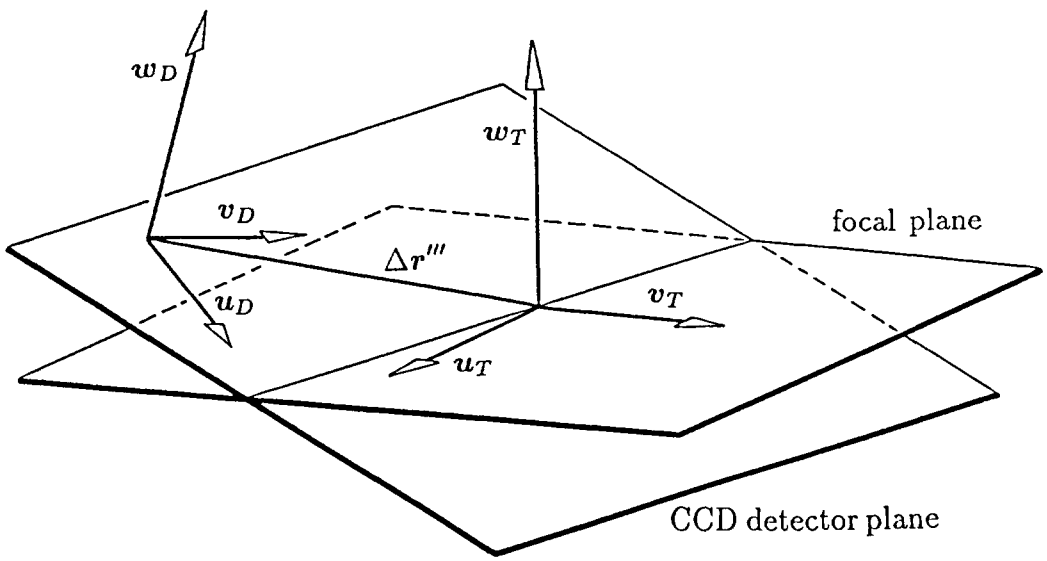

Figure 3.9: CCD detector and focal plane (simplified model)

pressed in CCD coordinates) and actually defines the reference point for the

estimation of the focal length (there is no other suitable reference for the focal plane and the assumption that the instrument is best focussed for the center of the CCD is reasonable). The transformations $\mathbf{T}$ and $\mathbf{O}_1$ have now a slightly different meaning and $\Delta\boldsymbol{r}'$ is the position of the CCD reference point $\Delta\boldsymbol{r}'''$ with respect to the focal plane coordinate system. The tilt $\mathbf{T}$ and the displacement $\boldsymbol{r}'$ of the detector with respect to the focal plane coordinate system can only be measured if the orientation and position of the focal plane system with respect to the standard coordinate system are defined by the optical axis of the telescope. The latter is only possible if the optical system (i.e. optical axis) is manifesting itself through distortions which must be taken into account by $\mathbf{O}_2$ (see also discussion of "centering error" and "plate tilt" in section 3.2.1).

If we furthermore assume perfect stability of the $[\boldsymbol{u}_D, \boldsymbol{v}_D, \boldsymbol{w}_D]$ with respect to the $[\boldsymbol{u}_T, \boldsymbol{v}_T, \boldsymbol{w}_T]$ system for a given angle ω we may also omit the focal plane reference system and write:

$$\boldsymbol{r} \;=\; \mathbf{R}_3(\varepsilon_m + \varepsilon_3)\mathbf{O}\mathbf{R}_3(\omega)\mathbf{T}(\boldsymbol{r}''' - \Delta\boldsymbol{r}'''). \tag{3.36}$$

In this representation the transformation $\mathbf{O}$ includes the field distortions due to imperfect optics as well as the non-orthogonality of the detector coordinate system. The tilt $\mathbf{T}$ of $\boldsymbol{w}_D$ with respect to $\boldsymbol{w}$ can not be separated from the direction of $\boldsymbol{w}$ and can thus only be determined if $\boldsymbol{w}$ is fixed to its a priori value (which would be equivalent to the determination of the tangent direction $\boldsymbol{w}$ while keeping $\mathbf{T}$ fixed). We may therefore either (arbitrarily) fix the detector coordinates of the tangent point at $\Delta\boldsymbol{r}'''$ and determine $\mathbf{T}$ or introduce the location of the tangent point as additional unknown parameter into the adjustment and omit $\mathbf{T}$. We decided for the second solution. In order to keep $\mathbf{O}$ simple in the first approach we describe $\mathbf{R}_3(\varepsilon_3)\mathbf{O}$ by a similarity transformation which may be separated into a symmetric (deformation) and asymmetric (rotation) part:

$$\mathbf{R}_3(\varepsilon_3)\mathbf{O} = f_0^{-1} r_0 \left[\mathbf{E} + \begin{pmatrix} r_1 & r_3 \\ r_3 & r_2 \end{pmatrix} + \begin{pmatrix} 0 & q \\ -q & 0 \end{pmatrix}\right], \tag{3.37}$$

where $\mathbf{E}$ is the unit matrix. It is obvious that not all parameters r_i and q may be determined simultaneously. We may e.g. estimate a common scale factor r_0 and fix r_1, r_2, r_3 at some a priori values or we may assess the entire asymmetric part and set r_0 equal to 1.

Probably equation (3.37) will not be sufficient to describe the optical characteristics of the telescope. The idea, however, is to analyze the residuals from the simple model given by (3.36, 3.37) for systematic signatures. If necessary we would then switch to a model of the type given by (3.35). A tilt of $\boldsymbol{w}_T$ with respect to $\boldsymbol{w}_D$ could then be represented by the coordinates of $\boldsymbol{w}_T$ in the detector

reference system (see (3.23)):

$$\mathbf{T}\begin{pmatrix} x \\ y \end{pmatrix} = \begin{pmatrix} (r_4 x + r_5 y)x \\ (r_4 x + r_5 y)y \end{pmatrix}, \tag{3.38}$$

where $(r_4, r_5, 1)$ are the components of $\boldsymbol{w}_T$ in the $[\boldsymbol{u}_D, \boldsymbol{v}_D, \boldsymbol{w}_D]$ system.

Determination of the model parameters

In terms of the classical astrographic reduction procedure (one plate $\equiv$ one set of plate constants) the above models require more than one reference star in order to determine all parameters. This forces us to combine the information from several frames in the case where only one reference object is in the field of view. Three different approaches are feasible:

a) Observation of dense reference star fields If a dense reference star field with accurate star positions is available the model parameters r_i and q may be determined for one particular pointing direction of the telescope from a single exposure. One should, however, be careful in using this technique for calibration purposes because at least the rotation q and probably also the values r_i may be direction dependent. In addition, the temporal stability for some parameters, especially for the focal length, cannot be guaranteed. Nevertheless such observations are very valuable in the model qualification process where systematic trends in the residuals and the order of magnitude of the parameters (and not their particular values) are of interest. With a few exceptions there are no dense reference star regions available so that they must be constructed by determining the positions of some "intermediate stars" from wide field astrographic plates. The latter should be from the same epoch (proper motion!); moreover the differential color refraction problem must be treated very carefully (the differential color refraction is different for photographic material and CCD detectors).

b) Use of the earth's rotation (fixed telescope) If we observe the position of a star with known apparent celestial coordinates with respect to the CCD coordinate system as it moves over the field of view of the fixed telescope (drive off) the scale in this direction may be determined. In addition, the orientation of the detector (q) with respect to the true equator may be estimated. The measurements are obtained by performing a series of short exposures with adequate temporal spacing (e.g. 10 frames during one field of view crossing of the reference star). Because of the shuttering problem (time tags from mechanical shutters are not accurate enough, see section 4.2) multi-exposure frames are not feasible and one frame must be read out for each exposure. On the other hand at the maximum angular velocity of the objects of $15'' \, s^{-1}$ the readout time is of no concern.

Figure 3.10 shows the combined data of ten successive exposures of a calibration series.

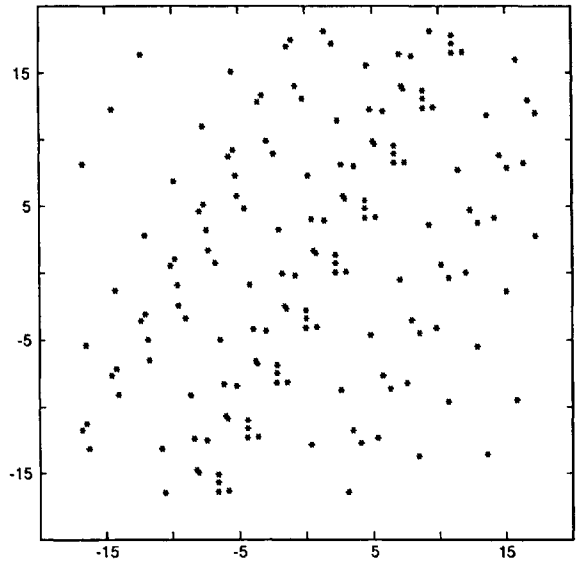

Figure 3.10: Combined frames of a calibration series. Ten individual frames, each exposed for 1 second, were superposed (on the computer) to generate this image. The telescope was fixed at azi= 90°, ele= 60° and images were taken each 24 s. The stars crossed the 35′ x 35′ field from bottom left to top right in approximately 3.5 minutes (zenith is up). For details see also section 6.

c) Use of satellite orbits If the reference frame is realized by the satellite orbits and not by the positions of the reference stars, i.e. if the stars are measured with respect to the moving object's trajectory (e.g. for the CQSSP), the same technique as described for b) may be applied but the earth's rotation is replaced by the satellite motion. From the observational point of view the only difference is the fact that the moving object may be tracked. Because all measurements are made with respect to the satellite position and not with respect to an earth fixed direction as in b) (there given by the fixed telescope) any possible tracking errors (or unknowns) may harm the mapping indirectly through the centroiding process only (asymmetric profiles). In other words, as long as the tracking errors during the exposures can be regarded as linear in time the method will be equivalent to the "earth rotation technique". In the remaining part of this section we will therefore discuss method b) only but we point out that all considerations would also apply for case c).

Calibration with fixed telescope (method b)) Observations stemming from a single telescope pointing direction may determine the scale with respect to one particular direction on the detector, namely the direction of the movement of the star. Furthermore the orientation of the detector with respect to the equatorial plane may be measured. If we determine a common scale factor r_0 and the rotation q only (r_1, r_2, r_3 fixed) observations from one direction are sufficient but a calibration of all r_i needs observation series from at least three different directions. Consequently we must assume that the parameters r_i are independent from the telescope position (or that such a dependence is known and taken into account) and stable over the time interval needed to perform the calibration observations in the different directions.

For each observation series in a given pointing direction we must solve for the tangent direction (2 parameters) and the detector orientation q (1 parameter). The tangent point has to be expressed in the horizon system (azimuth, elevation) where its components are constant for a particular series (fixed telescope!). The orientation q is determined separately for each direction because of the uncertainty in the telescope mount model i.e. in $\mathbf{R}_3(\varepsilon_m)$. We thus finally

need a minimum of: 3 series of 2 exposures (each including at least one reference star) in 3 different pointing directions, i.e. 12 observed detector coordinates of 6 known celestial directions,

to determine:

- 6 components of 3 tangential directions in the horizon system,
- 3 transformation parameters r_1, r_2, r_3 and 3 orientation parameters q_i.

More exposures per series (or more series) are required if r_4 and r_5 are to be determined too.

Apart from the reference stars which are needed to determine the tangent directions, the detector positions of additional unknown stars may be measured yielding an entire series of "rulers". Although all oriented in the same direction for a given telescope pointing, they allow — if measurements from different pointing directions are combined — the assessment of the geometry over the full field of view. The celestial coordinates of the unknown star have to be determined in the adjustment process too.

The following questions arise:

1. How stable are the model parameters?
2. What is the influence of catalogue errors in the reference star positions for the calibration process?

3. What is the influence of a refraction error?

4. What is the optimum calibration scenario?

Stability of the model parameters The most critical parameter in view of temporal stability is the effective focal length $f = r_0 f_0^{-1}$ (or the corresponding contributions to r_1, r_2, r_3). Depending on the mechanical construction of the telescope f is more or less temperature dependent. In a Cassegrain type instrument f depends e.g. critically on the distance between the primary and the secondary mirror. The current SLR telescope at Zimmerwald shows a change in the effective focal length of about 1 millimeter per 5° C temperature difference which corresponds to a relative change of scale of about $2 \cdot 10^{-4}$ per degree Celsius in its $f/2$ focus. This change is of the same order of magnitude as the accuracy of the scale factor determination. The latter may be roughly assessed by taking the centroiding accuracy, i.e. about 0.1 pixel (see section 4.1.3), and dividing it by the diameter of the field of view, i.e. by 500 to 1000 pixels, which results in a relative error of $2 \cdot 10^{-4}$ to $1 \cdot 10^{-4}$. This definitely asks for the telescope structure and the optics to be in thermal equilibrium and for ambient temperature changes of less than 1° C during the entire calibration run (approx. 15 min). If the telescope design contains some countermeasures (the telescope is then said to be athermalised) or if the focal length is considerably longer than a few meters this stringent requirement (which is hard to fulfill) can be loosened. The design of the new ZIMLAT telescope is therefore optimized with respect to the scale change and should (including correction optics) not exceed a change of $2 \cdot 10^{-5}$ per degree Celsius in the $f/4$ focus (see TELAS (1992)).

Apart from the common scaling factor r_0 the r_i, $(i = 1, \ldots, 5)$ are suspected to be more stable in time. They may, however, be subject to a bending of the telescope structure. We therefore assume that they may be possibly zenith distance dependent and will perform several calibration runs, each one at a constant but different elevation. The actual stability of the parameters can only be checked by extensive experiments at the telescope. Specifications for the number and frequency of calibration sessions (depending on the requested accuracy) must be established experimentally. The same approach has to be chosen for a potential zenith distance dependency.

It is thus evident that for every astrometric observation where sub-arcsecond accuracy over the entire field of view is required, the orientation q (because of possible errors in the mount model) and the common scaling factor r_0 (because of the focal length's temperature dependency) have to be determined in principle for every observation. This is done either by using the observation series itself (if the telescope drive was off e.g. for a close encounter of a geostationary satellite and a reference star) or by performing a single calibration series (using the same reference star as for the measurements of the target object) immediately before or

after the measurement. In the case where the satellite orbit defines the reference frame, the observation series from the close encounter of the satellite with the object to be measured (e.g. a catalogue star) may be used for the determination of the common scale factor and the orientation even if the telescope was moving (tracking).

Fixed telescope: influence of errors in the reference star position Errors $\Delta\alpha$, $\Delta\delta$ in the reference star position results in an erroneous tangent direction. The corresponding effects are given by equation (3.21); the quadratic terms are listed in Table 3.6. The small rotation due to an error $\Delta\alpha$ in right ascension introduces an error proportional to $\sin\delta_T\,\Delta\alpha|\boldsymbol{t}|$. For a field of view of 1° ($|\boldsymbol{t}_{\max}| = 0.5°$, provided the reference star passes near the center of the field) and $\Delta\alpha = 1''$ the maximum error at the edge of the field is on the order of 0.″01 (near the celestial pole) and thus negligible. The second order terms in (3.21) can also be neglected provided the error in the reference star position is on the order of one arcsecond or less. An error in the declination, however, has an influence on the determination of the scale considering that the scale may be expressed as

$$m = \frac{\cos\delta\Delta H}{\Delta l}, \tag{3.39}$$

where

- m is the scale factor;
- δ the apparent declination of the reference star;
- ΔH the change in hour angle;
- Δl the corresponding displacement on the detector.

The scale m may be expanded in terms of δ:

$$m = m_0 - m_0 \tan\delta_0\Delta\delta, \quad \text{where} \quad m_0 = \frac{\cos\delta_0\Delta H}{\Delta l}. \tag{3.40}$$

Assuming a maximum error of $\Delta\delta = 1''$ for the reference star position, the influence on m is less than $1 \cdot 10^{-5}$ for declinations up to about 64°. In order to maintain $1 \cdot 10^{-5}$ in m, $\Delta\delta$ must be less than 0.″5 at $\delta = 75°$ and $\Delta\delta < 0.''25$ at $\delta = 83°$. We should therefore avoid scale determinations at high declinations unless the reference star position is known very accurately.

Fixed telescope: influence of refraction errors For the following discussion we use the simple refraction model given in section 3.2.1:

$$d\Theta = k \tan \Theta, \tag{3.41}$$

where $d\Theta$ is the astronomical refraction, Θ is the zenith distance of the object, and k is a constant of about 60" (depending on the atmospheric conditions). During the calibration, a star is moving from A to B in the horizon system (see Figure 3.11). $\beta + 3/2\pi$ is the position angle of the apparent direction of motion of the star measured from the zenith-oriented vertical. Let us assume that we use a wrong refraction constant k_1 instead of the correct value k_0. In this case the star would move from C to D. There are two effects to be taken into account: a) the angle between the apparent direction of motion and the horizon changes (the angular distance $\overline{AC}$ is different from $\overline{BD}$), and b) the convergence of the verticals towards the zenith. A detailed calculation gives the following result for the change in the scale:

$$m = m_0 - m_0 \Delta k (1 + \sin^2 \beta \tan^2 \Theta), \tag{3.42}$$

where $\Delta k = k_1 - k_0$ is the error in the refraction constant. The first term in the parentheses is due to b) and the second term (depending on β) due to a).

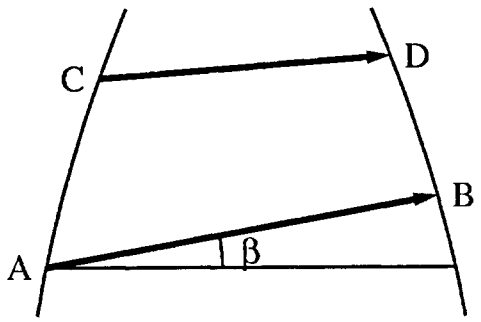

Figure 3.11: Apparent motion of stars in the horizon system for different refraction.

Optimum calibration scenario for fixed telescope For a complete calibration of all transformation parameters r_i and q we need observation series of stars passing at least in three different directions over the field of view (preferably at the same elevation in order to cope with possible elevation dependencies). A homogeneous distribution is achieved if these directions are separated by 60 degrees as indicate in Figure 3.12. The position angle β is given by $\beta = -\beta'$ where β' is

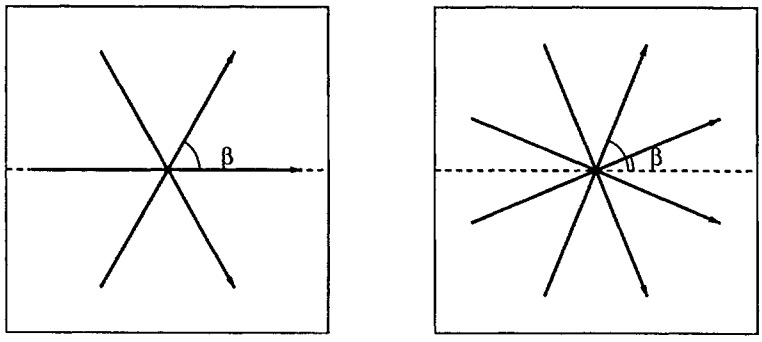

Figure 3.12: Field of view crossing directions for calibration. Zenith is up and West to the right.

the parallactic angle (angle between the direction towards the celestial pole and the direction to the zenith) which is defined as:

$$\begin{aligned} \sin\beta' \sin z &= \cos\varphi \sin H \\ \cos\beta' \sin z &= -\cos\varphi \sin\delta \cos H + \sin\varphi \cos\delta \\ \cos z &= \cos\varphi \cos\delta \cos H + \sin\varphi \sin\delta, \end{aligned} \tag{3.43}$$

where φ is the astronomical latitude of the observing station, z is the zenith distance, H and δ the hour angle and the declination of the reference star respectively. The angle β is determined unambiguously by (3.43). For $z \leq |\varphi|$ the maximum value of β is given by $|\beta_{\max}| = \arcsin(\cos\varphi / \sin z)$. The minimum values for the elevation h to achieve the necessary angles β for the 3, 4 or 5 direction case respectively at the latitude of Zimmerwald are:

$$\begin{array}{lllll} & \varphi = 47° & & \\ \text{3 directions:} & \beta_{\max} = 60° & \longrightarrow & h_{\min} = 38° \\ \text{4 directions:} & \beta_{\max} = 67.5° & \longrightarrow & h_{\min} = 42.4° \\ \text{5 directions:} & \beta_{\max} = 72° & \longrightarrow & h_{\min} = 44°. \end{array} \tag{3.44}$$

Given φ, β and z we derive for δ (from (3.43)):

$$\cos\beta' \sin z \cos\delta + \cos z \sin\delta = \sin\varphi. \tag{3.45}$$

As $\cos\delta$ is always positive, the expression $\sqrt{1-\sin^2\delta} = \cos\delta$ is unambiguous and we may substitute it in (3.45) which lead to a quadratic equation in $\sin\delta$:

$$\sin\delta = \frac{\sin\varphi \cos z \pm \cos\beta' \sin z \sqrt{\cos^2\varphi - \sin^2\beta' \sin^2 z}}{\cos^2 z + \cos^2\beta' \sin^2 z}. \tag{3.46}$$

From (3.43) we derive further

$$\begin{aligned} \cos\varphi \cos H &= \cos z \cos\delta - \cos\beta' \sin z \sin\delta \\ \cos\varphi \sin H &= \sin\beta' \sin z, \end{aligned} \tag{3.47}$$

from where the hour angle can be computed. The corresponding azimuth may be derived using the relationship between the equatorial and the horizon system:

$$\begin{aligned} \sin a &= \frac{(\cos\delta \sin\beta')}{\cos\varphi} \\ \cos a &= \frac{\sin\delta \sin z - \cos\delta \cos z \cos\beta'}{\cos\varphi}. \end{aligned} \tag{3.48}$$

Table 3.9 lists the hour angle, declination and azimuth of the positions corresponding to $\beta = \pm 60°$ for different elevations. From the two possible solutions we should always select that one with the smaller declination in order to minimize the influence of the reference star position errors (as discussed in the previous paragraph). Values for the case of 4 different calibration directions (position angles $\beta = \pm 22.5°$ and $\beta = \pm 67.5°$) are given in Table 3.10.

		Telescope pointing for $\beta = \pm 60°$ ($\varphi = 47°$)										
		Elevation [degree]										
		40	45	50	55	60	65	70	75	80	85	90
Azi	±	60	73	81	87	93	98	102	107	111	115	120
	±	24	5	6	14	19	23	27	30	34	37	120
H.A.	±	-5.1	-4.3	-3.6	-3.1	-2.6	-2.2	-1.7	-1.3	-.8	-.4	0
	±	-6.9	-7.7	-7.6	-6.7	-5.5	-4.1	-2.9	-1.8	-1.1	-.5	0
Dec		47	41	39	38	38	39	40	41	43	45	47
		71	86	84	77	70	65	60	56	53	50	47

Table 3.9: Telescope pointing for calibration with 3 field crossing directions. Values are given in degrees for the azimuth and declination and in hours for the hour angle. The second line always refers to the solution with the higher declination. Calculations for an observing site at 47° latitude.

Supercalibration An astrometric detector actually is a system consisting of different parts (a mount, an optical system and a detector in the narrow sense).

We may try to calibrate some of these components independently. Supercali-

		Telescope pointing for $\beta = \pm 22.5°$ ($\varphi = 47°$)									
		Elevation [degree]									
		45	50	55	60	65	70	75	80	85	90
Azi	±	146	147	147	148	149	151	152	154	156	157
	±	1	2	4	5	7	8	9	9	10	157
H.A.	±	−1.6	−1.4	−1.3	−1.1	−.9	−.7	−.6	−.4	−.2	.0
	±	−10.4	−10.4	−10.1	−9.5	−7.7	−3.7	−1.4	−.6	−.2	.0
Dec		7	11	16	20	25	29	33	38	42	47
		88	87	81	76	71	66	61	56	52	47

		Telescope pointing for $\beta = \pm 67.5°$ ($\varphi = 47°$)									
		Elevation [degree]									
		45	50	55	60	65	70	75	80	85	90
Azi	±	53	66	75	82	88	93	98	103	108	112
	±	8	8	17	24	29	34	38	42	46	112
H.A.	±	−4.9	−4.0	−3.4	−2.8	−2.3	−1.8	−1.4	−.9	−.5	.0
	±	−7.1	−7.0	−6.0	−4.8	−3.7	−2.6	−1.8	−1.1	−.5	.0
Dec		54	48	45	43	42	43	43	44	45	47
		84	83	75	68	63	58	55	52	49	47

Table 3.10: Telescope pointing for calibration with 4 field crossing directions. Values are given in degrees for the azimuth and declination and in hours for the hour angle. The second line always refers to the solution with the higher declination. Calculations for an observing site at 47° latitude.

bration is the mapping of the portion of the astrometric system that measures the positions. For photographic systems this would mean the calibration of non-linearities and the non-orthogonality of the coordinate axes of the measuring machine. In the case of a solid state detector this is the mapping of the pixel grid. Supercalibration relies on two assumptions: (a) the detector is stable between the calibrations and the actual astrometric observations, and (b) the test equipment is more accurate (and more stable!) than the detector. The first requirement seems to be met by solid state detectors; the second is a non-trivial technical challenge.

In the case of CCDs the geometry is defined by the manufacturing process. The geometric quality of the masks needed to produce integrated circuits is in general

improving with the integration density (and with the speed) of the devices. 0.5 μm line width technology is routinely available and chips with 0.1 μm or smaller line width are already manufactured. This suggests that the mask quality is in the order of a few 0.1 μm or even better.

For thick devices the geometrical properties change neither with the handling, with orientation in the gravity field nor with time. Thinned (backside illuminated) devices are not suitable for astrometric purposes due to possible orientation and temperature dependent bending of their foil-like sensitive part. Changes with temperature are very small and in most circumstances negligible: a 2000 x 2000 pixel CCD with a diagonal dimension of 560 mm (20 μm pixel) exhibits a maximum change of 0.17 μ (or approx. 0.01 pixel) per degree Celsius for the distance between two diagonal edges (assuming a linear thermal expansion coefficient of $3 \cdot 10^{-6}$ for silicon). Fortunately this would affect the detector in a homogeneous way, similar to a change in the effective focal length of the telescope (no supercalibration necessary). In addition, the detectors are usually kept within one degree Celsius (often even within a few tenths of a degree) during the observations (this stabilizes their photometric characteristics).

Few detailed investigations were performed until now. Mackay (1986) quotes Wright (1982) who found intrapixel non-uniformities of 10% to 30% for the photometric response of a EEV P8600 CCD. Stanton et al. (1987) examined an RCA CCD in a star-tracking configuration and found deviations of typically 0.05 pixel (full amplitude) from ideal performance. Surprisingly there are groups reporting milliarcsecond accuracies without supercalibration: Monet and Dahn (1983) state accuracies for single measurements of single stars of 4 mas (corresponding to 0.3 μm in this case). Repeated measurements with the stars typically placed within 5" (400 μm) of the same location on the CCD may produce parallaxes with uncertainties of 0.5 mas (0.04 μm). Such an accurate mapping performance would not be possible without an extreme uniformity of the CCD pixels and the grid of pixels itself.

Two methods are suitable for supercalibration: one uses stars with known positions (this technique may be compromised by atmospheric effects or uncontrolled changes in the telescope); the other measures the CCD in a laboratory environment. Experience from astrometric observations indicate that the CCDs currently used are essentially perfect at the 1 μm level and may well be superior to any test equipment at the 0.1 μm level. Therefore supercalibration is an extremely difficult task.

Open questions The dominating problem area of this calibration technique concerns the stability of the transformation parameters r_i. This stability depends on the performance of the actual telescope; answers may only be given through extensive experiments. The investigations performed with the 0.5 m SLR tele-

scope at Zimmerwald indicate a stability in the medium precision range down to about 0.″5. We must emphasize that the reason for this limitation does not primarily reside in the stability of the model parameters but mainly in the inadequate mapping scale of the telescope (4.13 arcs pixel^{-1}!), the modest optical performance of the optics (producing complicated position dependent point spread functions), and in deficiencies of our current centroiding technique. In particular the use of simple moment centroiding algorithms which result in accuracies of about 0.1 pixel for objects with good S/N (see section 4.1.3) is not optimal. The mapping scale of 4.13 arcs pixel^{-1} alone transforms into an accuracy of about 0.″4 for a single position measurement. Because we might select bright reference stars (yielding high S/N) for the calibration, we believe that 2-dimensional profile fitting procedures instead of moment centroiding methods might improve the centroiding accuracy by an order of magnitude to about 0.01 pixel (see 4.1.3). In Section 4.1.3 we will derive a value between 0.5 and 1 arcs pixel^{-1} as the optimum mapping scale for good (1″) seeing conditions which is a factor 4 to 8 smaller than the value of the current 0.5 m SLR telescope. Although this result was derived for moment centroiding algorithms only, we may assume that the values for fitting algorithms will be similar.

In addition, the poor optical quality of the telescope is compromising the quality of the measurements. Asymmetric profiles of the images in the center as well as distinct coma at the edge of the field (see Figure 6.4) give rise to magnitude dependent effects. The phenomena were not extensively studied, however, the results from a few examples indicate possible magnitude dependent systematic errors of up to 0.1 pixel.

3.3 The computation of coordinates

The parameters determined for the unknown object does depend on the model used in the relationship (3.9) between the observed quantities and the celestial coordinates of the object and the reference star. The "celestial coordinates" of the reference objects (stars) and the unknown object may (a) refer to different kinds of directions but also (b) to different coordinate systems. It is therefore important to recapitulate first the definition of standard coordinates and to outline the corresponding transformations to be applied in order to compute standard coordinates from a given type of position (e.g. catalogue positions).

3.3.1 Computation of standard coordinates

As defined in section 3.2.2 standard coordinates have to be computed from apparent topocentric refracted positions. This involves a series of transformations

which depend on the type of initial data (e.g. catalogue positions or (geometric) coordinate directions for a solar system object or satellite). The positions we find in star catalogues are (in principle!) the true positions of the stars as seen from the solar system barycenter referred to a mean equator and equinox of a reference epoch t_0. The apparent topocentric positions for a star may be computed as

$$\boldsymbol{r}(t') = \mathbf{N}(t)\mathbf{P}(t)f[g[\boldsymbol{r}_B(t_0) + (t - t_0)\dot{\boldsymbol{r}}_B(t_0) - \boldsymbol{o}_B(t)]], \tag{3.49}$$

where

- t' is the epoch of observation in terrestrial dynamical (TDT) time scale;
- t is the epoch of observation in barycentric dynamical (TDB) time scale;
- t_0 is the reference epoch and equinox in TDB time scale;
- $\boldsymbol{r}_B(t_0)$ is the radius vector (mean place) of the star in the coordinate system referred to the mean equator and equinox of t_0 with the origin in the solar system barycenter;
- $\dot{\boldsymbol{r}}_B(t_0)$ is the space motion of the star at t_0 as observed in the same reference system;
- $\boldsymbol{o}_B(t)$ is the barycentric position of the observer at t referred to the mean equator and equinox of t_0;
- $g[\ldots]$ is the function representing the gravitational deflection of light;
- $f[\ldots]$ is the function representing the aberration of light;
- $\mathbf{P}(t)$ is the precession matrix;
- $\mathbf{N}(t)$ is the nutation matrix;
- $\boldsymbol{r}(t')$ is the apparent topocentric place at epoch t' referred to the true equator and equinox of date.

The formula is given in vector notation to be easily compared with the corresponding algorithms needed for solar system objects. For stars, the time argument t' may be set equal to t. If the star's parallax is unknown the radial component of $\dot{\boldsymbol{r}}_B(t_0)$ has to be set to zero and the parallax must be set to a small but finite number e.g. $1 \cdot 10^{-4}$ arcs which places the object at a distance of 10 kpc. Another solution would be to use a unit vector for $\boldsymbol{r}_B(t_0)$ and to skip the parallax correction term $\boldsymbol{o}_B(t)$ as well as the similar parallax terms in the computation of the distance dependent gravitational deflection of light $g[\ldots]$ (all remaining transformations are independent on the distance). It may be worthwhile noting that for

milliarcsecond accuracy the observer's position has to be known to about 10^{-3} AU only (used for the computation of parallax and light deflection only) but the observer's velocity to about 1 km s^{-1} (corresponding to about $5 \cdot 10^{-5}$ of the earth's barycentric velocity!) (aberration). The time argument t (in the TDT time scale) has to be computed from TAI by means of the relation TDT = TAI + 32.184 s. UTC, the conventional time scale used for the observations, differs from TAI by an integer number of seconds. Due to the introduction of leap seconds (in order to maintain UTC within 0.9 s of UT1) the difference TAI-UTC changes with time and its value for a specific observation epoch has to be taken e.g. from IERS Bulletin B (). For detailed discussion and formulas for $g[\ldots]$, $f[\ldots]$, $\mathbf{P}(t)$ and $\mathbf{N}(t)$ as well as the relation between TDT and TDB we refer to the Explanatory Supplement to the Astronomical Almanac (Seidelmann 1992).

We should not forget to mention some peculiarities in the construction of star catalogues. Prior to 1984 the positions published in star catalogues were not barycentric true positions because they were not corrected for the so-called elliptic terms (E-terms) of aberration. In addition until 1960 the computation of aberration was based on an unperturbed heliocentric motion of the barycenter of the earth-moon system. Fortunately the elliptic terms of aberration experience only a small secular change (because changes in the eccentricity e and perigee π for the earth's orbit are small) which is why the effects may be considered constant for all epochs used in the computation of the mean positions in the catalogue. It is therefore possible and mandatory (where applicable) to compute E-terms for the mean epoch of observation of the catalogue stars (if necessary the mean epoch has to be treated for each star and possibly even for α and δ separately) and to correct the catalogue positions for this large effect (up to 0.″33). On the other hand the mean position cannot be corrected for the second deficiency because of the high frequency of the neglected perturbations.

Apparent topocentric positions of solar system objects referred to the mean equator and equinox of epoch t_0 are computed in the following way:

$$\boldsymbol{r}(t') = \mathbf{N}(t)\mathbf{P}(t) f[g[\boldsymbol{r}_B(t-\tau) - \boldsymbol{o}_B(t)]], \tag{3.50}$$

where

- τ is the light travel time in TDB for light arriving at the epoch of observation t';
- $\boldsymbol{r}_B(t-\tau)$ is the barycentric position of the object at epoch $t-\tau$ referred to the mean equator and equinox of t_0.

The other vector functions and matrices are the same as those in equation (3.49). Expression (3.50) differs from equation (3.49) only in the computation of the position $\boldsymbol{r}_B$ (ephemeris computation) and in the term related to the light travel time

τ. For stars we assumed a rectilinear constant motion and neglected variations in the light travel time (these being of the order $\mu\delta t$, where $\delta t \leq |\boldsymbol{o}_B|/c$, c :=speed of light, μ :=proper motion). It is always assumed that the definition of a true star position includes implicitly the light time (true positions are not geometric positions!). The reason is that a secular aberration due to the movement of the solar system barycenter in space cannot be distinguished from the light time correction (or the motion of the star) as long as the barycenter and the star both have a uniform rectilinear motion.

For the time arguments in (3.50) we may again use the approximation $t' = t$ for the majority of the objects ($t'-t$ is of the order of 1.5 ms at maximum). Obviously the observer's position $\boldsymbol{o}_B(t)$ has to be known much more accurately than in the case of stars. This is particularly critical in the case of low earth orbiting satellites where the station coordinates have to be known within a few centimeters in the International Terrestrial Reference Frame (ITRF). Consequently the polar motion and the UTC – UT1 correction have to be applied to the positions $\boldsymbol{r}(t')$ of these objects. In the case of artificial satellites care has to be taken to understand the definition of the particular reference system and time scale properly in order to transform the ephemerides and the corresponding time arguments into the celestial reference frame. Satellite ephemerides given in geocentric systems have not necessarily to be transformed into the barycentric system first. Formula (3.50) has to be adapted in this case: the light deflection $g[\ldots]$ may be neglected and the aberration $f[\ldots]$ has to be modified in a way to contain the diurnal aberration only (see also the discussion of the determined position for earth orbiting satellites in section 3.3.2).

3.3.2 Determined positions

We are in principle free to define any model for the relation between the observed quantities and the estimated parameters (positions) of the unknown object as long as the relation between the standard coordinates and the observables (given by the "plate" or astrographic reduction model) is identical for the reference objects and the program objects. The latter is in fact identical with the requirement for the inclusion of all known and calibratable instrumental effects. We may, however, argue for some additional requirements (some of them being reasonable for any experiments):

(a) All effects depending on local environmental conditions should be incorporated into the model.

(b) The fact that we observe differential quantities should be fully explored.

The first point calls for the mandatory inclusion of the refraction. The only way to strictly meet the second requirement is to use the same model and the

same set of parameters for both the reference and the unknown objects. This is again obvious for the refraction where the absolute error may be large compared to the aimed at accuracy but the same argument in principle holds for nutation, precession, aberration, etc. Although conventional constants for these transformations are available they may change from time to time. In addition if using identical models we may allow for a less precise calculation of these transformations especially for the nutation (a time consuming computation!) because any errors will contribute through second order terms only to the errors of the object position. In a certain respect, however, the model of the refraction may differ for the individual objects:

(a) If using wide passbands and if the objects exhibit large color differences, a color dependent refraction has to be applied or corresponding parameters have to be estimated (see section 3.2.1).

(b) For earth orbiting satellites the refraction has to be computed for a finite distance (the so-called "parallactic refraction correction" has to be applied).

These differences are not strictly model differences and we are only neglecting these effects in the case of similar object colors and large distances respectively.

In view of this discussion the best parameters to estimate for the unknown objects are their topocentric positions in the reference system in which the positions of the reference objects were defined. For reference stars this is the mean equator and equinox of the reference epoch of the catalogue, e.g. J2000 (such coordinates are also called "standard mean places"). When estimating these parameters the only residual difference in the models for the reference and the unknown objects resides in the distinction between the topocentric and the barycentric position. The reason for this difference is simply that we generally do not know the distance of the unknown objects (or the light travel time τ) and hence may use only the corresponding unit vectors for $\boldsymbol{r}_B(t-\tau)$ or $\boldsymbol{r}_B(t)$ in the equations (3.50) and (3.49) respectively. The relationship between the standard coordinates of the unknown objects and their positions to be estimated is also given by the inverse of the transformations (3.49) or (3.50) respectively, with the exception that the last step of the reduction of the parallax $\boldsymbol{r}_B = \boldsymbol{r}_t - \boldsymbol{o}_B(t)$, where $\boldsymbol{r}_t$ is the topocentric position of the object, is not performed.

Let us emphasize the meaning of these *topocentric positions* once more:

- By the term *position* we understand the direction of the emission point (location of the object at $t-\tau$ as seen in a system moving parallel to the solar system barycenter). This is the conventional definition of a star position.

- By *topocentric* we mean that the coordinate system origin is at the instantaneous position of the observer during observation. In other words, this is the coordinate difference between the observer's position at observation epoch t and the position of the observed object at emission time $t - \tau$, expressed in a barycentric coordinate system. We mention that coordinates depend on the choice of the metric, i.e. they depend on the actual model for the relativistic corrections, namely the light deflection and the transformation of the time arguments. The direction defined in this way is exactly the classical *astrometric place* from the point of view of the concept. There is, however, a difference in the realization in the sense that customarily gravitational light deflection, aberration, and in many cases also refraction are neglected in the computation of standard coordinates assuming that any residual differential effect is absorbed into the plate constants. This assumption is generally valid for sufficiently small fields. (Strictly speaking, the light deflection for solar system objects can not be absorbed into the plate constants because it is a function of position and distance.)

Artificial earth satellites

For any dynamical analysis we finally require a geometric direction (this is the coordinate difference between the observed object and the observer, both at coordinate time t). We should stress that this is not an observable physical quantity and thus can never be the direct result of an astrometric measurement. There is, however, another transformation to be applied due to the fact that satellite orbits usually are referred to a local inertial system moving with the instantaneous velocity of the earth's barycenter. The two components of the aberration stemming from the movement of the observer (stellar aberration) and the movement of the observed object (light time correction) can not be distinguished and we are therefore free to transform the direction from the barycentric inertial system into a local geocentric inertial system. In order to do that we have to apply the annual aberration again. The resulting directions will be topocentric standard places corrected for annual aberration (as far as we know there is no conventional expression for this type of place).

We may add at this point that the distance dependence of atmospheric refraction can not be neglected for earth orbiting satellites. The difference in refraction for an object at infinity and an object at finite distance is also called the "parallactic refraction correction". The effect amounts $2''.4 \tan z$ for an object at 200 km altitude. Details are discussed in the following section.

3.4 The influence of atmospheric refraction and turbulence

The intention of this section is not to derive models for the refraction and the atmospheric turbulence but to discuss their influence on differential astrometric measurements. We base our discussion on the classical model of a spherically symmetrical atmosphere. A comprehensive treatment of the subject may be found in Murray (1983). For atmospheric turbulence we refer to Lindegren (1980) and Han (1989).

3.4.1 Atmospheric refraction

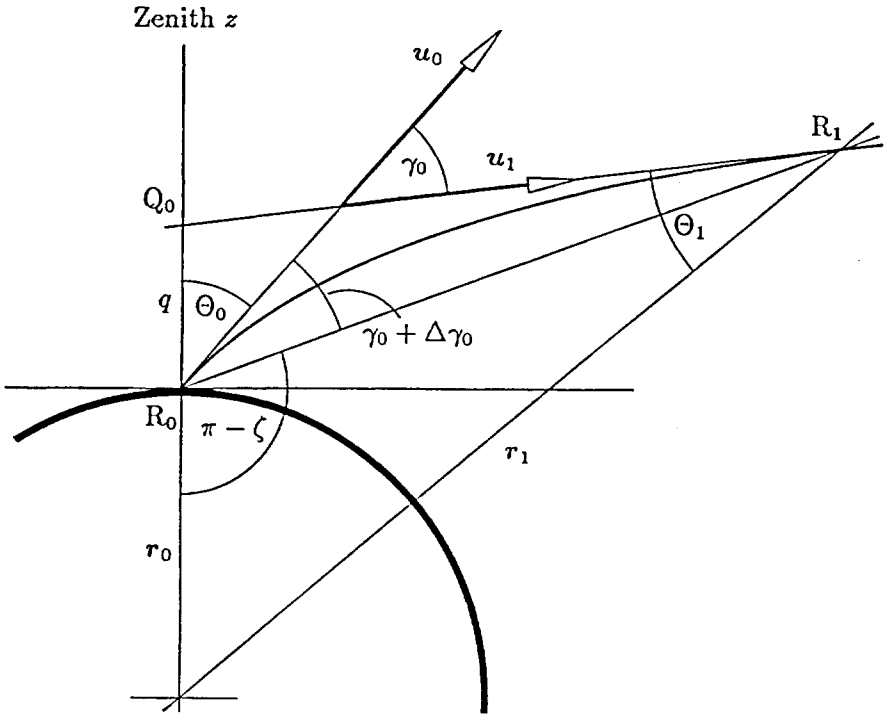

Figure 3.13: Atmospheric refraction

Let $\boldsymbol{r}_0$ and $\boldsymbol{r}_1$ denote the geocentric position vectors of the observer R_0 and the observed object R_1, respectively (see Figure 3.13). Let us furthermore denote $\boldsymbol{u}_0$ and $\boldsymbol{u}_1$ as the unit vectors along the tangents to the light trajectory at R_0 and R_1, respectively. The angle γ_0 between $\boldsymbol{u}_0$ and $\boldsymbol{u}_1$ is known as the *astronomical refraction*. The direction $\boldsymbol{u}_0$ is the "apparent direction" at which the observer sees the source and the angle Θ_0 is the "observed zenith distance". The direction along the straight line from R_0 to R_1 is the so-called "true direction" and the corresponding angle ζ between the zenith Z and this direction the "true zenith distance". Q_0 is the hypothetical point at the "equivalent height" q from which the

source would be observed at direction $\boldsymbol{u}_1$ provided that there is no atmosphere. From Figure 3.13 we derive the following relationship between the true and the observed zenith angle and the refraction:

$$\sin(\Theta_0 + \gamma_0 - \zeta) = \frac{q}{|\boldsymbol{r}_1 - \boldsymbol{r}_0|} \sin(\Theta_0 + \gamma_0). \tag{3.51}$$

For a source at infinity (for which $\frac{q}{|\boldsymbol{r}_1 - \boldsymbol{r}_0|} = 0$) this simplifies to

$$\zeta = \Theta_0 + \gamma_0. \tag{3.52}$$

The correction $\Delta\gamma_0 = \zeta - \Theta_0 - \gamma_0$ which has to be added for a source at finite distance $|\boldsymbol{r}_1 - \boldsymbol{r}_0|$ to the refraction γ_0 for a source at infinity reads as

$$\zeta = \Theta_0 + \gamma_0 + \Delta\gamma_0 \tag{3.53}$$

and is known as the *parallactic refraction correction*. It is equal to the angular distance between R_0 and Q_0 as seen from from R_1 or, in other words, $\Delta\gamma_0$ is the parallax with respect to R_0 and Q_0. The parallactic refraction correction may be neglected for all objects except earth orbiting satellites or, more explicitly, for all objects at distances greater than about 10^5 km (see below).

Assuming a spherically symmetrical atmosphere and a source outside the atmosphere, the astronomical refraction may be written as

$$\gamma_0 = k_1 \tan\Theta_0 + k_2 \tan^3\Theta_0, \tag{3.54}$$

with

$$\begin{aligned} k_1 &= n_0 - 1 - I, \\ k_2 &= -[I - \frac{1}{2}(n_0 - 1)^2], \end{aligned} \tag{3.55}$$

where

n_0 is the refractive index of the air at the location of the observer and

I is the integral describing the difference between a plane parallel and a spherically symmetrical atmosphere.

$$I = \int_{|\boldsymbol{r}_0|}^{|\boldsymbol{r}_1|} \frac{1}{|\boldsymbol{r}|} \log n \, d|\boldsymbol{r}|, \qquad (n = n(|\boldsymbol{r}|)), \tag{3.56}$$

were

$n(|\boldsymbol{r}|)$ is the refractive index of the air at the geocentric distance $|\boldsymbol{r}|$.

Formula (3.55) is a good approximation for zenith distances up to 80°.

To give an impression of the order of magnitude of the different terms we give a numerical example. For a temperature of $T_0 = 273.17$ K and a pressure of $p_0 = 101325$ Pa at the observer's location we find at a wavelength of $\lambda = 0.5893$ μm (sodium D-lines): $n_0 - 1 = 2.92104 \cdot 10^{-4}$, $I = 3.67 \cdot 10^{-7}$ (for a multi layer model atmosphere) and hence $k_1 = 60''.175$, $k_2 = -0''.0669$. The example illustrates the well known fact that the refraction is dominated by n_0, which in turn is only a function of the atmospheric conditions at $\boldsymbol{r}_0$. The influence from the remaining part of the light path through the atmosphere gives rise to a small correction I only (of the order of 10^{-3} of the total effect). The term proportional to $\tan^3 \Theta_0$ describing the difference between a plane-parallel and spherically symmetrical atmosphere model also gives rise to a correction of 10^{-3} only. This justifies the approximation $\gamma_0 = k \tan \Theta_0$ used in section 3.2 for discussing the effects of differential refraction. Because we are mainly interested in differential effects we will neither discuss different atmosphere models nor the computation of the term I. We will have to analyze the dependence of the primary component n_0 on the physical parameters, however.

Refractive index of air The refractive index n is a function of the density ρ (and thus also of temperature T and pressure p) of the air and of the wavelength λ of the light under consideration:

$$n = f(\rho, \lambda). \tag{3.57}$$

This relationship is in practice given by empirical formulas. Customarily used in increasing order of complexity are the *Gladstone-Dale*, *Barrell-Sears* (Barrell and Sears 1939), and the *Owens* (Owens 1967) formulae, the latter being recommended by the IAU. For numerical examples we used the Owens formula but for the following discussion the much simpler Gladstone-Dale expression is adequate:

$$n - 1 = \kappa_d \rho_d + \kappa_w \rho_w, \tag{3.58}$$

where ρ is the density and the suffixes d and w refer to dry air and to water vapour respectively. The coefficients κ_d and κ_w are functions of the wavelength only (which is in fact the difference between the Gladstone-Dale formula and the more sophisticated ones). Using the state equation for an ideal gas we may write:

$$n - 1 = \frac{1}{RT}(\kappa_d M_d p_d + \kappa_w M_w p_w), \tag{3.59}$$

where M_d and M_w are the molecular weights of dry air and water vapour respectively and R the gas constant. For numerical examples we will use the following values:

$$\begin{aligned} M_d &= 28.9644\ \mathrm{kg\,kmol^{-1}} \\ M_w &= 18.0152\ \mathrm{kg\,kmol^{-1}} \\ R &= 8314.32\ \mathrm{J\,K^{-1}\,kmol^{-1}}. \end{aligned} \tag{3.60}$$

It is convenient to write (3.59) in an alternative form where the wet component introduces a small correction to the refractivity calculated from the total pressure $p = p_d + p_w$:

$$n - 1 = \frac{\kappa_d M_d}{R}\frac{p}{T} + \frac{\kappa_w M_w - \kappa_d M_d}{R}\frac{p_w}{T}. \tag{3.61}$$

The water vapour pressure p_w is usually measured as a relative humidity h, the ratio of the water vapour pressure p_w and the saturation water vapour pressure p_s:

$$h = \frac{p_w}{p_s}. \tag{3.62}$$

The saturation pressure is strongly temperature dependent. Tabular values and

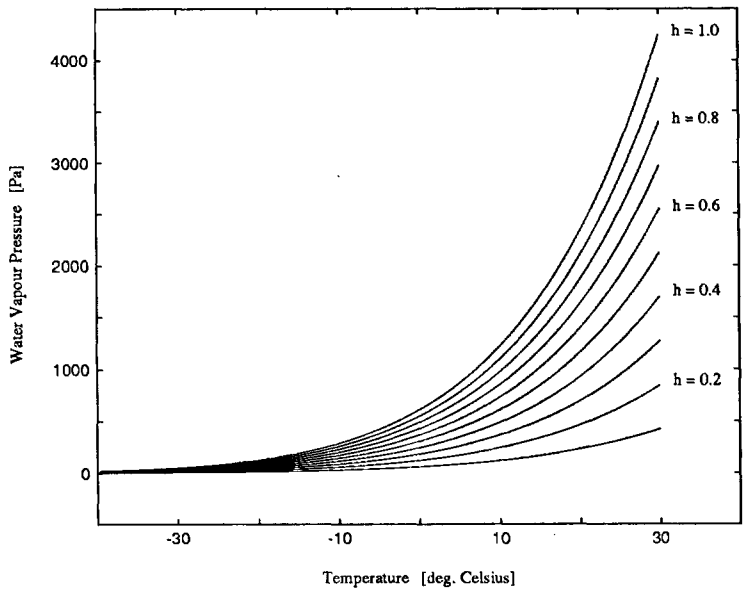

Figure 3.14: Water vapour pressure as a function of temperature for different values of relative humidity h.

an empirical formula for the corresponding saturation density ρ_s are given in Murray (1983):

$$\rho_s = \rho_{s0} e^{W(T)}, \tag{3.63}$$

where

$$\rho_{s0} = 4.849 \cdot 10^{-3}\ \mathrm{kg}\, m^{-3},$$

and

$$\begin{aligned} W(T) &= -3.982 + 0.068\,882\,9(T - 273.15) \\ &\quad -3.982 \cdot 10^{-4}(T - 273.15)^2 \\ &\quad +1.404 \cdot 10^{-6}(T - 273.15)^3 \qquad (T \text{ in K}). \end{aligned} \tag{3.64}$$

The water vapour pressure as a function of the relative humidity measurements is now given by the relation

$$p_w = \frac{RT}{M_w} h \rho_{s0} e^{W(T)}. \tag{3.65}$$

Figure 3.14 shows the water vapour pressure as a function of temperature for different values of relative humidity h (as defined by (3.65).

In order to derive expressions for κ_d and κ_w we compare (3.61) with the formula given by Owens (1967). We write Owens' numerical expression in the form given by Murray (1983):

$$\begin{aligned} 10^6(n-1) &= (0.237134 + \frac{68.39397}{130 - \lambda^{-2}} + \frac{0.45473}{38.9 - \lambda^{-2}})\frac{p_d}{T} f_d \\ &\quad +(0.648731 + 0.58058 \cdot 10^{-2}\lambda^{-2} - 0.71150 \cdot 10^{-4}\lambda^{-4} \\ &\quad +8.851 \cdot 10^{-6}\lambda^{-6})\frac{p_w}{T} f_w, \end{aligned} \tag{3.66}$$

where λ is the wavelength in micrometers,

$$f_d = 1 + p_d(5.790 \cdot 10^{-9} - \frac{9.3250 \cdot 10^{-6}}{T} + \frac{2.5844 \cdot 10^{-3}}{T^2}) \tag{3.67}$$

and

$$\begin{aligned} f_w &= 1 + p_w(1 + 3.7 \cdot 10^{-6} p_w) \cdot (-0.237321 \cdot 10^{-4} + \frac{2.23366 \cdot 10^{-2}}{T} \\ &\quad -\frac{7.10792}{T^2} + \frac{7.75141 \cdot 10^2}{T^3}). \end{aligned} \tag{3.68}$$

(In all numerical expressions we use SI units for temperature, pressure and density.) Comparing (3.59) with (3.66), (3.67) and (3.68) for $f_w = 1$ and $f_d = 1.0004615$ which is the value for $p_d = 101325$ Pa and $T = 288.15$ K yields

$$10^8(\frac{\kappa_d M_d}{R}) = 77.529 + 0.4349\lambda^{-2} + 0.00389\lambda^{-4} + 4.4 \cdot 10^{-5}\lambda^{-6} \tag{3.69}$$

and

$$10^8\left(\frac{\kappa_w M_w - \kappa_d M_d}{R}\right) = -12.656 - 0.1456\lambda^{-2} - 0.01100\lambda^{-4} + 8.41\cdot 10^{-4}\lambda^{-6}. \quad (3.70)$$

Using (3.60) we obtain

$$\kappa_d = 2.2255 \cdot 10^{-4} + 1.249 \cdot 10^{-6}\lambda^{-2} + 1.12 \cdot 10^{-8}\lambda^{-4} + 1.3 \cdot 10^{-10}\lambda^{-6} \quad (3.71)$$

and

$$\kappa_w = 2.9940 \cdot 10^{-4} + 2.679 \cdot 10^{-6}\lambda^{-2} - 3.28 \cdot 10^{-8}\lambda^{-4} + 4.08 \cdot 10^{-9}\lambda^{-6}. \quad (3.72)$$

3.4.2 Errors in the determination of pure refraction

Various errors may compromise the determination of the pure refraction. By "pure" we mean that we are restricting the discussion to the ideal case of a spherically symmetrical atmosphere excluding effects like refraction anomalies or seeing. In this context often much effort is spent on the discussion of different atmosphere models for the evaluation of the integral I (see equation (3.56)). However, I represents only a small correction in the order of 10^{-3} of the total refraction and it may in fact be shown that for zenith distances up to 70° errors in the determination of n_0 dominate any (model dependent) uncertainties in the computation of I (see e.g. Kurzyńska (1987)). Figure 3.15 gives the differences of (a) the approximation $(n_0 - 1)\tan\Theta_0$, (b) the term $k_1 \tan\Theta_0$ (equations (3.54), (3.55)), and (c) the complete correction term γ_0 as defined by equation (3.54) with respect to the refraction correction obtained when numerically integrating the correction using the US Standard Atmosphere (NASA, US Air Force, and US Weather Bureau 1962).

The accuracy of n_0 depends, of course, on the accuracy of the meteorological measurements at the location of observation. In order to assess these dependencies we write equation (3.61) in a more quantitative way using the values defined by (3.71) and (3.72) where λ was set to 0.5 μm:

$$n - 1 \simeq 7.9 \cdot 10^{-7}\frac{p}{T} - 1.2 \cdot 10^{-7}\frac{p_w}{T}. \quad (3.73)$$

Using (3.65) we may write:

$$n - 1 = a\frac{p}{T} - bh\rho_{s0}e^{W(T)}, \quad (3.74)$$

where

$$\begin{aligned} a &= 7.9 \cdot 10^{-7}\ \mathrm{K\,Pa^{-1}} \\ b &= 1.2 \cdot 10^{-7}\frac{R}{M_w} = 5.6 \cdot 10^{-5}\ \mathrm{m^2 kg^3}. \end{aligned} \quad (3.75)$$

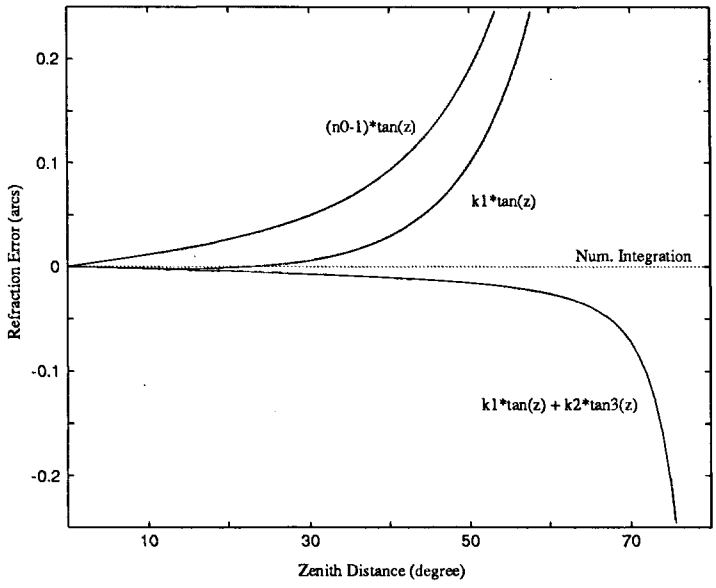

Figure 3.15: Different models for pure refraction with respect to a numerical integration of the US Standard Atmosphere. The refractive index n_0 was identical in all cases. For the computation of k_1 we set $I = 3.67 \cdot 10^{-7}$.

Error in the temperature

By taking the partial derivative of equation (3.74) with respect to temperature we obtain:

$$\frac{\partial(n-1)}{\partial T} = -\frac{ap}{T^2} - bh\rho_{s0}e^{W(T)}\left(\frac{dW(T)}{dT}\right). \tag{3.76}$$

Using a mean value of 60″ for $n-1$ (derived from (3.74) by inserting mean values for T and p) the error $\Delta(n-1)$ induced in refractivity by an error $\Delta T = 1$ K in temperature is

$$\Delta(n-1) = 0.''25. \tag{3.77}$$

Refraction errors $\Delta(n-1)$ as a function of temperature T for an error $\Delta T = 1$ K in temperature are given in Figure 3.16.

Error in the pressure

If we take the partial derivative of equation (3.74) with respect to the pressure p we may derive the error induced in $n-1$ by an error in the barometric pressure:

$$\frac{\partial(n-1)}{\partial p} = \frac{a}{T}. \tag{3.78}$$

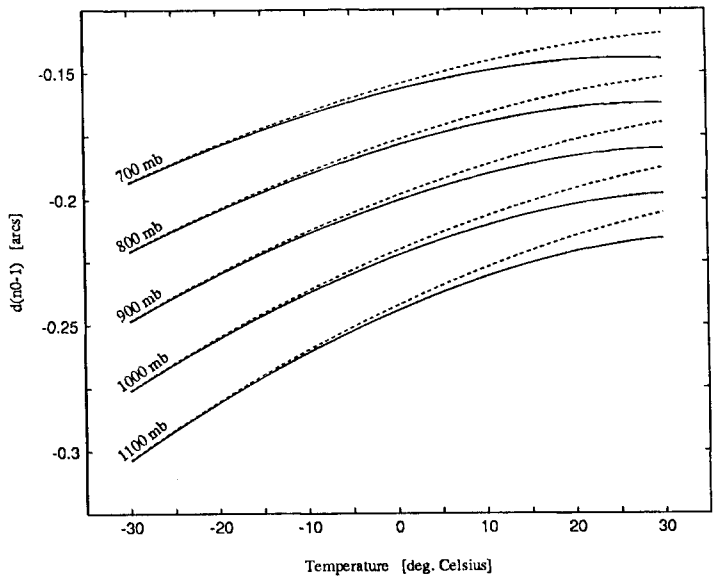

Figure 3.16: Refraction errors $\Delta(n-1)$ for an error of $\Delta T = 1$ K in temperature for different values of the pressure p as a function of the temperature T. The solid lines refer to 100% relative humidity ($h = 1$) whereas the dashed lines refer to $h = 0.5$.

Assuming $n - 1 = 60''$ as above we get an error in refractivity of

$$\Delta(n-1) = 0.''06 \quad \text{for an error in pressure of} \quad \Delta p = 1 \text{ mb.} \tag{3.79}$$

Error in relative humidity

By taking the partial derivative of equation (3.74) with respect to relative humidity h we finally obtain

$$\frac{\partial(n-1)}{\partial h} = -b\rho_{s0}e^{W(T)} \tag{3.80}$$

This allows us to compute the error $\Delta(n-1)$ as a function of temperature T for different errors Δh (Figure 3.17).

Conclusions

From the above results we may draw two conclusions:

(a) Uncertainties in the meteorological measurements (at the location of the observer) may easily introduce errors in the determination of the refraction of the order of a few tenths of an arcsecond.

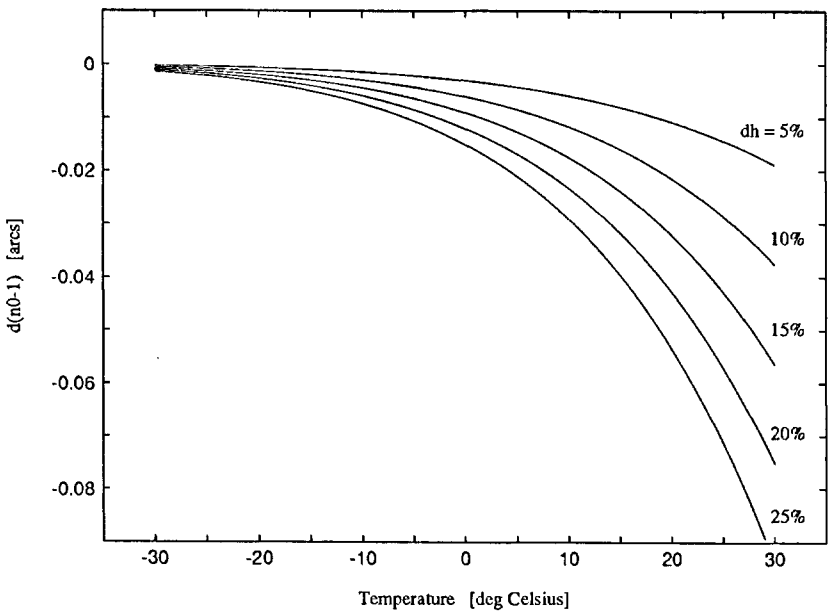

Figure 3.17: Refraction error $\Delta(n-1)$ as a function of temperature T for different errors Δh in relative humidity.

(b) The temperature is by far the most critical parameter. Temperature measurements are not primarily limited by the accuracy of the instruments but rather by potentially large, very local temperature gradients (e.g. inside the dome or even inside the telescope).

Let us mention that the explicit form of expression (3.57) is not critical for the computation of the astronomical refraction at visible wavelength's: The only difference between formulas (3.61), (3.71) and (3.72) (based essentially on the Gladstone-Dale relationship) and the Owens formula ((3.66)) resides in the two small correction functions $f_d(p_d, T)$ and $f_w(p_w, T)$. Examining these two functions for reasonable temperature and pressure ranges ($\Delta T = 80$ K, $\Delta p_d = 20000$ Pa, $\Delta p_d = 1000$ Pa) yields maximum differences from their mean values as assumed for the evaluation of κ_d and κ_w of the order of $1 \cdot 10^{-3}$ for f_d and 0.17 for f_w respectively. This on the other hand transforms into only 0.″06 and 0.″08 respectively for the refractivity n (note the extreme temperature and pressure range)!

3.4.3 Large scale anomalous refraction

Any correction to the pure refraction caused by deviations of the actual atmosphere from the idealized spherically symmetrical model is generally referred to

as *anomalous refraction*. The phenomena range from large scale deviations (over a good part or even the entire sky) with a slow temporal variability to stochastic changes with frequencies of many Hertz and spatial correlation lengths inferior to one arcminute. There is in fact a smooth transition between the classical refraction effect and the so-called seeing (image blurring, image motion, speckle structure). Consequently there is no strictly defined terminology and some authors refer to seeing as "atmospheric turbulence" whereas others still use the term "refraction anomalies". For the following discussion we will use the term "turbulences" for anomalies with spatial correlations smaller than the field of view ($\sim 1°$) and reserve the term "refraction anomalies" for large scale effects.

Large scale anomalies originate in particular from the inclination of the air layers of equal density with respect to the concentric layer model (i.e. there are "non-horizontal" layers). The result is a non-vanishing refraction component even in the zenith direction. Inclined air strata are the result of continuous winds in rather laminar air flows. The magnitude of refraction anomalies caused by this mechanism, of course, depends on the average meteorological conditions at a given observation site. In general, however, the effects tend to be much smaller than 0.″1 (see Kurzyńska (1988)).

3.4.4 The impact of refraction errors on differential observations

When observing position differences of objects in a narrow field (the case of the classical astrography) the major part of the refraction is common to all objects in the field and thus cancels out. The remaining part, the so-called "differential refraction" may be expressed by equation (3.27) used in the context of astrometry in the tangent plane. The notation in section 3.2.1 has to be adapted by replacing k in (3.27) by k_1 (see (3.54)) and by making the distinction between the observed zenith distance and the true zenith distance. Equation (3.27) was derived using a simplified refraction formula where the second order term $k_2 \tan^3 \Theta_0$ was neglected. Keeping in mind that $k_2 \sim 10^{-2} k_1$ this simplification is certainly justified.

The zero order terms in (3.27) are proportional to $k|\boldsymbol{t}_0|$, where $|\boldsymbol{t}_0| = \sqrt{\xi_0^2 + \eta_0^2} = \tan z_T$, z_T being the apparent zenith distance of the tangent point. These terms represents the common displacement of all objects in the field of view and therefore completely vanish in the reduction process (it is actually absorbed by the determination of the tangent direction).

First and second order terms in (3.27) are proportional to $k|\boldsymbol{t}_0|^2|\boldsymbol{t}|$ and $k|\boldsymbol{t}_0|^3|\boldsymbol{t}|^2$, respectively. It is therefore obvious that the influence of an error Δk of the constant of refraction on the differential position $\boldsymbol{t}$ of the object (in this case

with respect to the projection center) is of the order of

$$\Delta|\boldsymbol{t}| \approx \Delta k|\boldsymbol{t}_0|^2|\boldsymbol{t}| + \Delta k|\boldsymbol{t}_0|^3|\boldsymbol{t}|^2, \tag{3.81}$$

where

- $\boldsymbol{t}_0$ is the position of the projected zenith in the tangent plane and
- $\boldsymbol{t}$ a general location on the tangent plane.

The distance $|\boldsymbol{t}_0|$ may be expressed as

$$|\boldsymbol{t}_0| = \tan z_T, \tag{3.82}$$

where

- z_T is the zenith distance of the tangent direction $\boldsymbol{r}_T$.

Values for the linear and quadratic terms for different zenith distances and a "worst case" refraction error of $\Delta k = 1''$ are given in Tables 3.11 and 3.12. The

	Differential refraction — Linear terms							
	z [deg]							
	10	20	30	40	50	60	70	80
scale change $\cdot 10^6$	5.0	5.5	6.5	8.3	12	19	41	160
error [mas/deg]	18	20	23	30	42	70	149	579

Table 3.11: Linear error terms due to differential refraction. A worst case refraction error of $\Delta k = 1''$ was assumed. Scale changes for various zenith distances z are given in the first row. The second row indicates the induced maximum position error in milliarcseconds at 1° distance from the projection center.

computations were performed for an angular separation of $|\boldsymbol{t}| = 1°$. It is obvious that the contributions from the second order term are harmless. The linear term gives rise to errors up to $0''.05$ at $z = 60°$. We should emphasize that these are worst case figures for several reasons:

(a) The uncertainty in the constant of refraction is rarely greater than a few $0''.1$ for moderate zenith distances up to 60° (we are considering pure and large scale anomalous refraction only, not the stochastic components!).

$\|t\|$ [deg]	Differential refraction — Quadratic terms in mas					
	z [deg]					
	20	40	60	70	75	80
.2	0	0	0	0	1	2
.4	0	0	0	1	3	9
.6	0	0	1	3	7	21
.8	0	0	2	5	12	38
1.0	0	1	3	8	18	59

Table 3.12: Quadratic error terms due to differential refraction. Values in milliarcseconds for a worst case refraction error of $\Delta k = 1''$ are given for various distances $|t|$ from the projection center and for various zenith distances z.

(b) During the calibration of geometry (see section 3.2.2) part of a potential refraction error is absorbed by the (plate) scale factor(s). In particular, if the calibration measurements are all performed at the same zenith distance as the program observations (which was identified as the preferred calibration scenario) the linear term of the refraction induced error is absorbed completely by the scale factor. Due to the (slow) temporal variations of the large scale refraction anomalies care has to be taken that the geometry is calibrated immediately before and (or) after the actual observation. With these precautions the influence of refraction errors may easily be reduced to values below 0.″01 for field diameters up to 1°. (Again we are not considering the effect of atmospheric turbulence (a stochastic process) which also produces scale variations (of significant size, see section 3.4.7) but on much shorter time scales).

3.4.5 Atmospheric dispersion (color refraction)

So far we considered the effects of atmospheric refraction for monochromatic light only. Any light from a real source with a finite radiation spectrum will be dispersed in the atmosphere due to the fact that the refractive index is wavelength dependent. Writing the refraction formula (3.54) in differential form, using (3.55) (where we neglect I and the term $(n_0 - 1)^2$) we obtain

$$d\gamma_0 = (1 + (n_0 - 1)\tan^2\Theta_0)\tan\Theta_0 dn_0 + (n_0 - 1)\cos^{-2}\Theta_0 d\Theta_0, \qquad (3.83)$$

where $d\gamma_0$ and $d\Theta_0$ are changes in the refraction and the apparent zenith distance corresponding to changes dn_0 in the refractive index. The true zenith distance ζ must be independent of wavelength. For a source at infinity we therefore get

from equation (3.52)

$$d\gamma_0 = -d\Theta_0. \tag{3.84}$$

By substituting expression (3.84) in equation (3.83) we get

$$d\Theta_0 = -\frac{1 + (n_0 - 1)\tan^2\Theta_0}{1 + (n_0 - 1)\cos^{-2}\Theta_0}\tan\Theta_0 dn_0, \tag{3.85}$$

which may be approximated by

$$d\Theta_0 = (n_0 - 2)\tan\Theta_0 dn_0. \tag{3.86}$$

Values for the dispersion $d\Theta/d\lambda$ at $z = 45°$ corresponding to wavelength intervals $d\lambda = 10$ nm are given in Table 3.13 (the table may be used for different zenith distances Θ_0 by scaling the values with $\tan\Theta_0$). The calculations were made using

Atmospheric dispersion			
λ [nm]	$10\frac{d\Theta}{d\lambda}$ [arcs]	λ [nm]	$10\frac{d\Theta}{d\lambda}$ [arcs]
350	0.181	650	0.025
400	0.117	700	0.020
450	0.080	750	0.016
500	0.057	800	0.013
550	0.043	850	0.011
600	0.032	900	0.009

Table 3.13: Atmospheric dispersion at $z = 45°$ corresponding to wavelength intervals of 10 nm for $p_0 = 101325$ Pa, $T_0 = 273.15$ K, and no wet component.

equation (3.86) and (3.61) where we introduced formula (3.71) for the refractive index n_0 for standard conditions $p_0 = 101325$ Pa, $T_0 = 273.15$ K and neglected the wet component. The change of the refractive index with the wavelength was derived by taking the derivatives of equation (3.59) where equation (3.71) and (3.72) were substituted:

$$10^7\left(\frac{dn}{d\lambda}\right) = -\frac{1}{RT}[M_d p_d(24.89\lambda^{-3} + 0.448\lambda^{-5} + 0.078\cdot\lambda^{-7}) \\ M_w p_w(53.58\lambda^{-3} - 1.312\lambda^{-5} + 0.24\cdot\lambda^{-7}). \tag{3.87}$$

Figure 3.18 shows the scaled refractivity $n - 1$ as a function of the wavelength for dry air ($p_0 = 101325$ Pa, $T = 273.15$ K).

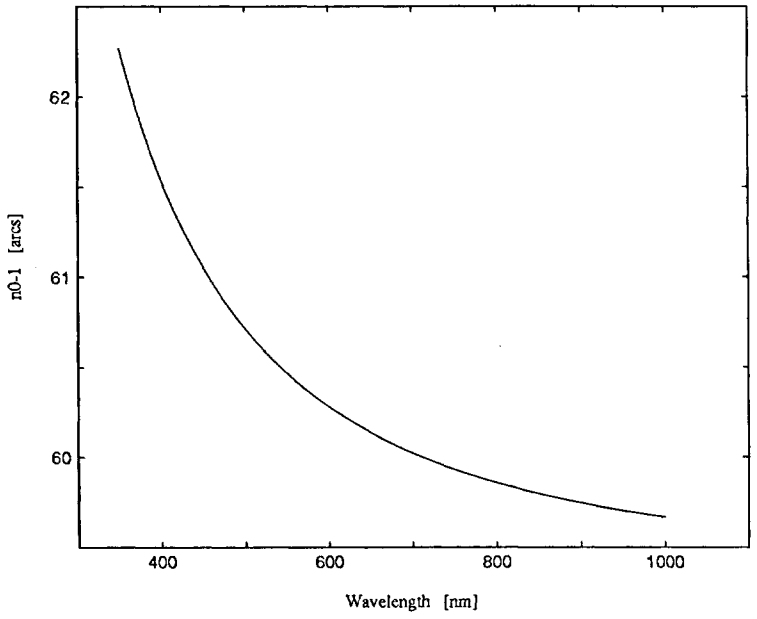

Figure 3.18: Scaled refractivity $n_0 - 1$ as a function of the wavelength λ for dry air.

As can be seen from Table 3.13 color dispersion is a huge effect which can not be neglected even if observing in a small passband of a few 10 nm. As a consequence the image of an object will be elongated along the direction to the zenith with the actual shape of the profile and the position of the light center both depending on the object's color (or more precisely on its spectral light distribution). Our CCD detector when used without filters has a passband of about 0.4 μm which may result in relative position displacements of up to 0.''3 for objects with extreme color differences.

Furthermore, the fact that neither the refraction $\gamma_0(\lambda)$ nor in general the intensity distribution $i(\lambda)$ of the object (nor the detector sensitivity) are linearly dependent on the wavelength leads to asymmetric profiles of the images along the dispersion direction. Color refraction therefore results not only in a general color dependent displacement of the image positions but is also responsible for further complications in the centroiding process:

(a) Asymmetric image profiles tend to produce magnitude dependent position estimates in the centroiding process, especially when symmetrical fitting functions are used. The actual behaviour has to be carefully studied for each particular centroiding algorithm. Magnitude effects are dangerous (because of their systematic nature) and hard to detect from the observational data unless a vast quantity of observations is analyzed. Simulation studies may

help in this context.

(b) Image profile shapes depend on the intrinsic colors of the object. Therefore the precise meaning of the centroid estimated by a particular algorithm is hard to define (it may actually depend on the object colors!). In other words, the centroid may deviate as a function of color from e.g. the light gravity center (first moment).

In any case we have to account for the color dispersion or the color refraction (the latter expression is often used to discuss the displacement of the "mean" position of the object's image). Three approaches are feasible:

(a) the use of a narrow passband,

(b) calculation of color dependent refraction corrections,

(c) estimation of color refraction parameters.

The use of a narrow passband

If very narrow passbands with a width of the order of a few nanometers are used color dependent position errors may be restricted to a few 0.″01 even for extreme cases (assuming that the refraction for the center wavelength of the passband has been applied). Magnitude effects stemming from the color dispersion are completely eliminated. The significant draw back of the method, of course, resides in the dramatic reduction of the overall efficiency of the detector system (compared to a setup without any filters). For a CCD detector with a broad spectral sensitivity range, the reduction factor may easily reach an order of 100! The technique is therefore suitable for relatively bright objects only.

Calculation of color dependent refraction corrections

As color dispersion is a non-linear effect we are not allowed, at least for broad passbands, to simply calculate the refraction for a "mean" or "effective" wavelength of the object considered. The only correct approach is to compute the refraction correction for the actual quantity of interest, namely the centroid of the object. This implies that in general the correction depends on the particular centroiding algorithm but we may nevertheless assume (for simplicity) that they all estimate the position of the object's light gravity center. Denoting the refraction corresponding to the light gravity center of the image of a point source by $\bar{\gamma}_0$ we get

$$\bar{\gamma}_0 = \frac{\int_0^\infty \gamma_0(\lambda) i_\lambda \tau_\lambda \varepsilon_\lambda q_\lambda d\lambda}{\int_0^\infty i_\lambda \tau_\lambda \varepsilon_\lambda q_\lambda d\lambda}, \tag{3.88}$$

where

$\gamma_0(\lambda)$ is the atmospheric refraction;

i_λ is the irradiance (in photons per square meter per nanometer and second) outside the earth's atmosphere;

τ_λ is the atmospheric transparency or transmission function; it is generally also dependent on the zenith distance z ($\tau_\lambda = f(z)$);

ε_λ is the optical efficiency of the telescope;

q_λ is the detective quantum efficiency of the detector and denotes the fraction of incident photons which is detected (the quantum efficiency is equivalent to the spectral response function).

Table 3.14 shows the position differences for various spectral types with respect to a solar type point source. The table was generated using equation (3.88) for $z = 60°$ and standard atmospheric conditions.

Color refraction — Impact on positions ($z = 60°$)					
Spectral type	CCD (470 – 880 nm)	Visual (500 – 610 nm)	R-band (570 – 700 nm)	I-band (740 – 880 nm)	10 nm (550 – 560 nm)
B0	320	55	36	17	.19
A0	180	36	20	6	.14
F0	80	15	11	3	.07
G0	0	0	0	0	0.0
K0	−90	−30	−12	−4	−.18
M0	−190	−73	−26	−6	−.39

Table 3.14: Color refraction — impact on positions. Position differences in mas for various spectral types relative to a solar type point source. The values were generated using equation (3.88) for $z = 60°$ and standard atmospheric conditions.

For small passbands where we may assume a linear dependence of the refraction on the wavelength ($d\Theta/d\lambda$ = const.) it can be shown that the refraction depends on the so-called "effective wavelength" $\bar{\lambda}$ only which is defined as

$$\bar{\lambda} = \frac{\int_0^\infty \lambda i_\lambda \tau_\lambda \varepsilon_\lambda q_\lambda d\lambda}{\int_0^\infty i_\lambda \tau_\lambda \varepsilon_\lambda q_\lambda d\lambda} \tag{3.89}$$

and thus

$$\bar{\gamma}_0 = \bar{\gamma}_0(\bar{\lambda}) = \gamma_0(n_0(\bar{\lambda})). \tag{3.90}$$

The refractive index $n_0(\bar{\lambda})$ corresponding to the effective wavelength $\bar{\lambda}$ is sometimes called the "effective refractive index". The restriction $d\Theta/d\lambda = \text{const.}$ over the passband leads to an upper limit for the bandwidth of approximately

100 nm	for $\bar{\lambda} > 0.6$ μm,	
50 nm	for 0.5 μm $< \bar{\lambda} <$ 0.6 μm, and	
10 nm	for 0.4 μm $< \bar{\lambda} <$ 0.5 μm	for a maximum error of 0.″01.

(See also Table 3.13 and Figure 3.18).

The mean wavelength itself, on the other hand, has to be known to within about 5 nm for red and visual and to better than 2 nm for blue passbands in order to guarantee the 0.″01 limit.

We emphasize that for broad band observations the spectral energy distribution of the source (as well as the spectral response function of the detection system) has to be known. If, however, the use of effective wavelengths is allowed these may be derived from photometric color information in terms of color indices provided that the astrometric observations are performed in one of the passbands of the photometric system under consideration. For the UBV system Cousins and Jones (1976) derived the following expressions (at zenith):

$$\begin{aligned} \bar{\lambda}_B &= 0.4383 + 0.0160(B-V)\ \mu\text{m} \\ \bar{\lambda}_V &= 0.5448 + 0.0075(B-V)\ \mu\text{m}. \end{aligned} \tag{3.91}$$

The corresponding effective refractivity may then be computed using equations (3.61), (3.66), (3.67) and (3.68).

Estimation of color refraction parameters

In many cases no spectral energy distribution and no photometric information is available for a particular object of interest. Then we have to extract the differential color refraction from the astrometric observations themselves. As we observe differential quantities in a small field of view we must examine the differential refraction as described by equation (3.27). The only difference for objects with various colors is that they all have their own refraction constant k (which we assume to be constant over the field of view). Assuming futhermore that standard coordinates for all objects were computed using one common refraction constant k, the terms $d\xi$ and $d\eta$ in (3.27) vanish for objects with the color for which k was computed. Objects with a slightly different refraction k' will be displaced by a

small correction $d\xi'$, $d\eta'$ which again may be described by equation (3.27) where $d\xi$, $d\eta$ have to be replaced by $d\xi'$, $d\eta'$ and k by $\Delta k = k' - k$:

$$\begin{aligned} d\xi' &= \Delta k[\xi_0 - (1+\xi_0^2)\xi - \xi_0\eta_0\eta \\ &\quad + \xi_0(2+\xi_0^2)\xi^2 + \eta_0(1+2\xi_0^2)\xi\eta + \xi_0(1+\eta_0^2)\eta^2] \\ d\eta' &= \Delta k[\eta_0 - \xi_0\eta_0\xi - (1+\eta_0^2)\eta \\ &\quad + \eta_0(1+\xi_0^2)\xi^2 + \xi_0(1+2\eta_0^2)\xi\eta + \eta_0(2+\eta_0^2)\eta^2], \end{aligned} \tag{3.92}$$

where ξ_0 and η_0 are the formal standard coordinates of the zenith as defined by equation (3.28).

For the worst case,Δk is of the order of 1" and we therefore neglect linear and higher order terms for field diameters small than 1°:

$$\begin{aligned} d\xi' &= \Delta k\xi_0 \\ d\eta' &= \Delta k\eta_0. \end{aligned} \tag{3.93}$$

If modified standard coordinates as defined in section 3.2.2 are used where the η-axis is oriented in the direction towards the zenith, the standard coordinates of the zenith are simply $\xi_0 = 0$, $\eta_0 = \tan z$, where z is the zenith distance of the tangent point. Consequently we have

$$\begin{aligned} d\xi' &= 0 \\ d\eta' &= \Delta k \tan z. \end{aligned} \tag{3.94}$$

The parameter Δk, often called "zenith correction", may now be introduced as an additional unknown into the relations (3.9) with the functional model given by the equations (3.93) or (3.94) respectively. It is evident that Δk can not be separated from the position differences of the objects as long as observations at a single zenith distance are considered. The $\tan z$ dependence asks for a series of observations at various zenith distances including exposures in the meridian and at extreme hour angles. The method is simple but of moderate interest for our applications due to the fact that it is limited to "static" objects and may thus be used for the determination of star positions only (e.g. for parallax or double star measurements).

3.4.6 Parallactic refraction correction

In order to derive the true zenith distance ζ of a source at a finite distance, the refraction γ_0 and the parallactic refraction correction $\Delta\gamma_0$ have to be added to the observed zenith distance according to equation (3.53). Using this definition of $\Delta\gamma_0$ and considering that γ_0 is a small angle we may approximate the relation (3.51) by

$$\Delta\gamma_0 = \frac{-q \sin\Theta_0}{|\boldsymbol{r}_1 - \boldsymbol{r}_0|}. \tag{3.95}$$

From Figure 3.13 it is obvious that the equivalent height q in contrast to the refraction does not depend on the refractivity of the air at the particular observation location but entirely on what happens to the light along the whole path through the atmosphere. For a spherically symmetrical atmosphere and a source outside the atmosphere, q may be expressed as (for the derivation see e.g. Murray (1983))

$$q = \frac{|\boldsymbol{r}_0| I}{\cos^2\Theta_0}, \tag{3.96}$$

where I is the integral defined by (3.56). Furthermore, although $|\boldsymbol{r}_0|I$ depends on the particular atmosphere model, we use the approximation given by Murray (1983)

$$|\boldsymbol{r}_0| I \simeq \frac{\kappa_d p_0}{g_0}(1 + I_1), \tag{3.97}$$

where g_0 is the gravitational acceleration at the height of the observer (assuming spherical symmetry) and I_1 is a model dependent quantity of the order of $1 \cdot 10^{-3}$. Using (3.71) for κ_d and standard values $T = 273.15$ K, $p_0 = 101325$ Pa and $g_0 = 9.80665$ m s^{-2} (sea level values) we obtain

$$q = \frac{2.34}{\cos^2\Theta_0} \text{ m}. \tag{3.98}$$

Relations (3.97) and (3.98) are given to enable error propagation considerations only.

Inserting equation (3.98) into equation (3.95) we have

$$\Delta\gamma_0 = -\frac{2.34 \tan\Theta_0}{|\boldsymbol{r}_1 - \boldsymbol{r}_0| \cos\Theta_0}, \tag{3.99}$$

where $|\boldsymbol{r}_1 - \boldsymbol{r}_0|$ is the topocentric distance of the object in meters.

For low earth satellites with a height $h \ll |\boldsymbol{r}_0|$ we substitute $|\boldsymbol{r}_1 - \boldsymbol{r}_0| \simeq h/\cos\Theta_0$ and thus get from equation (3.95)

$$\Delta\gamma_0 = -\frac{q}{h} \sin\Theta_0 \cos\Theta_0 = -\frac{q}{2h} \sin 2\Theta_0. \tag{3.100}$$

Using again equation (3.98) we may write

$$\Delta\gamma_0 = -\frac{2.4}{h}\tan\Theta_0, \tag{3.101}$$

where h is the height of the object in meters. In Figure 3.19 lines of equal parallactic refraction correction are given in a height versus zenith distance diagram. Given a certain accuracy threshold the area under this particular line is the domain where parallactic refraction must be applied.

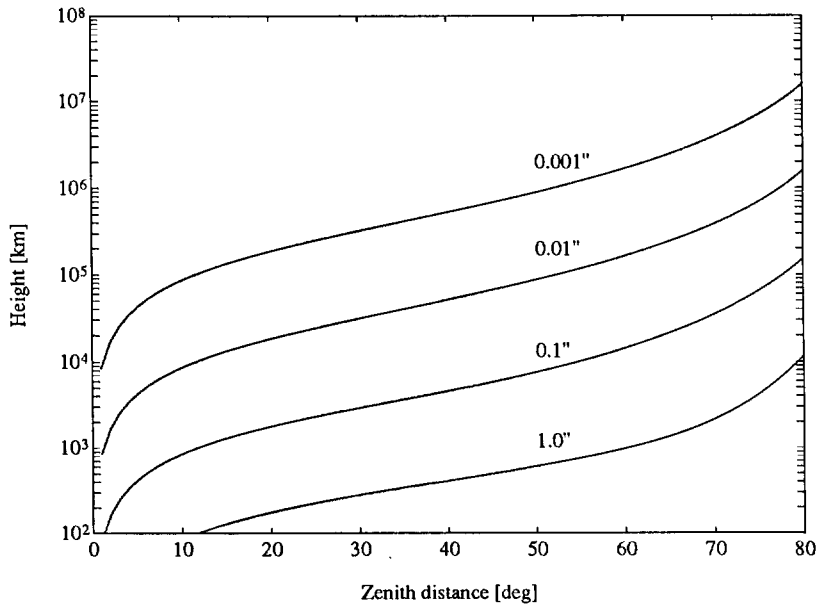

Figure 3.19: Lines of equal parallactic refraction correction $\Delta\gamma_0$ for varying height and zenith distance.

3.4.7 Atmospheric turbulence

The atmosphere influences the optical images in several ways. Among the effects like intensity scintillation, image blurring, speckle structure, image motion etc. the most important limitation for astrometric observations is the *image motion* or more precisely the motion of the centroid of the image of a point source. Image motion in this sense is the irregular deviation of the centroid of an object's image from the smooth path expected from the earth rotation and the refraction. An empirical relation for the variance of a star position was found by Hog (1968):

$$\sigma^2(t) = \frac{0.107}{\sqrt{t+0.65}}, \qquad \text{for } t \geq 0.2, \tag{3.102}$$

where t is the time in seconds and σ^2 the variance in arcseconds square. The slow decrease with time is due to the increasing spectral power density at low frequencies (or in the other words the refraction anomalies). For narrow field astrometry the situation fortunately improves considerably: if a purely differential technique is used i.e. if all objects are observed simultaneously (which is the case for all observation scenarios we have in mind) we may take advantage of the strong spatial correlation of the image motion within small fields. The important quantity will then be the time average of the *differential image motion between* pairs of objects in the field. In many cases the impact of the atmospheric turbulence is further reduced by using several reference objects (catalogue stars) to estimate the plate constant and the position of the object of interest. This is in fact equivalent to referring the program object position to the overall centroid of all reference objects within a certain radius and hence averaging the image motion within this radius. In particular, apparent scale changes, i.e. components of the differential motion which are proportional to the separation of the objects, are completely absorbed by the plate constants (even if different for the x and y direction). For integration times of a few minutes and field diameters in the order of 1° the scale changes seem to be dominant and theoretical residual effects of $\leq 10^{-4}$ arcs have been claimed (Connes 1978). Unfortunately the observation scenario foreseen for fast moving objects are all based on close encounters between two objects only and therefore do not allow exploitation of the potential of this "multi reference star" technique. In our case the plate scale is determined by observing the motion of the objects (either using the earth rotation or the known orbit of the object of interest as a reference) which means by differential positions derived from subsequent *non-simultaneous* observations! From observations with the Multichannel Astrometric Photometer (MAP) (Gatewood 1987), Han (1989) found for the standard error of the differential image motion δ:

$$\delta(t,s) = 140\frac{(\frac{s}{10'})^{0.32}}{\sqrt{t}} \text{ mas}, \qquad \text{for } t \gg 10 \text{ s}, \tag{3.103}$$

where t is the exposure time in seconds and s the angular separation between the two objects in arcminutes. The relation was derived from moderate 2″ seeing data and represents an upper limit including all observation and processing errors. Unfortunately this empirical relation does not cover integration times in the second and sub-second range. To our knowledge there are no readily available results from real observations (with respect to differential astrometry) in this domain. Analyzing the data from the new ZIMLAT telescope may close this gap in the near future.

The model (3.103) is closely related to one of the theoretical models of Lindegren (1980) (the amplitude being a factor of 1.5 higher in the latter case) based on the standard theory of atmospheric turbulence. The formula may be found in

Lindegren (1980, p. 46, equation 35b) and is valid for

$$14t \cdot \mathrm{s}^{-1} \ll 1.25s \cdot \mathrm{arcm}^{-1} \ll D \cdot \mathrm{m}^{-1}, \tag{3.104}$$

where D is the telescope aperture.

3.5 The error budget

It is our primary goal to establish the CCD observation technique for a special application, namely the observation of fast moving objects. In this section we come up with the error budget for this particular application. There is still a broad range of applications and hence the scientific questions and results may be of very different nature. Therefore errors stemming from external sources like the (catalogue) positions of the reference objects are not discussed. In addition, the field of possible applications goes along with a wide range of object characteristics forcing us to distinguish between different regimes and observation scenarios. The following list starts with the primary observable, the centroid of the objects, followed by the astrometric reduction model, the calibration of the model parameters, the intrinsic noise contribution from the atmosphere, and ends with a series of instrumental noise sources. Tables 3.15, 3.16, and 3.17 give an impression of the error budget in an overview.

1) Centroiding

Using moment centroiding algorithms the simulations (see section 4.1.3) as well as observational data from the 0.5 m SLR telescope (see chapter 6) show the position accuracy to be limited at about 0.05 to 0.1 pixel even for objects with high S/N. This is in agreement with the values found in the literature. Corresponding accuracies in arcseconds for the 0.5 m telescope may be found in Table 3.15 and lie between 0.″6 for very faint ($m_v > 15^m$, 1 s exposure) and 0.″1 for bright ($m_v < 12^m$, 1 s exposure) objects. Optimum sampling for the moment centroiding technique requires a pixel scale of about 0.5 σ (σ^2 is the variance of the PSF), i.e. a pixel size of about 1″ (for a good 1″ seeing). This scale will be realized at the $f/4$ focus of the new 1 m ZIMLAT telescope (see section 5.1.4) and the above accuracy figures may then be reduced roughly by a factor of 4. There will also be a significant gain in the S/N figures (and therefore in the limiting magnitude and the position accuracy for a given magnitude) due to the collecting area which is four times larger but also due to the increased focal length which reduces the sky background contribution.

Because of limited observational experience the degradation of the position accuracy for trailed (moving) objects is not yet well established. However, we

always try to avoid trailed images of the faint program objects by either using short exposure times or an optimum tracking technique which results in trailed images of the bright sources (reference stars) only.

The error budget is at present (column SLR in Table 3.15) dominated by the centroiding error (to some extent even for the planned ZIMLAT telescope as well). It is therefore mandatory to overcome this limitation in the near future by abandoning the moment centroiding method in favor of 2-dimensional profile fitting techniques. An improvement of the position accuracy by a factor of about 5 corresponding to a residual error of 0.01 pixel or 0.″01 (ZIMLAT) may be expected at least for the brighter objects. The new algorithms have to focus on fitting functions and on the treatment of trailed images.

2) Supercalibration

The position measuring system itself must generally be calibrated. In our case we are concerned with the grid geometry of the CCD array. (This does include the geometrical precision of the array but also possible intra-pixel non-uniformities.) Deviations from the ideal performance are expected to reach 0.05 pixel (full amplitude; 0.02 pixel rms) at maximum but might well be much smaller. These errors probably have a systematic distribution with respect to the CCD array (manufacturing process) but are (in general) random with respect to the observed objects.

The finite charge transfer efficiency of CCD detectors is the second error source in this context. The effect results in a slight spreading of the charge along the readout direction (along the parallel readout channels but also in the serial register). The transfer efficiency of currently used CCDs is, however, in most cases extremely high and the residual impact on the position error is of the same order of magnitude as the errors due to geometrical imperfections. This statement, of course, only holds if the detector is not saturated (maximum intensities well below the full well capacity). The finite charge transfer efficiency gives rise to systematic, probably magnitude dependent errors.

Given the small contribution of this error source, we do not intend to perform supercalibration measurements for our CCD detectors.

3) Astrometric reduction model / calibration of the model parameters

The standard coordinates have to be computed correctly from refracted topocentric apparent positions. If we assume the refraction correction to be perfect (it will be treated as a separate item) these (idealized) coordinates are accurate to within one milliarcsecond. The critical part of the model is the relationship between the standard and the measured (plate) coordinates. We currently use a

linear transformation between these two coordinate systems (with parameters to be estimated from observations). There may, of course, be additional deviations from the ideal gnomonic projection model like radial non-linear deformations stemming from imperfect optics. Although such effects could be introduced easily, the refinement of the model is always limited by the observational accuracy. Presently we see no signs of systematics (with respect to the location in the detector coordinate system) in position residuals down to the noise level of the position measurements themselves.

The delicate aspect of our calibration technique resides in our relying on the stability of some of the model parameters over time: The common scale and the orientation have to be stable during one close encounter; the remaining parameters during the entire interval between two calibration sessions. It is not easy to meet these requirements through the construction of the astrometric observation system; but again we do not see currently any changes above the centroiding accuracy. The maximum temperature generated scale change for the new ZIMLAT telescope is smaller than $2.5 \cdot 10^{-5}$ K^{-1} and should be therefore calibratable using temperature measurements from different locations in the telescope. The residual maximum error is expected to be less than 0.″01 for object separations of up to 10′ (assuming 0.5 K undetected temperature changes during one close encounter).

4) Atmosphere

Differential refraction We estimated the differential refraction error by analyzing the absolute refraction. The error in pure refraction for zenith distances below 60° is limited to about 0.″2 (using standard atmosphere models and meteorological measurements at the observer's location with accuracies of $\Delta p = 1$ mb, $\Delta T = 1$ K and $\Delta h = 10\%$). Refraction anomalies of the same order of magnitude have to be expected. Using the worst case value of 1″ for the absolute refraction error, a maximum error of 3 mas for the differential refraction at 0.6° from the tangent direction and a zenith distance of 70° can be extracted from Table 3.12.

Unfortunately the effect tends to be systematic, at least for time intervals of the order of hours.

Color refraction/dispersion The effect of color refraction on the estimated position of a point source may be found in Table 3.14. For large passbands (e.g. CCD response) the spectral type of the object has to be known to about 0.1 spectral classes (at least for early types) to limit the maximum position error of a single observation to 0.″01.

The effect of the dispersion in conjunction with specific centroiding algorithms was not studied (except for the moment centroiding technique).

The resulting position errors are highly systematic (zenith distance and probably magnitude dependent).

Atmospheric turbulence The impact on differential position measurements depends with a power of 0.32 on the angular separation of the object and decorrelates with time t according to $t^{-0.5}$ (see equation (3.103)). The main effect is a random scale variation. For 1 s exposures and angular distances between 1′ and 10′ the error is of the order of 0.″05 to 0.″14.

Due to the slow decrease with time (which stems from increasing spectral power at low frequencies, e.g. from refraction anomalies) this error is systematic over time scales of one close encounter (several seconds) but averages out for a series of close encounters (e.g. a pass of a satellite). (There is in fact a steady transition between turbulences and refraction anomalies.) We should mention that the temporal correlation in the formulas (3.102) and (3.103) is strictly valid only when observing in a given direction (we should therefore not simply sum up the exposure time of all frames taken during a close encounter to get the net effect).

Parallactic refraction correction This correction depends on the distance of the object, the atmospheric pressure at the observer's location, and to a certain extent on the spectral distribution of the object's light and the atmosphere model used. From equations (3.100), (3.96) and (3.97) we get e.g. $\partial\Delta\gamma_0/\partial p = \Delta\gamma_0/p$. Allowing for an error in the pressure measurement of $dp = 1$ mb ($dp/p = 1 \cdot 10^{-3}$) we get an error of $d\Delta\gamma_0 \sim 1 \tan\Theta_0$ mas for $h = 500$ km (see also Figure 3.19).

The same type of systematics are associated with this error source as for differential refraction errors.

5) Telescope (tracking)

If observing with a fixed telescope (drive off) wind exited vibrations or movements (e.g. due to free play or bending of the mount) may deteriorate the image quality. Because of the simultaneity of the observations this affects all objects in the field of view in the same way. The result is an increased centroiding noise (the S/N is decreased and the assumed profile shape may no longer be valid) and possibly a magnitude dependence due to asymmetric profiles.

Tracking errors are similar to vibrations and bending although the profile asymmetries may be more pronounced.

Systematic errors have to be expected in both cases. Over long time scales (several close encounters) part of the errors may average out. For the tracking errors, however, residual systematics in the tracking direction have to be expected.

6) Epoch registration/shuttering

For the station clock at the Zimmerwald observatory we may assume an epoch accuracy of ≤ 1 μs within UTC. This is sufficient even for the fastest objects (1 mas for a velocity of 1000″/s). In the combined mechanical-electronic shuttering technique as described in section 4.2 the parallel charge transfer on the CCD defines the beginning and the end of an exposure. As the total duration of a single transfer is about 0.8 ms we have to worry about the model for this transfer phase (e.g. the position and shape of the charge packets as a function of time). Due to the high temporal stability of the process it should be possible to find a deterministic model but the experimental determination of the model parameters will need sophisticated laboratory experiments.

Assuming a worst case of 0.4 ms for the shuttering accuracy leads to a position error of 0.″8 for very fast (2000″/s) and about 0.″04 for slow objects (50″/s). For future CCD controllers these values may be reduced by a factor of 5 to 10 even without laboratory calibrations thanks to the intrinsically higher parallel shift rate.

With respect to the detector coordinate system the effects are of a systematic nature (and thus, if the camera orientation is not changed, systematic with respect to the horizon system). The error can be compensated by intentionally observing the same object with complementary camera orientations.

7) Reference objects

Errors of the reference object positions are not discussed. The figures given in Table 3.17 should give an idea of the order of magnitude only. Errors in the reference object's position produces a systematic bias for the entire close encounter. Systematic components on longer time scales (for several close encounters) are given by the corresponding systematics in the reference object positions (e.g. zonal catalogue errors).

Error budget — Part 1: Centroiding error				
S/N[1]	m_v (1 s exposure)		Centroiding error[2] [arcs]	
	SLR	ZIMLAT	SLR	ZIMLAT
100	12.5	14.5	0.08	0.02
10 – 20	15.5 – 15	17.5 – 17	0.40	0.10
$\leq$10	$\geq$15.5	$\geq$17.5	0.60	0.15

[1]Assumed sky background 19 m_v arcs^{-2}. (For the computation of the S/N values we assumed Gaussian shaped images and defined the images to extend over the optimum threshold level as discussed in section 4.1.3).

[2]Values refer to moment centroiding; a considerable improvement is expected (especially for bright objects) if profile fitting techniques were to be used.

Table 3.15: Error budget — part 1: centroiding error.

Error budget — Part 2			
Source	Error	Type[1]	Remarks
Detector (Supercalibr.)			
0.5 m SLR	$\leq$ 0.″2	R(m)	1 μm grid precision assumed;
ZIMLAT	$\leq$ 0.″05	R(m)	probably much better
Reduction Model/Calibr.	$\leq$ 0.″01	S1	scale change due to temp. change in telescope (10′ object separation)
Differential Refraction	0.″003	S2 (S3)	max. at 0.6° from field center; refraction error $\Delta\gamma_0 = 1''$ assumed
Color Refraction			
broadband	0.″3[2]	S3m	CCD response (470 – 880 nm)
100 nm	0.″07		V-band
10 nm	0.″0004		
corrected (broadband)	0.″1		error in spectral classification ($\pm$1 class)
Color Dispersion	unknown	m	magnitude eqn. (asymmetric profiles)
Atmospheric Turbulence			
$\|t\| = 1.0$	0.″07	S1	1 sec integration
$\|t\| = 10.0$	0.″14		($\|t\|$ is the distance from the field center)

[1]Error type:

R	stochastic (random) component
m	magnitude dependent
S1	systematic error for one close encounter
S2	systematic component over time scales of hours
S3	long term systematic bias

[2]All color refraction errors are maximum errors for extreme spectral types!

Table 3.16: Error budget — summary (part 2).

Error budget — Part 3			
Source	Error	Type[1]	Remarks
Parallactic Refraction			
h=500 km	0.″003	S2	z=70°, Δp = 1 mb
Telescope (Tracking)	unknown	S1m[2]	
Epoch Registration			
v= 2000″/s	0.″002	S3[3]	$\leq$ 1 μs within UTC
Shuttering			
v= 2000″/s	0.″8	S3[4]	uncalibrated parallel shift
v= 50″/s	0.″04		timing error of 0.4 ms assumed
Reference Objects			
PPM	0.″27 (1990)	—	
HIPPARCOS	0.″002	—	
GPS prec. ephem.	0.″002	—	0.2 m orbit error (earth fixed!)
Lageos	0.″007	—	0.2 m orbit error

[1]Error type:

R	stochastic (random) component
m	magnitude dependent
S1	systematic error for one close encounter
S2	systematic component over time scales of hours
S3	long term systematic bias

[2]Residual systematics in the tracking direction have to be expected.

[3]Systematic effect with respect to the direction of motion of the object.

[4]Systematic component with respect to the horizon system. May be compensated by intentionally observing the same objects at complementary camera orientations.

Table 3.17: Error budget — summary (part 3).

Chapter 4

Technical Aspects

This chapter contains a lose collection of aspects which are often called "technical" and are therefore generally left out in a good part of the literature. These topics are in many cases not trivial. They not only limit the accuracy of the results but technical details eventually determine the actual realization of the observational process. The first section is devoted to object recognition and centroiding where we summarize the results of special investigations as performed by Verdun (1993) for his diploma thesis. The next section deals with a persistent problem in astrometry of (fast) moving objects namely the shuttering process or the epoch definition of the observed events.

4.1 Object recognition and centroiding

The purpose of the study (Verdun 1993) was to develop and test different object search strategies and centroiding algorithms taking into consideration the special characteristics of the observation technique. The S/N and the required real-time data processing seriously restricted the choice of the algorithms. In addition the possible elongation of the object images (trails) asks for a simple treatment making no assumptions about the shape of the object either in the search or in the centroiding process. Further studies might take a priori information concerning the image structure into account.

The following problems were addressed:

1. Performance and peculiarities of the algorithms under various conditions.
2. Optimum parameter values for different algorithms.
3. Optimum sampling.

The third item was very important for the definition of the optical parameters for the new ZIMLAT telescope to be installed at the Zimmerwald observatory in late 1995. Although this instrument will be jointly used for satellite laser ranging and optical astrometry, the most demanding optical specifications, and the definition of the corrector optics for different f-ratios in particular were essentially determined through this study.

4.1.1 Calibration and reduction of raw CCD data

The raw measurement data of the CCD detector must first be calibrated and corrected for instrumental effects. Extensive literature is available covering the subject e.g. McLean (1989); Kjeldsen and Frandsen (1992). We will therefore leave out details and limit the discussion to a brief overview. The following steps have to be performed:

1. Subtraction of the electronic biases:
   Electronic biases added during the readout process have to be corrected for by subtracting a bias frame which in the simplest case is obtained by reading out the CCD without any integration.

2. Subtraction of dark current:
   Dark current produced inside the detector may compromise long exposures. To correct this, a bias-corrected dark frame (exposure with shutter closed) with the same exposure time as the observation frame to be corrected is subtracted. Dark current accumulates over a wide intensity range proportional to the integration time and we may therefore also use a dark frame scaled for different exposure lengths.

3. Division by the flat-field:
   A so-called flat-field is the response of the detector to a homogeneous illumination. The bias-corrected, dark-current-subtracted, and normalized flat-field is used to correct for pixel to pixel quantum efficiency variations, vignetting of the telescope optics, etc. The acquisition of flat-fields is a delicate task. If e.g. an artificially illuminated screen (or dome) is used the spectral distribution of the illuminating source should be similar to the colors of the astronomical objects.

4. Bad pixels:
   Dead or hot pixels (also called "cosmetics") may either be taken into account by a bad-pixel map for the particular CCD detector or interpolated by means of a filter.

Additional effects like interference fringes from narrow atmospheric lines on some thinned backside illuminated CCDs may occur as well. In order to reduce

the noise introduced by the corrections, the calibration frames used in step 1 to 3 should be some "median" or "mean images" of many single exposures.

Especially cumbersome when searching for moving and hence in a sense transient objects are events produced by cosmic ray secondaries or radioactive decay products. The corresponding CCD records are called "cosmics". They mimic point-like or trailed bright sources. Fortunately the majority of the cosmic events can be identified by their distinct signature: the deposited charge is confined to a few pixels (trails are often only one pixel wide), the images are very sharp (the profiles differ significantly from seeing-convolved point sources) and the overall intensity is a few thousand electrons in a front side illuminated (thick) CCD. The events are mainly generated my muons which release about 80 electrons per micron of silicon thickness (front side illuminated CCDs are 20 to 80 μm thick). Their rate is about 1 to 2 events $\mathrm{cm}^{-2}\mathrm{min}^{-1}$ changing with altitude and solar activity. (We measure about 2 events min^{-1} with our PM512 chip in Berne.) Very rare α-particles ($\sim$ 3 $\mathrm{cm}^{-2}\mathrm{d}^{-1}$) produce massive 10^5 electron spikes. Low level X-rays from e.g. Schott UBK7 or GG385 glass or decay products from radioactive contaminated detector packing material may produce similar effects (McLean 1989).

In Figures 4.1 to 4.3 we give some examples of calibration frames for a PM512. A very nice trail from a cosmic ray event may be seen in Figure 4.4.

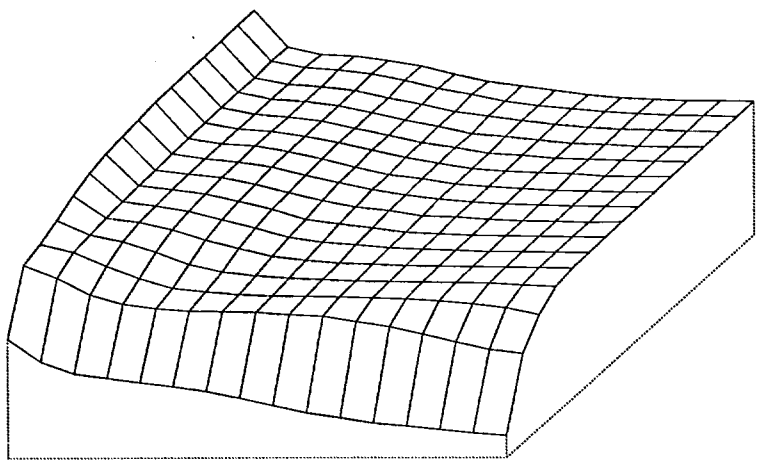

Figure 4.1: Bias structure of our PM512 CCD

The short exposures used in our application allow simplification of the calibration procedure somewhat. Dark current is negligible (the PM512 produces 0.14 $\mathrm{e}^{-}\mathrm{pixel}^{-1}\mathrm{s}^{-1}$ when operated in inverted mode at -45° C). We therefore only have to correct for the bias and for the flat-field. Concerning the cosmics we prefer to sort them out during the object recognition step rather than eliminating them

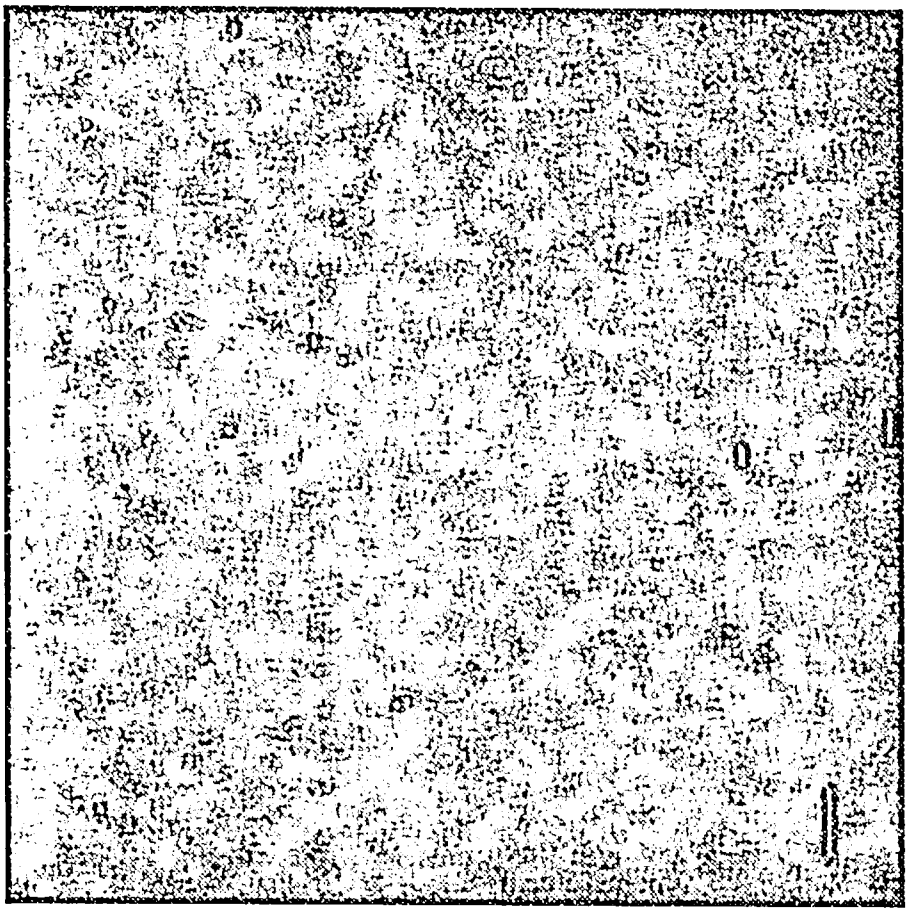

Figure 4.2: CCD dark frame (30 min.). Most of the structure is due to intrinsic variations of the dark current production. Some of the very bright, compact features are cosmics. The bright vertical strikes were produced by saturated hot pixels. These pixels produce electrons at such a high rate that they may even leave traces during the readout process (faint horizontal lines).

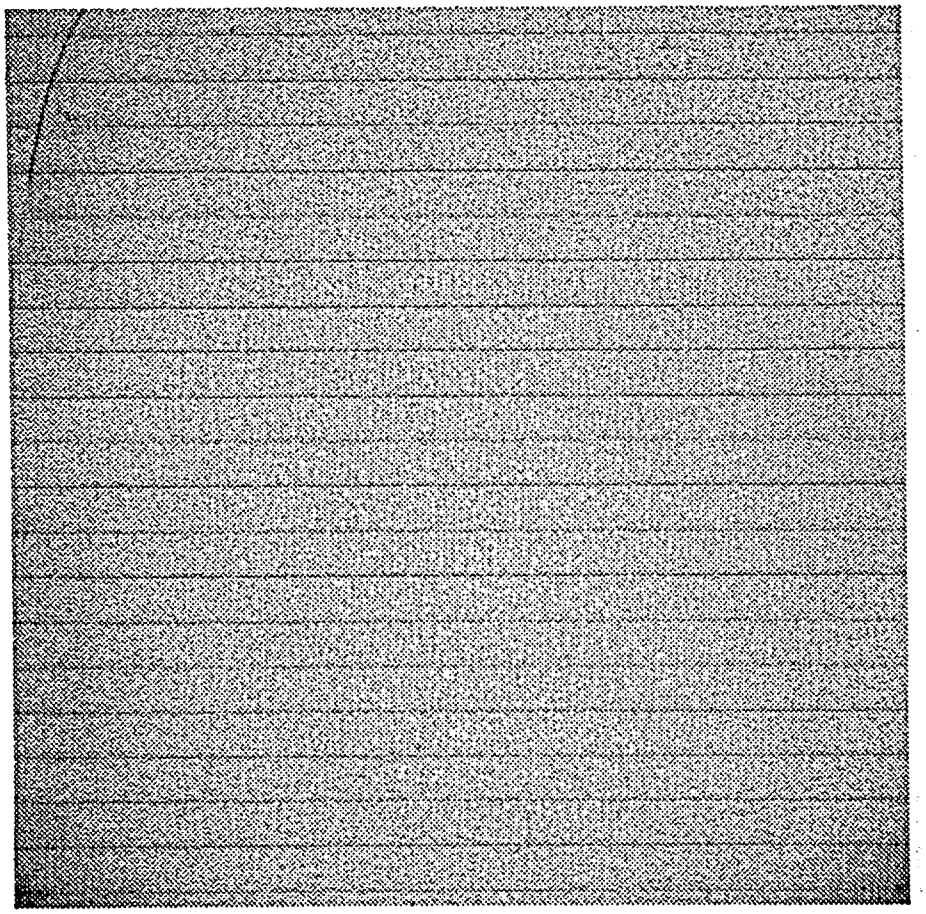

Figure 4.3: Sum of 5 flat fields. The frames where acquired at the 0.5 m SLR telescope during heavy fog (which proved to be an excellent "flat" illumination source!). The horizontal lines as well as the "scratch" at the upper left corner are sensitivity variations reflecting the manufacturing process (masks). Most of the vignetting is due to the telescope.

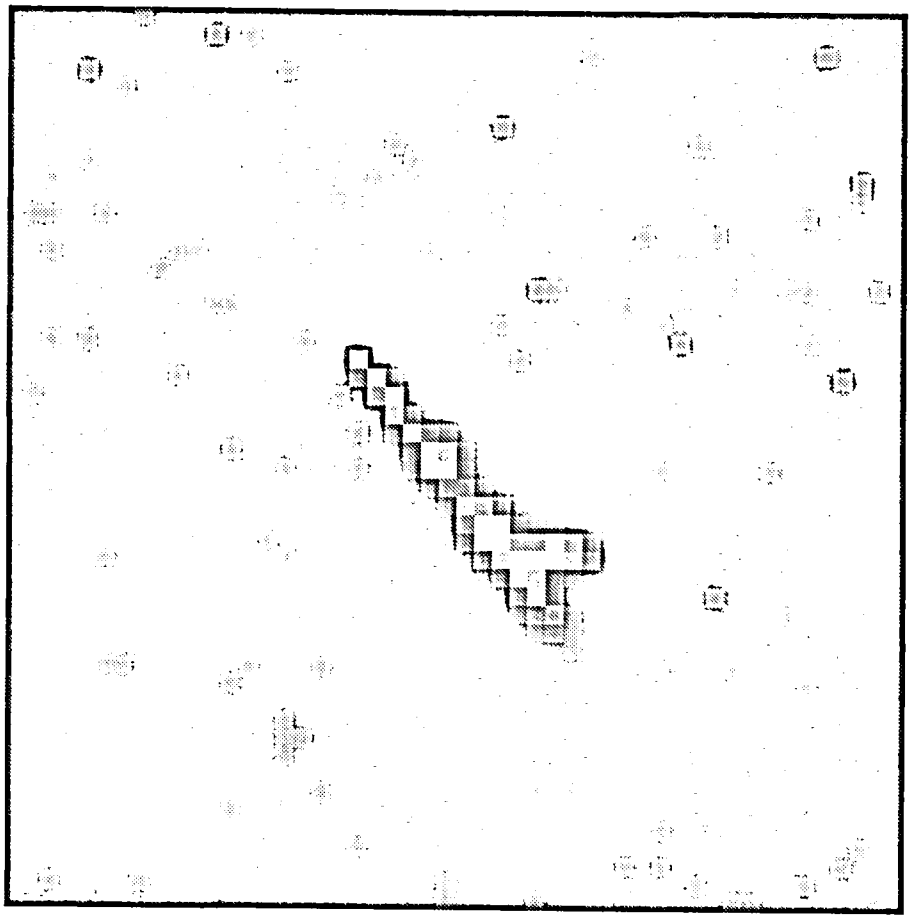

Figure 4.4: Cosmic ray event. A rare α-particle produced a massive electron spike and a secondary event.

with a separate filter algorithm. There still are some lose ends in our calibration procedure: a map of bad pixels should be implemented and the open question of how to correct subframes for the bias term without acquiring bias frames for each particular subframe has to be solved (hopefully the actual dependence on the location and the extent of the subframe may be described by a simple model).

4.1.2 Object recognition

The first question to be answered in any object recognition task is the following: what are the characteristics of an object allowing us to decide whether or not a particular pixel belongs to an object? The fact that an object is always superimposed on a background and is thus brighter than this surrounding background is a convenient characteristic common to all possible object definitions. Apart from that we may describe an object in rather different ways. A simple approach is e.g. to define it as a closed area of pixels surpassing the background intensity by a certain amount. On the other hand also a specific shape (2-dimensional profile) with a few adjustable parameters could be assumed.

The following sequence of steps can be identified in the object recognition process:

1. First background estimation:
   In this first attempt a simple model for the background intensity e.g. a constant value for the entire (sub-)frame is adequate.

2. Object search:
   The goal of this step is to find one or more pixels most likely pertaining to an object using their property of being brighter than the background.

3. Object recording / fitting:
   Starting from the pixel(s) found in step 2 the entire object has to be recorded by either using fundamental characteristics of an object like that there must be a closed boundary separating the object from the background or by fitting a 2-dimensional profile (e.g. a calibrated point spread function) through all pixels in a certain neighbourhood of the "first" pixels found.

4. Improved background determination:
   As the objects are now identified, new background parameters may be assessed using more sophisticated models than in step 1. The background may be modeled e.g. individually for small regions around each object by using data from "object free" regions or by subtracting the objects from the original frame and defining a background intensity based on this "cleaned" frame.

Step 3 and 4 have to be repeated iteratively until the background values and the object parameters have converged to stable values. If for some reason precise a priori coordinates are available step 2 may be skipped. The object search and the recording/fitting step may either be performed sequentially on the entire frame or each object may immediately be recorded/fitted after it has been found.

Determination of the background

The safest approach to assess the mean background of an area which still contains undetected objects is to analyze the histogram of the pixel intensities (i.e. the power spectrum). Assuming a dominant (in number) contribution from actual background pixels, a shot noise or Poisson distribution is expected. By fitting this distribution of intensities with a Poisson distribution (a "zero order" approach would be to take the arithmetic mean) we obtain a first estimate for the mean background level and its variance. In order to reduce the influence from bright sources the power spectrum may also be clipped at high intensities before fitting. In any case this first estimate will be slightly too high, the actual deviation from the true value being given by the number and brightness of the objects in the analyzed area. We should also be aware of gradients in the background which may force us to divide the frame into smaller regions (e.g. around the expected positions of the objects of interest) for individual background determination. Also a poor quality of the power spectrum fit is a telltale sign of compromising objects or gradients. It should be pointed out that in most cases an additional improved background determination is necessary as previously described (step 4).

Object search

The task of the object search algorithm is to identify one or several pixels pertaining to an object. We have therefore first to decide on the criterion for a pixel to belong to an object. The simplest approach would be to set a threshold which is above the background (e.g. n times the background variance) and to search for pixels exceeding this value. To achieve a confidence level of 95%, the threshold must be set to a minimum of 1.7 times the background rms above the mean background. Assuming a Gaussian profile the corresponding minimum S/N for an object is about 2.5 (Schildknecht et al. 1993). In order to detect even fainter objects we may correlate several pixels and test whether they form an ensemble (and are not individual pixels), i.e., an object or a part of an object. This filter approach reduces the minimum S/N for a detectable object to a value below 1 (e.g. to 0.8 for a 3 x 3 pixel filter and 99% confidence level). For more information we refer to Schildknecht et al. (1993).

In the current version of the processing software we implemented the following search strategy:

1. The frame is scanned for one or more pixel(s) complying with the detection criterion (a selectable threshold in units of the background rms above the mean background).

2. Starting with this pixel the object is recorded (reconstructed pixel by pixel) or fitted (for the algorithms see below).

3. The object is either accepted or rejected according to its characteristics determined during the recording/fitting process (e.g. brightness, extension, etc.). This is also the moment where cosmic ray events are discriminated. All accepted objects including their evaluated characteristics are stored in a list.

4. The remaining untested pixels, excluding already recognized objects, are now searched for further objects.

Due to its definition the algorithm finds the objects according to their location on the frame (e.g. from top left to bottom right). This may give rise to a problem in dense star fields with many faint sources: the list of detected objects may overflow before the frame is completely scanned. This may happen although in most cases we are interested in the, let us say m, brightest objects only. A straight forward solution is to delete the faintest object from the list each time an overflow is about to take place. Our approach is somewhat different. It is based on a slightly modified search strategy: instead of sequentially searching for the first pixel(s) fulfilling the detection criterion we always scan the entire image for the brightest pixel(s) meeting the requirement (and not pertaining to an already detected object). A distinct disadvantage of this algorithm (at least for frames with a moderate number of objects) is the necessity for many time consuming scans of the entire frame (one scan per detected object). A time optimized method will depend on the expected number of objects (i.e. the star density in the field) and must take into account the ratio of the time needed to test a pixel with the detection criterion versus the time spent to record/fit an object pixel.

Object recording

We define the term "recording" in this context as the process of identifying "all" object pixels starting from one or several pixels found by the search algorithm. It is, of course, never possible to find all pixels containing information about the object; we are always limited by noise preventing us from detecting the very faint parts of an object's image. Object recording methods for faint sources may be divided into two principal categories:

(a) A 2-dimensional model of the shape of the object's profile is assumed. The model is fitted to the data using the coordinates of the pixel(s) from the

search process as the initial object position. There is a wide variety of models and many different fitting approaches (van Altena and Auer 1975). A common technique is the calibration of a point spread function using bright objects in the field (the parameters may depend on the position in the field) and to determine only the position and amplitude when fitting the faint program objects. If the telescope optics and the seeing conditions are sufficiently stable, a map of point spread functions may be determined from a calibration frame and used to process successive frames.

(b) No assumptions concerning the shape of the object images are made. The object is defined as the sum of the pixels which lie around the initial pixel(s) found in the search step and exceed a certain threshold intensity. The expression "around" has to be specified e.g. in the sense that the pixels for a closed area including the initial pixel(s) (no isolated pixels) or that a closed border around the initial pixel(s) must exist.

The fitting of a point spread function has the advantage that the a priori information about the 2-dimensional shape of the images is exploited. In addition this shape may be calibrated using objects with a high S/N which means that we can take advantage of information from many well defined objects to describe the faint images with poor S/N. This, however, requires that the model of the image profiles is known beforehand and that all objects may be described by the same model (at least in the case where pre-calibrated functions are used). The latter does not hold in the case of moving objects where some of the images are trailed and others are not (or trailed in a different way). The images would have to be described by point spread functions smeared out along the direction of motion.

The second method, on the other hand, adapts itself to the shape of the images; but a serious disadvantage should not be neglected: each pixel is treated separately, it does not know anything about the remaining part of the object and is therefore more sensitive to the noise. We are in fact facing the same difficulties as in the object recording procedure and may react in the same way by correlating a few pixels using a small filter in order to lower the detection limit. This method, however, may never follow an object's profile as far out into the wings as a perfect fit of a point spread function does (underlining the word "perfect"!).

The following reasons eventually convinced us to favour the second method:

1. The relative motion of the moving object with respect to the stars prevents the use of stars to calibrate the model to be applied to the moving object's image.

2. Uncalibrated profile models (with more than three free parameters) may not be firmly fitted to the, predominantly faint, objects of interest.

3. Trailed images complicate the models.

4. The CPU requirements of the profile fitting algorithms would have been prohibitive for the present camera computer hardware (68040 processor) to accomplish this task in real time.

This decision consequently rules out profile fitting for the centroiding (the object recording and the centroiding step are actually identical when using any fitting method).

We briefly describe the two different object recording methods (for a detailed discussion see (Verdun 1993)). In both methods we need a threshold to test the pixels either on a pixel by pixel basis or using a small (2 x 2 to 3 x 3 pixel) filter. The optimum threshold value will be discussed in section 4.1.3. The first method starts from the initial pixel and tries to find all contiguous pixels exceeding the threshold. The second algorithm, again starting from the initial pixel, searches a border pixel (using the threshold criterion) and then "walks" along the border of the object until it has completely surrounded it. Every pixel inside this border is then defined as an object pixel. There are only marginal differences in the results of the two algorithms, but the second is slightly faster.

During object recording, a series of quantities (different moments) are summed up to allow the characterization of the object and its position. In addition to the number of pixels and the total intensity, the tensor of inertia is a useful quantity. It allows determination of the object's shape and orientation (i.e the length to width ratio and the position angle of a trailed image). Object characteristics are very important in discriminating unwanted objects (e.g. cosmics) but also the program objects itself (they help to find the "needle in the haystack").

4.1.3 Centroiding

There is a wide variety of techniques to compute image centers. It is generally recognized in the literature that simple moment centroiding algorithms may be accurate to about 0.05 to 0.1 pixel. This order of magnitude is confirmed by the investigations of Verdun (1993). To improve this figure, two-dimensional models have to be fitted to the images. Extensive discussions of the fitting technique may be found in van Altena and Auer (1975), intercomparisions of different methods (including moment techniques) are given in Bienaymé et al. (1988), Goad (1986), Bulau (1986), Lindegren (1978) and Stone (1989).

Pro and contra of the two principal approaches were already discussed in section 4.1.2 and arguments ruling out the fitting methods for the time being were given. We therefore assessed the characteristics and the performance of the simplest moment algorithm, the computation of the light gravity center, with

extensive simulations and confirmed the results by actual observations (Verdun 1993). In the remaining part of this section the main questions and the principal results of this study shall be summarized.

Main questions

1. *Influence of the signal width:* The optimum width of the object images is assessed in the presence of a constant background. This means that only the focussing or the seeing point spread function is varied (and not the pixel size).

2. *Minimum sampling:* The pixel size is varied for fixed objects and for background characteristics.

3. *Optimum threshold:* Optimum threshold to be used for the object recording.

4. *Centroiding accuracy:* Accuracy of the centroids with respect to the S/N of the images.

Simulation

Images with Gaussian profiles (and realistic shot noise) were generated on top of an uniform background of 6150 photoelectrons (549 ADU) per pixel. The latter has a corresponding shot noise of 78 electrons (7 ADU) per pixel. Camera gain (i.e. the ratio of electrons to ADU counts) was assumed to be 11.2 e^-/ADU. In general the simulation data was chosen to match the actual experimental setup (see Chapter 5) and sky conditions at Zimmerwald (0.5 m telescope, 4".1 pixel size, 1 s exposures, 19 m_V arcs^{-2} sky background). In order to study sampling effects, the signal centers may either be fixed (to a selectable value) or randomly distributed with respect to the pixel grid.

Signal width (focussing/seeing)

To assess the dependence of the centroiding accuracy on the signal width we generated a series of images with constant integral intensity (brightness) for different σ, where σ^2 is the standard deviation of the Gaussian profile. The image centers were intentionally kept at 0.35 pixel from the pixel center in x-direction (the offset in y-direction was set to 0). 20 independently generated objects per σ-bin were used. The object data are: integral brightness of 1241 ADU corresponding to a 495 ADU peak intensity at $\sigma = 1$; the threshold was set to 10 ADU which is equal to 1.4 times the background noise. The x-components of the centroiding residuals are shown in Figure 4.5. For signal widths from 0.1 to 0.4 pixel, strong

systematics due to the undersampling may be seen (this is actually the definition of "undersampling" in the context of our particular centroiding algorithm). In this region the algorithm is no longer able to locate the small image within the (almost single) pixel and the maximum error is given by the image's intentional offset from the pixel center. On the other hand the scatter within the σ-bins is growing with increasing signal width. This is due to the increasing contribution of the background noise and hence of the decreasing S/N.

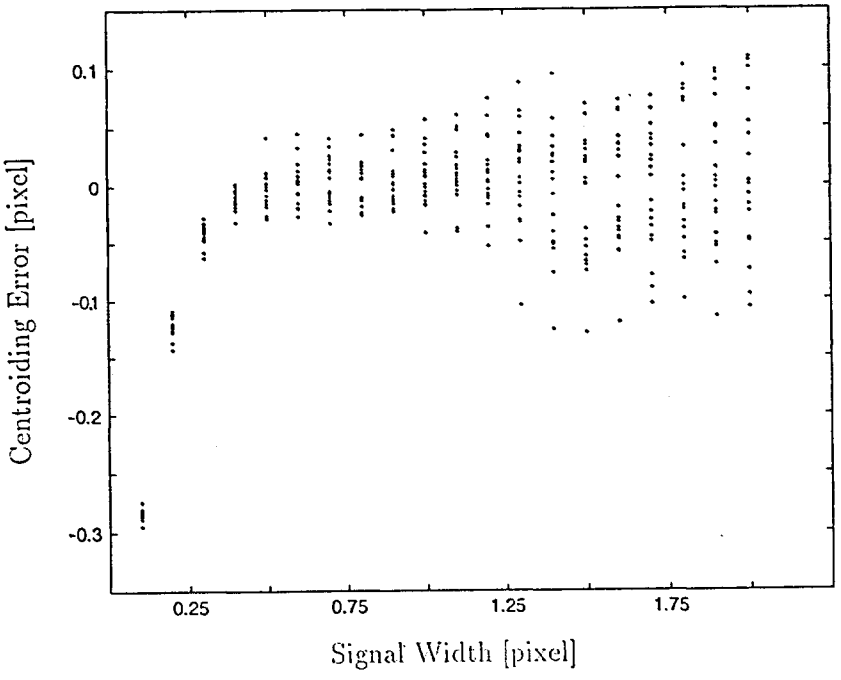

Figure 4.5: Centroiding error as a function of signal width (both in pixel).

Conclusion: The images must be focussed as well as possible; because the seeing spreads out the images in a similar fashion, the latter should also be minimal. Undersampling (with respect to this particular centroiding algorithm) starts at about σ=0.4 pixel.

Optimum sampling

In this simulation we did not vary the object diameter but the pixel size which corresponds to a variation of the telescope's focal length. Objects with constant brightness, constant width and randomly distributed centers for a series of pixel sizes were simulated. We studied two extreme cases. Figure 4.6 shows the results for the sky background dominated, Figure 4.7 for the detector (readout) noise dominated regime. Each pixel-size bin contains 100 objects, the center of the boxes indicate the mean and their height the standard deviation of the samples.

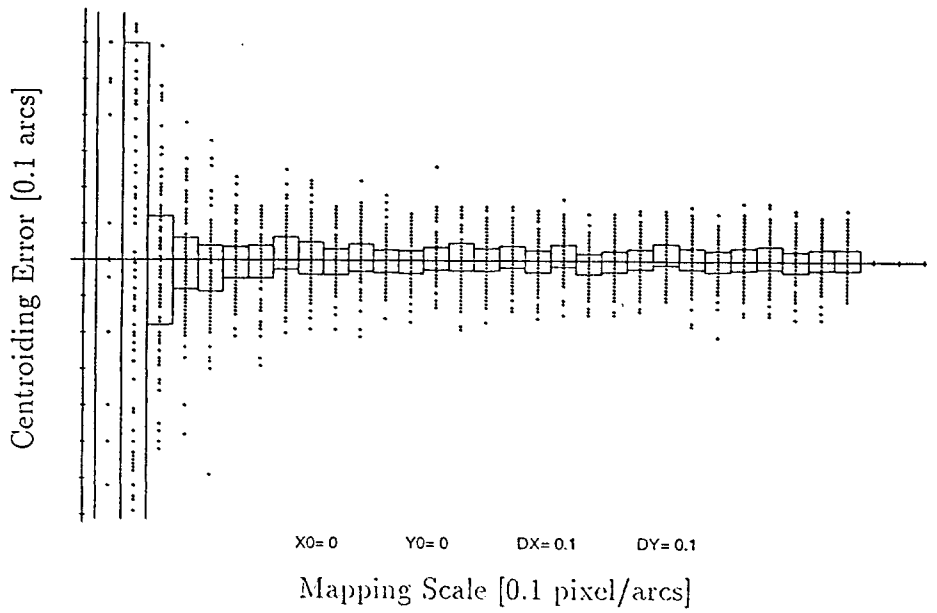

Figure 4.6: Centroiding error as a function of focal length for a sky background dominated regime. Tick mark units are 0.1 pixel/arcs for the ordinate and 0".1 for the abscissa.

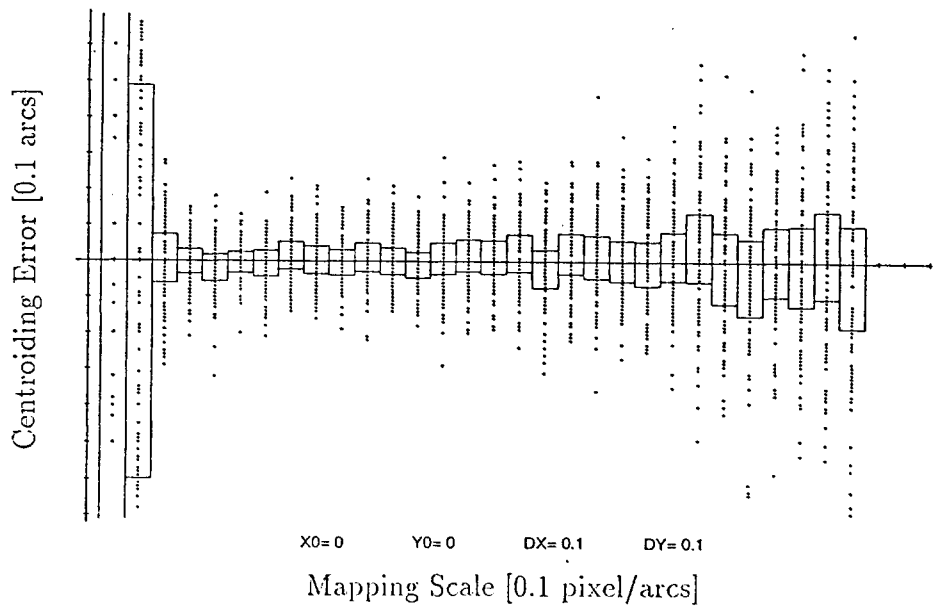

Figure 4.7: Centroiding error as a function of focal length for detector noise dominated regime. Tick mark units are 0.1 pixel/arcs for the ordinate and 0".1 for the abscissa.

The signal width is given in number of pixels per arcsecond and the residuals in arcseconds. The undersampling region may again be identified at signal widths below about 0.4 to 0.5 pixels. In the sky background dominated case the centroiding residuals remain constant for decreasing pixel size (increasing focal length). The reason resides in the fact that the background is "diluted" together with the object image and that the overall S/N remains thus constant (the latter defines the magnitude of the residuals). If detector background dominates, the residuals increase proportional to the number of pixels over which the object's image is spread (each pixel contributes a fixed amount of detector noise).

Conclusion: Undersampling is present for σ below 0.4 to 0.5 pixel. Oversampling should be prevented if operating in the detector noise dominated regime. Oversampling has no influence otherwise.

Optimum threshold

In order to determine the optimum value for the threshold, we generated an ensemble of ten objects in the brightness range from 100 to 6000 ADU. Ten images were generated for each object; the signal width σ was set to 1 pixel and the centers distributed normally. This ensemble of objects was processed with different threshold values. Figure 4.8 summarizes the results (for the x-components of the residuals). The solid vertical lines indicate the levels of one

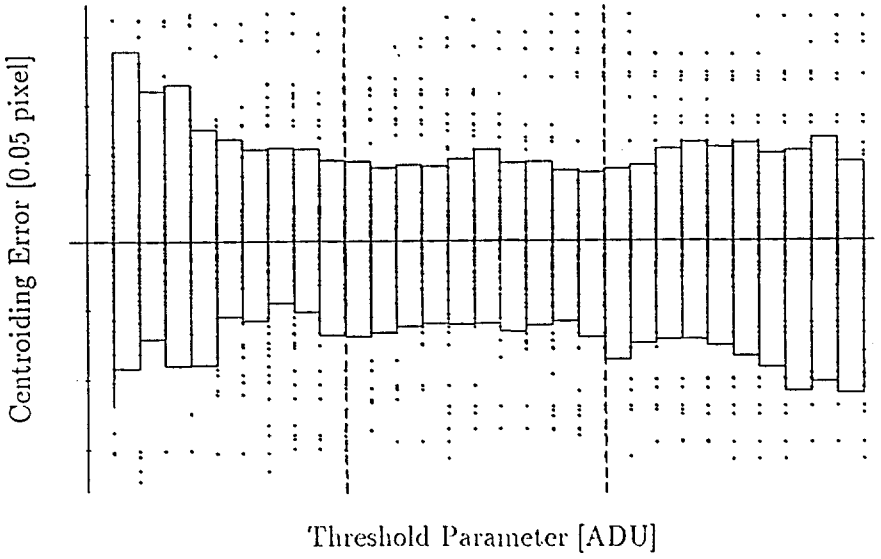

Figure 4.8: The x-components of the centroiding residuals for an ensemble of stars are given as a function of the centroiding cutoff parameter. Tick mark units are 0.05 pixel for the ordinate and 1 ADU for the abscissa.

and two times the background noise (7 ADU) respectively. Although it can not

be said from a single figure alone, the optimum threshold seems to lie somewhere between the vertical. For bright objects we have found an upper limit for the value of the threshold at about 3 % of the object's peak amplitude (brightest pixel). At the darker end we are limited by the object recording algorithm: if the threshold is near the background, the algorithm, not knowing anything about the object's shape, takes any background pixel which by chance (due to the noise) exceeds the threshold and shows up as a part of the object! The result of this process is shown in Figure 4.9.

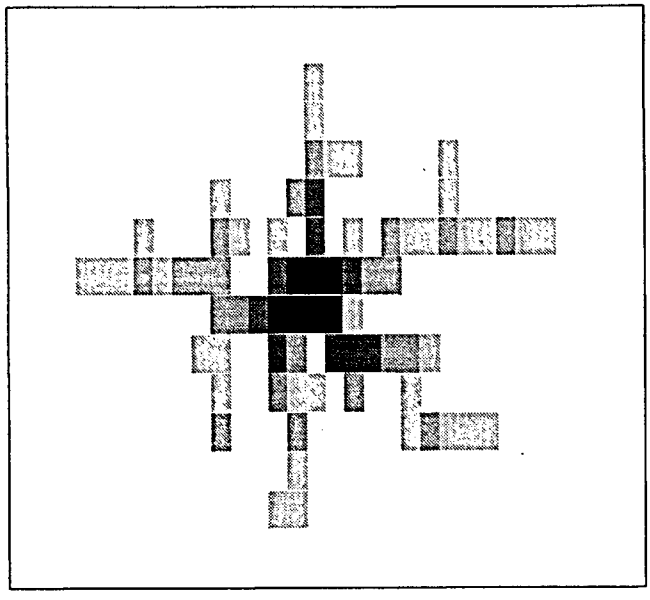

Figure 4.9: Result of an object recognition based on too low a threshold level.

We recently introduced a more reasonable threshold criterion. It is based on the maximization of the S/N for the object. On the one hand by using a high threshold value we lose a good part of the object i.e. of the signal; on the other hand as a result of a low threshold the object may include many background dominated pixels i.e. noise is added to the object.

Figure 4.10 shows the threshold value which optimizes the S/N (assuming a Gaussian image profile) as a function of the object magnitude (solid line; 0.5 m telescope, 1 s integration). The dotted line represents the old scheme where we set the threshold at 1.5 times the background noise for objects with $m_v \geq 10$ and at 3% of the brightest pixels for the brighter objects. At about $m_v = 16.5$ even the brightest object pixel is not reaching the threshold values and the S/N suddenly drops to 0. In reality the minimum threshold at the faint end of the spectrum is thus still given by the object recognition algorithm. Although the difference in

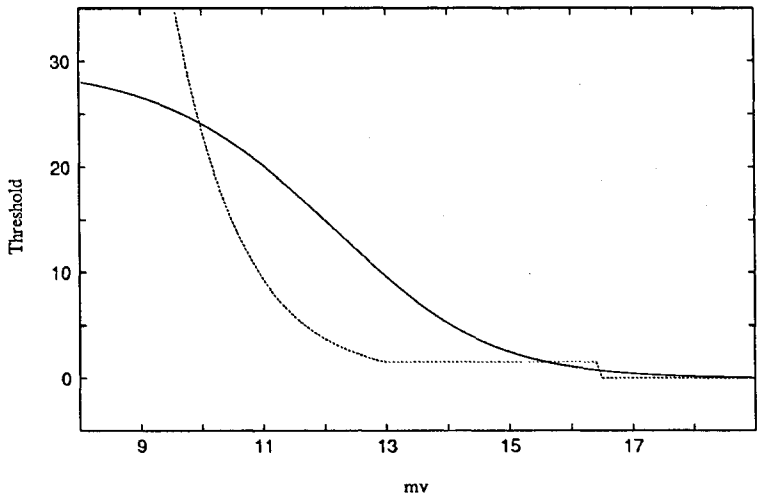

Figure 4.10: Optimum object recognition threshold. The solid line represents the threshold which optimizes the S/N (assuming a Gaussian image profile) with respect to the object magnitude (0.5 m telescope, 1 s integration). The old scheme is given by the dotted line (see text). The unit for the threshold value is the background noise.

the threshold values for both methods is significant, the resulting S/N does not change much (this is due to the fact that a threshold change affects pixels at the object border with a S/N per pixel of the order of 1).

Centroiding accuracy

In order to study the centroiding accuracy at the faint end an ensemble of 97 objects in the brightness range between 35 and 170 ADU (σ = 1 pixel, peak intensities from 14 to 69 ADU) corresponding to a S/N range between 1 and 16 were generated. 30 individual exposures of each object were analyzed with the threshold parameter set to 1.5 times the background noise. Centroiding residuals as a function of S/N are shown in Figure 4.11. Figure 4.12 shows the S/N versus the number of object pixels. Both, the S/N and the number of object pixels have to be understood as values determined by the object recognition algorithm and not as the "true" values from the object generation. If a centroiding accuracy of the order of 0.1 to 0.2 pixel is required, a minimum S/N in the range between 5 and 10 corresponding to object extensions of about 5 to 11 pixels is necessary. The systematics of the residuals for small S/N are due to an unpleasant behaviour of the particular object recording algorithm we used in this example (in this region the recorded objects look very ramous as in Figure 4.9). If using the second centroiding algorithm as described in section 4.1.2 ("border sneaker") the effect

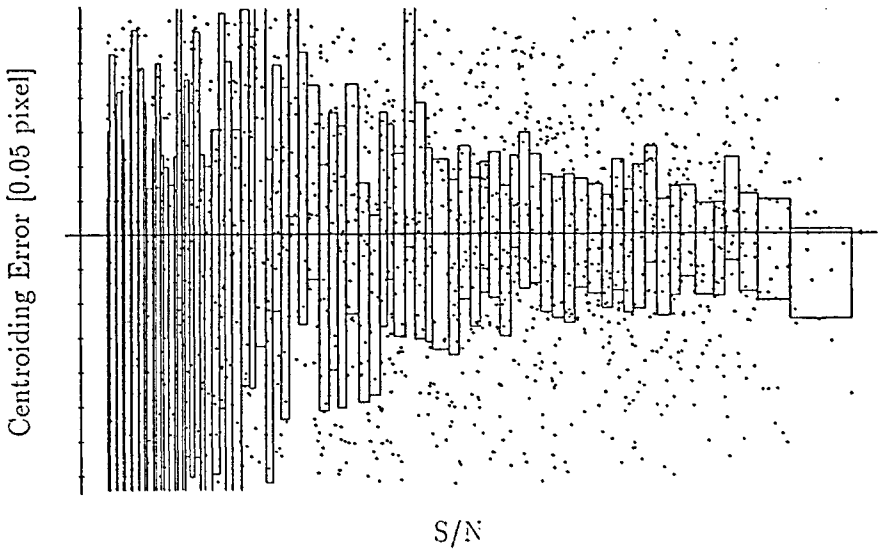

Figure 4.11: Centroiding error as a function of S/N. The x-components of the centroiding residuals for an ensemble of stars are given with respect to the S/N (as determined by the object recognition algorithm). The centroiding cutoff parameter was set to 1.5 times the background noise. Tick mark units are 0.05 pixel for the ordinate and 1 for the abscissa.

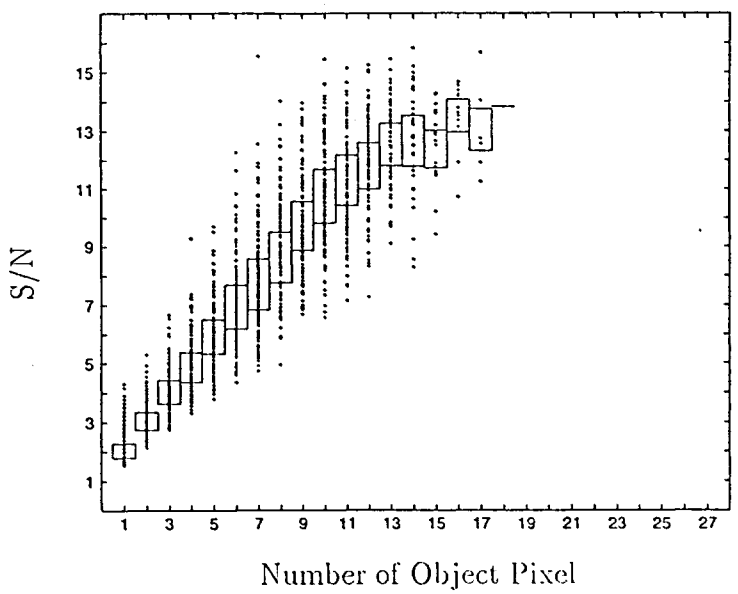

Figure 4.12: S/N as a function of number of object pixels (both determined by the object recognition algorithm). The results are based on the same data as in Figure 4.11.

vanishes completely. The turnoff in Figure 4.12 for high S/N is a pure selection effect.

Similar investigations were performed for bright objects. Table 3.15 gives an overview on the resulting accuracies. Visual magnitudes and accuracies were computed for the current experimental setup (0.5 m $f/2$ SLR telescope, see section 5.1.3) and for the future ZIMLAT telescope (see section 5.1.4). The values in Table 3.15 will have to be confronted with results from real observations (Chapter 6).

As stated several times the only solution to go beyond the 0.05 pixel limit is to switch from moment algorithms to 2-dimensional fitting methods. We expect to gain about a factor of 5 which would improve the position accuracy to 0.01 pixel for the brighter objects (see also Monet et al. (1987)). There is, however, not much information in the literature concerning the performance of fitting algorithms for faint objects with a poor S/N. We are planning further studies in this context. Also the optimum sampling will have to be assessed under these new conditions. Since there is furthermore no experience concerning the fitting of trailed objects new algorithms will have to be developed and tested preferably with real observations. By using filter techniques we also expect to push the object detection limit to below a S/N of 1 for tracked objects (Schildknecht et al. 1993). Trailed images would then be recognized even if their individual pixels exhibit a S/N below 1.

4.2 The shuttering and epoch registration technique

Time tagging the measurements is a major problem when using integrating detectors for the observation of moving objects. As we are not able to record the position and epoch for each individual photon, as in the case of photon counting devices, we must define the mean epoch of an exposure. This requires that both the beginning and the end of an exposure are precisely defined (a) through the shuttering of the frame (the ends of the trails have to be well defined) and (b) by registering the corresponding epochs. The difficulties increase with the angular velocity of the observed object. Taking the maximum angular velocity from Table 2.1 and requesting the maximum error introduced by the epoch registration to be below $0\overset{''}{.}1$ or $0\overset{''}{.}01$ respectively we end up with the stringent requirements listed in Table 4.1. No mechanical shutters will meet these specifications! The fastest commercially available blade type shutters (e.g "Uniblitz" from Vincent Associates) need about 5 ms to open or close an aperture of 25 millimeters. Moving slit shutters as used in photo cameras achieve comparable results although their minimum exposure times may be well below 1 millisecond (the latter is possible by making the slit very small but the time needed to cross the aperture is

Pos. error [arcs]	Epoch registration accuracy [μs]			
	ECS	GPS	LAGEOS	ERS1
0.01	660	330	40	5

Table 4.1: Minimum epoch registration accuracies needed to determine the position of moving objects to within 0.″01.

still of the order of 5 ms). We might try to model the movement of the shutter blades but this is most probably impossible to within the required accuracy due to the fact that the behaviour of such mechanical devices may strongly depend on temperature, humidity, orientation in the gravity field, etc. The bad experiences with mechanical shutters, rotating blades and tilting glass plates used in the early days of photographic satellite observations (Beutler 1976) confirm our scepticism. We therefore choose a different approach and make use of the special properties of the CCD devices: the entire accumulated frame on the CCD may be parallel-shifted very rapidly towards the serial register (see section 2.2.3). This shift operation occurs exactly simultaneously for all pixels and is in a certain sense equivalent to a motion of the detector with respect to the telescope. We use these characteristics for the shuttering process in the following way (a general explanation of the CCD readout technique was presented in sections 2.2.3 and 3.1.3):

1. The mechanical shutter is closed and the CCD continuously reads out (without digitizing the output charge) to clear it from residual charges.
2. The shutter is opened while the CCD is still kept in the clearing mode which means that the frame is continuously parallel-shifted.
3. After about 10 to 20 parallel shifts the CCD readout is stopped and the image integration on the "non-moving" detector starts.
4. At the end of the exposure, fast readout (skipping the pixels at the output) is again started with the shutter still open.
5. The shutter is closed after 10 to 20 parallel shifts.
6. After some further shifts allowing the shutter to close completely a normal readout of the frame (or subframe) is initiated.

The effect of this procedure is illustrated in Figure 4.13. Each object, intrinsically moving or not, is accompanied at either end by faint trails in the CCD parallel direction. The ratio of the mean intensity in the trails to the mean intensity in the

main object pixels is given by the ratio of their corresponding integration times. Our current CCD electronics takes about 0.8 milliseconds to perform a parallel transfer but this could be speeded up considerably in a future controller design (current "trail to object" ratios lie in the range of 10^{-2} to 10^{-3}). The method imposes a slight restriction on the CCD orientation for moving objects in the sense that the object movement should not exactly coincide with the parallel readout direction otherwise the trails would be inside the object image. We should also mention that 20 to 40 rows (two times 10 to 20) at the top of the frame are lost (which is of no importance in most cases).

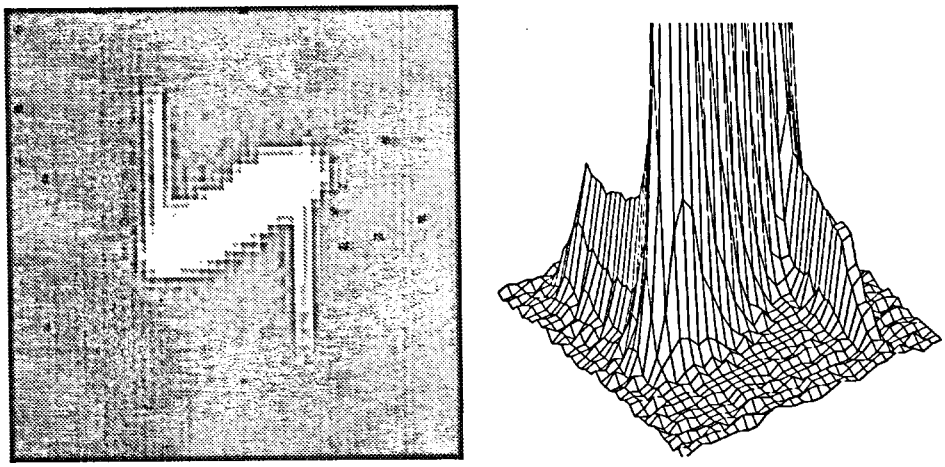

(a) (b)

Figure 4.13: Shuttering technique. All objects are accompanied at either end by faint trails in the CCD parallel direction (see text). A 0.1 s exposure of a bright object moving from left to right is shown in (a) (the serial register is at the top). The profile of this image is given in (b). Note the difference in brightness for the trails and the main part of the profile which would reach a height of 50 cm on this scale!

This technique was implemented by modifying the camera controller electronics which now permits a number of parallel shifts after the shutter is opened and before the shutter closes. In order to register the epochs, electronic outputs of certain CCD control signals had to be provided. These signals may be related precisely to the events of interest e.g. the stop and start of the parallel shifts. The epochs are actually registered by means of an event timer which is synchronized with the station master clock and has a resolution of 0.1 μs. Thanks to the fact that the synchronization error of the master clock with respect to UTC is

always known to within 1 μs in real time (to within 0.1μs a posteriori) the CCD exposures are time tagged with sufficient accuracy.

There remains the question of how to handle the trails in the centroiding algorithm. In the case of the moment technique they have to be left out by setting the threshold in the object recognition step to a sufficiently high level. This has to be done because the length of the trails is defined by the mechanical shutter and therefore is not precisely known! Fitting algorithms on the other hand must include a model of the trails (and clip them!) if they are bright compared to the main part of the object image. We would like to avoid this complicated technique by increasing the parallel clock rate of the CCD controller in the future.

Chapter 5

The Experimental Setup

5.1 Hardware

The performance of the CCD camera system was first tested in a controlled laboratory environment; after that all observations were performed at the Zimmerwald observatory. The observatory houses three telescopes in two domes: In the older part a 0.6 m $f/21$ Cassegrain and a 0.4/0.6 m f1/2.6 Schmidt telescope share a common tube on an equatorial mount. This system is primarily used for sky survey work with the Schmidt camera (supernova search using a photographic technique) whereas the Cassegrain instrument serves as a guiding telescope. There is no computer control, no angular encoders; the pointing (using setting circles) as well as the fine guidance (using an illuminated reticle at the Cassegrain) are done manually. A 0.5 m $f/2$ Cassegrain telescope is situated in the second dome. Mounted on a fully computer controlled alt-azimuth drive system it is part of the Zimmerwald satellite laser ranging (SLR) system. Although the optical quality of this telescope is modest (especially if compared with the 0.6 m Cassegrain) and its plate scale (4".1 per pixel) is far from ideal, all CCD observations were performed at this instrument. Obviously the computer control and the infrastructure (like the timing subsystem) available at the SLR station favoured this decision. Fortunately a new combined SLR and optical astrometry telescope, called ZIMLAT, is under development and will replace the 0.5 m SLR instrument in late 1995. The new 1 m telescope will have optimized optics for astrometric applications as well as a dedicated SLR Coudé path (see section 5.1.4). Sharing of telescope time is planned in the sense that 25% to 30% of the total time is allocated for astrometry (essentially all nights) whereas the daytime will be used for SLR observations. As we will use the 0.6 m Cassegrain in the "old" dome only very sporadically (e.g. for atmospheric turbulence studies at high magnification) we focus the following description on the existing SLR and the new ZIMLAT Telescope.

5.1.1 The experimental setup at Zimmerwald

Figure 5.1 gives an overview over the hardware components of the tracking and data acquisition system used for astrometric CCD observations (SLR telescope). The entire system operation is controlled by a microVax II station computer. The latter controls the telescope mount through a CAMAC interface system. This interface is also used for all time critical operations (like the precise epoch registration using event timers) and for data acquisition. The CCD camera subsystem consisting of the camera head located at the prime focus of the telescope, a liquid circulation refrigeration unit, camera controller electronics, and a camera control computer is connected to the station computer by a local area network (Ethernet) and an additional serial link. A router and a modem in combination with a 64 Kb leased line to the university network provide access to and from the computers in Berne as well as to the Internet. (The Astronomical Institute of the University of Berne is located in the city of Berne, about 15 km from Zimmerwald.) Last but not least we have access to the time keeping and intercomparison subsystem of the SLR station which guarantees an on-line epoch accuracy of 1 μs with respect to UTC or about 0.1 μs a few days after the observation (using time comparisons routinely performed in collaboration with the National Bureau of Metrology).

General data acquisition and control

A variety of data acquisition and control facilities are provided via the CAMAC interface system. This flexible system consists of a series of modules in a crate, each representing an interface with a specialized function. The CAMAC is connected to the station computer by a parallel type interface. The access is register oriented and the resulting read/write cycle time of the order of 1 μs. This rate is rather modest but the advantage of the system resides in the individual modules' capability to deal with a good part of the real time tasks. In connection with CCD astrometry the following tasks are related to CAMAC modules:

- Epoch registration
  An event timer module is used for precise epoch registration. Signals corresponding to the start and end times of the CCD exposures are output by the camera control electronics and fed into two separate inputs of the event timer. These signals are actually generated from the command signal sent to the mechanical shutter of the camera which itself is strictly related to the stop and start of the CCD parallel clock signals (for a description of the shuttering technique we refer to section 4.2). The computer detects an event either by sampling the module or by an interrupt generated by the module. The event timer's time base consists of a 10 MHz signal derived

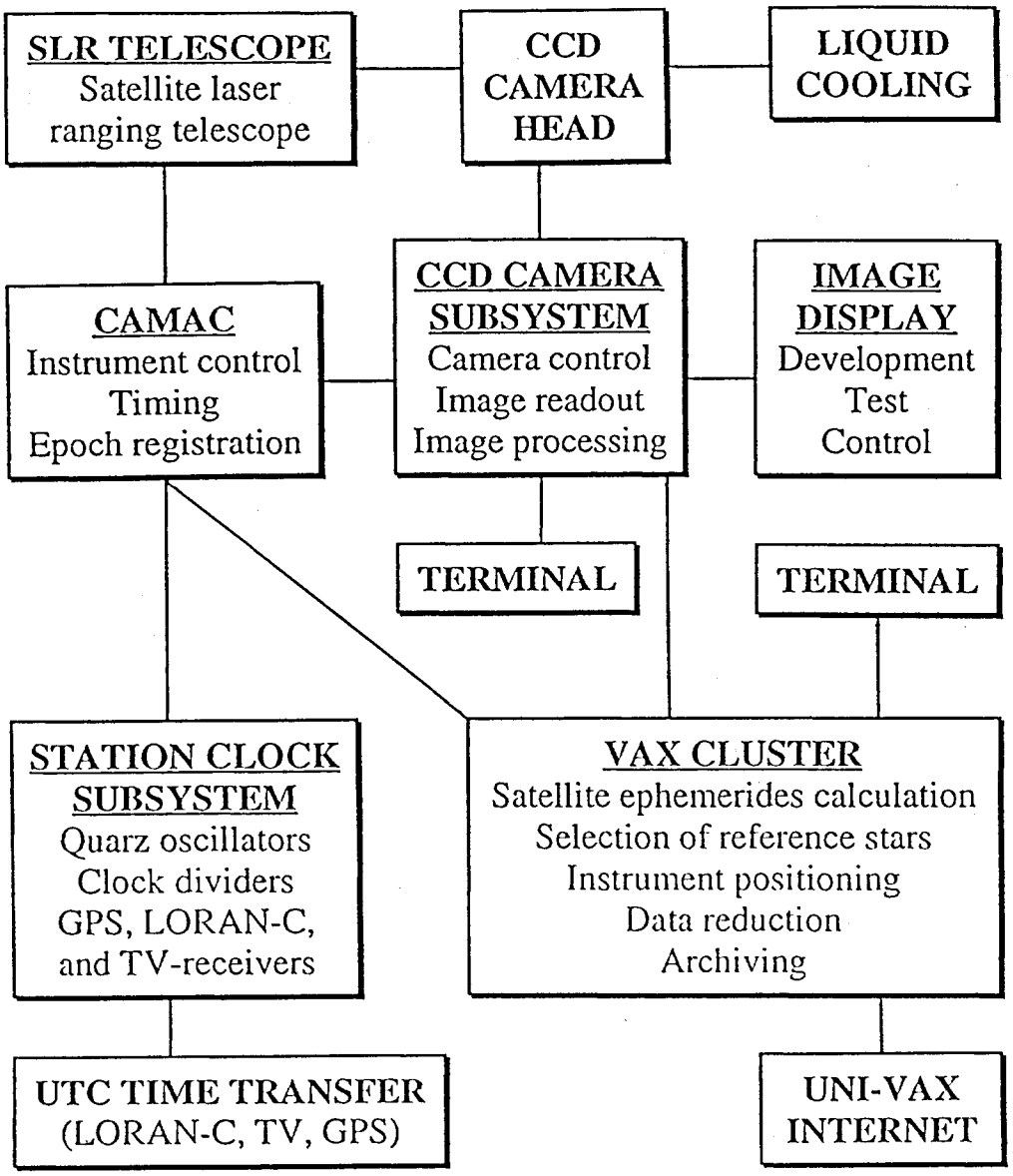

Figure 5.1: The experimental setup at Zimmerwald in overview.

from the station frequency base and a 1 PPS from the station clock. This allows registration of the fractional part of the epoch (fractions of one second actually) with a resolution of 0.1 μs. As the module is synchronized with the station master clock through the 1 PPS signal, the resulting epoch accuracy (expressed in UTC) is primarily given by the synchronization of the station clock to UTC. The more significant part of the epoch (from years to 10 ms) is provided by a CAMAC clock module (strictly slaved to the master clock). (The overlap between the "coarse" and the "fine" epoch registration is intentional to rule out ambiguities.)

- Telescope control
  The control of the telescope is performed through digital to analogue converters generating the reference voltages for the servo amplifiers and the counter modules registering the signals of the angular encoders. A good part of the tracking loop is implemented by software running on the station computer. The main data acquisition and telescope tracking program is therefore implemented as a collection of asynchronous tasks (each activated by its corresponding interrupt source). The fundamental tracking cycle is triggered by a 10 Hz signal from the station clock (via a CAMAC system interrupt).

The station computer is also directly connected with several smaller data logging systems (through direct serial links or serial bus systems). Let us mention in particular a meteo sensor package providing pressure, temperature and humidity with an accuracy of 0.1 mb, 1° C and 5%, respectively (these values are regularly calibrated; the location of the sensors, however, is always problematic; at present they are fixed on a mast about 6 m above the ground).

The station clock subsystem

The primary frequency base of the station time keeping system is a set of two essentially freely running high quality BVA quartz oscillators. They are not running completely free as their frequency drift caused by aging is compensated once per day by a variable frequency adjust voltage which is in turn controlled by the station computer. This control loop is, however, not closed in order to slave the oscillators to an external reference (e.g. defined by the time comparison measurement). Its purpose is to maintain the frequency offset to within certain limits ($1 \cdot 10^{-10}$). The frequency output of one of the two oscillators drives the primary station clock; the second serves as an independent control and backup unit (having its own 1 PPS divider). The initial synchronization of the master clock must be bootstrapped by several time systems: 1) the coarse epoch with an accuracy on the order of one millisecond is given by a long-wave HBG radio time signal receiver, 2) the precise epoch is then set by synchronizing the master clock with a

1 PPS signal from a LORAN-C navigation receiver (appropriately delayed for the signal travel time) resulting in an accuracy of one to two microseconds or by synchronizing with a 1 PPS GPS time signal produced by a geodetic GPS receiver. In the latter case the initial synchronization with respect to UTC is below 1 μs. This synchronization step is performed on rare occasions only (mainly after power failures which again occur very infrequently due to the battery buffered power supply system). The 1 PPS output signals from the master clock, the second oscillator, the LORAN receiver, and the GPS receiver are regularly (at least once per hour) compared by means of time interval counters and the results are stored in data logger systems. In addition, the master clock output is measured with respect to a certain TV signal pulse allowing a posteriori time intercomparison (using the so called TV intercomparison method) with the National Bureau of Metrology which keeps the Swiss UTC. The actual epoch of an event is eventually derived from the master clock reading by adding a correction given by the measurements "master clock - GPS" for the "real time" values and by adding corrections from the TV intercomparison for the a posteriori value. "Real time" epochs are usually good to within a few tenths of a microsecond (depending on the quality of the GPS measurements) and the a posteriori corrected epochs (available after one week) have an accuracy of about 50 ns.

5.1.2 The CCD camera subsystem

The camera subsystem consists of a commercially available Photometrics camera including the head electronics, a VME controller board, and a customer designed control computer. Figure 5.2 gives an overview of the system; main characteristics are given in Table 5.1 (for the quantum efficiency of the PM512 we refer to Figure 2.2).

The main element of the CE200 camera head is a front side illuminated PM512 chip which is cooled to -45° C by a Peltier element. Secondary cooling of the thermoelectric element is performed by a liquid circulation unit with a simple heat exchanger (there is no active cooling of the liquid but a simple fan supported radiator). As the CCD is placed at the prime focus of the SLR telescope care had to be taken to avoid thermally-induced turbulence caused by the excess heat of the camera head.

Apart from a video preamplifier and a differential line driver which are also placed in the camera head, all control electronics are located in the CE200 camera electronics unit. This unit is responsible for the generation of the clock signals (their shapes and amplitudes are determined by CCD-specific analogue boards), for the analogue to digital conversion of the video signal, as well as for the stabilization of the CCD chip temperature, and for the driving of the mechanical shutter.

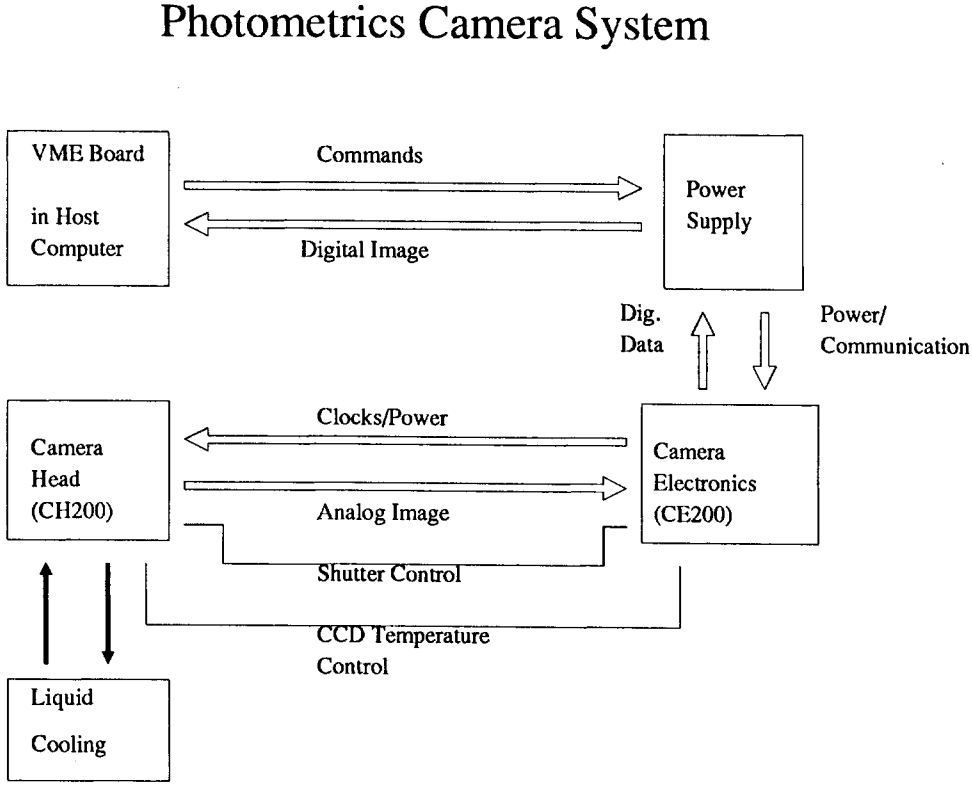

Figure 5.2: Block diagram of the CCD camera subsystem.

Specifications of the Photometrics CCD camera system	
Camera head/electronics	
Type	Photometrics CH200 / CE200
Readout rate	50 kHz
Dynamic range	14 bit
System noise	5 electrons
CCD temperature	-45°
Cooling	thermoelectric, secondary liquid cooling
Controller/host	Photometrics VME bus controller VME 68040 host running OS-9
CCD	
Type	Photometrics PM512, front side
Size	512 x 512 pixel
Pixel size	20 x 20 μm pixel
QE max.	0.6
Dark current	0.14 $e^{-}s^{-1}pixel^{-1}$
Full well capacity	133 ke^{-}

Table 5.1: Specifications of the Photometrics CCD camera system.

The actual sequencer for the clock signals and the master signals for the ADC board is located on the VME bus controller board. Apart from the timing sequences for the individual serial shift operations (and the timing for the double correlated sampling integrator) which are ROM based and locally generated in the CE200, all remaining control and clock signals are generated by the microcontroller on this board. The CE200 may be located far from the controller because all signals are transmitted by differential lines (image data is transmitted on a synchronous differential serial line). There is no local image memory on the controller and consequently all image data must be transferred into the memory of the host computer. This transfer takes place during the CCD readout process by means of a DMA controller on the VME interface card.

The programming of the controller is register oriented. All readout parameters like the camera gain, the CCD clock timing parameters, and the (sub-) frame definitions have to be stored in a series of registers. In addition, the DMA controller chip must be programmed before any CCD readout command is issued. The readout process may either be interrupt driven or controlled by polling the DMA interface from the host CPU.

The camera control computer hosting the VME controller board is a VME based modular system consisting of the following components:

- 25 MHz 68040 CPU board (EUROCOM-7) with 16 MB dual ported onboard RAM, embedded Ethernet and VME bus controller, 4 serial and 1 parallel interfaces.
- 2x520 MB SCSI hard disks, 40 MB hard disk, 5.25" floppy disk.
- 8MB RAM extension on a VME board.
- Video interface card with 512 KB video RAM, b/w video generator and an additional (unused) video frame grabber module.
- General purpose 32 line parallel interface including pulse generators and very flexible handshake lines.

5.1.3 The 0.5 m satellite laser ranging (SLR) telescope

This instrument was built for the purpose of satellite laser ranging (SLR). Consequently the optical design was optimized to project all light collected from a small solid angle (a few arcminutes) in the center of the field of view of the telescope onto the cathode of a photomultiplier at the Cassegrain focus. The secondary mirror is a lens with a coating on the side facing the primary mirror reflecting all light in a spectral band centered at the laser wavelength (562 nm, green) and

about 50 nm wide. The remaining part of the light passes through this lens. Together with an additional two lenses they form a field corrector for the prime focus where the CCD camera head is located. (For the laser observations the CCD is usually replaced by an intensified silicon target (ISIT) TV camera for tracking purposes.) As a consequence of this special setup we have to live with two disadvantages: a) the instrument can not be used for precise photometric work due to the imperfect knowledge and the rather complicated (side-lobes) characteristics of the "secondary mirror filter"; b) the imaging quality of the instrument is moderate, especially the large coma in the outer 50% of the field (7′ from the center to the edges) compromises the centroiding significantly (see Figure 6.4). In addition, the mount is not well suited for precise tracking (tracking accuracy is only a few arcseconds) and for very slow tracking (e.g. sidereal) due to the limited resolution of the encoders and serious backlash in the drives. Table 5.2 summarizes the main characteristics of the instrument.

Specifications of the 0.5 m SLR telescope	
Telescope	
Type	Cassegrain
Aperture	0.52 m
Prime focus	
$f/2$	50′ FOV; TV tracking camera
	35′ FOV used for CCD astrometry
Overall transmittance	≤ 0.5
Mount	
Type	alt-azimuth
Max. slew rate	$8° \, s^{-1}$
Max. acceleration	$8° \, s^{-2}$

Table 5.2: Specifications of the 0.5 m SLR telescope.

5.1.4 The new 1 m combined laser ranging and astrometric (ZIMLAT) telescope

Recognizing the limitations of the current SLR telescope (not only for astrometry but also for laser ranging) the design of a new combined instrument was initiated in 1990. The design phase is almost complete and manufacturing will start at the

end of 1994. The instrument will be a Ritchey-Chrétien system on an alt-azimuth mount. All astrometric observations will be performed with cameras located on an instrumentation platform at the Nasmyth focus. There are four different detector stations on this platform which can be selected using a motorized rotating flat mirror (switching between detectors will be matter of seconds only!). Three different corrector/reducer optics on the platform provide a 1 m, a 4 m and an 8 m focus. The entire platform is mounted on a derotator device to correct the field rotation caused by the alt-azimuth mount.

For the SLR measurements there is an additional Coudé path which is activated by sliding a dichroic beam splitter into the light path. (This beam splitter is located in the fork just in front of the passage through the bearing towards the Nasmyth focus.) The beam splitter is constructed to reflect the laser light (probably two wavelengths) into the Coudé path, whereas the remaining light from the telescope may be used in one of the detectors at the Nasmyth focus for guiding. In addition, this set up allows for simultaneous SLR and astrometric observations (e.g. of a laser satellite) while still preserving an "unobstructed" high quality (from both, the astrometric and the photometric point of view) focus.

The optical and major part of the mechanical design were driven by the demanding astrometric applications. Special emphasis was put on:

- image quality of the $f/4$ and $f/8$ foci (symmetric point spread function, in particular);
- athermalization of the main optics (to avoid significant changes in the focal length during single close encounters);
- thermal insulation and/or ventilation of the tube (the instrument will be used for SLR operations during daytime and may therefore not be kept at the expected night time temperature).

A summary of the specifications is given in Tables 5.3 and 5.4.

5.2 Software

The project is based on a large variety of different software components. In contrast to classical astrometric observations every step from the preparation of the observing session (scheduling), to the actual data acquisition, further to the data reduction, and to the processing relies on computer support. A detailed discussion of all the components is beyond the scope of this work. We give an outline of the general concepts only. The main tasks are:

Design specifications of the ZIMLAT telescope	
Telescope	
Type	Richey–Crétien
Aperture	1.0 m
Focal length	10.3 m
Field of view	40′ (without vignetting)
Primary	$f/1.95$
Secondary	0.33 m; $f/2.3$
Coudé path	for SLR operations
Nasmyth platform	
$f/1.2$	45′ FOV; TV tracking camera
$f/4$	13′ FOV; CCD astrometry
$f/4$	45′ FOV; CCD astrometry
$f/8$	FOV tbd; general use
Mount	
Type	alt-azimuth (fork)
Max. slew rate	azi: $30^\circ\,s^{-1}$ ele: $15^\circ\,s^{-1}$
Max. acceleration	azi: $6^\circ\,s^{-2}$ ele: $5^\circ\,s^{-2}$

Table 5.3: Specifications of the ZIMLAT telescope.

ZIMLAT — Optical performance		
	TV camera	CCD astrometry[1]
Focal length	1.22 m	4.0 m
Field of view	45′	13′
Vignetting	0 % at ±12′	0 %
	5 % at ±15′	
	30 % at ±22.5	
Spectral range	400 – 640 nm	450 – 900 nm
Distorsion (at edge)	2.8 %	0.29 %
Overall transmittance	0.6	0.6
PSF at 80 %		
without DBS[2]	42 μm at ±0.0	6.3 μm at ±0.0
	108 μm at ±22.5	7.6 μm at ±6.5
with DBS	58 μm at ±0.0	14.0 μm at ±0.0
	105 μm at ±22.5	13.8 μm at ±6.5

[1]The $f/4$, 45′ has similar characteristics over the entire field of view but the design of the reducer optics is not yet complete (same for the $f/8$).

[2]DBS: Dichroic beam splitter.

Table 5.4: ZIMLAT — optical performance.

Predictions/scheduling

- Computation of ephemerides (orbit integration),
- Determination of visible (satellite) passes,
- Identification and selection of close encounters with (catalogue) reference stars using the predicted orbits for the moving objects,
- Preparation of input data for the tracking and data acquisition components (ephemerides, subframe definition for close encounters, camera control parameters, etc.).

Observation

- Telescope control (tracking),
- Image data acquisition (camera control, exposure timing),
- Epoch registration,
- On-line data processing (object search, centroiding, improvement of camera control parameters, and subframe definitions).

Data processing

- CCD (raw) data reduction (bias, dark, flat field correction),
- Off-line object recognition and centroiding,
- Astrometric reduction (assessment of transformation parameters from calibration and program frames; determination of program object positions),
- Orbit determination and/or improvement for the moving objects,
- Image, instrument and object data archiving (e.g. position and orbit data base).

Simulation and tests

- Simulation of object images for moving and non-moving objects,
- Test of centroiding algorithms,
- Interactive image processing,

- Visualization and comparison of results.

A variety of criteria like the amount of data, the required processing (CPU) time, real-time or off line applications etc. influence the actual implementation. We tried, of course, to use (or adapt) existing software modules. This was possible for part of the prediction and telescope control where we could take advantage of the existing SLR software. For the interactive image visualization (not for the object recognition and centroiding!) and for some minor tests we use the ESO-MIDAS (ESO-MIDAS 1993) image display and processing package.

An overview over the hardware platforms currently used for this project (including the operating systems) may be found in Figure 5.3. The tasks run on the following platforms:

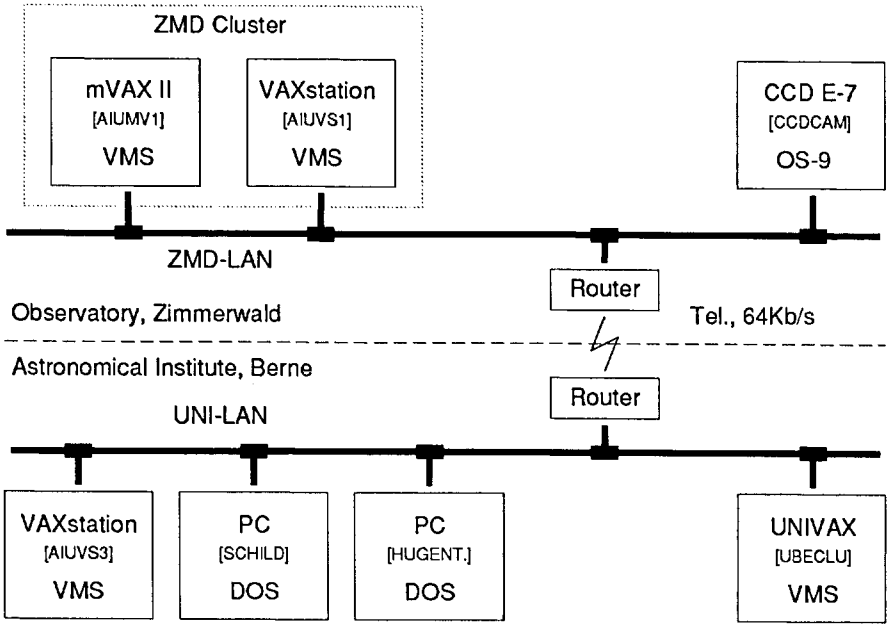

Figure 5.3: The computer resources in overview.

Orbit prediction	UNIVAX-Cluster (AIUVS3)
Input data for real time components	ZMD-Cluster
Telescope control epoch registration	AIUMV1
Image data acquisition	CCDCAM

Real-time image processing (centroiding)	CCDCAM
Astrometric reduction/orbit improvement	PC or AIUVS3
Interactive image processing (MIDAS)	AIUVS3 (ZMD-Cluster)
Simulations	UNIVAX-Cluster

5.2.1 Real-time components

The main design problem concerned the modularization of the real time components and the selection of the appropriate hardware platforms. Primary restrictions came from the telescope control (tracking loop) and from the epoch registration; both tasks have to be executed on the microVAX II (due to the CAMAC interface). The necessary accuracy for the exposure timing of the order of 1 to 10 ms also has to be considered. Two "master-slave" designs are feasible:

(a) The station computer (microVAX II) controls the real time operations as the master and operates the CCD camera (through the camera control computer) as an intelligent data acquisition subsystem (slave).

(b) The camera computer acts as the master and utilizes the station computer in a slave mode to control the telescope and to register the epoch data.

Both approaches have their advantages. While mode (a) may fully explore the existing design of the SLR real-time components (b) is more flexible in the sense that the camera may be operated independently from the station computer in cases where active telescope control and epoch registration is not required (e.g. for pure astronomical observations or laboratory experiments). We therefore modularized the system and designed the interfaces between the components in a way to allow both modes of operation!

The camera control computer performs several tasks in parallel. These tasks communicate with each other through high speed (Unix-like) pipes and share the image plus some house keeping data in common data blocks. All the inter-process communication in the pipes uses a simple protocol including the destination and the sender address as well as a data descriptor field (type and length of data packet). The design is not only modular and simple with well defined interfaces, but it allows an optimized resource sharing (the image processing module may e.g. perform the centroiding on the last frame while the data acquisition module is waiting for the exposure of the current frame to end). Figure 5.4 gives an overview of the camera software packages. The five principal modules perform the following tasks:

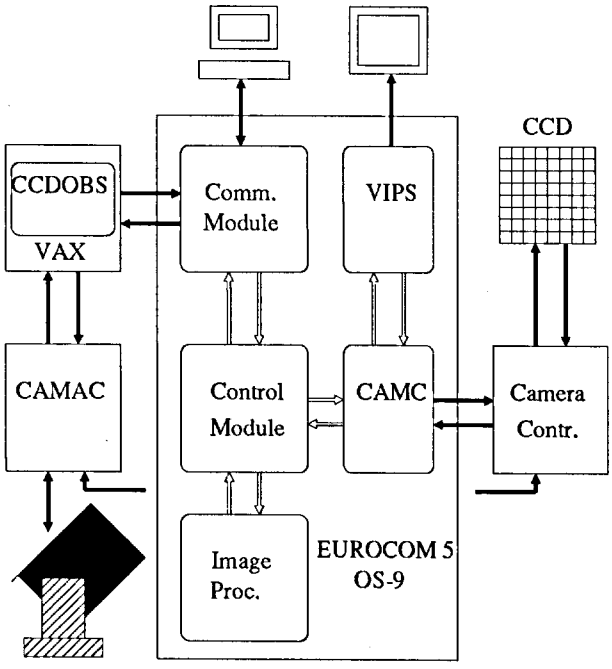

Figure 5.4: Camera software package.

Communication module — Controls the data flow between the local user terminal, the remote host (station computer) and the control module. In the mode (b) this module is responsible for the interactive menu-driven user interface whereas in mode (a) it is displaying status information on the console device.

Control module — Central module, responsible for the sequencing, maintains the image data base.

Image processing module — Performs the on-line object recognition and centroiding.

CAMC — Image data acquisition module, communicates with the camera controller board, controls the direct memory data transfers (DMA) and services controller interrupts.

VIPS — Displays the images, may perform some basic image processing in the image display memory.

Apart from the last two modules (which are modified versions of components delivered by the vendor of the integrated camera system) the entire software system had to be developed in the framework of this thesis. Special emphasis was put on the flexible menu driven user interface (when operated in mode (b)). It is in particular possible to acquire series of images in a manual mode. The program is e.g. able to manage the acquisition, processing, and archiving of the data stemming from an entire satellite pass. Therefore it has to handle (in hierarchical order) several subframes per frame, a series of frames per close encounter, and a number of blocks, each consisting of one close encounter series, per pass.

The module CCDOBS on the station computer is currently used in the slave mode (b) only. It consists actually of a number of interrupt routines (running partly asynchronously) servicing requests from the camera computer and the CAMAC modules (event counter) as well as running the telescope tracking loop. Although the camera software is able to operate in the slave mode (a) the corresponding master module on the station computer could not yet be completed.

Special attention had to be paid to the 10 ms accuracy required for the exposure timing. The fact that the exposures may be initiated by software only (the camera controller has no external trigger input) complicates the problem. As the station master clock and thus the UTC epoch is available from the station computer only, we had two options: either to trigger an interrupt routine in the camera computer by the station computer (via the communication link) or to synchronize the camera computer clock regularly and to let the latter perform the actual observation sequencing autonomously (according to preloaded information). We implemented the second option, again to allow for maximum flexibility. The real-time clock of the camera computer is synchronized every few hours (during observation periods) by means of a 1 PPS signal from the station clock; the coarse epoch is information requested through the station computer. Obviously all internal delays (including software delays e.g. the time needed by the interrupt routine to trigger the exposure) have to be calibrated carefully. The crucial point is not the calibration, however, but a characteristic of all multitasking operating systems: the CPU time is allotted to different processes in small portions ("slices") only. Consequently all processes, except interrupt routines with high priority, may be suspended for several time slice intervals (depending on the actual number of concurrent processes). Setting one time slice to 20 ms (shorter intervals would severely degrade the performance) and because 5 processes are running concurrently, the software delays for these processes will have a worst case jitter (peak to peak) of 100 ms. Unfortunately the exposure triggering currently used is not fully interrupt driven and therefore suffers from this problem (which may be tolerated for objects with angular velocities up to about $500'' s^{-1}$).

Chapter 6

Observations

6.1 Calibration of the mapping geometry

We will first discuss the full (off-line) calibration of the mapping geometry. This determination of the mapping function is a crucial aspect of every astrometric reduction. In our case this is even more critical than in classical astrometry because we have to perform dedicated calibration observations and must rely on them when reducing the measurements of the program objects.

6.1.1 Off-line calibrations

The observations were performed as described in section 3.2.2. Three series of ten consecutive observations were acquired with the telescope pointing at (azi,ele)=(93°,60°), (180°,60°) and (267°,60°). These pointing directions result in position angles $\beta = +60°, 0°, -60°$ for the apparent direction of movement of the stars with respect to the horizon (see Table 3.9). The actual observation epochs were carefully chosen in order to have a reference star crossing near the center of the field of view. Figures 6.1, 6.2 and 6.3 give, in the upper part, a superposition of ten observations in the mentioned directions. The images were produced by adding the ten frames and normalizing the result. It is not easy to interpret these images. In particular we should be aware of the fact that the relative locations of the stars in the sum are not the same as on the individual frames (e.g. an apparently very close pair of stars may well be separated by several arcminutes in reality).

The actual observations are performed automatically. In a first step the reference catalogue is searched for the next star passing the given earth fixed direction within a specified maximum angular distance. The corresponding epoch together with the known angular velocity and the directions of motion of the stars are then

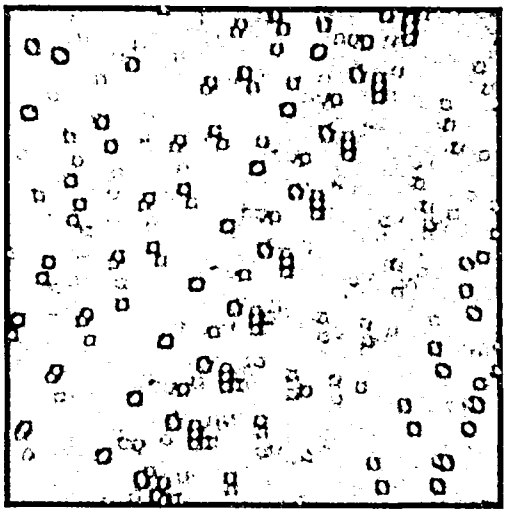

(a)

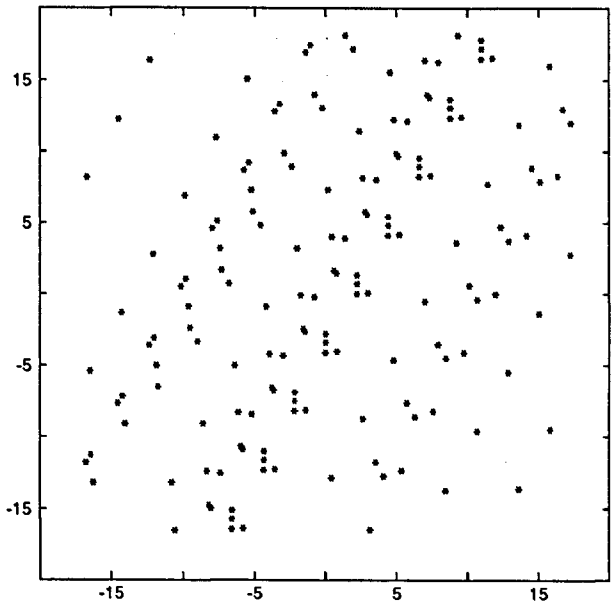

(b)

Figure 6.1: Calibration series at $\beta = 60°$ (azi=93°, ele=60°). (a) Superposition of 10 observations. (b) Positions of the (automatically selected) stars. The spacing between the exposures was 22 seconds (total 4 minutes). The frames were integrated for 1 second. The field size is 35′ x 35′. Zenith is up.

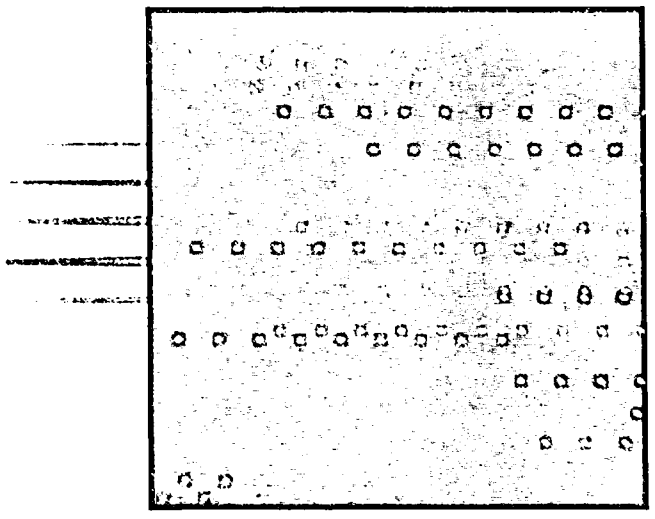

(a)

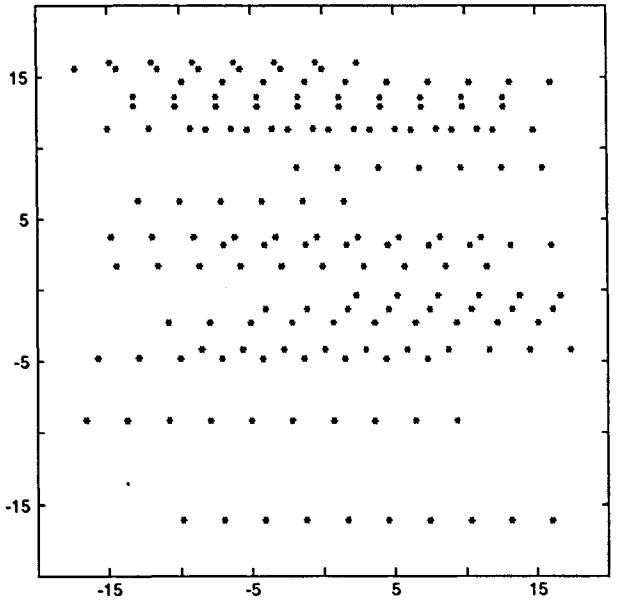

(b)

Figure 6.2: Calibration series at $\beta = 0°$ (azi=180°, ele=60°). (a) Superposition of 10 observations. (b) Positions of the (automatically selected) stars. The spacing between the exposures was 22 seconds (total 4 minutes). The frames were integrated for 1 second. The field size is 35′ x 35′. Zenith is up.

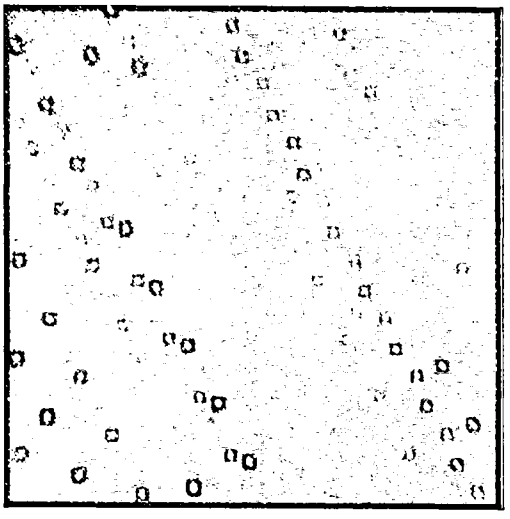

(a)

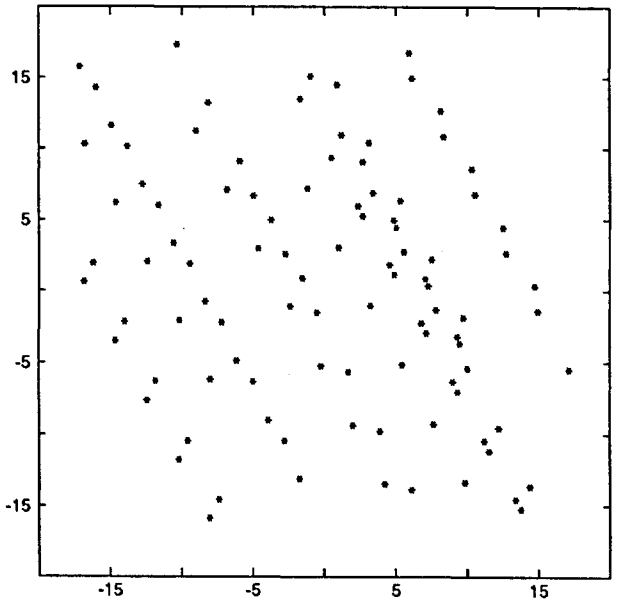

(b)

Figure 6.3: Calibration series at $\beta = -60°$ (azi=267°, ele=60°). (a) Superposition of 10 observations. (b) Positions of the (automatically selected) stars. The spacing between the exposures was 22 seconds (total 4 minutes). The frames were integrated for 1 second. The field size is 35′ x 35′. Zenith is up.

used to define the sequence of the exposures in such a way that the reference star exactly crosses the field of view during the ten exposures. The integration time for the individual frames is set to about one pixel crossing time. Short exposures make the centroiding easier (the images are barely elongated) while the overall quality of the measurement is not compromised due to the large number of relatively bright objects. All exposure data are downloaded to the camera, where the observation sequence is executed automatically.

The first task following the image acquisition consists of the object recognition including the identification of the corresponding images of the same star on the sequence of frames of a series. We use the following procedure:

(a) Frame number 1 is successively scanned for the n_1 brightest objects as outlined in section 4.1.2 (n_1 may well be of the order of 50 or even larger!). Cosmic ray event rejection as well as a coarse screening of the objects according to their characteristics takes place during this step. Unexpectedly elongated images may indicate a pair of (or several) unresolved point sources. Extended sources like galaxies will also result in unusual object characteristics. In our case the rejection algorithm is often invoked by the prominent coma features of bright objects in the outer part of the field of view (see below).

At the same time the centroids of the detected objects are determined as discussed in section 4.1.3.

(b) Starting from (1) approximate values for the telescope position (using the angular encoder readings and the a priori mount model), (2) the orientation ω of the CCD camera (user input; camera is usually fixed at 0°) and (3) the registered observation epochs, a transformation between the first and the second frame is established. This transformation allows prediction of the positions on the second frame for the objects already recognized.

(c) The second frame is scanned for the brightest objects in the same way as the first. The resulting list of positions is then correlated with the list of predictions from the previous frame. (It is also possible to directly search the objects according to the list of predicted positions.) Every unambiguously identified object is marked with a unique object number. With each new frame there may be objects having left the field of view and new ones entering it. The total number of objects is thus steadily increasing. Each object may have many (up to the number of frames) individual observations.

Steps (b) and (c) are repeated for all remaining frames of the series. The result is a list of n observed positions (CCD coordinates) of n_o objects ($n_o < n$). The celestial coordinates for all objects (except for the reference star) are unknown. The exact pointing direction of the telescope (i.e. the earth fixed coordinates of

a reference point, e.g. the center of the CCD) is not known as well. After having gone through the same procedure for all pointing directions of the calibration session, the data is transferred from the camera computer (where all the previous tasks were executed) to a more powerful Vax workstation for the astrometric reduction.

The detailed model for the astrometric reduction (mapping function etc.) was given in section 3.2.2. Therefore we may proceed directly to the discussion of results. In a first step each series was evaluated separately; a scale factor and an orientation were solved for. The results are presented in Table 6.1. The positions of the brightest objects selected are given in the lower part of Figures 6.1, 6.2 and 6.3. The overall rms between 0.″24 and 0.″39 corresponds to the estimated accuracies from the centroiding step. It is also in agreement with the experience gained in independent centroiding experiments. Individual star positions (from 5 to 10 observations) show an accuracy of 0.″1 to 0.″2. The scales are determined to within about $1 \cdot 10^{-4}$ to $2 \cdot 10^{-4}$. A simple calculation may show the consistency of these scale and position results: the position uncertainty of 0.″2 divided by the diameter of the field of view of 2100″ yields a scale uncertainty of $9.5 \cdot 10^{-5}$ which matches the above value nicely.

The three scale parameters estimated show significant differences (maximum relative change of about $7 \cdot 10^{-4}$). Although the observations were performed within a time interval of about 10 minutes the scale changes may be attributed (at least partly) to temperature changes in the telescope structure. It is known for the SLR telescope that the relative change in effective focal length is about $2 \cdot 10^{-4}$ per degree centigrade. The values in Table 6.1 would imply an (unreasonable) temperature change of 3° C during the observation period. On the other hand a small temperature change slightly defocusses the telescope which again deforms the object images. Due to the pronounced coma in the outer parts of the field (see below), this defocussing process is not homogeneous. The net result may well be a scale bias. We did not yet systematically study this effect but given the strong aberrations of the SLR instrument we expect its impact on the scale to be more pronounced than the influence stemming from the focal length change.

The variations seen in the orientation parameter q, however, are considered normal and reflect the uncertainties in the adopted mount model.

The large optical aberrations of the 0.5 m SLR telescope are apparent in Figure 6.4. Several impacts on the centroiding and the mapping process have to be expected:

- The asymmetric point spread functions may produce magnitude dependent centroids. When using a moment centroiding algorithm with a magnitude proportional threshold, this dependence may be significantly reduced. We currently use this technique for all observations (including calibrations) except for very faint sources.

Calibration run — separate processing	
Pointing direction #1	
rms	0.″242
scale r_0	(4.16358 ± 0.00010) arcs s^{-1}
rotation q	$(1.3021 \pm 0.0014)°$
rms of star positions	0.″09 to 0.″11
Pointing direction #2	
rms	0.″386
scale r_0	(4.16652 ± 0.00021) arcs s^{-1}
rotation q	$(1.2965 \pm 0.0029)°$
rms of star positions	0.″17 to 0.″20
Pointing direction #3	
rms	0.″318
scale r_0	(4.16620 ± 0.00018) arcs s^{-1}
rotation q	$(1.2830 \pm 0.0024)°$
rms of star positions	0.″11 to 0.″17

Table 6.1: Calibration run — separate processing.

- The main consequence for the mapping process is a linear distortion and thus a change in the scale factor. The dependence of the coma on the focus is inherited by the scale parameter.
- Quadratic and higher order radial distortions terms are generated.

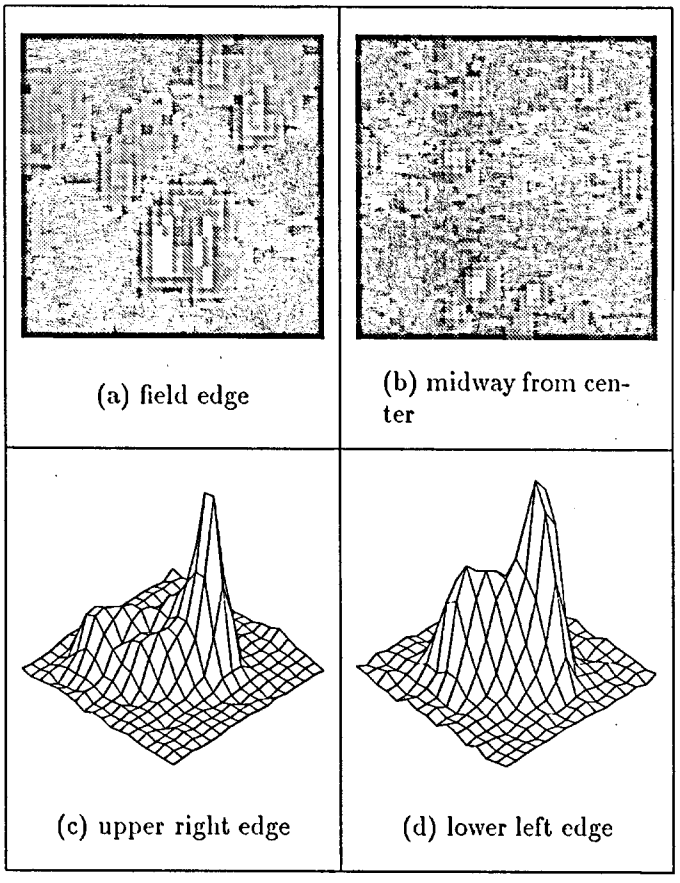

Figure 6.4: (a) An extreme example of coma (and additional aberrations) of a star image near the border of the field of the 0.5 m SLR telescope. (b) A subframe midway between field center and border. (c) and (d) Examples of point source profiles (measured point spread functions) from regions of strong aberration.

As the current mapping function does not take into account quadratic terms we analyzed the residuals of the calibration measurements for systematic radial components. The residuals were summed up in concentric annuli around the center of the field. The annuli were defined to cover the same area. The resulting radial components, shown in Figure 6.5, do not exhibit a systematic behaviour.

In a second step all observations were processed in a single adjustment where we solved for a common scale factor r_0 and individual orientation parameters q_i

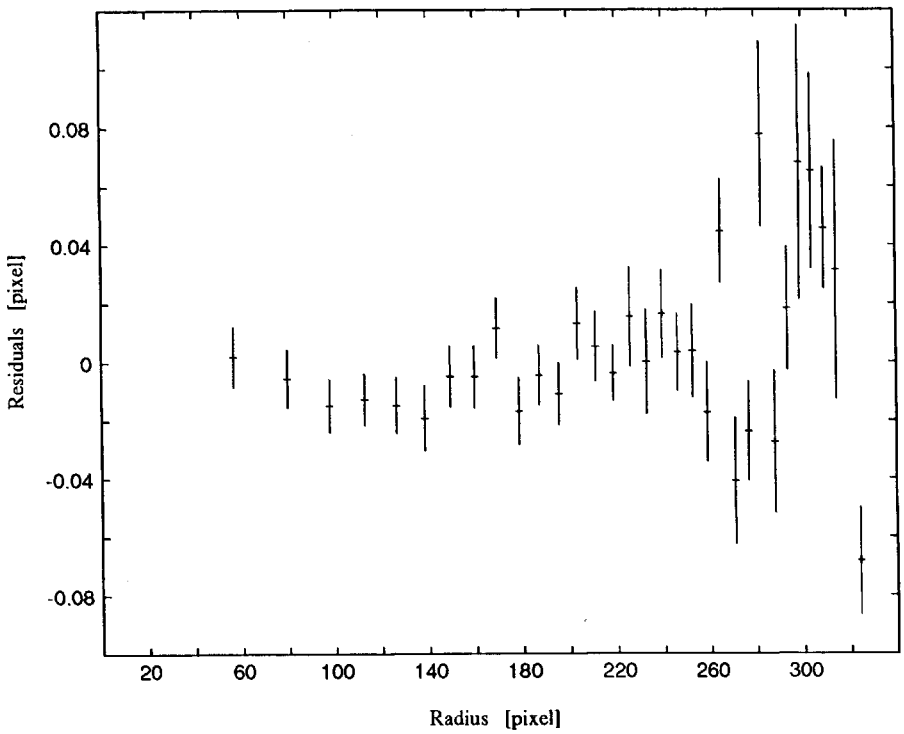

Figure 6.5: Radial components of the residuals of a calibration measurement as a function of the distance from the field center. The residuals were binned up in concentric annuli covering the same area (see text).

for each of the three pointing directions ($i = 1,2,3$). The results are given in Table 6.2. A total of 878 observations (CCD coordinates) was used to determine 222 parameters (the 4 mapping parameters r_0 and q_i, $i = 1,2,3$ for each field i; 6 coordinates of 3 pointing directions; 212 celestial coordinates of the 106 unknown stars). The overall rms of 0.″344 is slightly higher than the rms values from the separate processing of each pointing direction (Table 6.1). The reason must be sought in a real scale change during the observation period as described above. The common scale is determined to within about $1 \cdot 10^{-4}$. The orientation parameters did not change compared to the previous solution (their formal errors are slightly higher due to the higher rms error of the new solution).

Calibration run — adjusted for common scale	
rms	0.″344
scale r_0	(4.16510 ± 0.00010) arcs s^{-1}
rotation q	
field 1	$(1.3021 \pm 0.0020)°$
field 2	$(1.2965 \pm 0.0032)°$
field 3	$(1.2830 \pm 0.0033)°$
rms of star positions	0.″12 to 0.″18

Table 6.2: Calibration run — adjusted for common scale.

Table 6.3 lists the results of an adjustment where all mapping parameters (one infinitesimal rotation q for each direction, parameters r_1, r_2, r_3) were solved for. The observation data are identical with those underlying Table 6.2. The two components of the antisymmetric part of the transformation, r_1 and r_2, seem to be significantly different. This evidence is supported by the rms of this solution (0.″323) and by the lower formal error of the parameters r_1, r_2, r_3 compared to the common scale factor error of the former solution.

The difference between r_2 and r_1 might be attributed to a different scale along the CCD row and column directions. The fact that r_3 significantly differs from zero would further indicate a slight deviation from orthogonality. If the effect stems entirely from the CCD characteristics we would have to postulate that the CCD pixels are not perfectly quadratic. Their extension in x-direction would be about $5 \cdot 10^{-4}$ times smaller than in y-direction. This statement is somewhat inaccurate because actually we do not measure the pixel shape but only the deformation of the pixel grid.

Calibration run — all mapping parameters	
rms	0.″323
scale r_0 (fixed)	4.16510 arcs s^{-1}
rotation q	
field 1	$(1.3033 \pm 0.0026)°$
field 2	$(1.2755 \pm 0.0029)°$
field 3	$(1.3025 \pm 0.0029)°$
r_1	(-0.00014 ± 0.000037)
r_2	(0.00027 ± 0.000039)
r_3	(0.00036 ± 0.000031)
rms of star positions	0.″12 to 0.″16

Table 6.3: Calibration run — all mapping parameters.

Although, an inspection of the formal errors of the r_i seems to indicate that they are well determined, their values change significantly for different calibration sessions (the differences are much larger than the formal errors)! The conclusion was to inspect the model: In a first step we introduced tilt terms r_4 and r_5 (see equation 3.38). In some cases the determined values for these parameters (as well as the reduction of the rms) were barely significant, in others not. We then further refined the model and included terms taking into account deformations due to the imperfect optics (in section 3.2.2 this transformation was denoted by $\mathbf{O}_2$). The following expression was used to take care of radial (r_8, r_9) and objective decentering distortions (r_6, r_7):

$$\mathbf{O}_2 \begin{pmatrix} x \\ y \end{pmatrix} = \begin{pmatrix} r_6(x^2+y^2) + r_8(x^2+y^2)x \\ r_7(x^2+y^2) + r_9(x^2+y^2)y \end{pmatrix}. \tag{6.1}$$

None of these deformation parameters proved to be significant. It was therefore necessary to question the only remaining assumptions underlying the model, namely that the pointing direction of the telescope is earth fixed and that the movement of the stars is actually caused by the earth's rotation. The telescope drive motors were of course switched off during the measurements but there are no "active" brakes. In the absence of wind we would thus expect either a smooth motion of the pointing direction (stemming from thermal or bending effects, most likely in the zenith direction) or none at all. From a test where we fixed a com-

mon scale and orientation and solved for the pointing direction (in addition to the coordinates of all unknown stars) for each frame of a series we could immediately conclude that (see Figure 6.8): a) the spread of the values for the pointing direction is much larger than the determined formal errors and that b) the displacement of the pointing direction is not a simple function of time (the latter effect can not be seen from inspecting the figure). This result (b) is important because fixing a wrong common scale and (or) orientation would produce a systematic displacement of the pointing direction in right ascension. Obviously a movement of the (apparent!) pointing direction may have two causes which can not be separated (at least not in a single calibration series): a) the optical axis of the telescope (or the true pointing direction) is not stable with respect to an earth fixed frame, or b) the mean motion of the stars in the field ("mean" in the spatial sense, i.e. averaged over the field) is not entirely defined by the earth rotation but is also affected by e.g. atmospheric turbulence (or high frequency refraction anomalies).

6.1.2 Apparent pointing direction fluctuations

In order to get a deeper insight into the effect, we performed a calibration series (in one direction only) with different exposure times. The idea was to derive a spectrum for the fluctuations of the apparent pointing direction which could be compared with theoretical values for the spatially correlated part of the absolute image motion due to turbulence. An additional characterization of the effect could be drawn from a spectrum of the scale fluctuations. We selected two fields at the edge of χ Persei (an open cluster): one containing 11 to 13 relatively bright PPM reference stars and the other only one. (In order to avoid detector saturation it was necessary to select a field with faint stars, including unfortunately one reference star only, for the exposures with integration times longer than 1 s.) A total of 9 series with integration time ranging from 10 ms to 3 s was acquired. Each series consists of 14 to 15 individual 256 x 256 pixel frames (the gap between the frames, due to the readout, was approximately 3 s). The instrument was fixed (drive off) during the observations but repositioned between the series in order to observe the same star field. A summary of the observations may be found in Table 6.4.

The observations were processed in two modes:

(a) A scale (r_0), an orientation (q), the apparent pointing directions for each frame, and object coordinates for all unknown stars were determined for each series. For field 1 (series 1 to 6) the scale factors could be well determined from the known positions of the 11 to 13 PPM stars. The second field, however, containing one PPM star only had to be processed using as known the scale and orientation of the first frames of each series, i.e. these

	Calibrations with different exposure times								
	Field 1						Field 2		
Series	1	2	3	4	5	6	7	8	9
Exp. time [s]	0.01	0.05	0.1	0.2	0.5	0.8	1.0	1.5	3.0
# Eposures	15	15	15	15	15	14	15	15	15
# Stars	40	41	42	41	41	42	45	48	48
# Ref. Stars	11	12	13	12	12	13	1	1	1
# Obs.	355	436	424	435	438	386	515	519	444
N_{par1}	108	112	112	110	114	108	140	144	148
RMS_1	0".584	0".353	0".349	0".295	0".275	0".287	0".197	0".183	0".230
N_{par2}	80	84	84	82	86	82	110	114	118
RMS_2	0".580	0".354	0".349	0".299	0".274	0".286	0".198	0".187	0".233

Table 6.4: Calibrations with different exposure times. The number of parameters N_{pari} and the formal errors RMS_i correspond to two different processing modes. For an explanation we refer to the text.

parameters could be estimated with respect to the first frame only. (The a priori values were obtained in a separate step.)

(b) A common scale (r_0), an orientation (q) parameter per series, apparent pointing directions for each frame, and object coordinates for all unknown stars were determined for each series. In this case the common scale and orientation parameters for field 2 had to be fixed to a priori values.

The first processing scenario was supposed to reveal statistically significant displacements of the apparent pointing direction, scale and orientation, as well as potential residual systematic trends in the individual scale and orientation parameters. As a representative example we give the results of series 6. The determined scale parameters (relative to an a priori value) are shown in Figure 6.6. There is no significant trend and the values are normally distributed as can be seen from the error bars (formal 1-σ-errors). We conclude in particular that no refraction-induced ("air lenses") scale changes are seen at this accuracy level.

The corresponding orientation parameters can be found in Figure 6.7. Again, the results are consistent with a normal distribution. It is debatable whether the slight trend is significant, but it could not be identified in other series.

The apparent pointing directions, shown in Figure 6.8, exhibit a completely different behaviour! The large spread (as compared to the formal errors) indicates an intrinsic scatter of the apparent pointing direction. An even more pronounced example of this behaviour is given in Figure 6.9 where the results for series 3 are shown (shorter exposure time!).

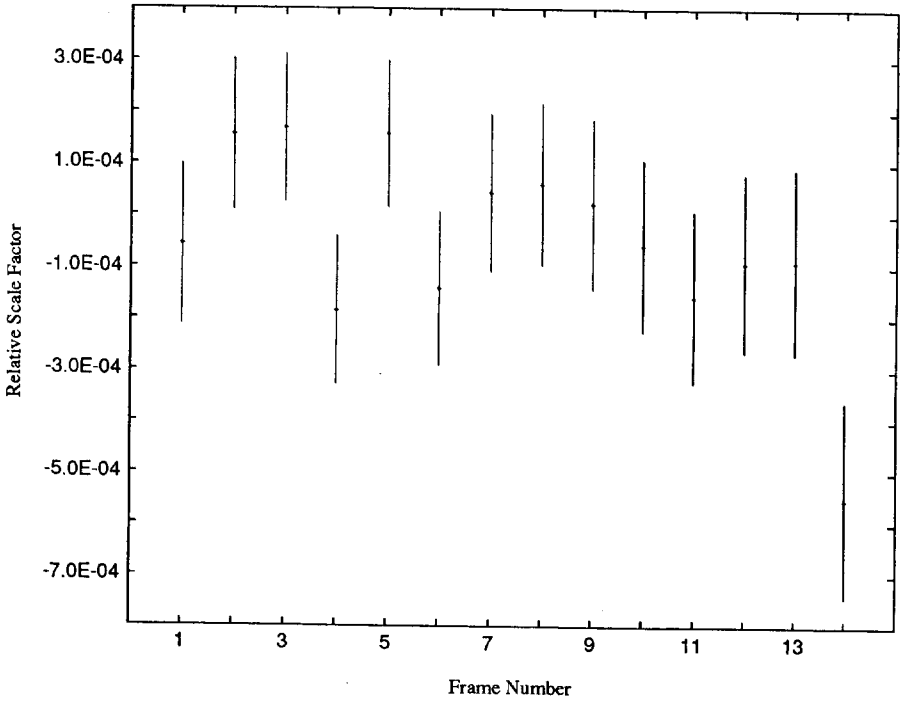

Figure 6.6: Scale factors of the individual frames of calibration series no 6 (Table 6.4). Scale factors relative to an a priori value are shown for the 14 individual frames of the series.

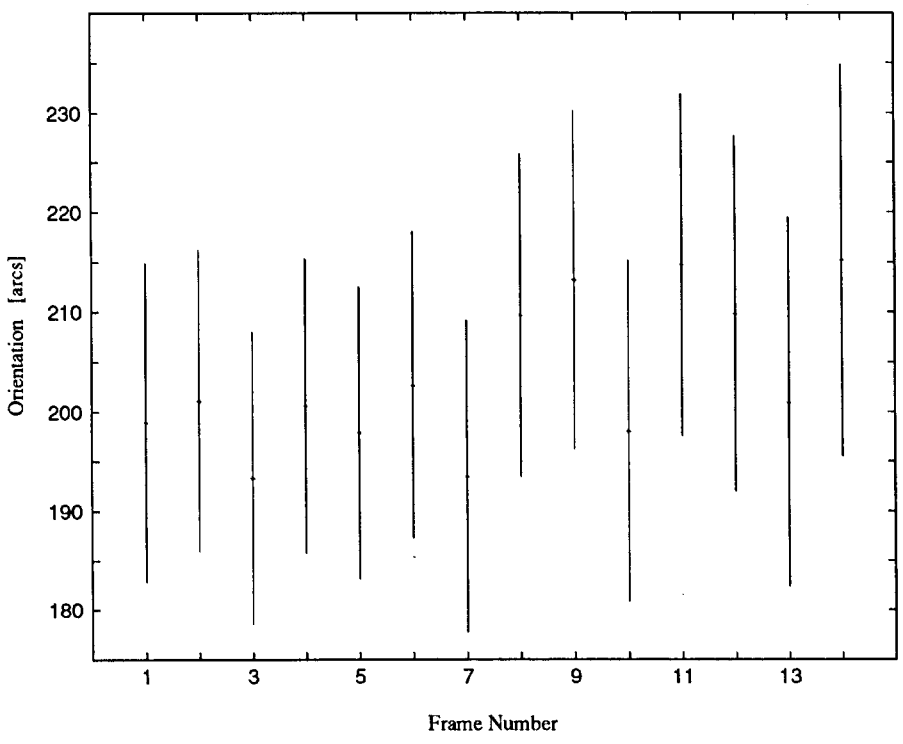

Figure 6.7: Orientation angles of the individual frames of calibration series no 6 (Table 6.4). Orientation angles relative to an a priori value are given for the 14 individual frames of the series.

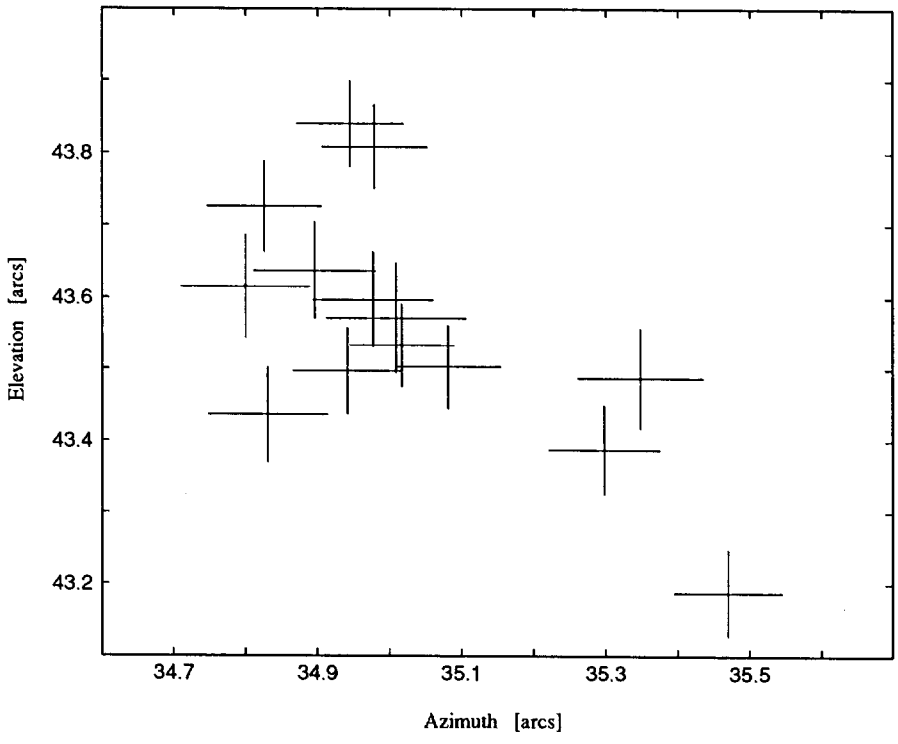

Figure 6.8: Apparent pointing directions of the individual frames of calibration series no 6 (Table 6.4). The crosses indicate the formal errors (1-σ) of the processing (the field is located at about 40° elevation; the origin was set arbitrarily).

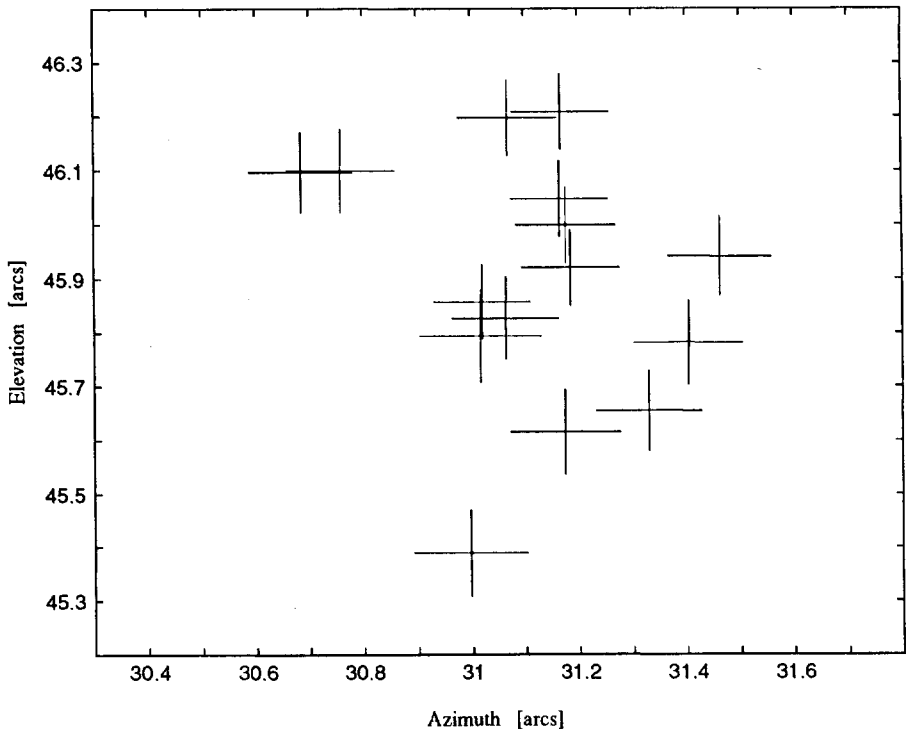

Figure 6.9: Apparent pointing directions of the individual frames of calibration series no 3 (Table 6.4). The crosses indicate the formal errors (1-σ) of the processing (the field is located at about 40° elevation; the origin was set arbitrarily).

In a second step we processed the entire data set in the mode b) where only one (common) parameter for the scale and the orientation were estimated. This was done to ensure that the determined pointing directions were not influenced by wrong scale or orientation parameters. We point out that the pointing direction and the scale parameters are strongly correlated if there is only one or a few reference stars. Furthermore an inhomogeneous distribution of the reference stars may give a similar type of correlation. However, although the values of the individual orientation parameters differ slightly from the results in case a) the overall behaviour is the same in both methods.

The spectrum of the pointing direction variations is given in Figure 6.10. There is a trend towards higher fluctuations for short integration times < 0.25 s. The results of the last two series for 1.5 s and 3 s do not fit into this picture. However, due to the lack of reference stars we had to fix the scale factors for field 2 which might have caused (due to the above mentioned correlations) systematic trends in the pointing directions in the individual series. If we omit the last two series we conclude: (a) The increasing power at high frequencies favors atmospheric refraction effects and seems to rule out telescope movements as the cause for the observed fluctuations, and (b) there is no systematic difference between the spectra of the azimuth and the elevation components. The quality achieved does not yet allow a detailed comparison with theoretical or empirical relations from the literature. The data would, however, be consistent with a $\sigma^2 = at^{-0.5}$ law (see also equation 3.102).

In a last step we tried to confirm the results of Figure 6.10 by a simple repeatability test:

All frames of a series were mapped to a "mean" frame through a 4 parameter Helmert (similarity) transformation (2 offsets, 1 orientation parameter, 1 scale). The parameters of the "mean" frame of a series (CCD coordinates of all (common) objects) and the Helmert transformations for each frame were estimated in the same adjustment process.

As this processing does not know anything about the physics, the resulting series of translation parameters essentially reflects the movement of the stars across the field of view due to the earth rotation. In order to compare the translation parameters with the apparent pointing directions derived from the astrometric reduction we extracted the high frequency parts of this motion by subtracting a polynomial of degree one. The resulting spectrum is given in Figure 6.11. It confirms the corresponding (independently determined!) values in Figure 6.10 (1 pixel $\equiv$ 4.″17). The two last series (where we suspected a weakness in the astrometric reduction) fit much better into the overall picture here.

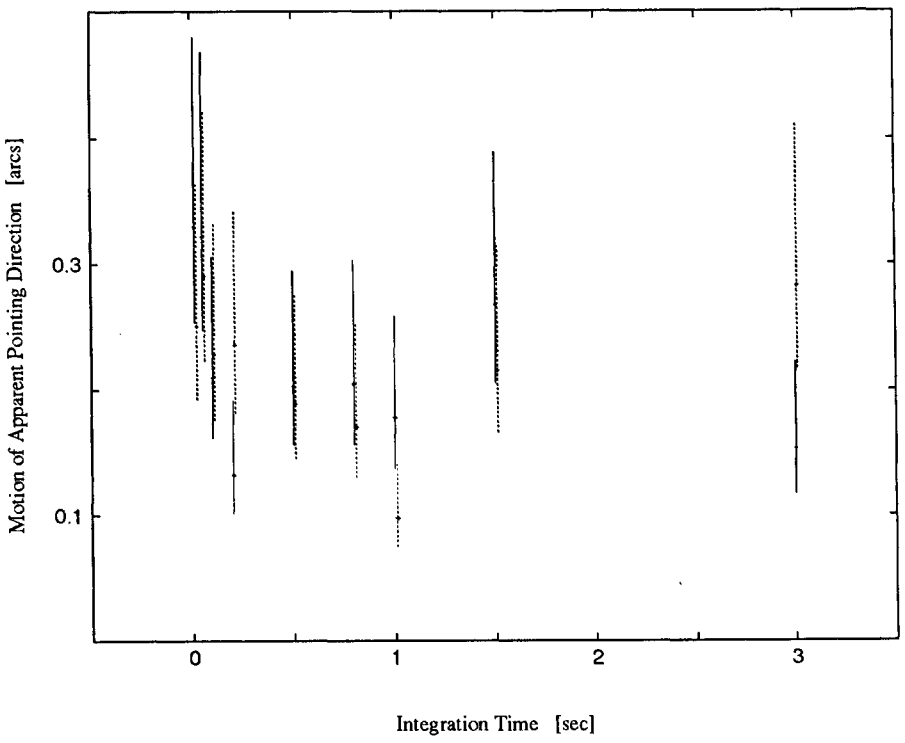

Figure 6.10: Spectrum of apparent pointing direction changes derived from the observations described in Table 6.4 by an astrometric reduction. The error bars indicate 95% confidence levels of a χ^2 test. Solid and dotted line error bars refer to the azimuth and elevation components respectively.

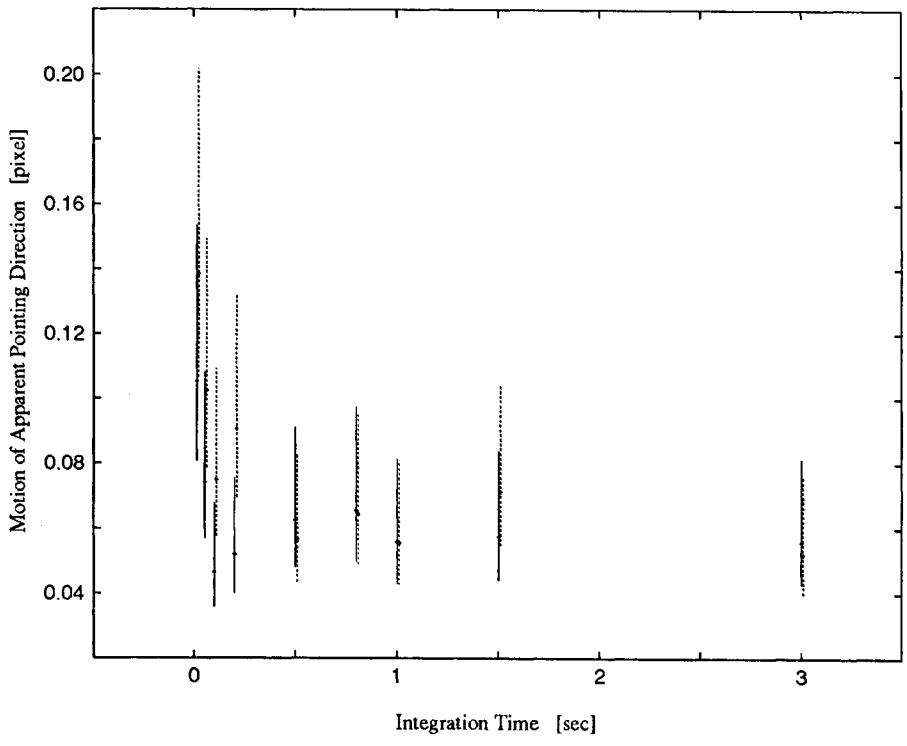

Figure 6.11: Spectrum of apparent pointing direction changes derived from the observations described in Table 6.4 by using Helmert transformations. The error bars indicate 95% confidence levels of a χ^2 test. Solid and dotted line error bars refer to the x- and y- components (CCD coordinates) respectively.

Conclusions

There is clear evidence for an apparent pointing direction motion due to the high frequency components of atmospheric refraction. This effect is well known. The actual spectrum for a particular location and for particular atmospheric conditions, however, may be extracted from observations only. The above results are preliminary because a) the amount of data is small (one night, two fields only), and because b) the noise level and the formal errors of the determined spectrum (both about 0.″2) are most likely caused by the mapping scale of 4.″1 s^{-1} and the moderate optical quality of the telescope.

We must emphasize that this atmospheric effect only influences the off-line calibrations which make use of the earth rotation (there mainly the determination of the mapping scale may be biased) and does not compromise the actual observations! Let us conclude this section with three statements:

(a) If the mapping scale is stable for a reasonably long time interval (requirement for telescope construction) we may average the refraction induced effect by acquiring many calibration series.

(b) In certain cases it may be possible to use star clusters with accurate astrographic position data from independent sources to calibrate the mapping.

(c) Any pointing direction variation, stemming from the atmosphere or the telescope, does not harm the observations in any way if we rely on the known ephemerides of a moving object and not on the earth rotation for calibration.

6.2 Objects in the geostationary ring and in geostationary transfer orbits

In this section we discuss a selection of observations performed in different contexts. The requirements concerning the position accuracy were different but in general they were moderate, in a range between a few 0.″1 and 1″. Also the angular velocities were small in general (objects in geostationary or geostationary transfer orbits) which made these applications attractive for first tests of our technique. Projects requiring high positional accuracy (like the CQSSP) and projects involving high angular velocities had to be postponed until after the completion of the new ZIMLAT telescope (due to moderate optical quality and insufficient tracking performance of the SLR instrument).

6.2.1 COGEOS objects

In the framework of the COGEOS project (Nobili 1987) objects in the geostationary ring were observed at Zimmerwald. The COGEOS project asks either for small, spin stabilized (and hence optically faint) satellites or uncontrolled small objects like "dead" satellites, apogee boost motors or rocket upper stages. The following examples should give an impression of our current capabilities.

Meteosat 5

Meteosat 5 is a relatively small spin stabilized European weather satellite. Its main characteristics (Janin 1993) are given in Table 6.5.

Meteosat 5 characteristics	
COSPAR designation	91015B
Type	weather satellite
Size	3.1 m long, 2.1 m diameter
m_v	≥ 12
Orbital elements	
Semi-major-axis	42164 km – 23.54 km ("geostationary")
Eccentricity	$4.7 \cdot 10^{-5}$
Inclination	0.27°
R.A. of ascending node	29.9°
Argument of perigee	335.4°
Longitude	357.6°
Drift rate	0.32°/day
Osculation epoch	1993 October 11.964

Table 6.5: Characteristics of Meteosat 5.

Figure 6.12 shows the positions determined during four close encounters observed on the night of August 16–17, 1993. The series were acquired at 23:36, 0:13, 1:33 and 2:37 UT respectively. Each series consists of 10 frames exposed for 5 s each and separated by about 7 s. A detailed view of the second encounter is given in Figure 6.13. The scatter of the determined positions is in good agreement with the formal errors indicated by the error bars. It is also obvious from Figures 6.12 and 6.13 that the "mean" position of a single encounter may be determined with an accuracy of a few tenths of an arcsecond.

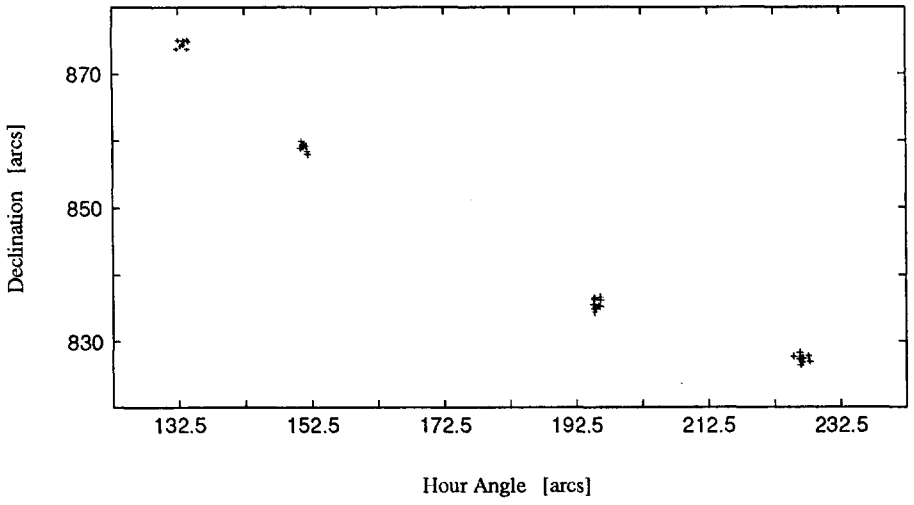

Figure 6.12: Four close encounters of the European weather satellite Meteosat 5 with four different PPM reference stars. The observations were performed during the night of August 16–17, 1993 at 23:36, 0:13, 1:33 and 2:37 UT respectively. The satellite was moving from north-east (upper left) to south-west (bottom right). (Both coordinates have an arbitrary offset).

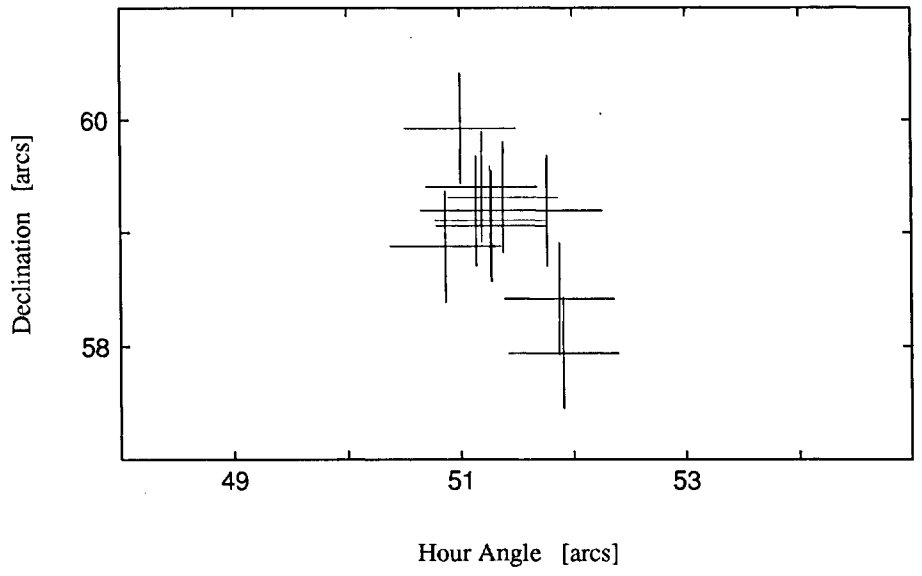

Figure 6.13: Detailed view of encounter no 2 of Figure 6.12.

Intelsat 4a f-6

The characteristics for the small communication Intelsat 4a f-6 are given in Table 6.6. We observed 6 encounters during two nights, namely on April 19 1993 at 22:53, 23:18, 23:42 and on April 21 at 0:22, 1:10, 2:25 UT respectively. 35 individual observations could then be used to determine an orbit for Intelsat 4a f-6. Table 6.7 gives the resulting orbital elements. (The ESA log values in this table must not be considered as the "truth"; they have a moderate accuracy and may even contain gross errors.) The corresponding residuals may be found in Figure 6.14. The formal rms error of 0".66 as estimated by the orbit determination program meets the requirements of the COGEOS programme without any problems!

Intelsat 4a f-6 characteristics	
COSPAR designation	78035A
Type	communication satellite
Size	2.8 m long, 3.4 m diameter
m_v	≥ 14
Orbital elements	
Semi-major-axis	42164 km – 31.92 km ("geostationary")
Eccentricity	$9.5 \cdot 10^{-4}$
Inclination	7.04°
R.A. of ascending node	59.2°
Argument of perigee	352.5°
Longitude	83.5°
Drift rate	0.34°/day
Osculation epoch	1993 September 7.969

Table 6.6: Characteristics of Intelsat 4a f-6.

6.2.2 Co-located geostationary satellites

Customarily a so-called "slot" of 0.1° in longitude is allocated for each geostationary satellite. The increase of commercial communication and TV satellites enforced the co-location of several satellites in the same slot. Currently there are slots with up to 3 satellites. An example is given in Figure 6.15. One slot represents a space cube with a sides of about 75 km long (assuming a maximum inclination of 0.1°). Studies have demonstrated that the collision risk is

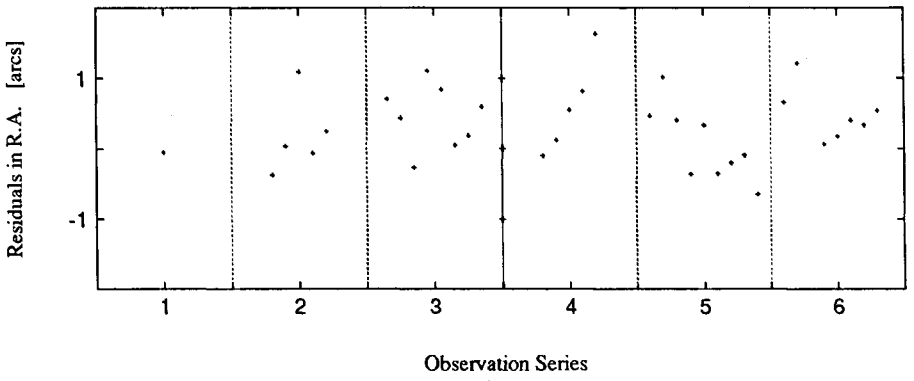

(a)

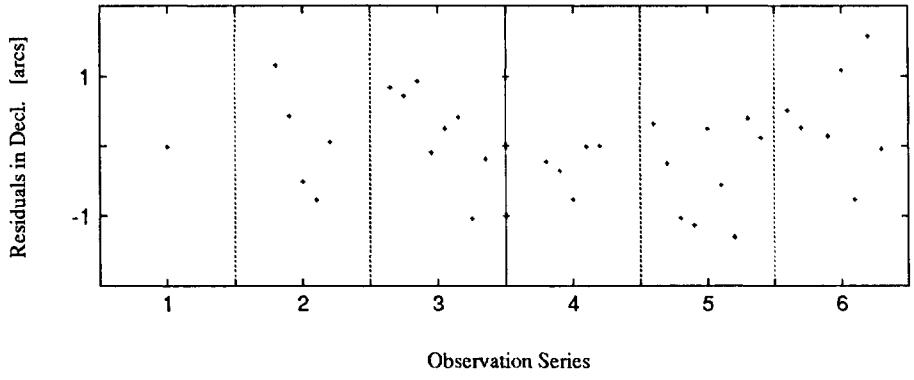

(b)

Figure 6.14: Residuals of an orbit determination for Intelsat 4a f-6 (see also Table 6.7). The "time" on the abscissa is not uniform, the gaps between the observation series were left out (first night to the left, second to the right hand side).

Intelsat 4a f-6 — Orbit determination		
Number of observations	2x35	
Arc length	26.5 hours	
rms (per coordinate)	0".66	
Osculating elements		
	Estimated	Esa log
Semi-major-axis −42164 km	(−20.245 ± .11) km	(−20.185) km
Eccentricity	(.0008485 ± .0000061)	(.0009282)
Inclination	(6.66993 ± .00011)°	(6.72233)°
R.A. of ascending node	(60.90861 ± .00030)°	(61.07533)°
Argument of perigee	(337.03988 ± .46)°	(335.20179)°
Mean anomaly	(198.37518 ± .46)°	(202.19274)°
Osculation epoch	1993 April 19.000729	(49096.000729)

Table 6.7: Results of the orbit determination for Intelsat 4a f-6.

no longer negligible under these circumstances. Because all geostationary satellites are controlled using essentially the same strategies (in order to minimize the fuel consumption) the collision probability is further increased. Special orbit constellations are an efficient countermeasure. Nevertheless, the risk (and the necessary maneuvers to reduce it) critically depends on the knowledge of the exact satellite positions. In many cases, the accuracy of the positions available to the control stations is very moderate. The determined orbits are mostly based on distance (transponder) measurements, the directions are only extracted from a single ground antenna. Obviously the accuracy is limited by these inaccurate direction measurements from angular encoders of the antenna (finite beam width, "flexible" structure!) and not by the distances measured with an accuracy of a few meters. The resulting orbit is at best accurate to about 1 to 2 km (constant biases given by the calibration uncertainties of the antenna direction might well be even much larger!). (Another error source lies in the differences found in the orbits computed by different processing institutions using the same observations!)

Astrographic positions from optical observations improve the situation considerably. Even moderate accuracies of a few tenths of an arcsecond (0".1 corresponds to 17.5 m in the geostationary ring!) reduce the positional uncertainty by at least one, probably by two orders of magnitude. By observing the relative positions of the co-located satellites we may in addition derive high precision differential

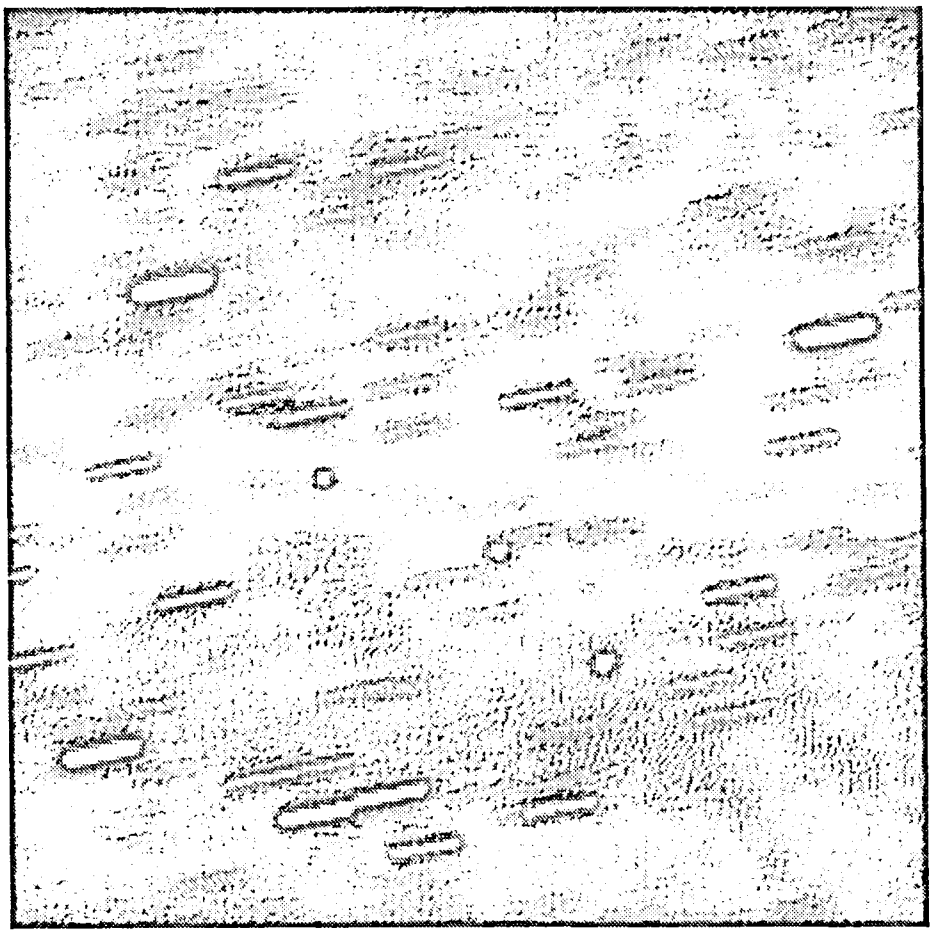

Figure 6.15: Observation of the geostationary satellites ASTRA 1A, 1B, 1C located at 19° east. Frame taken on July 28, 1993, 21:12 UT. Integration time was 5 seconds. The field size is 17′ x 17′ (175 x 175 km in geostationary ring). Zenith is down, west is to the left.

orbits free of potential star catalogue errors. Figure 6.16 shows a sequence of observations of the two geostationary TV satellites TDF-1 and TDF-2 during a close encounter with a reference star. The obtained positions are accurate to about 0.″4

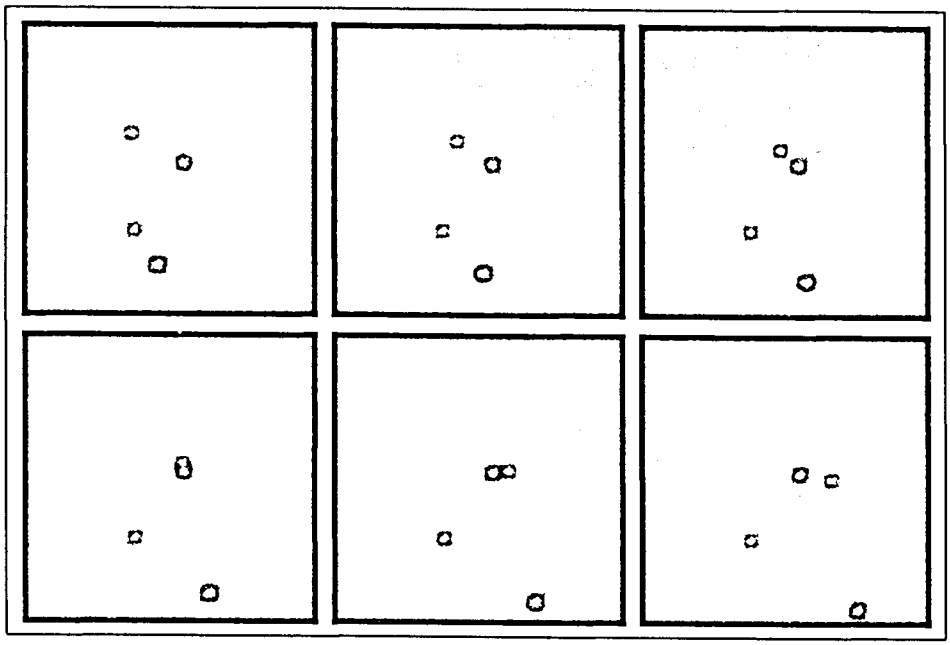

Figure 6.16: Sequence of frames showing stars trailing past the geostationary television satellites TDF-1 and TDF-2 at 19° west (row-wise from top left to bottom right). The frames were integrated for 1.1 seconds each. The field size is approximately 18′ x 18′ and the distance between the satellites is about 1′. Zenith is up, west to the right.

for a single measurement and to about 0.″2 for the entire close encounter (not taking into account catalogue errors). The relative satellite positions also may be measured with an accuracy of about 0.″2.

6.2.3 HIPPARCOS — plans and facts

Originally the European High Precision Parallax Collecting Satellite (HIPPARCOS) was planned to reach a geosynchronous orbit. The scientific mission called for an orbit accuracy of about 1 km. This could have been barely achieved with the measurements from the single ground station located at Odenwald, Germany. ESA therefore planned to perform periodic calibration sessions to control the performance of the angular encoders of the ground antenna. It was agreed to use optical position measurements acquired by the Zimmerwald observatory for these

calibrations. Unfortunately the apogee motor of the satellite failed and Hipparcos stayed "forever" in its geostationary transfer orbit. Consequently the entire mission had to be redesigned and Hipparcos had to be tracked by several ground stations. Given this situation the most critical aspect of the orbit determination was no longer the insufficient observation accuracy (with range measurements from several stations it was not necessary to rely on angular antenna data) but the modeling of the significant non-gravitational forces at the perigee (at a height of 500 km only!). Today we know that the mission was highly successful despite the apogee motor failure and that the original scientific goals (with a few exceptions) could be reached! Optical observations, on the other hand, were of no interest until the end of the mission on August 15, 1993 when the spacecraft was decomissioned and all tracking using the telemetry link ceased. We acquired the first optical observations of Hipparcos after its end of life on Nov 22, 1993. Its actual position was several 10′ away from the predicted positions, computed by numerically integrating the latest set of elements released by ESA. Figure 6.17 shows a superposition of 5 frames, exposed about 4 s each, and separated by about 25 s.

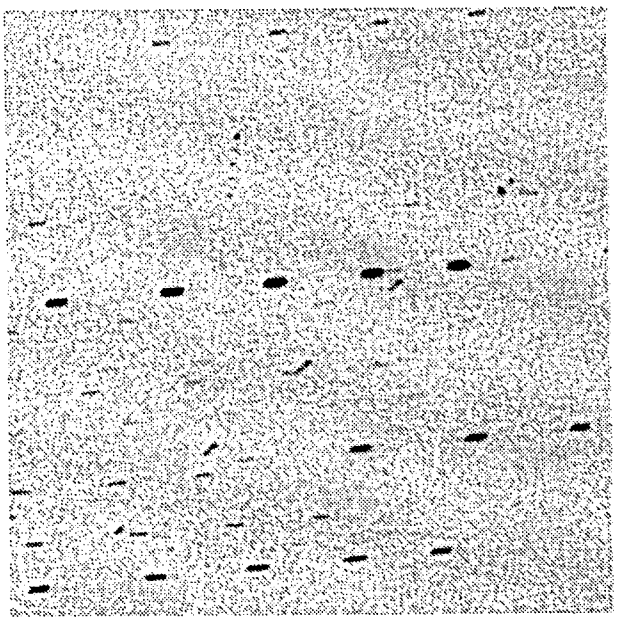

Figure 6.17: Observations series of Hipparcos. Superposition of 5 frames each exposed for about 5 s. Spacing between observations was about 25 s. Hipparcos is the — obviously tumbling — object moving from top right to bottom left. The slower object in the upper part of the picture is "Statsionar Raduga 13". Zenith is up, west is to the right.

In order to analyze the obvious (and expected) tumbling of the object (which

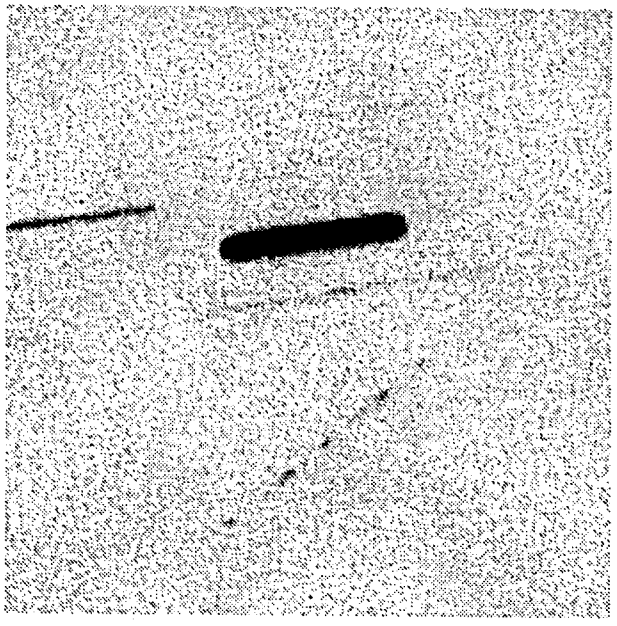

Figure 6.18: Observations of Hipparcos. 20 sec exposure of the tumbling spacecraft. Zenith is up, west is to the right.

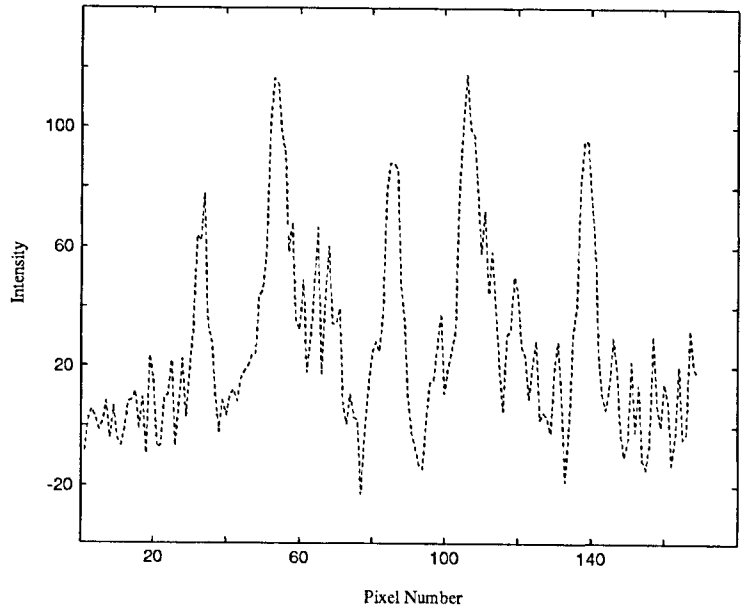

Figure 6.19: Observed light curve of Hipparcos as derived from the frame in Figure 6.18. The intensities are not calibrated (arbitrary units).

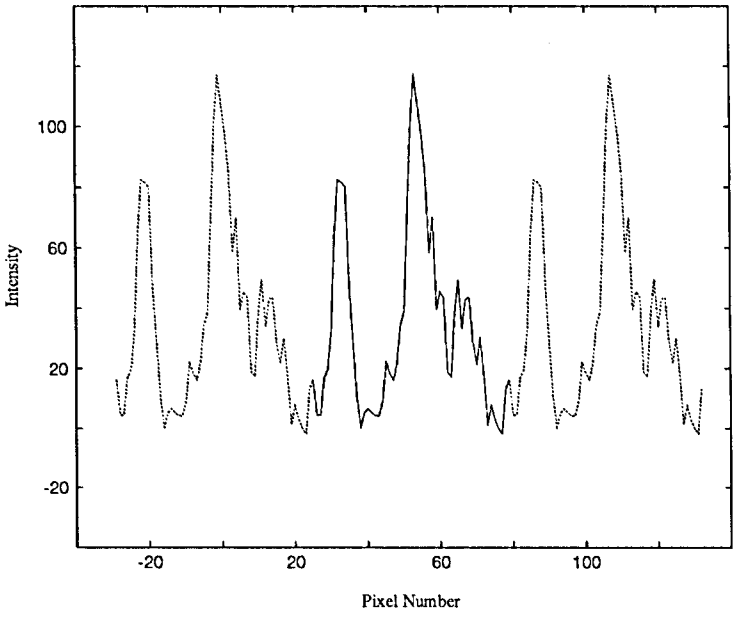

Figure 6.20: Reconstructed light curve of Hipparcos.

now is space debris!) more closely, a single frame was exposed for 20 s (Figure 6.18). The result of a photometric analysis of the trail is given in Figure 6.19. From this result and from the photometric data of the 5 frames in Figure 6.17 we were able to reconstruct the periodic light curve (Figure 6.20). The period is about 55 pixels corresponding to 7.8 s. This period of the light curve must not be the actual rotation rate. In fact the rotation period may be a multiple of the observed period (Hipparcos has 3 axisymmetrically arranged solar panels!).

To our knowledge these are the first optical observation of the Hipparcos spacecraft freely available after its end of life. It would be interesting to compare the observed (multiples of the) rotation period with the expected spin rate (given by the total angular momentum in the time of deactivation).

6.3 Photometric observations of GPS satellites

Is has already been shown in the case of the Hipparcos observations that the photometric data extracted from the CCD images are of remarkable quality. It was therefore quite natural to use the same method for other events like the entering/exiting of the earth's shadow by GPS satellites. These eclipse events are of special interest for the GPS orbit modeling in two respects:

(a) to check the predicted shadow entry and exit times, and what is more important,

(b) to observe the actual spacecraft attitude and possible attitude changes at the end of the eclipse.

Both events are critical for the correct modeling of the radiation pressure forces; the latter is also of interest to locate the exact position of the antenna emitting the GPS signals. Attitude changes after the end of the eclipse are expected because theoretically the satellites should rotate by 180°(about an axis pointing to the earth) during the eclipse. This rotation, however, seems to be postponed for technical reasons until after the end of the eclipse.

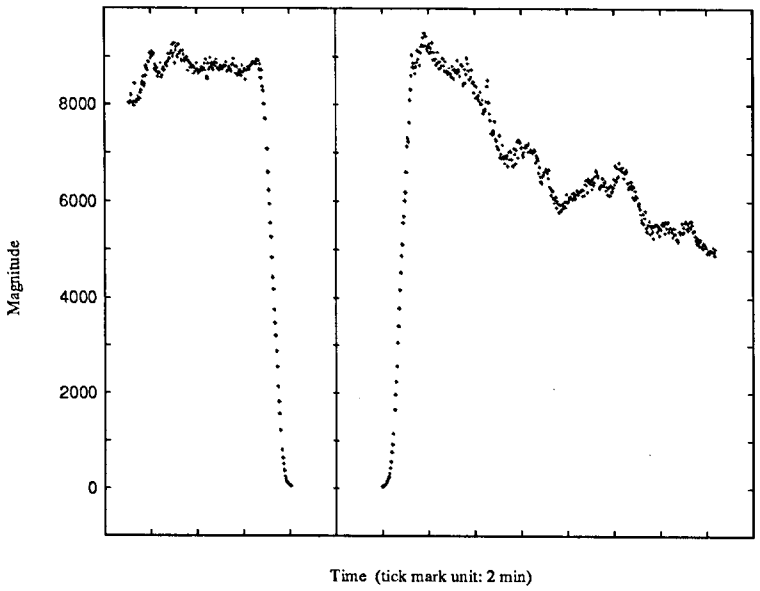

Figure 6.21: Photometric light curve of an eclipse of the GPS satellite PRN 22. The time interval when the satellite was completely in eclipse was skipped. The apparent (linear) magnitude is not calibrated. The satellite reached a maximum magnitude of about $m_v = 10$.

The observations were a challenge from the technical point of view. On the one hand a high repetition rate of the measurements on the order of 1 observation per second was necessary for a sufficient temporal resolution; on the other hand the exit phase should be monitored for up to 30 minutes (the attitude changes are slow). These requirements could only be met by (a) restricting the CCD data to a small 50 x 50 pixel subframe (thus reducing the amount of image data as well as the readout time) and by (b) exposing consecutive series of several

hundred frames. The satellite was then automatically identified on all frames and its photometric magnitude estimated with respect to the background. Obviously this method is compromised by possible changes in the background intensity. For a relative calibration (in time) one would like to have always at least one star in the field of view to which the intensity of the satellite could be linked but this would lead in most cases to much larger subframes!

Figure 6.21 shows the light curve from an eclipse of GPS satellite PRN 22. The duration of the eclipse was about 53 min and the actual shadow entry and exit phases lasted for about 1 min. The scatter of the data points is consistent with pure shot noise. It is, however, not yet clear how much of the small variations have to be attributed to changes of the atmospheric transparency (cirrus clouds). A rough calibration of the photometric data led to a maximum apparent magnitude of about $m_v = 10$ shortly before and after the eclipse and a relative precision of the measurements of about $0.01 m_v$. Figure 6.22 shows the data from a similar eclipse of the GPS satellite PRN 25. In this case there are prominent variations of the apparent magnitude after the shadow exit which we believe to be real. The data gap in the middle of this phase was caused by a malfunction of the data acquisition software.

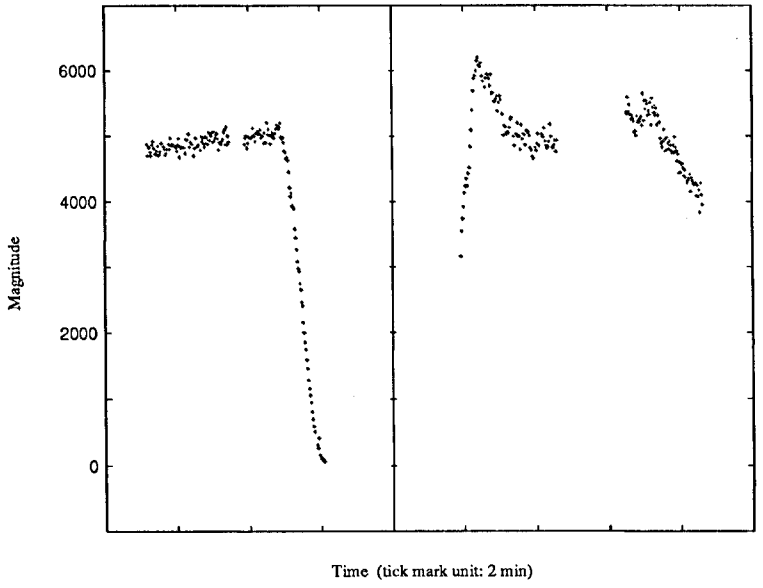

Figure 6.22: Photometric light curve of an eclipse of the GPS satellite PRN 25. The time interval when the satellite was completely in eclipse was skipped. The apparent (linear) magnitude is not calibrated. The satellite reached a maximum magnitude of about $m_v = 10$.

Chapter 7

Summary and Outlook

Measuring the positions of fast moving objects is a challenging task from the observational point of view. With a few exceptions classical astrographic techniques using photographic materials are not capable of observing the faint optical signals of artificial satellites. Their high angular velocities of several hundred arcseconds per second with respect to the reference stars require more sensitive detectors and observation techniques substantially different from the classical ones. Furthermore shuttering and epoch registration are critical issues. Mechanical shutters usually do not solve the problem with sufficient accuracy.

The selection of an appropriate detector played a key role in this work. Given the two primary requirements — high quantum efficiency and geometric stability — we had to choose between two types of optoelectric sensors: integrating devices and photon counters. Candidates were CCD detectors (integrating device), Ronchi ruling type sensor combinations and image dissector tubes (photon counters). The overall requirements of our application eventually favored the CCDs.

High precision astrography asks for a small field of view (much smaller than a degree) in order to minimize the influence of refraction anomalies and atmospheric turbulence. In combination with the high angular velocity of the objects of interest this leads to short exposure times, generally in the order of a few tenths of a second. As a consequence the technique is based on the observations of close encounters between the moving object and a reference star: a series of ten to one hundred short exposed frames are acquired during each encounter. Several problem areas may be identified: a) the CCD must be read out efficiently, b) the shuttering problem must be solved, c) the observations produce a vast amount of data in a short time interval, and d) the fact that only one reference star is within the field of view requires a new astrographic reduction technique.

A significant reduction of the CCD readout times may be achieved by reading out subframes only. This poses no problems from the technical point of view,

however, it requires precise predictions for the positions of the objects of interest and extensive real time readout control procedures.

The shuttering problem was solved in an elegant way by exploiting the inherent capabilities of the CCD detectors. Using this technique the observation epochs may be defined with an accuracy well below a millisecond.

The data rate is significantly different than in classical astrography. Fully automated data acquisition, and real-time image processing are mandatory. In particular automated object search procedures, identification of objects (on consecutive frames of a series) and centroiding are mandatory.

In the presence of only one reference star in the field of view we have to abandon the classical "plate by plate" reduction methods. Mapping models had to be developed which include common parameters for several frames (e.g. distortion terms) but only few frame dependent parameters (e.g. the detector orientation angle). These parameters are then determined by combining the observations from a series of frames. Furthermore we have to distinguish between parameters which may be established using data from actual observations (close encounter series) and parameters asking for dedicated calibration observations.

A detailed analysis of the error budget revealed that the accuracy is currently limited by the object image centroiding. Achieving good centroiding results requires a) perfect optics (symmetrical and narrow PSF), b) a good S/N, and c) an optimum mapping scale. There is no way to avoid the necessity of high quality optics. A high S/N requires a large telescope aperture (may not be compensated by increasing the exposure times), small detector system noise, tracking (of faint objects), good seeing (narrow seeing-convolved PSF), and a clear atmosphere. (Unfortunately most of these conditions may not be altered for a given observatory). The optimum mapping scale simulations and the centroiding of real images suggest a value of about 1″ per CCD pixel (i.e. $f/4$ focus) assuming a moderate seeing of 2″ (the seeing-convolved PSF should cover about 4 pixels at FWHM). From the error analysis we further conclude that color dispersion and the resulting object-color dependent displacement of the centroids are critical issues. They may either be handled by observing in narrow passbands (reducing the sensitivity of the sensor system considerably!) or by including appropriate correction terms into the astrometric reduction. The latter requires that photometric data of the object of interest are available.

The calibration of the mapping was identified as a critical issue. Currently we predominantly use the "earth rotation" method where we observe the motion of the stars with the telescope fixed. For each close encounter one detector orientation angle and the mapping scale are estimated (using the data from the entire observation series). The remaining parameters are determined from extensive (off-line) calibrations. The "earth rotation" method relies on the "fixed telescope direction" which may be viewed as a disadvantage. Short periodic re-

fraction anomalies compromise this technique at the 0.″3 level. If the focal length of the telescope is sufficiently stable, the scale factor might be determined from extensive pre- and post-observation calibrations too (attenuating the influence of refraction anomalies). The optimum procedure for the determination of the mapping parameters, however, uses the orbit information of the moving object (provided that these data are available and accurate). In this approach a common displacement of the objects in the field of view (e.g. caused by refraction anomalies) has no influence. In particular we may track objects (tracking is never perfect!) without compromising the astrometric reduction.

The observations from the experimental setup at Zimmerwald confirm the theoretical considerations. Results from measurements of objects in geostationary and geostationary transfer orbits show position accuracies on the order of 0.″4 for a single observation. These values may be improved by using series of observations as can be seen from the residuals of the corresponding orbit determinations. Practical experience futhermore proved that the developed technique may serve as the basis for optical observations of moving objects in general. In particular the result from photometric observations of artificial satellites are promising. We may also mention the ESA study on "CCD algorithms for space debris detection" which is currently performed at our institute.

The current results are severely limited by the optical performance of the SLR telescope used. However, the new ZIMLAT telescope to be installed in summer 1995 will have optics optimized for astrometric applications. The actual improvement in accuracy when using this new instrument is difficult to predict but we expect at least one order of magnitude.

Further developments of the observation technique must focus primarily on three domains: a) the automation of the observation scheduling (orbit prediction), the data acquisition (including telescope control and observation sequencing), and on-line data processing, b) the improvement of the centroiding accuracy by using 2-dimensional PSF fitting algorithms, and c) extensive calibration observations. The latter is mandatory to optimize the calibration procedure (and consequently also the observation scenarios). In addition it allows assessment of the magnitude and the behaviour of the refraction anomalies at the particular observation location at Zimmerwald.

It is evident that the technique has the potential to generate a come-back of ground based optical astrometry of fast moving objects, in particular artificial satellites, after more than two decades of "hibernation".

Appendix A

Signal to Noise Ratio and Limiting Magnitudes

We have to introduce the *signal to noise ratio* (abbreviated as S/N hereafter) when studying detection limits or limiting magnitudes. In this context the term "signal" has to be understood in the narrow sense as the signal stemming from the source of interest (object) whereas "the noise" is due to the object *and* the background. In order to compute the S/N we first have to define the area over which the signal and the noise components are to be integrated. For a single channel detector system this area simply is the field of view. In the case of an imaging sensor we usually use the area "over which the source is detected". From the observational point of view this is not a well defined quantity. The area over which the *image of a point source* (defined by the actual point spread function (PSF) of the atmosphere and the telescope) may be detected depends on the algorithms used (e.g. the threshold setting) and the noise level itself. Usually we get the maximum value for the S/N of a point source if we consider an area smaller than that associated with the detectable maximum extent of the source. Theoretically the PSF refers to an infinite area (see also the discussion on optimum threshold in section 4.1.3). The area over which the image of an object is extended may e.g. be defined using the variance or the "full width at half maximum" (FWHM) of its profile. We may state:

(a) There is no unique way defining the S/N. Therefore S/N values may not be compared unless the particular definitions are precisely known (ideally the computations should be based on the same algorithms). Comparisons are particularly problematic if the considered detection area depends on the S/N.

(b) For many applications the detection area has to be defined in order to maximize the resulting S/N. Actually the centroiding and determination

of photometric quantities should be based on this "optimum object diameter". (Obviously the photometric estimates must be corrected for missing contributions from outside the finite "aperture".)

S/N for static point sources

Let us derive the relations for the S/N in the common case of a point source observed with an integrating multichannel detector. The results will also be valid for photon counting systems except that the system noise may be neglected (due to their high internal gain) and the detective quantum efficiency must be reduced due to the dead time (recovery time) of the detector after each event (the effect is also refered to as "pile-up error").

Let us introduce the following quantities:

D the telescope diameter in meters;

f the focal length of the telescope in meters;

F the focal ratio of the telescope, i.e. $F = D/f$;

d the detector pixel size in meters;

p the detector pixel size in arcseconds, i.e. $p = (d/f)206265$;

t the exposure time in seconds;

$\dot{S}_o$ the mean signal associated with the object (point source) in photons per second as registered by the detector. More precisely $\dot{S}_o$ is refered to as illuminance. For detectors exploiting the photoelectric effect $\dot{S}_o$ is often given by the number of photoelectrons or simply electrons per second;

m the number of pixels over which the source is detected. This area is determined by the convolution of the atmospheric and the instrumental PSF, the pixel size (a function of the focal length of the telescope), and the used detection algorithm;

$\dot{S}_s$ the mean sky background signal in photons (electrons) per second and pixel as registered by the detector;

$\dot{S}_d$ the mean detector dark current in photons (electrons) per second and pixel;

$\sqrt{S_r}$ the detector system readout noise in equivalent photons (electrons) per pixel (square root of the variance of the Poisson distribution). This noise includes the actual detector readout noise, the digitization noise, plus any additional noise stemming from the detector calibration process (except for the dark current removal which is discussed separately), and

n the CCD "on-chip binning" factor (common for both pixel directions).

We may now express the signal S_{tot} at the detector output integrated over m pixels of the object's image as

$$S_{tot} = (\dot{S}_o + m(\dot{S}_s + \dot{S}_d))t. \tag{A.1}$$

In order to extract the signal due to the source of interest the contributions of the background sources (including sky, atmospheric, as well as instrumental background) have to be subtracted. There are many different ways of doing that, including sophisticated ones like iterative two-dimensional modeling of the PSF. For the following discussion we use the simplest method, by determining the mean background signal, S_b, from "object free" regions (the resulting S/N does not vary significantly for different techniques). Defining by $< x >$ the expectation value (estimated value) for a parameter x we may write

$$S_b = \langle(\dot{S}_s + \dot{S}_d)t\rangle = \langle\dot{S}_s + \dot{S}_d\rangle t \tag{A.2}$$

as estimated from k "object free" pixels and integration time t. The associated noise per pixel, σ_b, is given by:

$$\sigma_b^2 = \frac{1}{k}\left(\langle(\dot{S}_s + \dot{S}_d)t\rangle + \frac{S_r}{n^2}\right), \tag{A.3}$$

where n denotes the *on-chip binning* factor (in both pixel directions). This factor is only relevant for CCD detectors where binning can be used to reduce the overall readout noise, otherwise we have $n = 1$ in the above equation.

The background reduced (detected) signal S for the source may then be written as

$$S = (\dot{S}_o + m(\dot{S}_s + \dot{S}_d) - m < \dot{S}_s + \dot{S}_d >)t. \tag{A.4}$$

Assuming no correlation between the individual components and neglecting seeing and scintillation effects the overall noise σ is

$$\sigma^2 = \dot{S}_o t + m(1 + \frac{1}{k})\left((\dot{S}_s + \dot{S}_d)t + \frac{S_r}{n^2}\right), \tag{A.5}$$

resulting in a S/N of

$$(\mathrm{S/N})^2 = \frac{(\dot{S}_o t)^2}{\dot{S}_o t + m\alpha\left((\dot{S}_s + \dot{S}_d)t + \frac{S_r}{n^2}\right)}, \tag{A.6}$$

where $\alpha = 1 + 1/k$. If the area from which the background is determined is large enough ($k \gg 1$) we have $\alpha \approx 1$ and the S/N becomes optimal (this is not always possible, e.g. in crowded star fields).

Before discussing equation (A.6) we want to remind ourselves of the meaning of the individual terms and relate them to their physical sources.

S_o, the total signal from the point source, is given by

$$S_o = j_o D^2 t, \tag{A.7}$$

where j_o is the illuminance per square meter per second:

$$j_o = \int i_\lambda \tau_\lambda \varepsilon_\lambda q_\lambda d\lambda, \tag{A.8}$$

where

- i_λ is the irradiance (in photons per square meter per nanometer per second) outside the earth's atmosphere;
- τ_λ is the atmospheric transparency or transmission function; it is in general zenith distance dependent, i.e. $\tau_\lambda = f(z)$;
- ε_λ is the optical efficiency of the telescope;
- q_λ is the detective quantum efficiency of the detector and denotes the fraction of incident photons actually detected (the quantum efficiency is equivalent to the spectral response function).

The description of the sky signal (per pixel) is similar:

$$S_s = j'_s t \frac{d^2 D^2}{f^2} (206265)^2, \tag{A.9}$$

where j'_s is the surface brightness in photons per square meter per arcsecond squared:

$$j'_s = \int i'_s \tau'_\lambda \varepsilon_\lambda q_\lambda d\lambda \tag{A.10}$$

- i'_s is the surface brightness in photons per square meter, arcsecond square and wavelength inside the earth's atmosphere at the zenith.
- τ'_λ is the zenith distance dependent atmospheric correction; $\tau'_\lambda = \tau'_\lambda(z)$; $\tau'_\lambda(0) = 1$.

We introduced the sky brightness as measured on the surface of the earth (denoted by a prime) because the atmosphere is contributing to the background too.

The detector dark current is proportional to the integration time too whereas the readout noise is added once only per exposure and pixel.

Examining equation (A.6) it is obvious that the optimum S/N is obtained a) by minimizing the instrumental noise constituents $\dot{S}_d$ and S_r, b) by reducing the area m covered by the image of the point source and c) by using on-chip binning resulting in $n > 1$. (We assume $\alpha = 1$ in our further discussion.) There is not much to say about a): the number m, however, is a critical quantity influenced by many different factors; m is in particular a function of the particular telescope and detector used. Two main regimes may be distinguished:

(a) m is dominated by the PSF of the telescope:
The PSF should be smaller than the seeing disk. If this is not the case the the optics must be improved!

(b) m is dominated by the atmospheric PSF:
A reduction of the telescope's focal length (magnification) will reduce the seeing disk (typically of the order of 1" to 2"). The lower limit for m is dictated by the sampling criterion of the particular application. Optimum sampling is defined by the actual objective and may e.g. be different for imaging and position determination of point sources (see section 4.1.3 and Verdun (1993)). In any case, the object size must not be smaller than one pixel otherwise all sky background which does not lie within the object but still is inside the single pixel is (unnecessarily) added.

We should also emphasize that we are only reducing the contributions from the dark current $m\dot{S}_d$ and the readout noise mS_r when minimizing m but not from the sky background because m is proportional to f^2 and $\dot{S}_s$ is diluted with f^{-2} (see also equation (A.9) for d=const)!

On-chip binning reduces the readout noise but it also decreases the sampling. If a reduced sampling is required this should preferably be done by reducing the focal length of the telescope and not by on-chip binning. On-chip binning should be used only in applications where certain tasks may be performed allowing a lower resolution in favor of an enhanced S/N but where in general the high resolution (unbinned) mode must be preserved.

We finally discuss the required integration time to achieve a given S/N in particular in view of the ratio of the "background to object signal" and the readout noise. If we define the background to signal ratio as

$$r = \frac{m(\dot{S}_s + \dot{S}_d)}{\dot{S}_o}, \tag{A.11}$$

the required number of photons from the object may be derived from equation (A.6) (for n=1, $alpha = 1$)

$$\dot{S}_o t = \frac{1}{2} s^2 (1+r) \left(1 + \sqrt{1 + \frac{4 m S_r}{s^2 (1+r)^2}} \right), \tag{A.12}$$

where s is the S/N. We distinguish two regimes:

a) object dominated, $r \ll 1$:

$$\text{for} \quad \sqrt{m S_r} \ll s: \qquad t \simeq \frac{s^2}{\dot{S}_o} \tag{A.13}$$

$$\text{for} \quad \sqrt{m S_r} \gg s: \qquad t \simeq \frac{s\sqrt{m S_r}}{\dot{S}_o}, \tag{A.14}$$

where $\sqrt{m S_r}$ is the overall readout noise.

a) sky dominated, $r \gg 1$:

$$\text{for} \quad S_r \ll (\dot{S}_s + \dot{S}_d): \qquad t \simeq \frac{s^2 r}{\dot{S}_o} \tag{A.15}$$

$$\text{for} \quad S_r \gg (\dot{S}_s + \dot{S}_d): \qquad t \simeq \frac{s\sqrt{m S_r}}{\dot{S}_o}. \tag{A.16}$$

Figure A.1 shows the variation of the magnitude with exposure time for lines of equal S/N. The S/N was computed using equation (A.6) where m was replaced by an intensity dependent area resulting from the optimum threshold as discussed in section 4.1.3 (this threshold optimizes the S/N for Gaussian image profiles). The calculations were based on the following values: atmospheric transmission=0.88, optical transmission=0.5 for the SLR and 0.6 for the ZIMLAT telescope, CCD characteristics as given in Table 5.1 (conversion from magnitudes (m_v) to photons: 16.0 $m_v \rightarrow$ 8000 ph $s^{-1}m^{-2}$).

S/N for moving point sources

The situation is quite different if the source is moving across the pixels during the exposure. The number of pixels m within the object's image is steadily growing with time:

$$m = m_0 + \frac{\sqrt{m_0}}{t_p} t, \tag{A.17}$$

where

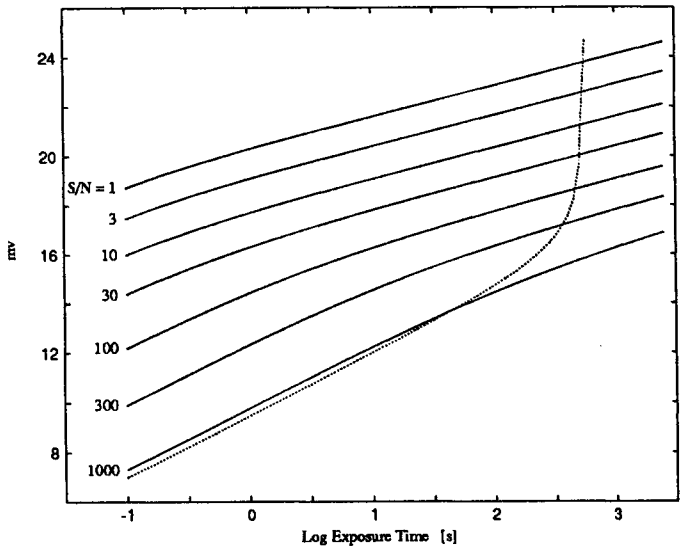

(a) 0.5 m SLR

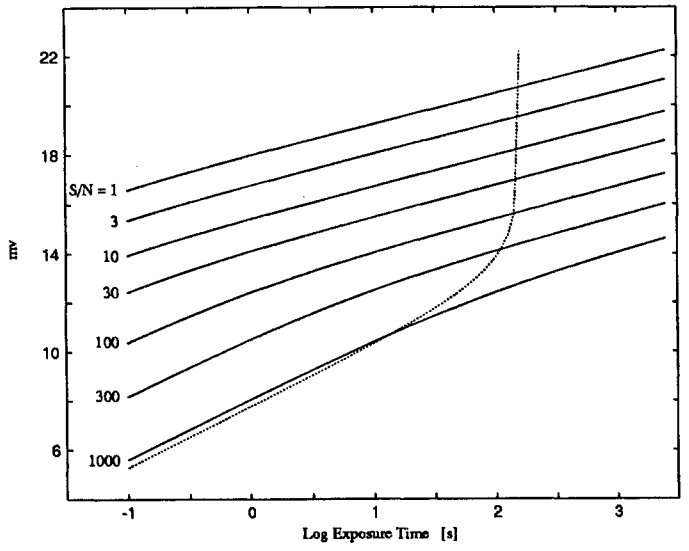

(b) 1 m ZIMLAT

Figure A.1: Variation of the magnitude with exposure time for lines of equal S/N. An optimum threshold as described in section 4.1.3 was used to compute the S/N. The dotted lines indicate the detector's saturation level at 133 ke^- (saturation below the dotted line). A sky background of 19 $m_v\,arcs^{-2}$ and a detector readout noise of 5 e^- were assumed.

m_0 is the number of pixels illuminated by the source at a given instant;

t_p is the pixel crossing time.

$$t_p = \frac{p}{v}, \tag{A.18}$$

where v is the object's angular velocity in arcseconds per second and p the pixel size in arcseconds. After each pixel crossing time $\sqrt{m_0}$ new pixels (which were already filled with background noise) are added to the object's image and $\sqrt{m_0}$ pixels (which accumulate noise only from then on) are left behind. The overall S/N therefore quickly reaches a maximum after a few pixel crossing times (at least if the signal to background ratio is low).

Using (A.17) we immediately derive an expression for the S/N from equation (A.6):

$$s = \frac{\dot{S}_o t}{\sqrt{m_0 S_r + (\dot{S}_o + m_0(\dot{S}_s + \dot{S}_d) + \sqrt{m_0} v S_r)t + \sqrt{m_0} v(\dot{S}_s + \dot{S}_d)t^2}} \tag{A.19}$$

We may now confirm the result from the above discussion and show that the S/N is not growing indefinitely as in the static case (see equations (A.13), (A.14), (A.15), (A.16)) but reaches a maximum asymptotically (we neglect the dark current signal $\dot{S}_d$ as it is very small and might be introduced easily by $\dot{S}'_s = \dot{S}_s + \dot{S}_d$):

$$s_\infty = \lim_{t\to\infty} s = \frac{\dot{S}_o}{\sqrt{\sqrt{m_0} v S_s}} = \frac{\dot{S}_o}{\sqrt{m_0 \dot{S}_s}}\sqrt{t_o} = \sqrt{\frac{\dot{S}_o t_o}{r}}, \tag{A.20}$$

$r = \frac{m_0 \dot{S}_s}{\dot{S}_o}$ is the ratio of the signal (a) from the sky background in the m_0 pixels covered by the object's image and (b) from the total signal stemming from the object;

t_o is the time interval during which the image moves by one object diameter $\sqrt{m_0}$ (object crossing time).

The object crossing time is given by

$$t_o = \frac{\sqrt{m_0}}{v}. \tag{A.21}$$

Equation (A.20) reflects the fact that in the S/N of all components which grow proportional to $\sqrt{t}$ (e.g. all shot noise from source signals growing proportional

with time) vanish for a sufficiently long integration time (this is actually the reason why the S/N in the static case may always be improved by increasing the exposure time). The only remaining noise term in (A.20) stems from constituents growing $\sim t^2$. This term is due to the sky background accumulating $\sim t$ in each individual pixel. In addition the total area covered by the object's trailed image is growing proportional to the exposure time. It is important to notice that this limiting value is independent of the readout noise signal S_r.

We still have to answer the question how "soon" this maximum S/N is reached in order to define the minimum integration time (a longer integration does no harm with respect to S/N). We define the time t_κ needed to achieve a certain fraction κ of the limiting S/N as

$$\kappa s_\infty = s(t_\kappa) \tag{A.22}$$

Using equation (A.19) we obtain

$$t_\kappa = \frac{\sqrt{(1+r_{so}+r_{ro})^2 + 4r_{ro}r_{so}(\frac{1}{\kappa^2}-1)} + (1+r_{so}+r_{ro})}{2r_{so}(\frac{1}{\kappa^2}-1)} t_o, \tag{A.23}$$

where

$r_{so} = \frac{m_0 \dot{S}_s}{\dot{S}_o}$ is the ratio of the sky signal (in the m_0 pixels covered by the object) to the object signal;

$r_{ro} = \frac{m_0 S_r}{\dot{S}_o t_o}$ is the ratio of the detector readout signal (from the m_0 pixels covered by the object) to the object signal (which accumulates in each pixel over a time interval t_o).

As in the static case we consider the two regimes namely the object dominated ($r_{so} \ll 1$) and the sky dominated ($r_{so} \gg 1$). In addition we will have to discern the cases of dominating and negligible readout noise for each regime.

Object dominated, $r_{so} \ll 1$:

$$\text{for} \quad r_{ro} \ll 1: \qquad t_\kappa \simeq \frac{t_o}{r_{so}(\frac{1}{\kappa^2}-1)} = \frac{\dot{S}_o}{m_0 \dot{S}_s} \cdot \frac{t_o}{(\frac{1}{\kappa^2}-1)} \tag{A.24}$$

$$\text{for} \quad r_{ro} \gg 1: \qquad t_\kappa \simeq \frac{r_{rs} t_o}{(\frac{1}{\kappa^2}-1)} = \frac{S_r}{\dot{S}_s t_o} \cdot \frac{t_o}{(\frac{1}{\kappa^2}-1)}, \tag{A.25}$$

where

$r_{rs} = \frac{S_r}{\dot{S}_s t_o}$ is the ratio of the detector readout signal (per pixel) to the sky signal (per pixel) accumulated over a time interval t_o.

Equation (A.24) describes the situation where the detector readout noise is negligible compared to the source signal whereas (A.25) is valid for the detector noise dominated case. We should be careful in interpreting the time interval t_κ and keep in mind that t_k is only a measure for the time it takes to reach a certain fraction of the maximum S/N but that t_κ does not define the maximum itself. Although an increased sky signal $\dot{S}_s$ in (A.24) e.g. does lower t_κ this is certainly not desirable because it reduces the maximum achievable S/N according to equation (A.20) (the maximum is reached sooner but at the price that it is smaller). Obviously the same argument holds for decreasing values $\dot{S}_o$ or t_o. The only possibility to optimize t_κ without deteriorating the S/N is to reduce the readout noise in (A.25) because the maximum S/N does not depend on S_r (see equation (A.20)).

Sky dominated, $r_{so} \gg 1$: In order to discuss the limiting values for the sky dominated regime we write equation (A.23) in a somewhat different form:

$$t_\kappa = \frac{\sqrt{(1+\frac{1}{r_{so}}+r_{rs})^2+4r_{rs}(\frac{1}{\kappa^2}-1)}+(1+\frac{1}{r_{so}}+r_{rs})}{2(\frac{1}{\kappa^2}-1)}t_o. \qquad \text{(A.26)}$$

In contrast to the case where the object was dominating the sky we compare the readout noise signal with the sky signal (r_{rs}) in order to distinguish between dominating and negligible readout contribution:

$$\text{for} \quad r_{rs} \ll 1: \qquad t_\kappa \simeq \frac{t_o}{\frac{1}{\kappa^2}-1} \qquad \text{(A.27)}$$

$$\text{for} \quad r_{rs} \gg 1: \qquad t_\kappa \simeq \frac{r_{rs}t_o}{\frac{1}{\kappa^2}-1} = \frac{S_r}{\dot{S}_s t_o}\cdot\frac{t_o}{(\frac{1}{\kappa^2}-1)}. \qquad \text{(A.28)}$$

Two facts are of interest: (a) if the readout noise is negligible t_κ will depend on t_o (i.e. the object velocity) only, (b) if readout noise is dominant t_κ is identical for the sky and the object dominated cases (equations (A.28, A.25)).

Considering that there are three independent quantities $\dot{S}_o, \dot{S}_s$ and S_r to be compared with each other (6 possible combinations) we may ask whether the cases already discussed above cover all "new" cases. Beginning with $\dot{S}_o$ we see from equation (A.24) that if $\dot{S}_o$ is dominating the other two components $\dot{S}_s$ and S_r, t_κ will obey the relation (A.24) whether or not the sky background is greater than the readout signal (r_{rs} is of no importance if $r_{so} \gg 1$). If the sky signal is dominant, equation (A.27) is applicable ($r_{so} \gg 1$ and $r_{rs} \ll 1$). Again (A.27) is valid for all readout to object signal ratios r_{ro}. Finally equation (A.25) and (A.28) describe the two possible cases where the readout signal is greater than both the sky and the source signal. Once more the behavior of t_κ is identical. We thus summarize:

$$\text{for} \quad r_{so} \ll 1 \quad \text{or} \quad r_{ro} \ll 1: \quad t_\kappa \simeq \frac{t_o}{r_{so}(\frac{1}{\kappa^2}-1)} = \frac{\dot{S}_o}{m_0 \dot{S}_s}\cdot\frac{t_o}{(\frac{1}{\kappa^2}-1)}, \qquad \text{(A.29)}$$

$$\text{for} \quad r_{so} \gg 1 \quad \text{or} \quad r_{rs} \ll 1: \quad t_\kappa \simeq \frac{t_o}{\frac{1}{\kappa^2} - 1}, \tag{A.30}$$

$$\text{for} \quad r_{ro} \gg 1 \quad \text{or} \quad r_{rs} \gg 1: \quad t_\kappa \simeq \frac{r_{rs} t_o}{\frac{1}{\kappa^2} - 1} = \frac{S_r}{\dot{S}_s t_o} \cdot \frac{t_o}{(\frac{1}{\kappa^2} - 1)}. \tag{A.31}$$

As an example we compute the t_κ needed to reach 90 % of the maximum S/N and κ after one object crossing time t_o for the sky dominated case:

$$t_\kappa = 4.26 t_o \quad \text{for} \quad \kappa = 0.9, \quad \kappa = \frac{1}{\sqrt{2}} \quad \text{for} \quad t_\kappa = t_o. \tag{A.32}$$

This shows that an upper limit for the exposure time of the order of a few object crossing times (usually corresponding to a few pixel crossing times ($t_o \sim (2 \cdots 4) \cdot t_p$)) is adequate.

Figures A.2, A.3, A.4 illustrate the above discussion for realistic examples. All calculations were based on the following values (new ZIMLAT telescope): $\dot{S}_s$ = 17.5 $m_v\,arcs^{-2}$ (sun at z=105°), S_r = 5 photons; telescope: 1 m f=1/4 m_0 = 4 (scale=1"/pixel), atmospheric transmittance=0.88, transmittance of optics=0.6, conversion from mag (m_v) to photons: 16.0 $m_v \rightarrow$ 8000 ph $s^{-1}m^{-2}$. The examples are therefore all in the sky dominated regime described by (A.30).

Figure A.2 illustrates the dependence of the S/N on the object velocity for $\dot{S}_o$ = 18.5 m_v. For the moving objects we clearly see that the S/N reaches an asymptotic value and that the maximum decreases for faster objects. A variation of the signal for a moving object changes the maximum S/N but leaves the t_κ constant (Figure A.3) and a different readout noise changes t_κ only (Figure A.4). An example for a very fast moving object (e.g. low orbiting debris particle at 750 km altitude) is given in Figure A.5. (Figure A.2, A.3, A.4 are all plotted to the same scale).

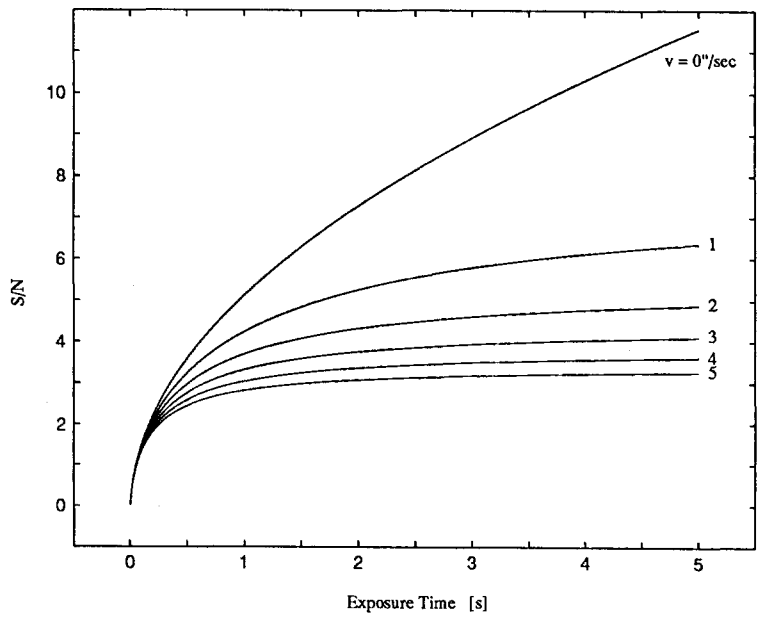

Figure A.2: S/N of moving objects for various velocities. (1 m ZIMLAT telescope, $\dot{S}_o = 18.5$ m_v, $\dot{S}_s = 17.5$ $m_v\,arcs^{-2}$, $S_r = 5$ photons, $v = 5$ arcs s^{-1}).

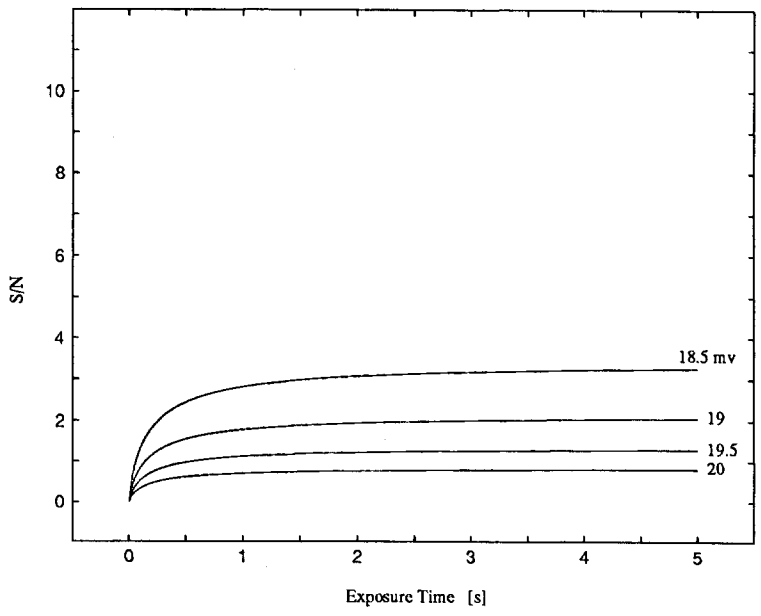

Figure A.3: S/N of moving objects for various magnitudes. (1 m ZIMLAT telescope, $v = 5$ arcs s^{-1}, $\dot{S}_s = 17.5$ $m_v\,arcs^{-2}$, $S_r = 5$ photons).

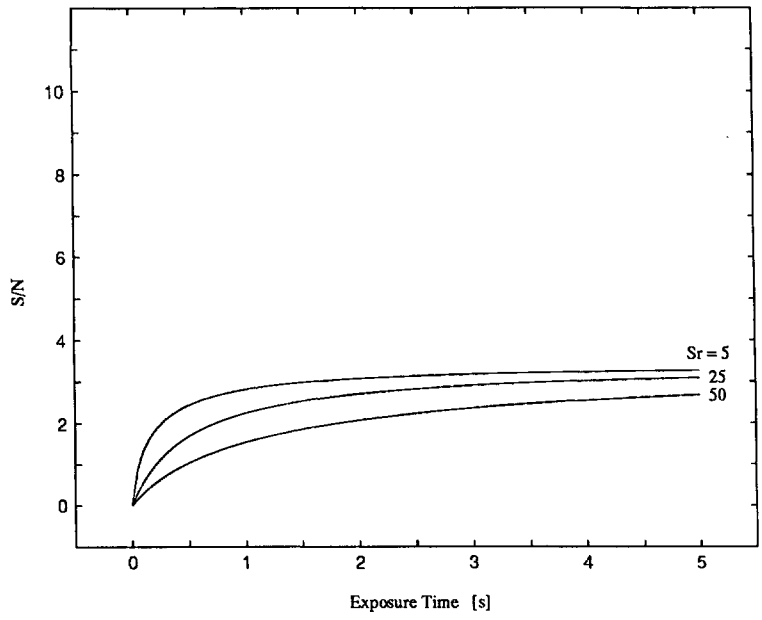

Figure A.4: S/N of moving objects for varying readout noise. (1 m ZIMLAT telescope, $\dot{S}_o = 18.5$ m_v, $v = 5$ arcs s^{-1}, $\dot{S}_s = 17.5$ $m_v\,arcs^{-2}$).

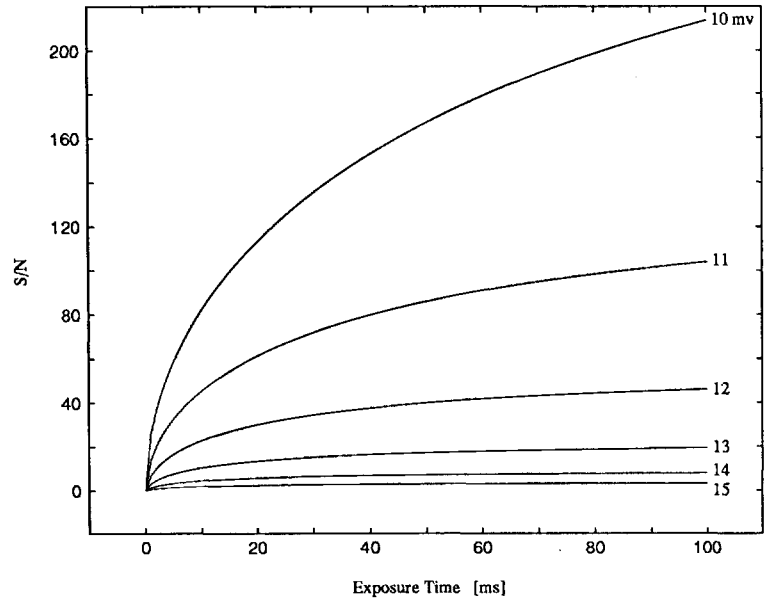

Figure A.5: S/N of fast moving objects for various magnitudes. (1 m ZIMLAT telescope, $v = 2000$ arcs s^{-1}, $\dot{S}_s = 17.5$ $m_v\,arcs^{-2}$, $S_r = 5$ photons).

Appendix B

Glossary of Abbreviations

ADC	Analog to digital converter
ADU	Analog to digital conversion units
BVA	High quality crystal oscillator type
CAMAC	Interface standard for real time data acquisition systems
CCD	Charge coupled device
COGEOS	International Campaign for Optical Observations of Geosynchronous Satellites
CPU	Central processing unit
CQSSP	Coupled Quasar, Satellite, and Star Positioning
CSSP	Coupled Satellite, and Star Positioning
DMA	Direct memory access
ESA	European Space Agency
ESO	European Southern Observatory
FOV	Field of view
GPS	Global Positioning System
HBG	Swiss long wave time signal transmitter
HIPPARCOS	High precision parallax collecting satellite
IAU	International Astronomical Union

IGS	International GPS Service for Geodynamics
ITRF	International Terrestrial Reference Frame
ISIT	Intensified silicon target (TV camera)
MAMA	Multi-anode microchannel array (detector)
MOS	Metal oxide switch
PPM	Position and proper motion star catalogue
PSF	Point spread function
RAM	Random access memory
SCSI	Small computer system interface standard
SLR	Satellite laser ranging
S/N	Signal to noise ratio
VLBI	Very long baseline (radio) interferometry
VMEbus	Computer bus standard
ZIMLAT	Zimmerwald Laser Ranging and Astrometry Telescope (1 m)

Units

arcs	Arcseconds
mas	Milliarcseconds
m_v	Apparent visual magnitudes
Kb	Kilobits
KB	Kilobytes
MB	Megabytes
PPS	Pulse per second

Bibliography

Barrell, H. and J. Sears (1939). The refraction and dispersion of air for the visible spectrum. *Philosophical Transactions of the Royal Society of London 238*, 1–64. Series A, Mathematical and Physical Sciences, A. 786.

Bauersima, I. (1984). Coupled quasar, satellite, and star positioning (CQSSP). Mitteilungen der Satelliten-Beobachtungsstation Zimmerwald 13, University of Berne, Astronomical Institute, Berne, Switzerland.

Beutler, G. (1976). *Eine numerische Methode zur integralen Auswertung von Satellitenbeobachtungen.* Dissertation, University of Bern, Astronomisches Institut der Universität Bern, Bern. Phd thesis.

Beutler, G., I. I. Mueller, and R. E. Neilan (1994). The international GPS service for geodynamics (IGS): Development and start of official service on 1 January 1994. *Bulletin Géodesique 68*(1), 43–51.

Bienaymé, O., C. Motch, M. Crézé, and S. Considère (1988). The compared efficiency of centering algorithms. In S. Debarbat, J. Eddy, H. Eichhorn, and A. Upgren (Eds.), *Mapping the Sky. Past Heritage and Future Directions*, Number 133 in IAU Symposia, Paris, France, June 1–5, 1987, pp. 389–392. International Astronomical Union: Kluwer Academic Publishers.

Bulau, S. (1986). Simulations of various centroiding algorithms. In D. L. Crawford (Ed.), *Instrumentation in Astronomy VI*, Volume 627/2 of *Proceedings of SPIE – The International Society for Optical Engineering*, Bellingham, Washington, USA, pp. 680–687.

Connes, P. (1978). Parallaxes and detection of dark companions: Atmospheric limitations. In F. Prochazka and R. Tucker (Eds.), *Modern Astrometry*, Number 48 in IAU Colloquia, Vienna, Austria, September 11–14, pp. 339–354. International Astronomical Union: Institute of Astronomy (University Observatory), Vienna.

Cousins, A. and D. Jones (1976). Numerical simulation of natural photometric systems. *Memoirs of the Royal Astronomical Society 81*, 1–23.

Eichhorn, H. (1974). *Astronomy of Star Positions.* New York: Frederick Ungar Publishing Co.

ESA (1994). ESOC contract no. 10623/93/D/IM(SC) CCD-algorithms for space debris detection.

ESO-MIDAS (1993). European Southern Observatory – Munich Image Data Analysis System, version NOV93, European Southern Observatory.

Gatewood, G. D. (1987). The multichannel astrometric photometer and atmospheric limitations in the measurements of relative positions. *The Astronomical Journal 94*(1), 213–224.

Goad, L. (1986). Digital image centering. In D. L. Crawford (Ed.), *Instrumentation in Astronomy VI*, Volume 627/2 of *Proceedings of SPIE – The International Society for Optical Engineering*, Bellingham, Washington, USA, pp. 688–692.

Googe, W., H. Eichhorn, and C. Lukac (1970). The overlap algorithm for the reduction of photographic star catalogues. *Monthly Notices of the Royal Astronomical Society 150*, 35+.

Green, R. M. (1985). *Spherical Astronomy*. Cambridge: Cambridge University Press.

Han, I. (1989). The accuracy of differential astrometry limited by the atmospheric turbulence. *The Astronomical Journal 97*(2), 607–610.

Hog, E. (1968). Refraction anomalies: The mean power spectrum of star image motion. *Zeitschrift für Astrophysik 69*, 313–325.

IERS Bulletin B. IERS Central Bureau, Observatoire de Paris, Paris, France.

Janin, G. (1993). Log of Objects Near the Geostationary Ring 12, European Space Operations Centre, Mission Analysis Section, Darmstadt, Germany.

Kjeldsen, H. and S. Frandsen (1992). High-precision time-resolved CCD photometry. *Publications of the Astronomical Society of the Pacific 104*, 413–434.

Kurzyńska, K. (1987). Precision in determination of astronomical refraction from aerological data. *Astronomische Nachrichten 308*(5), 323–328.

Kurzyńska, K. (1988). Local effects in pure astronomical refraction. *Astronomische Nachrichten 309*(1), 57–63.

Lindegren, L. (1978). Photometric astrometry — a comparison of methods for precise image location. See Prochazka and Tucker (1978), pp. 197–217.

Lindegren, L. (1980). Atmospheric limitations of narrow-field optical astrometry. *Astronomy and Astrophysics 89*, 41–47.

Mackay, C. D. (1986). Charge-coupled devices in astronomy. *Annual Review of Astronomy and Astrophysics 24*, 255–283.

McLean, I. S. (1989). *Electronic and Computer-Aided Astronomy.* Ellis Horwood Library of Space Science and Space Technology. Chichester and New York: Ellis Horwood Ltd. / John Wiley & Sons.

Monet, D. (1988). Recent advances in optical astrometry. *Annual Review of Astronomy and Astrophysics 26*, 413–440.

Monet, D. and C. Dahn (1983). CCD astrometry. I. preliminary results from the KPNO 4-m/CCD parallax program. *The Astronomical Journal 88*, 1489–1507.

Monet, D., C. Dahn, H. Harris, H. Ables, C. Luginbuhl, J. Pier, and F. Vrba (1987). Sub-milliarcsecond astrometry of VB10. *Bulletin of the American Astronomical Society 19*, 641. Late Paper Abstracts from the 169^{th} Meeting of the American Astronomical Society, 4–8 January 1987, Pasadena, California.

Morgan, J. and J. Timothy (1988). Status of the MAMA detector. development program. See Robinson (1988), pp. 557–567.

Murray, C. (1983). *Vectorial Astrometry.* Bristol: Adam Hilger Ltd.

NASA, US Air Force, and US Weather Bureau (Eds.) (1962). *U.S. Standard Atmosphere, 1962.* Washington, D.C.: U.S. Government Printing Office.

Nobili, A. M. (1987). An international campaign for optical observations of geosynchronous satellites (COGEOS): Scientific aims and organization. *CSTG Bulletin* (9), 19–30.

Owens, J. C. (1967). Optical refractive index of air: Dependence on pressure, temperature and composition. *Applied Optics 6*(1), 51–58.

Prochazka, F. and R. Tucker (Eds.) (1978). *Modern Astrometry*, Number 48 in IAU Colloquia, Vienna, Austria, September 11–14. International Astronomical Union: Institute of Astronomy (University Observatory), Vienna.

Robinson, L. (Ed.) (1988). *Instrumentation for Ground-Based Optical Astronomy*, The Ninth Santa Cruz Summer Workshop in Astronomy and Astrophysics, July 13 – July 24, 1987, Lick Observatory. Springer-Verlag, New York.

Röser, S. and U. Bastian (1991). *PPM Star Catalogue.* Heidelberg: Astronomisches Rechen-Institut.

Schildknecht, T. (1990). CQSSP: A new technique for establishing the tie between the stellar and quasar celestial reference frames. In J. Huges et al. (Eds.), *Reference System*, Number 127 in IAU Colloquia, Washington D.C., pp. 341–347. International Astronomical Union.

Schildknecht, T., G. Beutler, U. Hugentobler, and A. Verdun (1994). ESA study proposal REFQ/3-7882/93/D/IM CCD-algorithms for space debris detection.

Schildknecht, T., U. Hugentobler, and A. Verdun (1992). Optical astrometry of fast moving objects. In A. Lopez Garcia et al. (Eds.), *Proceedings of the Second International Workshop on Positional Astrometry and Celestial Mechanics*, Valencia, pp. 321–325.

Schildknecht, T., U. Hugentobler, A. Verdun, and G. Beutler (1993). Ground based optical observations of space debris using CCD techniques. In W. Flury (Ed.), *Proceedings of the First European Conference on Space Debris*, Darmstadt, pp. 85–90.

Seidelmann, P. K. (Ed.) (1992). *Explanatory Supplement to the Astronomical Almanac.* Mill Valley, California: University Science Books.

Stanton, R. H., J. W. Alexander, E. W. Dennison, T. A. Glavich, and L. F. Hovland (1987). Optical tracking using charge-coupled devices. *Optical Engeneering 26*(9), 930–938.

Stone, R. (1989). A comparison of digital centering algorithms. *The Astronomical Journal 97*(4), 1227–1237.

TELAS (1992). Zimmerwald 1 meter laser / astrometric telescope. Rapport final de l'étude de définition. Technical report, TELAS.

Turon, C., A. Gómez, F. Crifo, and M. Perrymann (1992). The Hipparcos input catalogue. *Astronomy and Astrophysics 258*, 74–81.

van Altena, W. and L. Auer (1975). Digital image centering. In C. de Jager and H. Nieuwenhuijzen (Eds.), *Image Processing Techniques in Astronomy*, Volume 54 of *Astrophysics and Space Science Library*, Utrecht, March 25–27, pp. 411–418. D. Reidel Publishing Company.

Verdun, A. (1993). Objekterkennung und Zentroidbestimmung bei CCD-Richtungsbeobachtungen. Master's thesis, University of Berne, Astronomical Institute. Druckerei der Universität Bern.

Wright, J. (1982). *The application of imaging charge-coupled devices in astronomy.* Dissertation, University Cambridge, Engl. PhD thesis.

"Geodätisch-geophysikalische Arbeiten in der Schweiz"

(Fortsetzung der Publikationsreihe "Astronomisch-geodätische Arbeiten in der Schweiz") der Schweizerischen Geodätischen Kommission (ab Bd. 34):

34 1982 Lösung von Parameterbestimmungsproblemen in Himmelsmechanik und Satellitengeodäsie mit modernen Hilfsmitteln. G. Beutler. 257 Seiten.

35 1982 Schwere-Anomalien und isostatische Modelle in der Schweiz:
I. Zum Konzept der isostatischen Modelle in Gebirgen am Beispiel der Schweizer Alpen. E. Klingelé und E. Kissling.
II. Aufbau der Kruste und des oberen Mantels in der Schweiz. E. Kissling.
III. Gravimetrische Untersuchungen in der Kontaktzone Helvetikum/Aar-Massiv. P.J.Cagienard, H.-G. Kahle, St. Müller und E. Klingelé. 169 Seiten, 1 Karte.

36 1984 Ein gravimetrisches Krusten-Mantel-Modell für ein Profil im nördlichen Alpenvorland bis an die Ligurische Küste. H. Schwendener. 160 Seiten.

37 1986 Les levés aéromagnetiques de la Suisse. E. Klingelé. 69 Seiten.

38 1986 Lokale Schwerefeldbestimmung und gravimetrische Modellrechnungen im Satelliten (GPS)- Testnetz "Turtmann" (Wallis). I. Bernauer, A. Geiger. 106 Seiten.

39 1989 125 Jahre Schweizerische Geodätische Kommission
I. Bedeutung geodätischer Raumverfahren für Landesvermessung und Geodynamik. (R. Sigl)
II. Beitrag der Geodäsie zur Geodynamik. (H.-G. Kahle)
III. L'état actuel de la recherche sur les movements de l'écorce terrestre en Suisse. (F. Jeanrichard)
IV. Die Satellitengeodäsie im Dienste der globalen Geodynamik. (I. Bauersima)
V. Die Veranstaltungen zum 125 Jahr-Jubiläum der Schweizerischen Geodätischen Kommission. (W. Fischer). 62 Seiten.

40 1989 Integrale Schwerefeldbestimmung in der Ivrea- Zone und deren geophysikalische Interpretation. B. Bürki. 186 Seiten.

41 1990 ALGESTAR satellitengestützte Geoidbestimmung in der Schweiz. U. Marti. 61 Seiten plus Punktprotokolle.

42 1990 Höhensysteme, Schwerepotentiale und Niveauflächen: Systematische Untersuchungen zur zukünftigen terrestrischen und GPS-gestützten Höhenbestimmung in der Schweiz. B. Wirth. 204 Seiten.

43 1990 Gravimetrisches Geoid der Schweiz: Potentialtheoretische Untersuchungen zum Schwerefeld im Alpenraum. A. Geiger. 231 Seiten.

44 1991 Rapid Differential Positioning with the Global Positioning System (GPS). E. Frei. 178 Seiten.

45 1992 Dreidimensionales Testnetz Turtmann 1985-1990 Teil I. F. Jeanrichard (Hrsg.) Autoren: A.Geiger, H.-G. Kahle, R. Köchle, D. Meier, B. Neininger, D. Schneider, B. Wirth. 183 Seiten.

46 1993 Orbits of Satellite Systems in Space Geodesy. M. Rothacher. 243 Seiten.

47 1993 NFP 20. Beitrag der Geodäsie zur geologischen Tiefenstruktur und Alpendynamik. H.-G. Kahle (Hrsg.) Autoren: I. Bauersima, G. Beutler, B. Bürki, M. Cocard, A. Geiger, E. Gubler, W. Gurtner, H.-G. Kahle, U. Marti, B. Mattli, M. Rothacher, Th. Schildknecht, D. Schneider, A. Wiget, B. Wirth. 153 Seiten plus 90 Seiten Anhang.

48 1994 Ionosphere and Geodetic Satellite Systems: Permanent GPS Tracking Data for Modelling and Monitoring: Urs Wild, 155 Seiten.

49 1994 Optical Astrometry of Fast Moving Objects using CCD Detectors : Thomas Schildknecht, 200 Seiten.